NEAR-SOURCE WIND DEVELOPMENT AND POLLUTION DISPERSION OVER COMPLEX TERRAIN

Submitted in partial fulfillment of the requirements for

the degree of

Doctor of Philosophy

in

Department of Mechanical Engineering

Zhihao Li

B.S., School of Naval Architecture and Ocean Engineering,
Huazhong University of Science and Technology

M.S., Department of Civil, Architectural & Environmental Engineering,
The University of Texas at Austin

Carnegie Mellon University Pittsburgh, PA

August 2021

ACKNOWLEDGEMENTS

I am thankful for my four years spent at Carnegie Mellon University. Working with so many great people in this community, I genuinely appreciate everything we shared, and I will enshrine the best memories in my heart wherever I go. It is time for me to say goodbye and start a new journey in my life now.

Special thank you to Professor Satbir Singh, my research advisor, and mentor for offering indispensable guidance and inspiration for my research. During my Ph.D. study, he was extensively involved in each step of my research and gave me professional and knowledgeable support. His positive attitude towards any barrier, as well as his strictness on research, helped me grow a lot on my path of becoming a mature researcher. He also helped me with my career search and introduced me to his connections in the industry. I want to thank Professor Albert Presto, my co-advisor, for giving me so many insightful and earnest suggestions for my research. The support and encouragement from both of my advisors have accompanied me in the most challenging times during my Ph.D. I learned a lot from them on conducting research and big-picture thinking.

I also want to thank the rest of my committee members: Professor Peter Adams, Professor Ryan Sullivan, and Hamish Gordon. I feel so lucky that they could serve on my thesis committees. They provided me with the help to choose the right direction of research and complete my dissertation.

Also, I would like to express my sincere gratitude to Allegheny County Health Department (ACHD), without whose sponsorship I could not finish this study. Special thanks to Tony Sadar and Jason Maranche of ACHD. I would also like to acknowledge the support from the Extreme Science and Engineering Discovery Environment (XSEDE) under grant number ASC110028 through the Pittsburgh Supercomputing Center (PSC) and other computational resources used in

this research, including the Arjuna cluster from the Viswanathan Research Group and CAPS cluster.

I also would like to offer my sincere thanks to the staff in the Mechanical Engineering Department, Chris Hertz and Edward R Wojciechowski Jr. I appreciate all the help throughout my Ph.D. study. During the COVID-19 pandemic, Ed helped me maintain my servers so that I can safely work from home. I would like to thank my friends: Rebecca Tanzer-Gruener and Xinjia Yu, for helping me collect weather data and fly the drone and Wentai Zhang for introducing me to scikit-learn for analyzing data.

Lastly, my genuine gratefulness goes to my family for their unconditional love. I am fortunate that all the wonderful people around me helped me through this meaningful period of my life.

ABSTRACT

Starting from 2018, the research group CAPS (Center for Atmospheric Particle Studies) from Carnegie Mellon University has been conducting extensive measurement campaigns to study the wind development and pollution dispersion near Pittsburgh. A monitoring network of five anemometers and four multi-pollutant sensors were deployed around the Clairton Coke Works, a major source of sulfur dioxide (SO_2) in the nearby region. While the anemometers continuously and simultaneously measured wind speed and direction at fixed heights, vertical wind profiles were measured by flying a drone mounted with a 3D anemometer. To better understand the atmospheric dispersion of pollution, five tracer release experiments were conducted by emitting nitrous oxide (N_2O) on the ground level at a constant emission rate and sampling along the coverage route with a mobile lab on a van.

Surrounding the coke plant, a $6.4\,km \times 6.4\,km$ computational study domain with a height of $1\,km$ was created based on the digital terrain model. A map of variable aerodynamic roughness length was created based on the land use pattern to account for the surface structures. The meteorological data from the nearby airport, sounding and reanalysis data were considered to obtain proper boundary conditions. Using Computational Fluid Dynamics (CFD), the Reynolds-Averaged Navier-Stokes (RANS) equations together with the $k-\varepsilon$ equations and the scalar transport equation were solved under various meteorological conditions over the complex terrain.

For steady-state simulations of wind development, comparisons show that predicted wind speeds are reasonably close to the measured mean wind speeds. The CFD model also predicts the correct trend of varying wind speeds across multiple monitoring sites. However, there are situations when the measured data is strongly influenced by local effects, such as the buildings and tree canopy around the anemometers. After such effects are considered, the predicted wind speeds

become closer to the measured ones. The predictions for atmospheric dispersion of N_2O under neutral conditions show good agreement with the mean values of multiple passes from tracer release experiments. A total of 28 cases of steady-state CFD simulations of hourly SO_2 dispersion were performed when the monitored SO_2 concentrations within the domain were high. Different sampling techniques and statistical performance measures were used when evaluating CFD model predictions with those from measurements and the predictions from the current regulatory model, AERMOD. Comparisons show that the developed CFD model that incorporates atmospheric boundary layer characteristics, complex terrain, and multiple high-temperature sources successfully predicts the steady-state SO_2 plume from the coke plant. The overall performance of the developed CFD model is better than that of the regulatory model, AERMOD. AERMOD sometimes predicts the correct concentration due to the wrong reason. To further investigate the sub-hourly development of SO_2 plumes, transient simulations that update wind direction at a 1-minute resolution for multiple hours were performed. However, the predicted concentrations toward the end of the simulated hour from the transient CFD simulations cannot be fully understood yet. It is recommended that the steady-state CFD model should be used in conjunction with AERMOD for investigations of SO_2 dispersion near the plant.

TABLE OF CONTENTS

ACKNOWLEDGEMENTS 2
ABSTRACT 4
TABLE OF CONTENTS 6
LIST OF TABLES 9
LIST OF FIGURES 10
NOMENCLATURE 18
Chapter 1 Introduction and background 20
1.1 Atmospheric boundary layer 20
1.2 Traditional modeling of pollution dispersion 24
1.2.1 Gaussian-based dispersion modeling 24
1.2.2 Photochemical modeling 26
1.3 CFD modeling 28
1.4 Site description 32
1.5 Objectives of current research 35
Chapter 2 Numerical model 38
2.1 Computer code 38
2.2 Governing equations 39
2.2.1 Continuity equation 39
2.2.2 Momentum equation 39
2.2.3 Equation for pressure 40
2.2.4 $\boldsymbol{k-\varepsilon}$ turbulence model 41
2.2.5 Equation for energy 42
2.2.6 Passive scalar transport equation 43
2.3 Monin-Obukhov similarity theory 45
Chapter 3 Measurements and data analysis 48
3.1 Data sources 48
3.1.1 Sounding data 49
3.1.2 Reanalysis data 50
3.1.3 Data from stationary monitors 54
3.2 Selection of new monitoring sites 55
3.3 Analysis of weather and pollution data 59
3.3.1 Characteristics of wind 60

3.3.2 Atmospheric inversion 65
3.3.3 Statistics of SO_2 concentration 66
3.4 Tracer release measurements 70
Chapter 4 Model setup 76
4.1 Geometry and mesh 76
4.2 Variable aerodynamic roughness length 79
4.3 Inlet boundary conditions 81
4.3.1 Curve fitting to obtain vertical profiles 81
4.3.2 Specific setup for steady-state and transient simulations 88
4.4 Surface boundary conditions 91
4.5 Stack exit boundary conditions 94
4.6 Other boundary conditions 99
Chapter 5 Model validation 101
5.1 Verification of CFD model for 2D flow 101
5.2 Validation of 3D CFD model 103
5.2.1 Comparison with wind measurements 103
5.2.2 Comparison with tracer release measurements 110
5.3 Simulations of SO_2 dispersion 113
5.3.1 Sampling techniques 113
5.3.2 Simulations using the steady-state model 115
5.3.3 Detailed comparisons of CFD and AERMOD 122
5.3.4 Simulations using the transient model 125
5.4 Recommendations for model deployment 132
Chapter 6 Exploratory studies using the CFD model 134
6.1 Effects of the terrain complexity 134
6.1.1 Irregular topography 134
6.1.2 Variations in land use 136
6.2 Effects of atmospheric stability 139
6.3 Importance of ground cooling 147
Chapter 7 Conclusion and future work 152
References 156
Chapter 8 Appendix 163
8.1 Sensitivity test of the CFD model 163
8.1.1 Effects of stack exit conditions 163

8.1.2 Effects of variable physical properties of air 165
8.1.3 Mesh independence study 167
8.2 Cavity effect at the Lincoln site 171
8.3 Heat island effect at the plant site 173

LIST OF TABLES

Table 1.1: Pairs of model constants used in different $k-\varepsilon$ models..... 30
Table 3.1: Comparison between NARR and ERA5 reanalysis data. 51
Table 3.2: Descriptions of wind measurement sites within the study domain that are used for model validation..... 56
Table 3.3: Statistics of inversion strength, height, and frequency over recent years. 66
Table 4.1: The color and number legend for different land cover classes and the corresponding mean aerodynamic roughness length. 81
Table 4.2: Stack parameters for SO_2 modeling. 94
Table 4.3: Boundary conditions specified in the CFD model. 100
Table 5.1: Parameters that describe different stability classes. 101
Table 5.2: Summary of validation cases for wind development over the complex terrain. 110
Table 5.3: Summary of the 28 cases of SO_2 dispersion simulations. 116
Table 5.4: Summary of the differences between case 13 and case 20. 124
Table 5.5: Computational resources needed for steady-state and transient simulations..... 133
Table 6.1: Summary of the four cases of different wind conditions and inversion strengths..... 145
Table 8.1: Summary of different mesh configurations in the mesh independence study. 167

LIST OF FIGURES

Figure 1.1: The structure of the atmosphere and the simplified vertical absolute temperature profiles over the diurnal cycle, adapted from Stull [8] and Sadar [9]..... 21
Figure 1.2: Relative spectral energy (i.e., energy per unit frequency) as a function of time scale, adapted from Stull [8]. The energy gap can be identified between the synoptic scales and the turbulent scales..... 22
Figure 1.3: Time series of the horizontal wind speed and wind direction from a ground win sensor using raw data and different averages. 23
Figure 1.4: Air pollutant dispersion from an elevated point source in a Gaussian dispersion model, adapted from Oke et al. [17]. 25
Figure 1.5: The Eulerian and Lagrangian approaches that are used to model pollution dispersion, adapted from McMurry et al. [22]. 27
Figure 1.6: All six monitoring locations for SO_2 in Allegheny County. The Downtown Pittsburgh location does not have a monitor, but it is shown as a reference. 33
Figure 1.7: SO_2 1-hour design values from EPA standards and measurements reported by the monitors in Allegheny County over recent years [57,58]. 34
Figure 1.8: A photo showing the operation of the U.S. Steel's Clairton Coke Works [59]. After being released from the plant, SO_2 travels in the form of a plume that widens with distance from the plant. SO_2 exits the stacks with a much higher temperature than that of the ambient air..... 34
Figure 1.9: A map showing the county airport (KAGC), Liberty monitor, and the coke plant. The wind rose generated using wind speed and direction from KAGC shows the dominant southwest wind direction. 35
Figure 1.10: Height contours of the $6.4\ km \times 6.4\ km$ study domain centered around the Liberty monitor. The coke plant is located southwest of the Liberty monitor. 36
Figure 3.1: Locations of different meteorological data sources outside the computational domain. These sources are considered to be permanent, and they are used to generate vertical boundary profiles to be specified at the inlet of the domain. 48
Figure 3.2: Typical examples of two stability classes that can be determined from the sounding data using the Skew-T plot. Red solid line: air temperature. Red dash line: dry adiabats. Black solid line: equal temperature from $1000\ mb$. 50
Figure 3.3: Comparison between the vertical profiles of wind speed from original reanalysis data

(NARR and ERA5) and sounding data. The first point from sounding is used to illustrate the interpolation of reanalysis data based on the height of sounding data to create a paired dataset for $R2$ analysis of same height levels. The horizontal dash line intersects with the straight lines from the reanalysis data, and the points of intersection (shown as circles) will be compared with the sounding data (shown as solid dots). 51
Figure 3.4: Comparison between the reanalysis data with the sounding data for wind speed. 53
Figure 3.5: Comparison between the reanalysis data with the sounding data for air temperature. 54
Figure 3.6: Wind measurements in the study domain for CFD model validation. 55
Figure 3.7: Colocation of two anemometers at the Lincoln site to find out the reasons for low wind speeds. 57
Figure 3.8: Time series of wind speed and wind direction from the two anemometers and the drone at the Lincoln site. 58
Figure 3.9: Vertical profiles of wind speed over dense canopy from drone measurements at the Lincoln site and schematic of the vertical profile from Stull [8]. 59
Figure 3.10: Time series of hourly averaged wind speed and wind direction from different locations. Each line shows the mean value as solid line $\pm$ the standard deviation (STD) as shade. 60
Figure 3.11: Wind roses and mean wind speed at different sites. 62
Figure 3.12: Mean vertical profiles of wind speed at each hour over a six-month period. Time is shown in Zulu. The local Eastern Standard Time zone is 4 hours behind Zulu time. 63
Figure 3.13: Normalized mean vertical profiles of wind speed from SODAR using 2 clusters... 63
Figure 3.14: Standard deviation of the hourly wind direction using data at Liberty and the SODAR site for all wind directions. 64
Figure 3.15: Standard deviation of the hourly wind direction at $40\ m$ AGL for different wind speed ranges. 65
Figure 3.16: Standard deviation of the hourly wind direction using data at Liberty and the SODAR site filtered for southwest wind directions. 65
Figure 3.17: SO_2 measurement in the study domain for CFD model validation. 67
Figure 3.18: SO_2 roses and mean SO_2 concentration at different sites and their straight-line distances to the center of the coke plant. 68

Figure 3.19: Time series of wind speed, wind direction, SO_2 measurements, and emission rate from 01/02/2019 to 01/04/2019. Two time periods with high SO_2 concentrations can be identified. One is around 03:00, 01/03/2019 and another is at 04:00, 01/04/2019. 69
Figure 3.20: The driving paths and mean concentrations of N_2O above the ambient level of three unique tracer release experiments. The release setup consists of a cylinder that stores N_2O in the liquid phase, a flow meter that controls the emission rate, and rubber hoses that connect the cylinder outlet, the flow meter, and the gas exit on top of a 2-meter pole. The red star on the map shows the release location. 71
Figure 3.21: Time series of N_2O measurements in different passes during a release. The rightward arrow (→) indicates the sampling van moves to the east, and the leftward arrow (←) indicates the van modes to the west on the route. 72
Figure 3.22: N_2O measurements during each pass and the mean of these passes. A Gaussian plume is created by fitting the mean pass data shown as the solid curve. 73
Figure 3.23: Weather condition reported by different sensors during trace release 1. 74
Figure 3.24: Weather condition reported by different sensors during trace release 2. 74
Figure 3.25: Weather condition reported by different sensors during trace release 3. 75
Figure 4.1: Top views of the complex terrain in different stages of the process to obtain computational mesh of the complex terrain. 77
Figure 4.2: Different views of the computational mesh. 78
Figure 4.3: Top views of the mesh show the difference in mesh quality. 78
Figure 4.4: The conversion from land cover data to aerodynamic roughness length that will be used in the CFD model to include the effects of different surface structures. 79
Figure 4.5: Illustration of steps to obtain the variable roughness map. The figure on the left shows the southwest corner of the study domain which uses the land cover map and satellite image from Google Earth as background. The computational grid from CFD is overlaid on top. The grid centroids are shown as ⦿. 80
Figure 4.6: Inconsistency between the measurements and the theoretical wind profile when calculating the profile with one reference location. 82
Figure 4.7: Flowchart of the curve-fitting procedure used in the present work to obtain boundary conditions at the inlet of the study domain. 83
Figure 4.8: Fitting wind data to obtain the wind profiles can lead to a bad agreement between the

temperature data from measurements and the calculated temperature profile. 85
Figure 4.9: Fitting two profiles simultaneously can minimize the errors for both the vertical profiles wind speed and temperature. 86
Figure 4.10: Evaluation of the profiles from curve fitting and comparison with measurements from soundings..... 87
Figure 4.11: Fitted profiles in comparison with available data. 88
Figure 4.12: The mean STD data from Liberty and SODAR can be fitted to a smooth curve to estimate wind direction variations at different height levels. 89
Figure 4.13: Tow cases of variable wind direction along with height. Case 1 shows a larger wind direction value from the 1-minute Liberty data than the 1-hour data (shown as "Direction: 1 Hour"). The distribution of wind direction in the vertical direction used in the transient simulation will make the wind directions at higher levels closer to the 1-hour wind direction. .. 90
Figure 4.14: Changes in weather conditions within two consecutive hours are generally small as the vertical profiles of wind speed and air temperature for the two cases are close to each other. 91
Figure 4.15: Stacks are shown with Google Earth and the representation in the computational mesh in CFD. 95
Figure 4.16: Schematic of the difference in stack exit face between the real stack and the counterpart used in the CFD model. 96
Figure 4.17: Dimensions of different cells near a stack exit that range from $16\ m$ to $4\ m$..... 97
Figure 4.18: Temperature contour and velocity vectors colored by the vertical component (Uz) near one stack exit to show the effects of buoyant plume. 98
Figure 4.19: Time series of the 1-hour mean SO_2 concentration from the Liberty monitor and the total emission rate from the coke plant scaled at 1-hour level..... 99
Figure 5.1: The $5000\ m\ \times 500\ m$ 2D domain used to verify the horizontal homogeneity of the CFD model..... 101
Figure 5.2: Vertical profiles extracted at different locations away from the inlet show horizontal homogeneity under different conditions. 102
Figure 5.3: Neutral case 1, 04/13/2018 0 Zulu, wind direction 240°. 105
Figure 5.4: Neutral case 2, 08/02/2018 0 Zulu, wind direction 201°. 106
Figure 5.5: Neutral case 3, 10/03/2018 0 Zulu, wind direction 252°. 106

Figure 5.6: Stable case 1, 04/11/2018 12 Zulu, wind direction 204°. 108
Figure 5.7: Stable case 2, 10/23/2018 12 Zulu, wind direction 205°. 109
Figure 5.8: Stable case 3, 11/25/2018 12 Zulu, wind direction 239°. 110
Figure 5.9: Contours of model predicted N_2O concentration compared with measurements for release 1 under northwest wind direction. 111
Figure 5.10: Contours of model predicted N_2O concentration compared with measurements for release 2 under southwest wind direction. 112
Figure 5.11: Contours of model predicted N_2O concentration compared with measurements for release 3 under northwest wind direction. 112
Figure 5.12: The sampling cylinder and arc used in CFD to account for the uncertainty in wind direction specified at the inlet. 113
Figure 5.13: The schematic to show the creation of the sampling arc. The yellow lines and blue lines are auxiliary lines to identify the two ends of the arc (in red). The Liberty monitor lies in the middle of the sampling arc. 114
Figure 5.14: Summary of the 5-hour simulation period for Jan. 4, 2019. Wind speeds and directions from KAGC, Liberty, and the CFD model are shown. SO_2 concentrations from CFD, AERMOD using the sampling arc are compared with those of measurements. CFD results for SO_2 concentrations are presented with the box, whose values range from $1/10$ of the value extracted at the Liberty monitor to the maximum value on the arc. The maximum values from CFD are connected as a solid line in red, and the maximum values from AERMOD are connected as a solid line in purple. The total emission rate from the plant is also presented. ... 115
Figure 5.15: summary of the 5-hour simulation period for Apr. 3, 2019. Wind speeds and directions from KAGC, Liberty, and the CFD model are shown. SO_2 concentrations from CFD, AERMOD using the sampling arc are compared with those of measurements. CFD results for SO_2 concentrations are presented with the box, whose values range from $1/10$ of the value extracted at the Liberty monitor to the maximum value on the arc. The maximum values from CFD are connected as a solid line in red, and the maximum values from AERMOD are connected as a solid line in purple. The total emission rate from the plant is also presented. ... 116
Figure 5.16: Comparison between predictions using different sampling methods and measurements at Liberty for SO_2 concentrations of the 28 cases. 117
Figure 5.17: The scatter plot of all 28 cases using the sampling cylinder from two wind data

input settings in AERMOD. The calculated statistical measures are also shown. 119
Figure 5.18: The scatter plot of all 28 cases using the sampling cylinder from CFD and AERMOD. The calculated statistical measures are also shown. 120
Figure 5.19: The scatter plot of all 28 cases using the sampling arc from CFD and AERMOD. The calculated statistical measures are also shown. 121
Figure 5.20: Q-Q plot for the 28 cases. “Liberty” shows the monitored data. “Liberty: CFD” shows the CFD predictions at the exact Liberty site. “Liberty: AERMOD” shows the AERMOD predictions at the exact Liberty site. “Cylinder: CFD” shows the maximum CFD predictions using the sampling cylinder. 122
Figure 5.21: Vertical profiles used in CFD and AERMOD for case 10. 123
Figure 5.22: Vertical profiles used in CFD and AERMOD for case 13. 124
Figure 5.23: Vertical profiles used in CFD and AERMOD for case 20. 124
Figure 5.24: Predicted wind direction variation within 1 hour along the diagonal line when updating the inlet wind direction uniformly at every 1 minute (strategy 1). 127
Figure 5.25: Predicted wind direction variation within 1 hour along the diagonal line for variable inlet wind direction along with height (strategy 2). 127
Figure 5.26: Comparison of time series in wind direction and SO_2 concentration between Liberty measurements and the results from transient simulation using strategy 1. For CFD, the extracted values at the Liberty monitor are used in the time series. The dash lines in wind direction show the 1-hour average values. The dash lines in SO_2 concentration show the 40-minute average values. 128
Figure 5.27: Comparison of time series in wind direction and SO_2 concentration during 08-09Z 04/03/ between Liberty measurements and the results from transient simulation. For CFD, the extracted values at the Liberty monitor are used in the time series. The dash lines in wind direction show the 1-hour average values. The dash lines in SO_2 concentration show the 40-minute average values. White star: Liberty site. Yellow star: Liberty Way site. Wind vectors on the ground levels are also shown. 129
Figure 5.28: Comparison of time series in wind direction and SO_2 concentration during 04-05Z 02/03/2019 between Liberty measurements and the results from transient simulation. For CFD, the extracted values at the Liberty monitor are used in the time series. The dash lines in wind direction show the 1-hour average values. The dash lines in SO_2 concentration show the 40-

minute average values. White star: Liberty site. Yellow star: Liberty Way site. Wind vectors on the ground levels are also shown. 130
Figure 6.1: Contours of height above the ground and wind vectors colored by the magnitude of the vertical wind speed..... 134
Figure 6.2: Contours of horizontal wind speed and wind direction at $10\ m$ AGL..... 135
Figure 6.3: Contours of horizontal wind speed and wind direction at $200\ m$ AGL..... 136
Figure 6.4: Contours of horizontal wind speed (m/s) in the first cells AGL using variable and uniform $z0$. 137
Figure 6.5: Contours of turbulent diffusivity ($m2/s$) in the first cells AGL using variable and uniform $z0$. 137
Figure 6.6: Vertical profiles up to $700\ m$ AGL for different variables at different locations using variable and uniform $z0$..... 138
Figure 6.7: Vertical profiles to $170\ m$ AGL for different variables at different locations using variable and uniform $z0$..... 138
Figure 6.8: Vertical profiles to $700\ m$ AGL for different variables at different locations under stable and neutral conditions..... 139
Figure 6.9: Contours of TKE ($m2/s2$) under different thermal stability classes and terrain types. 141
Figure 6.10: SO_2 concentration contour and streamtraces under different thermal stability conditions over different terrain types. 142
Figure 6.11: Turbulent diffusivity ($m2/s$) contour under different thermal stability conditions. 143
Figure 6.12: Fitted vertical profiles that are specified at the inlet for the four cases of different wind conditions and inversion strengths..... 143
Figure 6.13: Contours of SO_2 concentration (in log scale) on the ground and on the slice that passes through the plant center and aligns with the inlet wind direction..... 144
Figure 6.14: Contours of SO_2 concentration (in linear scale) on the ground the plume created with isosurfaces of 20 ppb. Two vertical lines up to $1000\ m$ are shown at the monitoring sites. 144
Figure 6.15: Box plots of the measurements and the CFD predictions for the 4 cases. The dash line in the box of Liberty measurements shows the mean value. 145

Figure 6.16: Box plots of the measurements and the CFD predictions normalized by emission rates for the 4 cases. 145
Figure 6.17: Schematic of the mountain-valley breezes that are formed at different times of the day due to uneven heating of air. 147
Figure 6.18: Schematic of the 2D simulation of downdraft flow under calm wind speed and a constant ground cool rate. 149
Figure 6.19: Comparison of SO_2 mass fraction at different hours for the two cases. 151
Figure 6.20: Comparison of turbulent viscosity ($m2/s$) at different hours for the two cases. 151
Figure 8.1: Extraction lines across the computational domain to be used in the sensitivity test of the CFD model. 163
Figure 8.2: Comparison of results from the annualized exit condition and ambient condition. . 164
Figure 8.3: Curve fitting results of different physical properties of air as a function of temperature. 166
Figure 8.4: Comparison of SO_2 concentration distribution using constant properties and temperature-dependent properties. 167
Figure 8.5: Comparison of results from Mesh-1, Mesh-2, and Mesh-3. 169
Figure 8.6: Comparison of results from Mesh-2, Mesh-4, and Mesh-5. 170
Figure 8.7: Wind speed contours with the bare ground and the displaced ground. 172
Figure 8.8: Predicted profiles at the Lincoln site using the simplified 2D terrain. 172
Figure 8.9: Heat flux studies on the coke plant that can be related to the heat island effect. 174
Figure 8.10: Representation of the heat island effect in CFD and the wind profile. 174
Figure 8.11: Velocity vectors and magnitude contours on the ground and slice cut along dominant wind direction with the heat island on and off. 175

NOMENCLATURE

Abbreviations

ABL	Atmospheric Boundary Layer
AGL	Above Ground Level
CAMx	Comprehensive Air quality Model with extensions
CFD	Computational Fluid Dynamics
CMAQ	Community Multiscale Air Quality
CTM	Chemical Transport Model
EPA	The United States Environmental Protection Agency
ERA5	ECMWF Reanalysis v5
FAC2	Factor of Two of Observations
FB	Fractional Bias
KAGC	Allegheny County Airport
LES	Large Eddy Simulations
MG	Mean Bias
MOST	Monin–Obukhov Similarity Theory
MRLC	Multi-Resolution Land Characteristics
NAAQS	National Ambient Air Quality Standards
NARR	North American Regional Reanalysis
NLCD	National Land Cover Database
NMSE	Normalized Mean Square Error
NWP	Numerical Weather Prediction
NWS	National Weather Service
PASDA	Pennsylvania Spatial Data Access
PBL	Planetary Boundary Layer
PISO	Pressure Implicit with Splitting of Operators
PM	Particulate Matter
RAMP	Real-time Affordable Multi-Pollutant
RANS	Reynolds-Averaged Navier-Stokes
SIMPLE	Semi Implicit Methods Pressure Linked Equations
SODAR	Sound Detection and Ranging
STD	Standard Deviation
TKE	Turbulent Kinetic Energy
WRF	Weather Research and Forecasting

Symbols

k	Turbulent kinetic energy
ε	The dissipation rate of turbulent kinetic energy
c_i	Mean concentration of species i
x, y, z	Cartesian coordinate, z is the height above the ground
H_s, h_s, Δh	Effective stack height, actual stack heigh, and the plume rise height
E	Emission rate

$\hat{\sigma}_y$, $\hat{\sigma}_z$	Lateral and vertical standard deviations of the concentration field
t	Time
K	Turbulent diffusion coefficient in the continuity equation for species
i, j	Indices in index notation
u, $\bar{u}$	Mean velocity vector
τ , τ_t	Mean stress tensor and Reynolds stress tensor
ρ	Density
p_{rgh}	Pseudo hydrostatic pressure
p	Total pressure
g	Gravitational acceleration
μ, μ_t	Dynamic viscosity, turbulent dynamic viscosity
ν, ν_t	Kinematic viscosity, turbulent kinematic viscosity
T, θ	Absolute and potential temperature
G_k, G_b	Production of turbulence due to mechanical shear, buoyancy
β	Coefficient of thermal expansion
C_{μ},$C_{\varepsilon 1}$,$C_{\varepsilon 3}$, $C_{\varepsilon 3}$, σ_k, σ_{ε}	$k-\varepsilon$ model constants
u_1, u_2, u_3	Horizontal (u_1, u_2) and vertical (u_3) component of velocity vector
h	Specific enthalpy
K	Kinetic energy per unit mass in the energy equation
q	Heat source or sink per unit mass
α , α_t, α_{eff}	Laminar, turbulent, and effective thermal diffusivities
Pr, Pr_t	Prandtl number and turbulent Prandtl number
D , D_t, D_{eff}	Laminar, turbulent, and effective mass diffusivity
Sc , Sc_t	Schmidt number and turbulent Schmidt number
ϕ	Passive scalar, mass fraction between the scalar and fluid
S_{ϕ}	Source of passive scalar per unit mass
R	Ideal gas constant
u_*	Velocity scale, friction velocity
θ_*	Temperature scale
L	Obukhov length
c_p	Specific heat
τ_w	Wall shear stress
ν_{tp}	Turbulent kinematic viscosity on the wall
κ	Von Karman constant
θ_0	Potential temperature on the ground level
ϕ_{ε}, ϕ_m	Parameters in similarity theory
K_s	Sand grain roughness height
$\bar{C}$, C_p	Average over the dataset and model prediction
k	Thermal conductivity as in physical properties of air

Chapter 1
Introduction and background

The atmosphere is essential for life on Earth. As the state of the atmosphere, weather consists of several meteorological parameters, including air temperature, wind, pressure, humidity, etc. The atmosphere is constantly evolving. The uneven heating of the earth by the sun causes air temperature differences and leads to the wind. Due to natural sources and anthropogenic activities, air pollutants are released into the atmosphere. With sufficient concentrations, they can lead to air pollution at different levels. Air pollution may harm the health of humans, animals, plants, or even microbes. In addition, it is capable of damaging infrastructure and ecosystems. Air pollutant concentration has a close relationship with the meteorological parameters [1–4], among which local wind plays a significant role in determining air pollution levels. Wind speed is considered an essential indicator for improving air quality in polluted areas [5–7]. In addition, it is widely established that different vertical temperature distributions in the atmosphere lead to different behavior of pollutant dispersion in the atmosphere. Thus, the ability to predict the effects of wind and temperature variation in the atmosphere has remarkable impacts on understanding the air quality.

1.1 Atmospheric boundary layer

The atmosphere is comprised of multiple layers, and the lowest of them is the troposphere. The atmospheric boundary layer (ABL) is defined as the lowest part of the troposphere, which is directly influenced by the earth's surface. It is often referred to as the planetary boundary layer (PBL) or simply the boundary layer. Turbulence, generally referred to as rapid and random fluctuations of wind velocity, plays a crucial role in dispersing pollutants. Within the ABL, wind shear caused by the drag near the ground and vertical air movement resulting from buoyant forces

generate turbulence. Air pollutants are transported by the wind and mixed by turbulence. The structure and the atmosphere and its evolution over the diurnal cycle are shown in Figure 1.1.

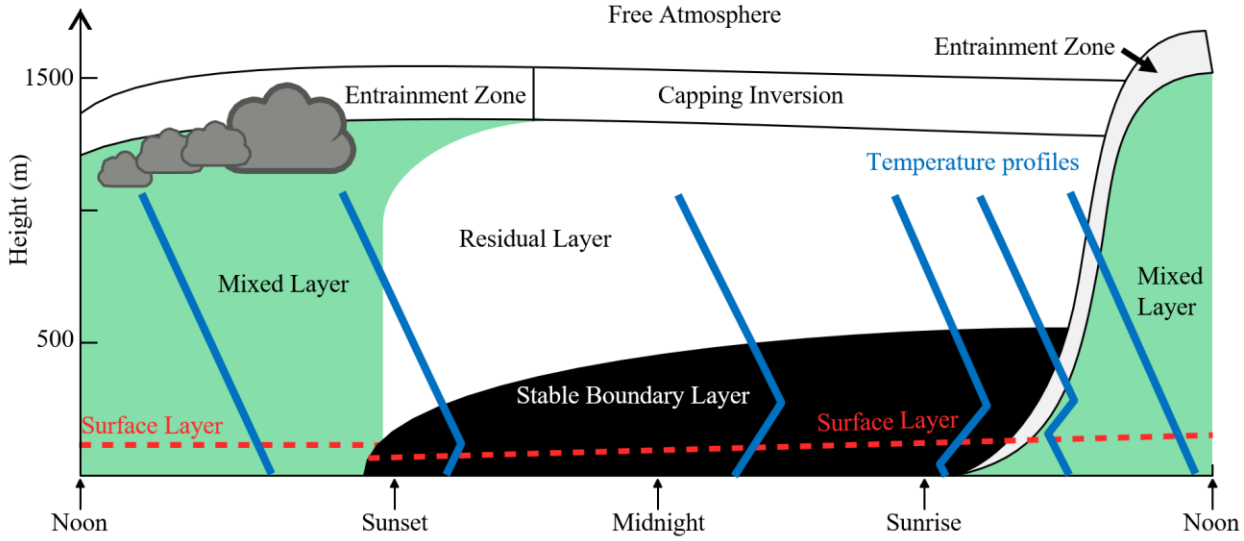

Figure 1.1: The structure of the atmosphere and the simplified vertical absolute temperature profiles over the diurnal cycle, adapted from Stull [8] and Sadar [9].

Right above the ABL, the capping inversion is characterized by strong inversion. "Inversion" indicates that the potential temperature of air increases with height. The capping inversion acts as a lid to suppress the rising of thermals. Turbulence within the ABL has difficulty penetrating the capping inversion and is thus considered to be confined. During fair weather, the ABL evolves over the course of a diurnal cycle due to surface heating by the sun during the day and surface cooling at night. The thickness of the ABL varies in space and time. Typically, it is about 1 to 2 km thick [10]. The entrainment zone above the ABL means the free atmosphere is entrained into the top of the ABL.

The structure and behavior of the flow within the ABL can be characterized by atmospheric stability. Atmospheric stability describes the tendencies of the vertical movement of air parcels. On a sunny day with light wind, the surface is warmer than the air, and the boundary layer is unstable. Heated air rises from the ground and keeps moving, contributing to the production of

turbulent kinetic energy and the mixing of air and pollutants. Neutral boundary layers form under windy conditions with a slight difference in temperature between the ground and air. The ABL is stable when the ground surface is colder than the air, and such condition usually develops during a clear night over land. Stable conditions (equivalent to inversions) are long known for causing increasing concentrations of pollutants.

The flow in the ABL is turbulent as characterized by the existence of a wide range of scales of the motion in terms of space and time, by the random features of the state variables (e.g., velocity, temperature), etc. [11]. Figure 1.2 shows an example of the spectrum of wind speed near the ground. There is a clear gap between the turbulent scales and synoptic scales (in the order of $10^5 - 10^7\ m$). Turbulence has time scales of up to 30 minutes and several hours. Motions to the left of the gap are considered the mean flow, while motions to the right constitute turbulence, which causes the wind speed to change constantly.

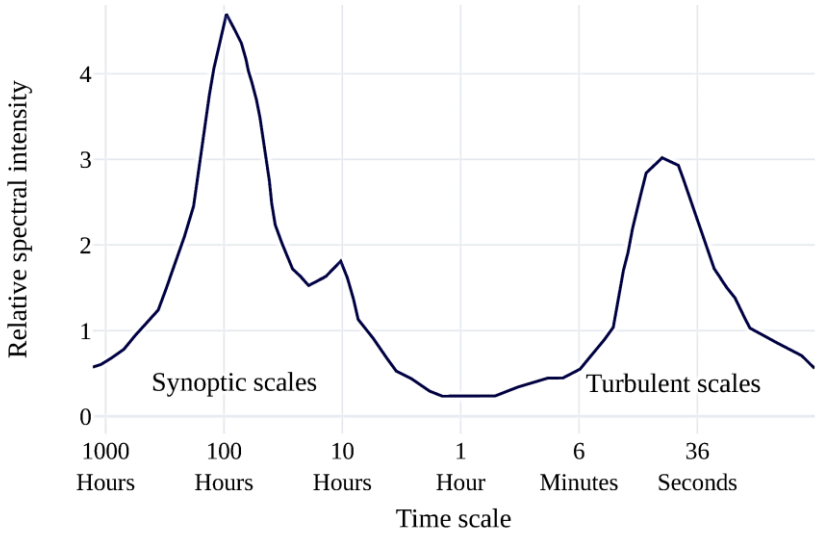

Figure 1.2: Relative spectral energy (i.e., energy per unit frequency) as a function of time scale, adapted from Stull [8]. The energy gap can be identified between the synoptic scales and the turbulent scales.

An example of the time record of wind speed and direction reported by an anemometer

mounted 2 m above ground level (AGL) is shown in Figure 1.3. The raw wind speed fluctuates between 0 to 6 m/s during this hour, but the 1-minute average wind speed has a much smaller range of $0.5 - 2.3\ m/s$. The 10-minute average wind speed brings this range down to $0.6 - 1.6\ m/s$ and the hourly average wind speed is $1.2\ m/s$. The differences in ranges are more significant in terms of wind direction. The wind direction from the raw data can easily change 180° or more within 1 minute. However, the 1-minute average wind direction only varies within about 90°. The 10-minute average wind direction shows a smaller range of about 50°.

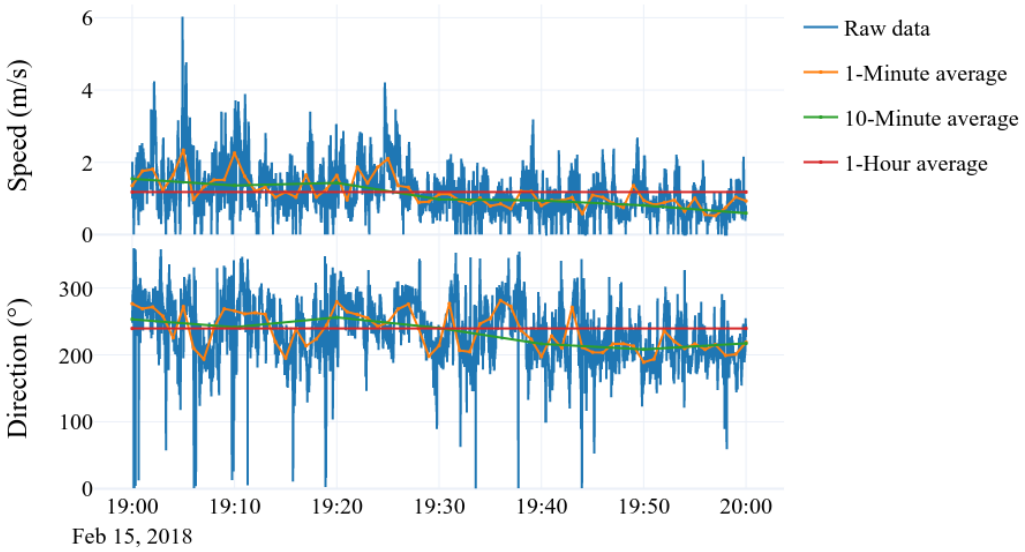

Figure 1.3: Time series of the horizontal wind speed and wind direction from a ground win sensor using raw data and different averages.

The vertical profiles of wind speed and temperature take different forms under different stability conditions. Due to turbulence, the wind speed is constantly fluctuating, so the wind and other profiles described in this study will be the mean profiles, not the instantaneous ones. To describe the physics of the surface layer, which is within the lowest 5% to 10 % of the ABL [10,12], A. Obukhov found a universal length scale, the Obukhov length, for exchange processes in the surface layer. Soon, the Monin-Obukhov similarity theory was developed in 1954 [13] and

quickly became the starting point for modern micrometeorology [14]. Using the experimental data obtained during the 1968 Kansas measurement campaign over a flat wheat field, Businger et al. found that the predictions of the Monin–Obukhov similarity theory were satisfied over the entire stability range of the observations [15].

The aerodynamic roughness length, z_0, is a vital length scale in the surface layer. z_0 indicates the height above the ground at which the mean wind speed becomes zero in the logarithmic wind speed profile. The effects of different surface structures, such as buildings and vegetation, should be represented by different values of z_0. Studies show z_0 varies from about $0.01\ m$ over water and can grow up to a few meters over irregular forests and cities [8]. For uniform terrain of fixed z_0, the logarithmic law represents the wind profile well up to heights of at least $150\ m$ with strong winds [16]. Even if the terrain is not uniform and local wind profiles are not logarithmic, it is believed that the logarithmic law can represent the averages over large horizontal areas [16].

1.2 Traditional modeling of pollution dispersion

Nowadays, air pollution is usually monitored with an observation network consisting of fixed stations deployed near the emission sources to capture the time-dependent concentrations. To better understand the state of the air quality over a specific region with a limited number of permanent monitoring stations, the dispersion of pollutants needs to be simulated by computational models at different scales.

1.2.1 Gaussian-based dispersion modeling

Traditionally, Gaussian plume models are used to predict the steady-state, time-averaged concentration of pollutants at locations downwind from emission sources, which can be a point, area, and volume sources. Figure 1.4 illustrates the main concept in the Gaussian plume models.

A plume rises from an elevated stack (which is usually treated as a point) that continuously emits pollutants at a certain rate. As the pollutants enter the atmosphere, they form a plume that is advected by the mean wind profile and mixed by turbulence parameters that have direct control over its spreading.

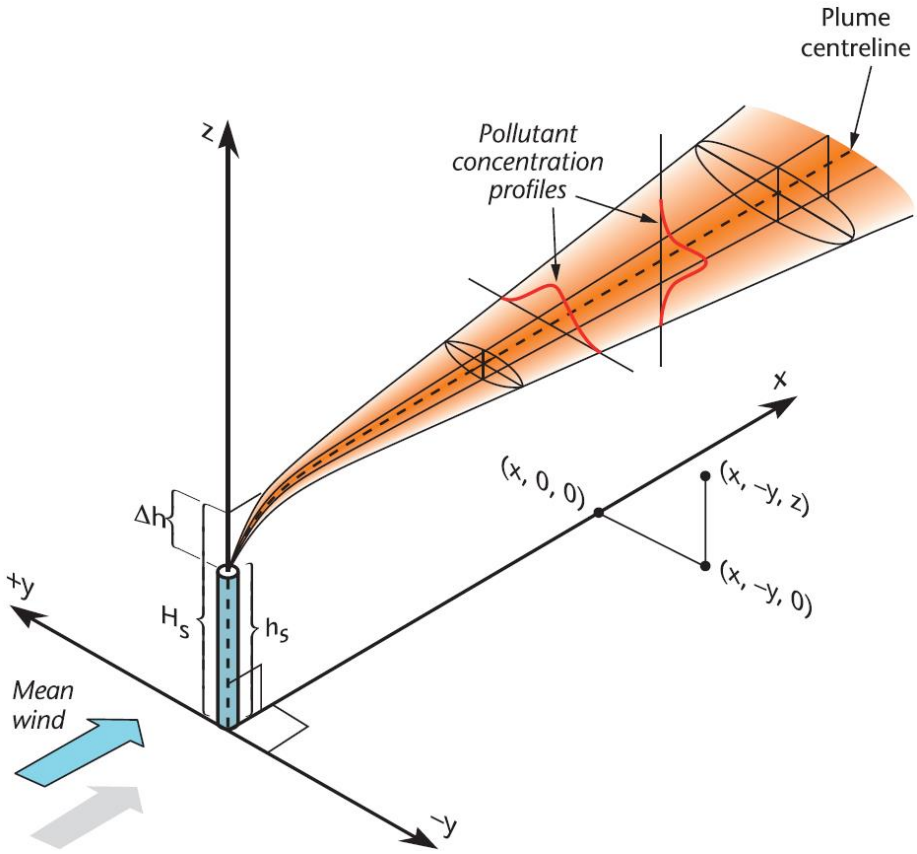

Figure 1.4: Air pollutant dispersion from an elevated point source in a Gaussian dispersion model, adapted from Oke et al. [17].

Equation (1.1) describes the mean concentration c_i (in g/m^3) of an air pollutant at any point in space (x, y, z) downstream of a stack:

$$c_i(x,y,z) = \frac{E}{2\pi\hat{\sigma}_y\hat{\sigma}_z\bar{u}} \exp\left(-\frac{y^2}{2\hat{\sigma}_y{}^2}\right)\left[\exp\left(-\frac{(z-H_s)^2}{2\hat{\sigma}_z{}^2}\right) + \exp\left(-\frac{(z+H_s)^2}{2\hat{\sigma}_z{}^2}\right)\right] \quad (1.1)$$

where $\bar{u}$ is the mean wind speed (in m/s) at stack height, E is the emission rate (in g/s). $\hat{\sigma}_y$ and $\hat{\sigma}_z$ (in m) are the lateral and vertical standard deviations of the concentration field, which are related to turbulent fluctuations. The effective stack height H_s (in m) is the sum of the actual stack heigh h_s and the plume rise Δh. Inputs of the mean wind speed, turbulence, and plume are crucial for predicting air pollutant dispersion in this model.

Some well-known air quality dispersion models, such as AERMOD [18] and CTDMPLUS [19] are preferred and recommended by the United States Environmental Protection Agency (EPA) to simulate the pollution dispersion pattern for regulatory purposes. The AERMOD modeling system is used to model the pollutants in the near field ($< 50\ km$) over a simple or complex terrain. A terrain is considered to be complex if it has irregular topography and variations in land use that will generate inhomogeneities of turbulence and winds. However, Gaussian-based dispersion models, like AERMOD, are derived from the analytical solution of the scalar transport equation (also known as the continuity equation of species) under idealized hypotheses of uniform flow with homogeneous turbulence, which are rarely satisfied in the flow above a complex terrain [20]. Some reasons can justify the use of the Gaussian models: they are simple to use fast to generate results; they have been evaluated against a number of experiments [21]. These models are typically used in the permitting process to estimate the concentration of pollutants at specified ground-level locations surrounding an emissions source.

1.2.2 Photochemical modeling

Since Gaussian plume models do not take into account the flow field directly, Eulerian (that uses a fixed coordinate system) and Lagrangian (that employs a moving frame of reference) approaches are needed to model the dispersion and transformation of emissions. Schematics of the Eulerian and Lagrangian approaches are shown in Figure 1.5.

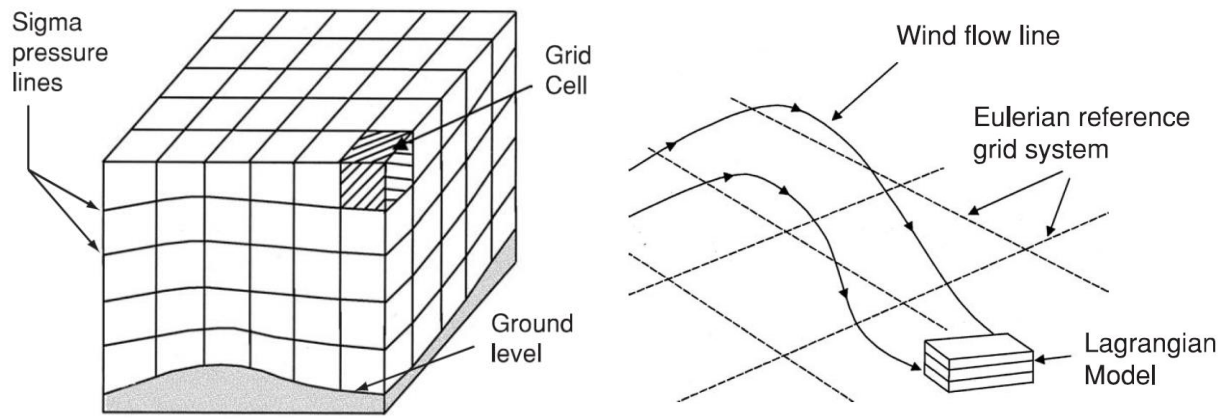

(a) Schematic of 3D Eulerian framework. (b) Schematic of 1D Lagrangian framework.

Figure 1.5: The Eulerian and Lagrangian approaches that are used to model pollution dispersion, adapted from McMurry et al. [22].

Based on the above two approaches, photochemical models, also known as Chemical Transport Models (CTMs), have been developed and routinely used for regulatory analysis and attainment demonstrations. Most models have adopted the 3D Eulerian grid modeling mainly because of its ability to better characterize physical processes in the atmosphere and predict the species concentrations throughout the entire computational domain. Some well-known modeling systems include the Community Multiscale Air Quality (CMAQ) model system and the Comprehensive Air quality Model with extensions (CAMx) modeling system. A typical photochemical model simulates the emission, dispersion, chemical reaction, and deposition by marching the Eulerian continuity equation for species (or pollutants in this context) forward in time (t) for each interested chemical species (i) in the domain. To describe the time evolution of species concentration within each grid cell as a volume average including all the essential physical and chemical processes operating on that volume, the equation is written as follows:

$$\frac{\partial c_i}{\partial t} = \underbrace{-\nabla \cdot \bar{u} c_i}_{\text{Advection}} + \underbrace{\nabla \cdot K \nabla c_i}_{\text{Diffusion}} + \frac{\partial c_i}{\partial t}\Big|_{\text{Emission}} + \frac{\partial c_i}{\partial t}\Big|_{\text{Chemistry}} + \frac{\partial c_i}{\partial t}\Big|_{\text{Removal}} \qquad (1.2)$$

where K is the turbulent diffusion coefficient.

Photochemical models can be applied at different spatial scales, ranging from local scale (10^2 to $10^4\ m$) to city scale (10^4 to $10^5\ m$) to regional/meso- scale (10^4 to $10^6\ m$), national/macro-/synoptic scale (10^5 to $10^7\ m$), and global scale ($> 10^8\ m$) [23]. The spatial resolution is dependent on the meteorological inputs since vertical wind profiles, and the turbulence parameter can only be obtained from other models, such as numerical weather prediction (NWP) models or empirical relations. In practice, these models usually employ a coarse grid resolution in the order of a few kilometers and up to 100 kilometers. Thus, they have difficulty in resolving detailed pollution concentration over complex terrains, such as the local-scale or even micro-scale ($\leq 10^2\ m$) pollution dispersion [24].

1.3 CFD modeling

The characteristics of the flow field over a certain region, in terms of wind speed and, most importantly, the turbulence, cannot be adequately described by a single or even multiple profiles as used by traditional dispersion models. CFD simulations are capable of resolving the flow field at very fine levels, which makes them ideal for simulating flow over complex terrain to study near-source pollution dispersion. CFD simulations solve conservation equations of mass, momentum, energy, and species within a computational domain. Different CFD models have been widely applied to various engineering problems. For simulations of flow within the ABL, examples include the predictions of pollution dispersion [25–30], the energy production of wind farms [31,32], the spread of wildfire [33], the assessment of pedestrian comfort in an urban environment [34], etc. However, some common considerations are needed when developing a CFD model for ABL flows over complex terrain.

First, the inlet boundary conditions, such as mean wind speed and mean air temperature

profiles as functions of vertical height, are usually generated according to the Monin–Obukhov similarity theory with empirical parameters estimated from flat terrain[14]. Such profiles are valid within the surface layer, which is only within 100 m above the ground surface. Above the surface layer, there is no widely accepted theory of the mean profiles. However, many researchers have applied the surface layer profiles across the full height of ABL over complex terrain: Balogh et al. applied the theoretical profiles to the inlet of a $6\ km \times 6\ km \times 1\ km$ (length by width by height) complex terrain [35]; Bechmann et al. used a $5.6\ km \times 5.6\ km \times 1.5\ km$ computational domain [36]; Breedt et al. used a $35.3\ km \times 24.900\ km \times 6\ km$ computational domain [37]. Besides, in many cases [38,39], the theoretical profiles are estimated from measurements at one height level using equations derived from the horizontal homogeneity assumption (i.e., no gradients along stream-wise direction) [40]. In addition, these theoretical profiles may not be suitable for the inlet of complex terrains as the parameters are derived from flat terrain. Breedt et al. applied an artificial smoothing around the terrain so that the inlet profiles can be applied on completely flat terrain as it removes terrain features across boundaries [37]. But it is unclear if the different smoothing methods will lead to different predictions. Li et al. proposed two methods of determining the inlet profiles: one is to fit the velocity into an empirical law, and the other one is to interpolate the values from a precursor simulation of the upstream region [41]. The latter required more computing power, and the improvement in accuracy was limited [41]. Temel et al. [12] and Miao et al. [42] coupled a CFD model with a Weather Research and Forecasting (WRF) model that is used to obtain realistic inflow conditions. Vertical wind and temperature profiles can be obtained from direct measurements (e.g., atmospheric sounding) and data assimilation (e.g., reanalysis products). Since the simulation results depend strongly on the boundary conditions, a methodology that utilizes all available data sources is needed to obtain good quality vertical profiles of wind speed,

temperature, and turbulence suitable for complex terrain.

Second, turbulence models are used in CFD to predict the effects of turbulence on the flow field, and model constants or coefficients need to be specified. In many cases, simulations of ABL flow are performed using the RANS equations together with the $k-\varepsilon$ turbulence model [38,43,44]. The constants in the $k-\varepsilon$ model must be properly chosen in order to correctly simulate the effects of turbulence within the ABL [40]. Multiple sets of model constant for the $k-\varepsilon$ model have been used in the literature, which are summarized in Table 1.1.

Table 1.1: Pairs of model constants used in different $k-\varepsilon$ models.

$k-\varepsilon$ model	κ	C_μ	σ_k	σ_ε	$C_{\varepsilon 1}$	$C_{\varepsilon 2}$	$C_{\varepsilon 3}$
Launder and Spalding (1974) [45]	0.4	0.09	1	1.3	1.44	1.92	–
Hagen et al. (1981)	0.4	0.026	0.9	1.22	1.44	1.92	–
Crespo et al. (1985)	0.4	0.033	1	1.3	1.21	1.92	0.8
Raithby et al. (1987)	0.4	0.033	1	1.3	1.44	1.92	–
Richards and Hoxey (1993)	0.42	0.013	1	3.22	1.44	1.92	
Alinot and Masson (2005)	0.42	0.033	1	1.3	1.176	1.92	$C_{\varepsilon 3}(z/L)$
Bechmann and Sørensen (2010)	0.4	0.11	1	1.3	1.55	1.92	–
Richards and Norris (2011)	0.433	0.09	1	1.3	1.44	1.92	–
van der Laan et al. (2016)	0.4	0.03	1	1.3	1.21	1.92	$C_{\varepsilon 3}(\zeta)$
Piroozmand et al. (2020)	0.41	0.09	1	1.3	1.44	1.92	$C_{\varepsilon 3}(U)$

For example, based on experimental data and findings under neutral ABL [46], Alinot and Masson used the model constants of $C_\mu = 0.033$ and $C_{\varepsilon 1} = 1.176$ [44]. Different values and vertical profiles of $C_{\varepsilon 3}$ were proposed under different stability classes, and the CFD simulation results of flow over uniform flat terrain showed a slight improvement over the standard $k-\varepsilon$ model constants [44]. There is much less consensus over the specification of model constant $C_{\varepsilon 3}$, which appears with the buoyancy team in the dissipation equation. Many different values of this constant ranging from -0.8 for unstable conditions up to 2.15 for stable conditions have been reported in the literature [44,47,48].

Third, uniform aerodynamic roughness length is commonly used throughout the terrain surface [25,26,33], even though the common aerodynamic roughness length may vary from $0.001\ m$ to $1.300\ m$ in near-source dispersion [18]. In CFD models, the effects of the actual roughness obstacles above the ground are generally included by using wall functions based on experiments with sand-grain roughness [49]. For complex terrain, the aerodynamic roughness length of the obstacle is usually converted to an equivalent sand-grain roughness height by multiplying a factor of 30 [50]. This conversion implies that the half-height of the wall-adjacent cell needs to be at least the height of the equivalent sand-grain roughness. When generating the computational mesh for a region with a high aerodynamic roughness length (e.g., $1.0\ m$ for mountainous areas), the height of the wall-adjacent cell needs to be at least $60\ m$. The accuracy of CFD simulations can be compromised following such conversion [50]. Parente et al. proposed a new wall model based on aerodynamic roughness, which does not impose strict limitations in terms of near-wall grid resolution [51]. Using the aerodynamic-based wall model, comparisons of the predictions of the CFD model for uniform surface roughness and variable surface roughness for flow over complex terrain are necessary.

Fourth, a number of CFD models [12,35,52] have been developed and evaluated using the famous Askervein hill [53] and Bolund island experiments [54]. Measurement data for wind at multiple locations and height levels are crucial for model evaluation. The abundance of data from wind measurement is one of the main reasons these two locations are popular. However, almost all the data collected in the Askervein hill are essentially under neutral conditions [53]. Because the size of the Bolund island is small (maximum height is $12\ m$ and the length is approximately $150\ m$), the effect of atmospheric stratification can be neglected, which makes it ideal for the validation of neutral flow models [54]. When developing a new CFD model for wind development

and applying it over complex terrain, comparisons between model predictions and field measurements under different meteorological conditions will be important to evaluate the model.

Finally, the emission condition or even the governing equations are usually simplified. In most cases, only the emission rate is specified in simulations of atmospheric pollution dispersion. Amorim et al. used CFD to model the dispersion of carbon monoxide emitted by road traffic and treated the emission sources as line sources, and the traffic produced turbulence was not considered [28]. When simulating exhaust gas dispersion from chimneys of a power plant, Toja-Silva et al. ignored the buoyancy effects[55]. When it comes to real-world applications, there are multiple important factors to consider at the same time, such as complex terrain, stability class of the atmosphere, and emission conditions. Since buoyancy plays a key role under stable and unstable conditions, ignoring its effect may lead to errors in predicting turbulence. In this study, the SO_2 plumes emitted from the stacks have high temperature and are thus highly buoyant, which cause a small region of an unstable environment with high turbulent diffusivity.

1.4 Site description

EPA has established the National Ambient Air Quality Standards (NAAQS) for six principal pollutants, including SO_2. The current attainment-level standard for the design value of SO_2, established in 2010, is 75 parts per billion (ppb) based on the 3-year average of the 99th percentile of the yearly distribution of 1-hour daily maximum concentrations. Exposure to elevated levels of SO_2 has detrimental effects on the human respiratory system, even if the exposure is only for a few minutes [56]. In order to evaluate exposure levels, it is important to understand the spatial and temporal evolution of SO_2 in the valley under different meteorological conditions and emission scenarios. Pittsburgh's Allegheny County, which is located southwest of the U.S. state of Pennsylvania, has been ranked the worst among U.S. counties in terms of air quality. As of May

5, 2021, Allegheny County is still designated as “nonattainment” due to high SO_2 concentrations reported by monitors [57]. Figure 1.6 shows a map of monitoring sites in Allegheny CountyThe model of the SO_2 monitors is the Model T100 SO_2 Analyzer from Teledyne API, which uses ultraviolet fluorescence to measure SO_2 in the ranges of $0 - 50\ ppb$ and $0 - 20{,}000\ ppb$ with a detection limit of $0.4\ ppb$. The precision of the monitors is 0.5% of reading above $50\ ppb$.

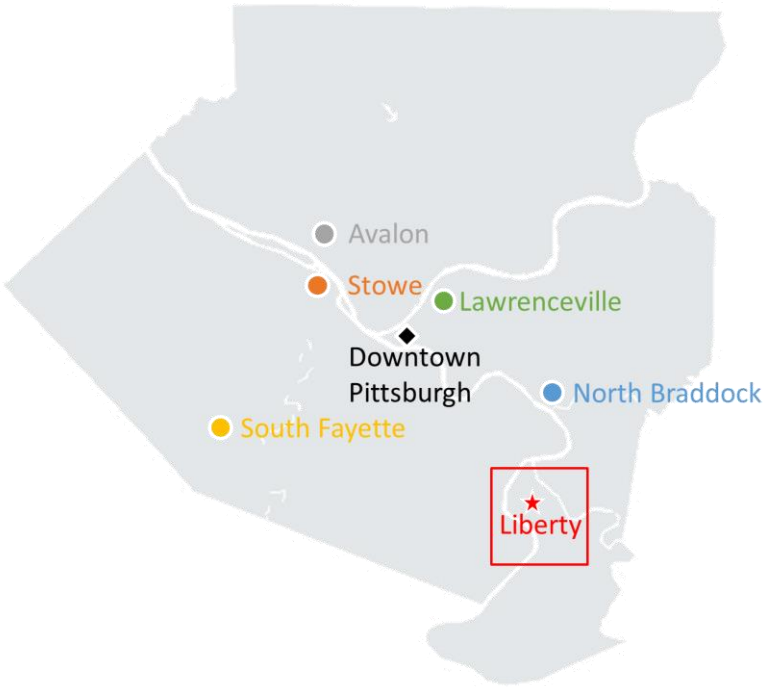

Figure 1.6: All six monitoring locations for SO_2 in Allegheny County. The Downtown Pittsburgh location does not have a monitor, but it is shown as a reference.

Figure 1.7 shows the SO_2 1-hour design values from EPA standards and measurements in Allegheny County. All other monitors show attainment-level SO_2 values besides the Liberty monitor. At the Liberty monitoring site, there is a long history of higher than attainment-level SO_2 concentrations has been recorded. Moreover, such exceedance episodes are most likely to be occurring at other locations in the valley, where continuous monitoring of SO_2 is not available. The main source of SO_2 near the Liberty site is the coking process of coal from U.S. Steel’s Clairton Coke Works shown in Figure 1.8.

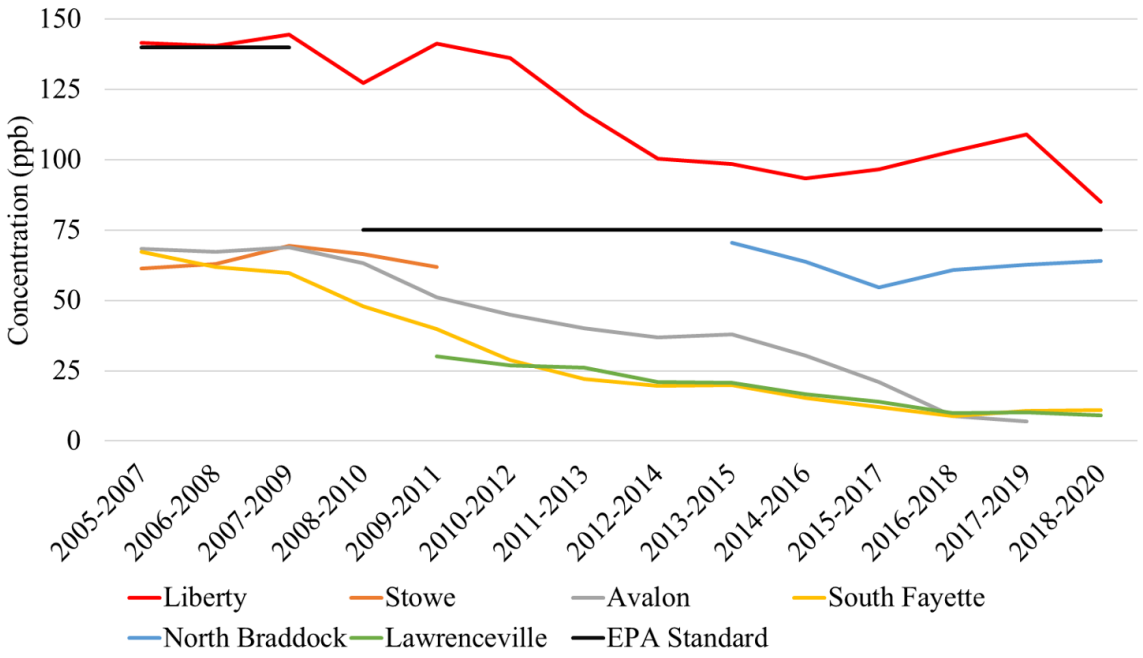

Figure 1.7: SO_2 1-hour design values from EPA standards and measurements reported by the monitors in Allegheny County over recent years [57,58].

Figure 1.8: A photo showing the operation of the U.S. Steel's Clairton Coke Works [59]. After being released from the plant, SO_2 travels in the form of a plume that widens with distance from the plant. SO_2 exits the stacks with a much higher temperature than that of the ambient air.

The coke plant is 2 km southwest of the Liberty monitoring site. Figure 1.9 (a) shows the locations of the coke plant, the Liberty site, and the distances. The nearby Allegheny County Airport (KAGC) records wind speed and direction that are measured at 10 m AGL. A wind rose

is generated using data from KAGC from 1945 to 2019, as shown in Figure 1.9 (b). Near this region, the dominant wind direction is from the southwest, and the most common wind speed range is between 2 m/s and 6 m/s. The southwest wind brings SO_2 emitted from the plant to the Liberty monitor; thus, high SO_2 concentrations have been recorded over the years.

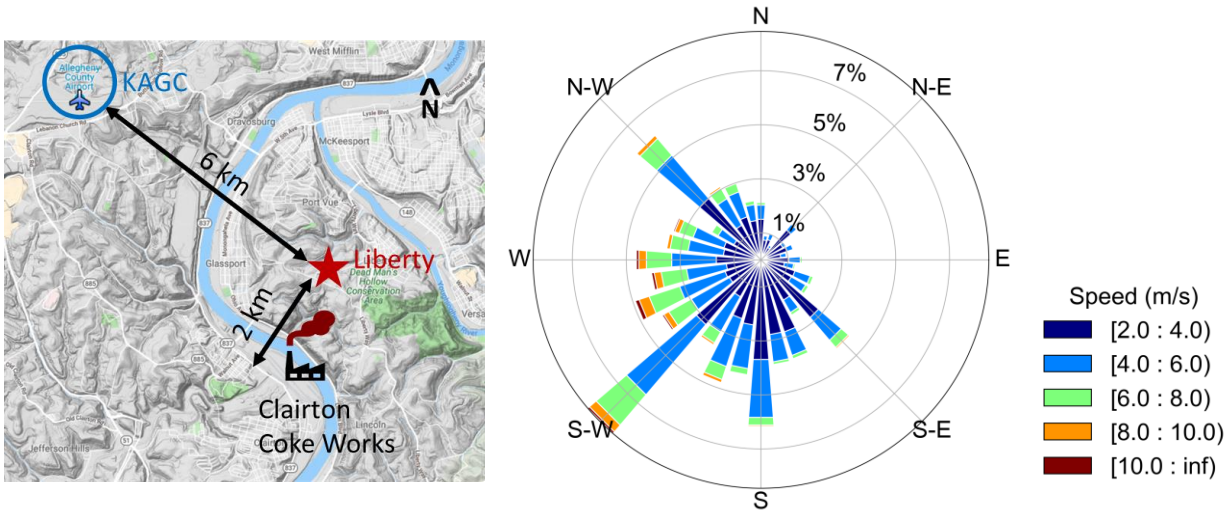

(a) Locations of monitors and plant (b) Wind rose (data from 1945 to 2019) at KAGC

Figure 1.9: A map showing the county airport (KAGC), Liberty monitor, and the coke plant. The wind rose generated using wind speed and direction from KAGC shows the dominant southwest wind direction.

1.5 Objectives of current research

Given the challenges of simulating atmospheric flow and pollution dispersion over complex terrain, the present work focuses on:

1) a method to construct a model for predicting wind development and SO_2 dispersion over a complex terrain with a high-quality computational grid,
2) a method to generate reliable inlet boundary conditions with inputs from ground-level and vertically-distributed weather data sources,
3) comparison of wind velocity predictions from the developed CFD model with multiple measurements made inside the complex terrain,

4) investigation of sampling strategies to compare steady-state and transient simulations of pollutant dispersion with a single-point measurement,
5) evaluate the developed CFD moel and compare its performance with AERMOD using different statistical measures, and
6) identification factors that lead to exceedances under different conditions using the developed CFD model.

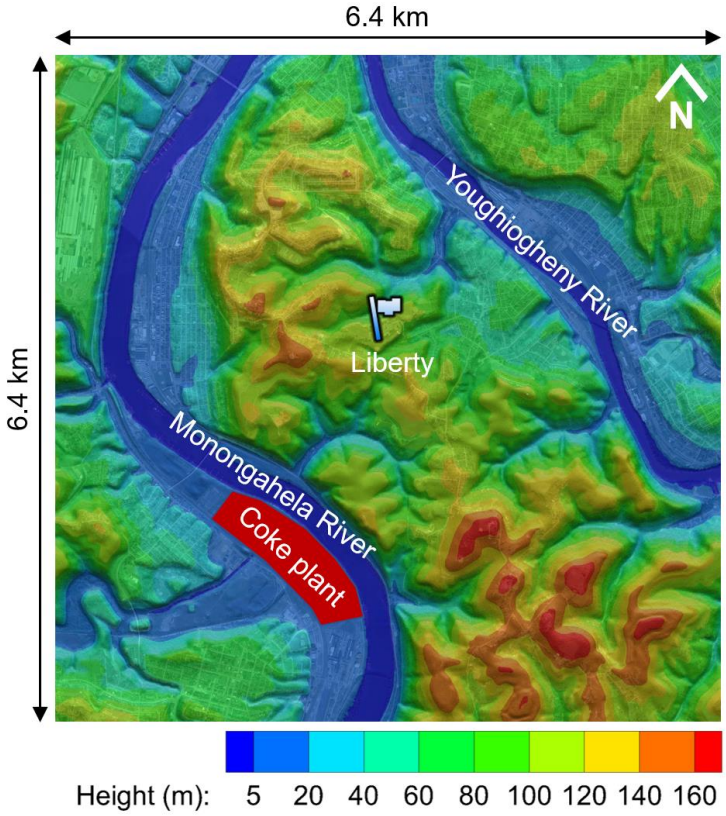

Figure 1.10: Height contours of the 6.4 km × 6.4 km study domain centered around the Liberty monitor. The coke plant is located southwest of the Liberty monitor.

The size of the study domain, the location of the coke plant, and the Liberty monitoring site are shown in Figure 1.10. There are two rivers flowing through this region: the Monongahela River is located on the west, and the Youghiogheny River is located on the east. The lowest point within the domain is located on the surface of the Monongahela River, and its height is set to 0 m.

The highest point ($174\ m$) is located on the mountain top near the southeast corner. The land-use types over this domain include industrial land, low-intensity residential area, and deciduous forest.

Chapter 2

Numerical model

The open-source CFD code OpenFOAM [60] is used for the development of the CFD model. This chapter describes the equations related to the CFD model in the present work.

2.1 Computer code

There are plenty of commercial and open-source CFD codes available. In this work, the CFD model is developed based on OpenFOAM version 4.1 released in October 2016. OpenFOAM is a C++ toolbox for the development of numerical solvers and pre-/post-processing utilities for CFD models. OpenFOAM provides multiple standard solvers in different categories, such as incompressible flow, heat transfer, multiphase flow, Lagrangian particle tracking, combustion, etc. A steady-state solver for turbulent flow of compressible fluids, "buoyantSimpleFoam", can be used to allow for temperature-driven density gradients and resultant buoyant forces. The corresponding transient solver is called "buoytantPimpleFoam". The software development based on current code involves:

1) improving standard steady-state and transient solvers to improve robustness,
2) adding pollution dispersion models that output pollution concentration in ppb,
3) implementing the aerodynamic-based roughness wall model,
4) adding the buoyancy effects due to the large temperature difference near the stack exits and the atmospheric stability to the standard $k-\varepsilon$ model,
5) combing OpenFOAM build-in functions with Python APIs (Application Programming Interfaces) for requesting weather data and setting up boundary conditions, and
6) using Python scripts to schedule jobs on supercomputers and post-process results with tools from OpenFOAM for sampling and probing data in the computational domain.

2.2 Governing equations

Reynolds averaging is the process of dividing an instantaneous flow variable into its mean and fluctuating components. By performing Reynolds averaging on the governing equations for fluids, the Reynolds-averaged Navier–Stokes equations and other related equations can be obtained [61].

2.2.1 Continuity equation

For a compressible flow, the conservation law of mass gives the continuity equation:

$$\frac{\partial \rho}{\partial t} + \frac{\partial}{\partial x_i}(\rho u_i) = 0 \tag{2.1}$$

where ρ is the density. u is the mean velocity vector, and x is the Cartesian coordinate.

2.2.2 Momentum equation

The vector form of the momentum equations can be written as:

$$\frac{\partial}{\partial t}(\rho u_i) + \frac{\partial}{\partial x_j}\left(\rho u_j u_i\right) = -\frac{\partial p}{\partial x_i} + \rho g_i + \frac{\partial}{\partial x_j}\left(\tau_{ij} + \tau_{t_{ij}}\right) \tag{2.2}$$

where p is the pressure. g is the gravitational acceleration. τ is the mean stress tensor and τ_t is the Reynolds stress tensor. This study focuses on the flow over a small region within only a few hundred meters above the ground, so the Coriolis force is neglected in the momentum equations. The Boussinesq approximation for density is often used in a variable-density flow, such as buoyancy-driven flows, when the overall density variation is small. If the temperature differences are below 15° for air, this approximation introduces errors in the order of 1%. However, when temperature differences are larger, the error may be more substantial, and the solution may even be qualitatively wrong [62]. For this study, the stack exits have a mean temperature of $529\ K$ while the mean annual temperature in Pittsburgh over the past 30 years is around $284\ K$. Given such a large temperature difference, the Boussinesq approximation for density is not chosen.

For convenience, the pressure gradient and gravity force terms are usually rearranged in the following form:

$$\begin{aligned} -\frac{\partial p}{\partial x_i} + \rho g_i &= -\frac{\partial \left(p_{rgh} + \rho g_j x_j\right)}{\partial x_i} + \rho g_i \\ &= -\frac{\partial \left(p_{rgh}\right)}{\partial x_i} - \left(g_j x_j\right)\frac{\partial \rho}{\partial x_i} \end{aligned} \tag{2.3}$$

The new term p_{rgh} is called the pseudo hydrostatic pressure, which is the pressure in excess of the hydrostatic pressure over the total pressure p. From the definition: $p_{rgh} = p - \rho g z$, where z is the height above the ground. This rearrangement is a common approach in CFD to simplify the pressure boundary conditions in compressible flow solvers. Finally, the momentum equations become:

$$\frac{\partial}{\partial t}(\rho u_i) + \frac{\partial}{\partial x_j}\left(\rho u_j u_i\right) = -\frac{\partial \left(p_{rgh}\right)}{\partial x_i} - \left(g_j x_j\right)\frac{\partial \rho}{\partial x_i} + \frac{\partial}{\partial x_j}\left(\tau_{ij} + \tau_{t_{ij}}\right) \tag{2.4}$$

2.2.3 Equation for pressure

The solution of the coupled continuity equation and the momentum equations is not straightforward because an explicit equation for the pressure is missing. The common practice is to derive a Laplacian equation for the pressure by taking the divergence of the momentum equations and by substituting it in the continuity equation. OpenFOAM implements the SIMPLE (Semi Implicit Methods Pressure Linked Equations) algorithm [63] for steady-state solvers [64]. For transient solvers, the PIMPLE algorithm is implemented that combines the PISO (Pressure-Implicit with Splitting of Operators) [65] with the SIMPLE. The pressure equation can be derived as:

$$\frac{\partial}{\partial x_i}\left[\rho \frac{1}{A_\mathrm{P}}\frac{\partial \left(p_{rgh}\right)}{\partial x_i}\right] = \frac{\partial \rho}{\partial t} + \frac{\partial}{\partial x_i}\left(\rho HbyA - \rho \frac{1}{A_\mathrm{P}}\left(g_j x_j\right)\frac{\partial \rho}{\partial x_i}\right) \tag{2.5}$$

where HbyA and A_P are terms after the discretization of the momentum equation [64]. For the

transient solver, it is found that the $\frac{\partial \rho}{\partial t}$ term makes the solver diverge quickly. The density variation in time is not expected to be large for the simulations performed under this study, so the $\frac{\partial \rho}{\partial t}$ term is ignored.

2.2.4 $k-\varepsilon$ turbulence model

The problem of finding the value of the Reynolds stress is recognized as a closure problem. To solve such a problem, Jones et al. [66] proposed the $k-\varepsilon$ model, which is widely used to simulate turbulence in atmospheric flows. This model is a semi-empirical model based on the transport equations of k and ε, and it relates the turbulent kinematic viscosity $\nu_t = C_\mu \frac{k^2}{\varepsilon}$ to the Reynolds stress term $\tau_{t_{ij}}$ under the Boussinesq hypothesis on turbulence modeling and eddy viscosity as follows

$$\tau_{t_{ij}} = \rho \nu_t \left(\frac{\partial u_i}{\partial x_j} + \frac{\partial u_j}{\partial x_i} \right) - \frac{2}{3} \left(\rho k + \rho \nu_t \frac{\partial u_k}{\partial x_k} \delta_{ij} \right) \tag{2.6}$$

With the addition of the buoyancy effects, the model is called "buoyantKEpsilon" in the OpenFOAM code. The transport equations for k and ε are written as:

$$\frac{\partial}{\partial t}(\rho k) + \frac{\partial}{\partial x_i}(\rho u_i k) = \frac{\partial}{\partial x_j}\left[\left(\mu + \frac{\mu_t}{\sigma_k} \right) \frac{\partial k}{\partial x_j} \right] + G_k + G_b - \rho \varepsilon \tag{2.7}$$

$$\frac{\partial}{\partial t}(\rho \varepsilon) + \frac{\partial}{\partial x_i}(\rho u_i \varepsilon) = \frac{\partial}{\partial x_j}\left[\left(\mu + \frac{\mu_t}{\sigma_\varepsilon} \right) \frac{\partial \varepsilon}{\partial x_j} \right] + C_{\varepsilon 1} \frac{\varepsilon}{k}(G_k + C_{\varepsilon 3} G_b) - C_{\varepsilon 2} \rho \frac{\varepsilon^2}{k} \tag{2.8}$$

G_k is the production of k due to mechanical shear, which is given by:

$$G_k = \tau_{t_{ij}} \frac{\partial u_i}{\partial x_j} \tag{2.9}$$

G_b is the production of k due to buoyancy, which is given by:

$$G_b = \beta g_i \frac{\mu_t}{Pr_t} \frac{\partial \theta}{\partial x_i} \tag{2.10}$$

where β is the coefficient of thermal expansion. μ_t is the kinematic viscosity. Pr_t is the turbulent Prandtl number. θ is the potential temperature for air. For stable stratification, buoyancy tends to suppress turbulence level; thus, the corresponding values of G_b are negative. The model constants proposed by Crespo et al. [46] and later adopted by Alinot and Masson [44] are used in this study: $C_\mu = 0.033$ and $C_{\varepsilon 1} = 1.176$ for all stability classes. As for $C_{\varepsilon 3}$, which is the degree to which ε is affected by buoyancy, there is less consensus in the literature. Moreover, these values have been tested for ABL flows without the presence of hot plumes rising from stacks, as is the case in the present work. The hot plumes create a strongly buoyant local environment. For strongly buoyant flows, Henkes et al. proposed the following expression for $C_{\varepsilon 3}$ [67]:

$$C_{\varepsilon 3} = \tanh \left| \frac{u_3}{\sqrt{u_1^2 + u_2^2}} \right| \tag{2.11}$$

where u_3 is the vertical component of the flow velocity vector, and u_1 and u_2 are the horizontal components. When the vertical component of the wind is weak or when the horizontal component is very strong, $C_{\varepsilon 3}$ becomes close to 0.

2.2.5 Equation for energy

From the first law of thermodynamics, the energy conservation equation in a system can be derived in multiple forms, such as specific internal energy, specific enthalpy, and the most commonly used form: temperature. The compressible solvers with heat transfer in OpenFOAM implement the more general forms of the energy equation in terms of specific internal energy and enthalpy. The energy equation in terms of specific enthalpy can be derived as [68] :

$$\begin{aligned} &\frac{\partial}{\partial t}(\rho h) + \frac{\partial}{\partial x_i}(\rho u_i h) + \frac{\partial}{\partial t}(\rho K) + \frac{\partial}{\partial x_i}(\rho u_i K) - \frac{\partial p}{\partial t} \\ &= \frac{\partial}{\partial x_i}\left(\rho \alpha_{eff} \frac{\partial h}{\partial x_i}\right) + \rho u_i g_i + q \end{aligned} \tag{2.12}$$

where h is the specific enthalpy (unit: J/kg), and K is the kinetic energy per unit mass (unit: m^2/s^2). q is the heat source or sink per unit (unit: W/m^3). The mechanical sources are often ignored [68]. By further ignoring the pressure term, the energy equation in terms of specific enthalpy can be simplified as:

$$\frac{\partial}{\partial t}(\rho h) + \frac{\partial}{\partial x_i}(\rho u_i h) = \frac{\partial}{\partial x_i}\left(\rho \alpha_{eff} \frac{\partial h}{\partial x_i}\right) + q \tag{2.13}$$

Pontiggia et al. discussed that if the absolute temperature is employed, it is not possible to balance the adiabatic profile of absolute temperature by varying the pressure along the vertical direction [27]. Therefore, it is convenient to solve for the potential temperature in the system of equations. The transport equation for the potential temperature is written as

$$\frac{\partial}{\partial t}\left(\rho c_p \theta\right) + \frac{\partial}{\partial x_i}\left(\rho c_p u_i \theta\right) = \frac{\partial}{\partial x_i}\left(\rho c_p \alpha_{eff} \frac{\partial \theta}{\partial x_i}\right) + q \tag{2.14}$$

where the effective thermal diffusivity α_{eff} is the sum of laminar diffusivity α and turbulent thermal diffusivity α_t and it is given as: $\alpha_{eff} = \alpha + \alpha_t = \frac{\nu}{Pr} + \frac{\nu_t}{Pr_t}$. In this study, the Prandtl number $Pr = 0.7$ and turbulent Prandtl number $Pr_t = 0.85$. The specific enthalpy is linked to the potential temperature θ by $h = c_p \theta$, where c_p is the specific heat capacity at constant pressure. For perfect gas under the weak compressible assumption, the equation of state is [25]

$$p = \rho R \theta \tag{2.15}$$

With the equation of state, the production of k due to buoyancy given in equation (2.10) can be simplified to

$$G_b = -g_i \frac{\mu_t}{\rho Pr_t} \frac{\partial \rho}{\partial x_i} \tag{2.16}$$

2.2.6 Passive scalar transport equation

Once emitted from their sources, air pollutants quickly become part of the air. Unlike

temperature or pressure, they do not directly affect the wind field in the atmosphere; therefore, they are commonly considered passive scalars transported by the wind. To simulate the dispersion of a passive scalar ϕ, which can be SO_2, N_2O or any other non-reactive chemical species, the scalar transport equation (also known as the continuity equation for the species of interest) is described as:

$$\frac{\partial}{\partial t}(\rho\phi) + \frac{\partial}{\partial x_i}(\rho u_i \phi) = \frac{\partial}{\partial x_i}\left(\rho D_{eff}\frac{\partial \phi}{\partial x_i}\right) + S_\phi \tag{2.17}$$

where the effective mass diffusivity D_{eff} is the sum of mass diffusivity D and turbulent mass diffusivity D_t and it is given $D_{eff} = D + D_t = \frac{\nu}{Sc} + \frac{\nu_t}{Sc_t}$. The Schmidt number Sc and the turbulent Schmidt number Sc_t are set to 1 in this study. The emission rate (in g/s) of the scalar will be specified into the source term S_ϕ, which has the unit in $g/(s \cdot m^3)$. Equation (2.17) will be solved after the converged solution of the flow field is obtained. As a passive scalar (N_2O or SO_2 for this study), ϕ is the mass ratio between the scalar and fluid, which is air in this study. To get the concentration of the passive scalar in g/m^3, the value of ϕ needs to multiply with the density of air ρ. After that, a conversion factor is needed to convert the concentration in g/m^3 to the concentration in ppb. At the typical conditions for temperature ($T = 298.15K$) and pressure ($p = 101.325 \times 10^3\ Pa$), the volume of n moles of any gas can be calculated from the ideal gas law,

$$V = \frac{nRT}{p} \tag{2.18}$$

where $R = 8.314472\ \frac{m^3 \cdot Pa}{K \cdot mol}$ is the gas constant. From the molecular weight (MW), the mass of n moles of gas $M = n\,mol \times MW\ g/mol = n \times MW\ g$. The conversion factor for SO_2 ($MW = 64.066\ g/mol$) can be calculated as

$$\text{Conversion factor for } SO_2 = \frac{1}{M_{SO2}} \frac{nRT}{P} \times 10^9$$
$$= \frac{n \times 8.314472 \times 298.15}{n \times 64.066 \times 101.325 \times 10^3} \times 10^9 \qquad (2.19)$$
$$= 381{,}878.55 \frac{ppb}{g/m^3}$$

The molecular weight of N_2O is 44.013 g/mol, so the conversion factor for N_2O is 555,868.30 $\frac{ppb}{g/m^3}$.

2.3 Monin-Obukhov similarity theory

Dimensional analysis was used to derive the relationships of wind speed and potential temperature with respect to height [10]. Under the assumption of dry air, the Monin–Obukhov similarity theory was developed on the basis of the logarithmic vertical profiles. Another main assumption is that the surface turbulent fluxes drive the dynamics within the surface layer and thus determine the relevant scales, such as the velocity scale (also knowns as friction velocity) u_* and the temperature scale θ_*. The Obukhov length, L, defined for dry air is:

$$L = -\frac{u_*^3}{\kappa \frac{g}{\theta}\left(\frac{Q}{\rho c_p}\right)} \qquad (2.20)$$

where κ is the von Karman constant, Q is the surface heat flux. The Monin-Obukhov length is an estimate of the height where the production (or removal) of turbulence due to buoyancy G_b is comparable with the production of turbulence due to mechanical shear G_k. The velocity scale u_* is defined as:

$$u_* \equiv \sqrt{\frac{\tau_w}{\rho}} = \frac{\nu_t}{u_*} \frac{\partial u}{\partial z} \qquad (2.21)$$

where the wall shear stress $\tau_w = \rho \nu_t \frac{\partial u}{\partial z}$. The temperature scale θ_* is given by:

$$\theta_* = \frac{\alpha_t}{u_*}\frac{\partial \theta}{\partial z} \tag{2.22}$$

The Monin-Obukhov similarity theory describes the mean flow and temperature under different stability conditions as functions of the Obukhov length. Along height z, the mean profiles of horizontal wind speed u and potential temperature θ are related to the universal similarity functions ϕ_m and ϕ_h [69] :

$$\left(\frac{\kappa z}{u_*}\right)\frac{\partial u}{\partial z} = \phi_m\left(\frac{z}{L}\right) \tag{2.23}$$

$$\left(\frac{\kappa z}{\theta_*}\right)\frac{\partial \theta}{\partial z} = \phi_h\left(\frac{z}{L}\right) \tag{2.24}$$

The widely used universal functions from Businger et al. are based on observations from the 1968 Kansas experiment [15]. In the neutral and stably-stratified ABL, ϕ_m and ϕ_h are given as [14]

$$\phi_m = 1 + 4.7\frac{z}{L}, \qquad 0 < \frac{z}{L} < 1 \tag{2.25}$$

$$\phi_h = 0.74 + 4.7\frac{z}{L}, \qquad 0 < \frac{z}{L} < 1 \tag{2.26}$$

In many practices, such as in [27,44], ϕ_m and ϕ_h are simplified to

$$\phi_m = \phi_h = 1 + 5\frac{z}{L}, \qquad 0 < \frac{z}{L} < 1 \tag{2.27}$$

From equation (2.23) and equation (2.25), the velocity as a function of height above ground z can be calculated as [8]

$$u(z) = \frac{u_*}{\kappa}\left[ln\left(\frac{z}{z_0}\right) + \phi_m - 1\right] \tag{2.28}$$

From equation (2.24) and equation (2.25), the equation for potential temperature is derived as

$$\theta(z) = \frac{\theta_*}{\kappa}\left[ln\left(\frac{z}{z_0}\right) + \phi_h - 1\right] + \theta_0 \tag{2.29}$$

where θ_0 is the potential temperature on the ground level. It should be noted that the coefficients

associated with ϕ_m and ϕ_h were derived from the flat terrain with uniform and small aerodynamic roughness length, and different experiments yield different numbers. As for κ, literature reported values measured in the atmosphere and wind tunnels to vary between 0.35 and 0.43 [14]. In this study, κ is set to 0.41.

The turbulent viscosity is expressed as:

$$\mu_t(z) = \frac{\rho \kappa u_* z}{\phi_m} \tag{2.30}$$

Based on measurements of the turbulent kinetic energy budget terms in the surface layer over a flat terrain [16], the dissipation rate of turbulent kinetic energy is obtained

$$\varepsilon(z) = \frac{{u_*}^3}{\kappa z}\phi_\varepsilon \tag{2.31}$$

where

$$\phi_\varepsilon = \phi_m - \frac{z}{L}, \qquad L > 0 \tag{2.32}$$

Since $\mu_t = \rho C_\mu \frac{k^2}{\varepsilon}$, the relationship between turbulent kinetic energy and its dissipation rate is obtained:

$$k = \sqrt{\frac{\mu_t(z)\varepsilon(z)}{\rho C_\mu}} = \frac{u_*^2}{\sqrt{C_\mu}}\sqrt{\frac{\phi_\varepsilon}{\phi_m}} = 5.48 u_*^2 \sqrt{\frac{\phi_\varepsilon}{\phi_m}} \tag{2.33}$$

where the constant 5.48 has been experimentally determined for the neutral atmospheric boundary layer [16]. This constant implies that under the neutral condition, $C_\mu = 0.033$, which is different than the originally proposed constant of 0.09.

Chapter 3

Measurements and data analysis

Measurements of wind speed and pollution concentration are essential to understand the ABL. The boundary profiles at the inlet of the domain are key to an accurate CFD simulation. This chapter discusses the measurements and explains the development of a curve-fitting method to generate boundary profiles at inlet based on the Monin-Obukhov similarity theory with inputs from multiple data sources.

3.1 Data sources

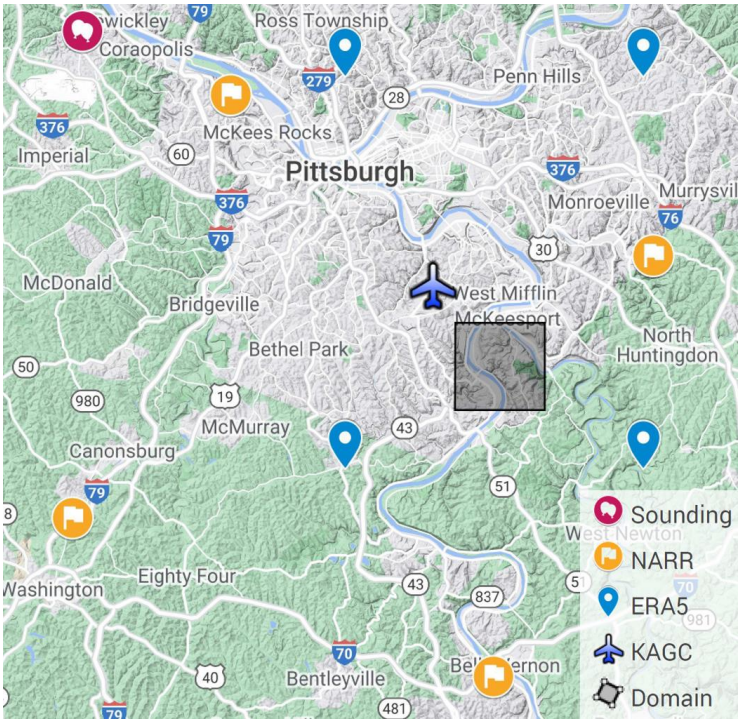

Figure 3.1: Locations of different meteorological data sources outside the computational domain. These sources are considered to be permanent, and they are used to generate vertical boundary profiles to be specified at the inlet of the domain.

Multiple meteorological data sources are utilized with their locations shown in Figure 3.1. The sounding data are reported twice at 00:00 in Zulu time (00Z) and 12:00 in Zulu time (12Z).

The North American Regional Reanalysis (NARR) dataset provides wind speed and temperature at 17 pressure levels (from $1000\ mb$ to $10\ mb$) for every 3 hours from 00Z to 21Z. The ECMWF Reanalysis v5 (ERA5) has an hourly resolution. The nearby airport KAGC reports wind speed and direction measured at $10\ m$ above ground level (AGL).

3.1.1 Sounding data

To measure wind, temperature, and various other properties in the atmosphere, the National Weather Service (NWS) launches a weather balloon twice a day at multiple locations across the US. Such measurement process is called atmospheric sounding, or simply as sounding. The balloon is equipped with a radiosonde capable of transmitting instantaneous weather and GPS position data back to the ground station. Since the balloon travels fast, the radiosonde can only take about $4-6$ measurements before rising over the ABL. The sounding data can provide valuable information about the vertical structure of the atmosphere. Normally, the sounding data can show the vertical temperature distribution up to $20\ km$, which is not necessary for the purpose of studying the behavior of ABL. The height of ABL is up to $1-2\ km$, so only the sounding data below this height is plotted, as shown in Figure 3.2. The Skew-T plots generated from the sounding data are used to determine the stability class of the atmosphere. The neutral condition is easily determined if the temperature profile is parallel to any of the dry adiabatic lapse rate lines. Strictly speaking, the stable class is identified when the environmental lapse rate is less than the moist adiabatic lapse rate. Since the moisture in the air is not modeled, and the air in the CFD model is dry, the stable class is identified when the environmental lapse rate is less than the dry adiabatic lapse rate. In Figure 3.2 (a), the neutral class is easily determined since the temperature line is parallel to any of the dry adiabatic lapse rate lines. Strictly speaking, the stable class is identified when the environmental lapse rate is less than the moist adiabatic lapse rate. Since the moisture in

the air is not modeled, and the air in the CFD model is dry, the stable class is identified when the environmental lapse rate is less than the dry adiabatic lapse rate. From the sounding data, when the atmosphere during a certain time period is determined as in stable class, it is often obvious to find the increase of absolute temperature along with the height.

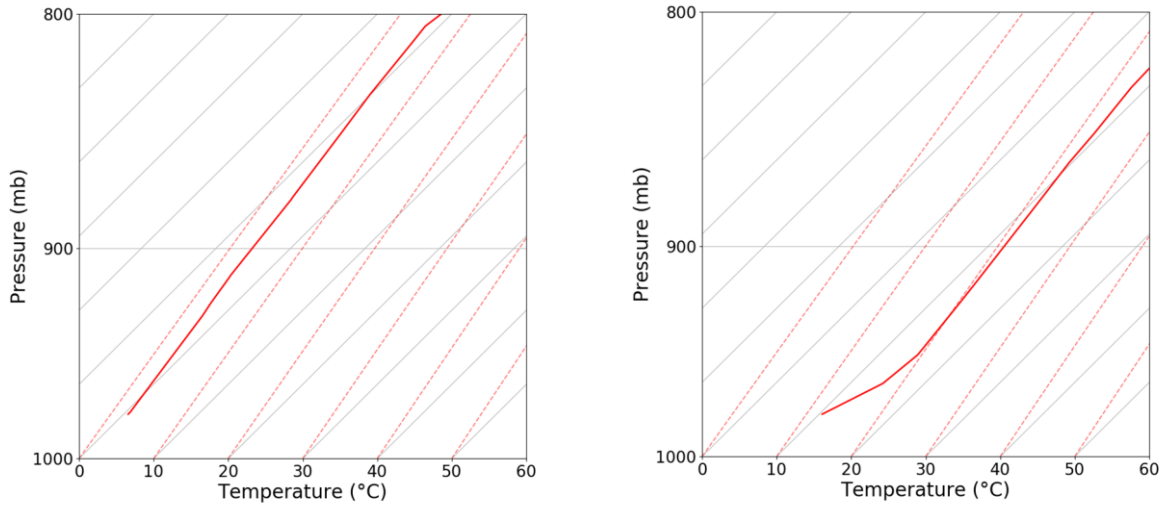

(a) Neutral stability class (b) Stable stability class

Figure 3.2: Typical examples of two stability classes that can be determined from the sounding data using the Skew-T plot. Red solid line: air temperature. Red dash line: dry adiabats. Black solid line: equal temperature from 1000 mb.

3.1.2 Reanalysis data

Reanalysis data is generated by ingesting available observations over the period being analyzed and provides a dynamically consistent estimate of the atmosphere at each time step. The shared features and differences of the NARR data and the ERA5 data are shown in Table 3.1. At the beginning of this research, only the NARR data was available. Later in Jun. 2018, the ERA5 dataset was published. We started focusing on using ERA5 in Sep. 2019. The comparison between the sounding data and the NARR data is shown in Table 3.1. Since there are 4 locations surrounding the study domain, where the reanalysis data (both NARR and ERA5) are available, as

shown in Figure 3.1, their mean values are calculated for later analysis. An example of the vertical profiles of wind speed from the reanalysis data and the sounding data is shown in Figure 3.3.

Table 3.1: Comparison between NARR and ERA5 reanalysis data.

Dataset	ERA5	NARR
Data type	Gridded	
Temporal coverage	1979 to present	
Horizontal coverage	Global	North American
Resolution	$0.25° \times 0.25°$	$0.30° \times 0.30°$
Vertical coverage	1000 hPa to 1 hPa	1000 hPa to 100 hPa
Vertical resolution	37 pressure levels	29 pressure levels
Temporal resolution	Hourly	3-Hourly
Key variables	Air velocity, air temperature, sensible heat flux	

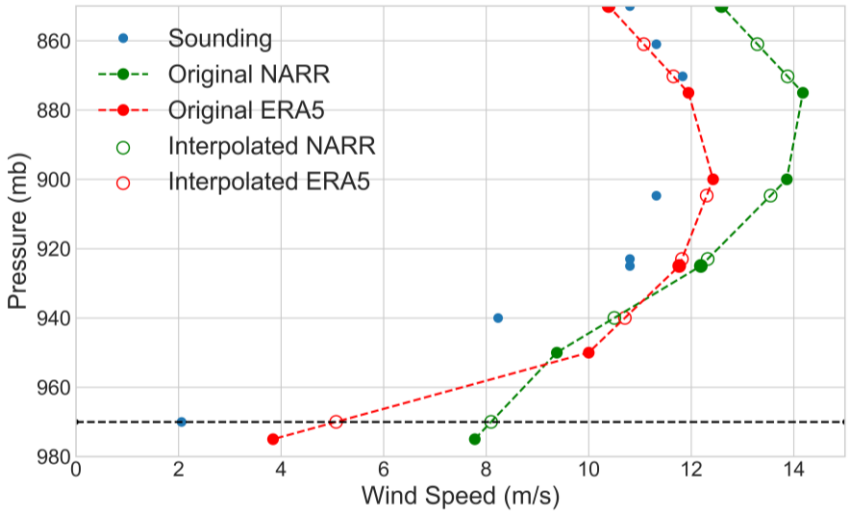

Figure 3.3: Comparison between the vertical profiles of wind speed from original reanalysis data (NARR and ERA5) and sounding data. The first point from sounding is used to illustrate the interpolation of reanalysis data based on the height of sounding data to create a paired dataset for R^2 analysis of same height levels. The horizontal dash line intersects with the straight lines from the reanalysis data, and the points of intersection (shown as circles) will be compared with the sounding data (shown as solid dots).

The sounding dataset reports data at different pressure levels than the reanalysis dataset. Besides, the reanalysis data has fewer data points along the vertical direction compared to the sounding data. So, a linear interpolation is performed at pressure levels reported by the sounding data whose corresponding height is between 0 to 5 km for direct comparisons as illustrated in Figure 3.3. The interpolated reanalysis data will be used to determine their quality.

Using data in Mar. 2019 reported at 00Z and 12Z, R^2 analysis is performed for the NARR and ERA5 data as shown in Figure 3.4 and Figure 3.5. For wind speed, the R^2 value is usually greater than 0.92 if the height is limited to 5 km. When the height limit is changed to 1 km, which is the height of current study domain, R^2 value becomes much lower for NARR at 0.68, and slightly lower for ERA5 at 0.89. As for the temperature, the R^2 value is always higher than 0.95. These findings agree with the common understanding that the reanalysis data is considered to be of better quality above the ABL. The data close to the ground is prone to have relatively larger errors. High R^2 values of the reanalysis data give confidence for later development of the curve-fitting methodology to obtain vertical profiles described in the next chapter.

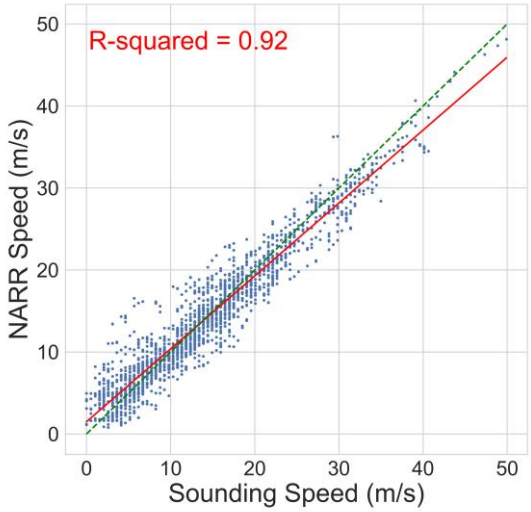

(a) NARR data within 5 km

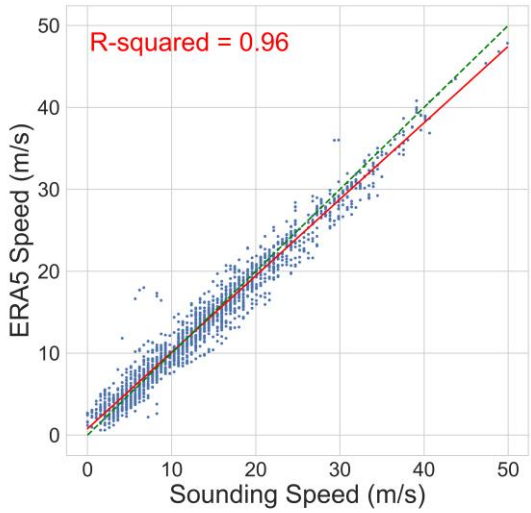

(b) ERA5 data within 5 km

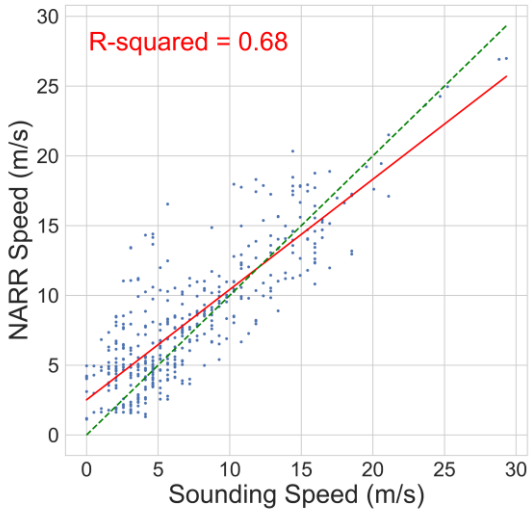

(c) NARR data within 1 km

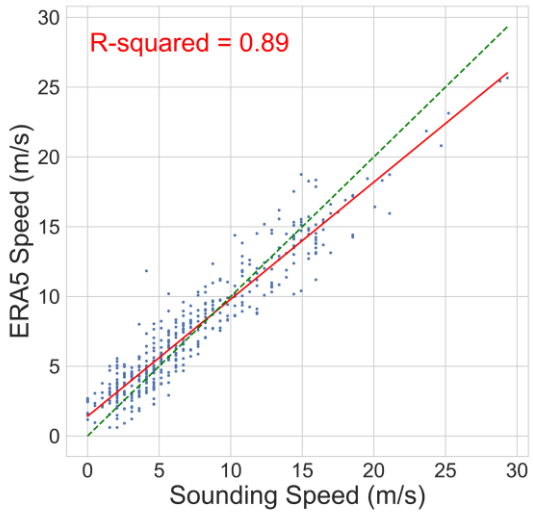

(d) ERA5 data within 1 km

Figure 3.4: Comparison between the reanalysis data with the sounding data for wind speed.

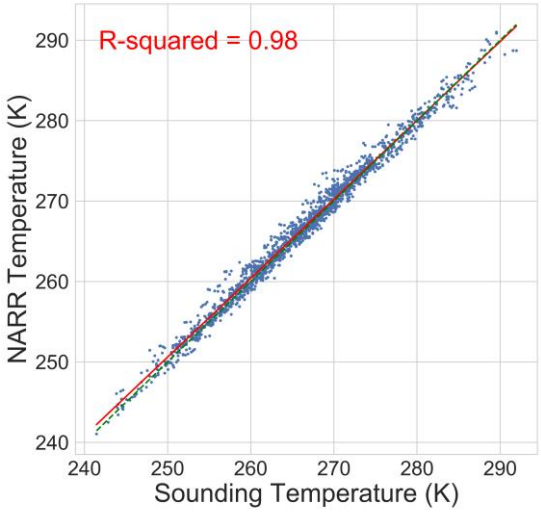

(a) NARR data within 5 km

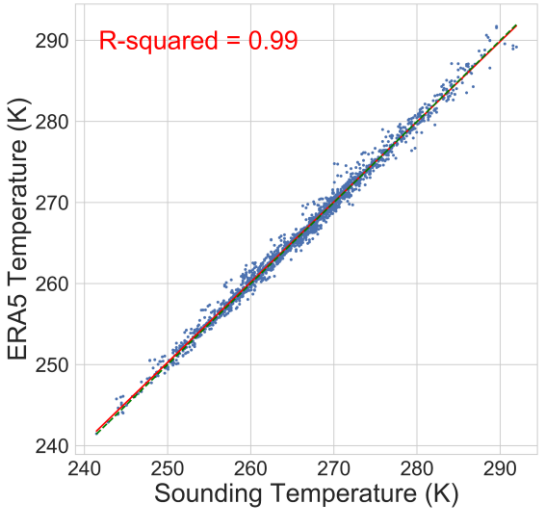

(b) data height within 5 km

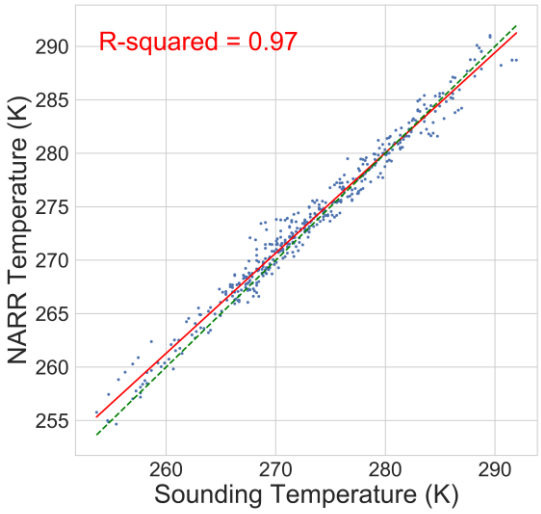

(c) NARR data within 1 km

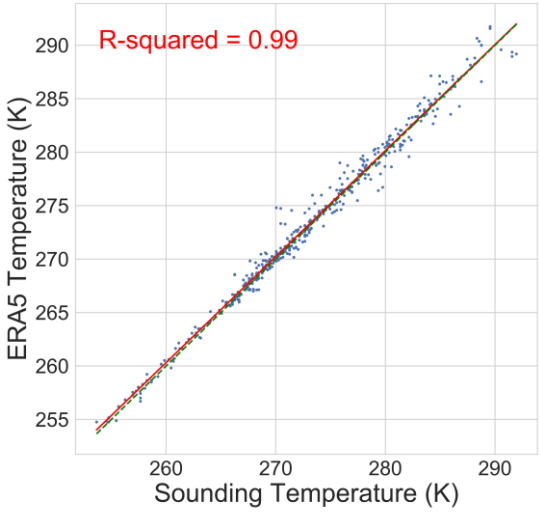

(d) ERA5 data within 1 km

Figure 3.5: Comparison between the reanalysis data with the sounding data for air temperature.

3.1.3 Data from stationary monitors

In addition to the sounding data, airport weather stations are a crucial part of the weather observation. Wind speed and direction are measured at 10 m above ground level (AGL) using ultrasonic wind sensors mounted on poles fixed to the ground. Air temperature is also recorded, but usually at the height of 2 m AGL. The Liberty monitoring station is located on top of a school building and is maintained by ACHD. There are multiple sensors that gather wind and temperature data and pollutants data such as SO_2 and fine particulate matter (PM). Stationary monitors at the Liberty site also serve as permanent data sources, but they are used for model validation and evaluation. Besides, a Sound Detection and Ranging (SODAR) device that uses sound waves to detect wind speed and direction at various elevations above the ground is located within the coke plant area. SODAR is often used in the study of micrometeorology, air quality, and atmospheric dispersion. The SODAR in this study is the XFAS model from Scintec Corporation, and it can report wind speed and direction from 40 m and up to 2000 m AGL at a 20 m resolution. The

measurement range of horizontal wind speed is from 0 to 50 m/s and for vertical speed is from -10 to 10 m/s. The accuracy of horizontal wind speed is within 0.1 to 0.3 m/s, and the accuracy of vertical wind speed is within 0.025 to 0.1 m/s depending on the operation mode. The accuracy of wind direction is within 1.5° when wind speeds are larger than 2 m/s. The ACHD SODAR saves wind data by averaging 15 minutes of measurements from 40 m up to 200 m AGL.

3.2 Selection of new monitoring sites

In order to find the optimal locations for installing new anemometers in the study domain, a preliminary CFD simulation was performed with assuming neutral ABL and uniform aerodynamic roughness length. From the simulation results, the velocity contour together with the streamlines near the ground can show where the wind speed and direction are the most different than other locations. The idea behind it is that: if there are three locations that show almost the same wind speed and direction, then there is no need to deploy monitors at all three locations.

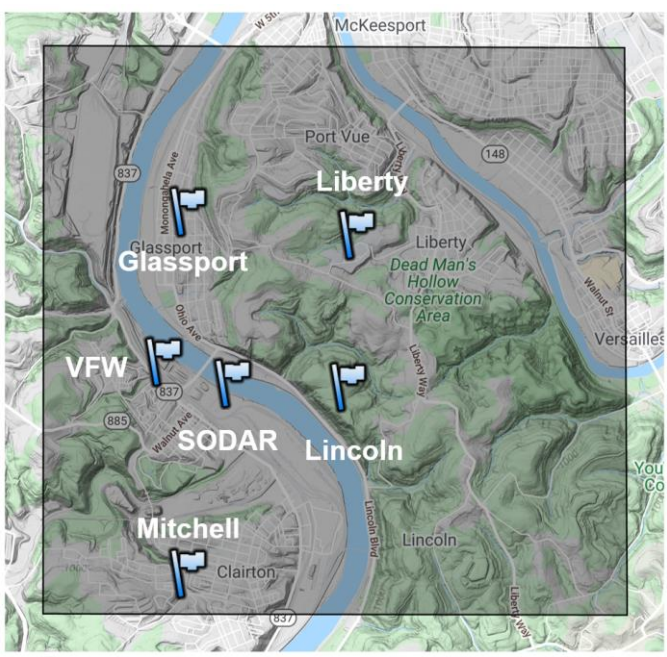

a) All measurement sites for wind speed and direction within the study domain

(b) Photo of the R. M. Young anemometer mounted on a pole

Figure 3.6: Wind measurements in the study domain for CFD model validation.

Multiple 2D and 3D ultrasonic anemometers from R. M. Young Company have been logistically deployed to cover the variation in land use, elevation, and terrain feature, so the sensor network is able to detect interesting flow patterns within the domain. These anemometers can detect a wide range of wind speeds ($0 - 40\ m/s$) with high accuracy (error: $\pm 3\%$) and quick response time ($<\ 1\ s$). As shown in Figure 3.6, in addition to the existing Liberty and SODAR sites, new sites are labeled as Mitchell, VFW, Glassport, Lincoln based on their locations.

Table 3.2 summarizes the key features of these sites. Note that the elevation is the height of the ground at the location with respect to the lowest point in the domain, which has a global elevation of $221\ m$ above sea level. The height AGL is the height of the sensor with respect to the local ground. Sensors are mounted at AGL height varying from $2\ m$ at the Mitchell location to $16\ m$ at the Liberty location.

Table 3.2: Descriptions of wind measurement sites within the study domain that are used for model validation.

Location	KAGC	Liberty	SODAR	Mitchell	Glassport	Lincoln	VFW
Easting (m)	591115	596165	594772	594482	594056	595097	593937
Northing (m)	4467441	4464307	4462658	4460663	4464732	4462581	4462931
Elevation (m)	160	121	10	92	18	132	18
Height AGL (m)	10.0	16.0	-	2.0	7.7	5.3	3.7
z_0 (m)	0.10	0.52	0.71	0.59	0.68	0.50	0.44

The Lincoln site is different from other sites because it is located on a small open ground surrounded by trees. First, to confirm if the anemometer at the Lincoln site is reporting good quality measurements, another anemometer was placed next to the original anemometer, as shown in Figure 3.7 (a). From Figure 3.7 (b), the time series of the wind speed from the two anemometers look very close, with a R^2 value of 0.98.

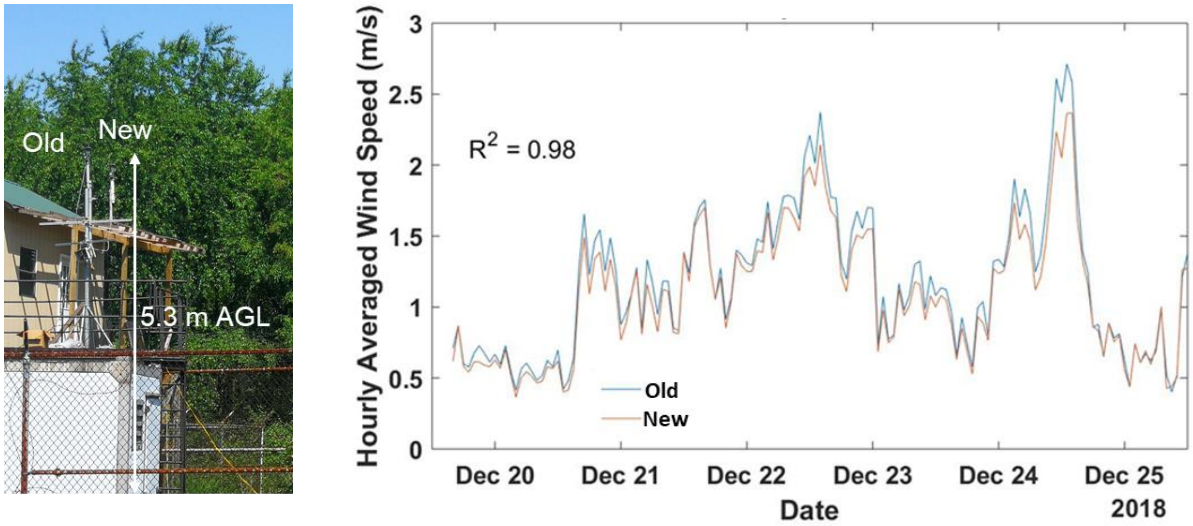

(a) Photo of the site (b) Time series of the hourly averaged wind speed data

Figure 3.7: Colocation of two anemometers at the Lincoln site to find out the reasons for low wind speeds.

To further investigate the low wind speed at the Lincoln site, multiple drone-based measurements were conducted. A DJI Matrice 600 drone mounted with a 3D anemometer was used to measure wind speed at different height levels near the surface (up to $100\ m$ AGL). The anemometer is mounted on the top of the drone to minimize the induced vertical wind speed. Figure 3.8 shows the time series of 2-minute average wind speed and wind direction from the two anemometers and the drone at the Lincoln site on May 25, 2019, for about 20 minutes. It can be seen that the wind speed and direction from the drone are very close to those of ground sensors, and they share the same trend. During the measurement period, the drone hovered at the same height as the two anemometers. However, due to the accuracy of the height sensor on the drone, the drone was initially hovering at a higher height. Towards the last 5 minutes of the drone flight, after visually checking the hovering height of the drone and lowering the drone to the same height level of the ground sensors, the drone-measured wind speeds became much closer to those of the ground sensors. The wind directions from the three sensors were very consistent. At 11:08, the

discrepancy is only due to the plotting style of wind direction, as a wind direction of 1° and 359° should only be considered to be differed by 2°, not by 358°. At 5.3 m, the wind speed at the Lincoln remains consistently low.

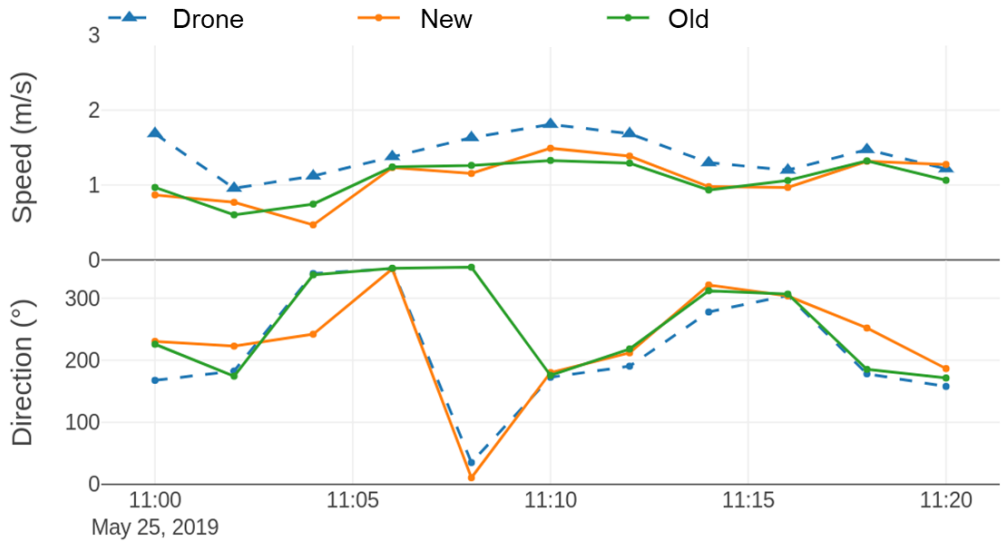

Figure 3.8: Time series of wind speed and wind direction from the two anemometers and the drone at the Lincoln site.

Multiple drone flights to measure the vertical profiles of wind speed are conducted, and the results are shown in Figure 3.9 (a). Wind speed profiles from several drone flights show a sudden drop in wind speed below the tree line at around 20 m AGL. The solid lines are from the drone measurements, and the dash lines are from a fitted logarithm wind profile. The thick canopy layer acts like obstructions above the ground surface in the real world, so the wind speed near the canopy height is reduced, as shown in Figure 3.9 (b). Due to such local effects at the Lincoln site, wind speed data from the Lincoln site will not be used to validate the CFD model. Further details are provided in the Appendix.

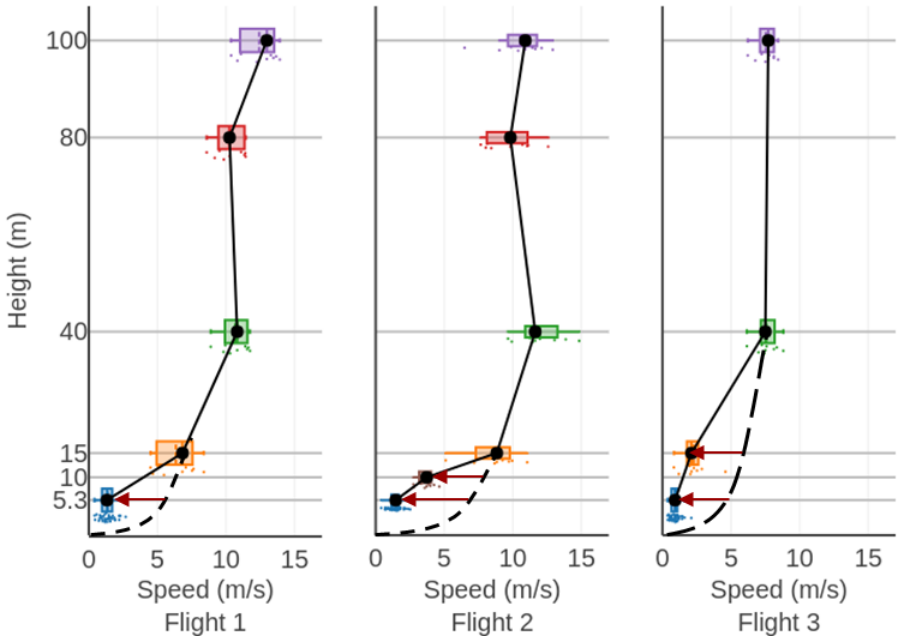

(a) Drone measured vertical profiles of wind speed at the Lincoln site

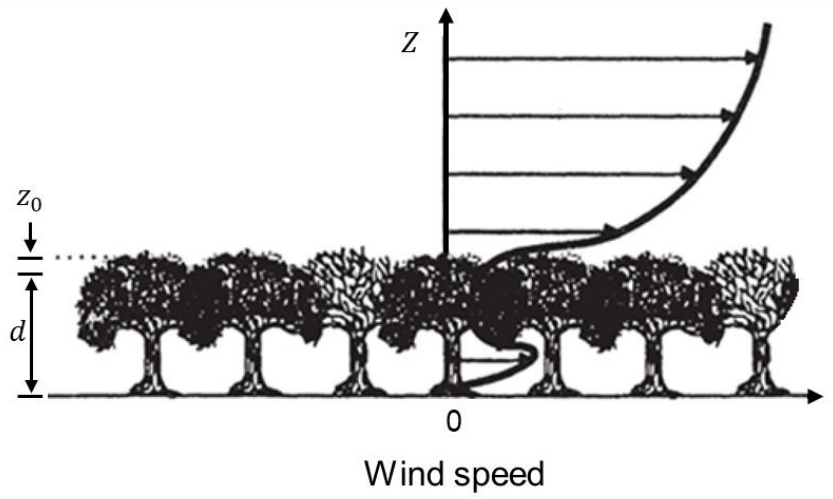

(b) Sketch of the wind profile over dense canopy, adapted from Stull [8]

Figure 3.9: Vertical profiles of wind speed over dense canopy from drone measurements at the Lincoln site and schematic of the vertical profile from Stull [8].

3.3 Analysis of weather and pollution data

After collecting over one year of wind data and over two years of pollution data within the study, together with measurements from permanent monitors, we can observe general patterns

shared across multiple monitoring sites and site-specific patterns.

3.3.1 Characteristics of wind

Figure 3.10 shows the time series of hourly averaged wind speed and direction from Aug. 1 to Aug. 7 in 2018. Each line shows the mean value ± the standard deviation (STD) using hourly averaged data except Liberty. Wind speed and direction fluctuate a lot over this week, which is typical, and no clear pattern can be found at one site. However, it can be seen that wind speed and direction at different sites are changing with time, but a clear site-to-site trend is retained. Overall, the wind speed at KAGC is the fastest. The wind speed at Liberty is slower than that of KAGC. As for the Mitchell sensor and Glassport sensor, they report much lower wind speed. The reported wind direction can change dramatically over the course of one day, but different sites maintain a similar trend. For example, when one location reports wind direction changes from west to south, other locations will show the same general trend in change in wind direction.

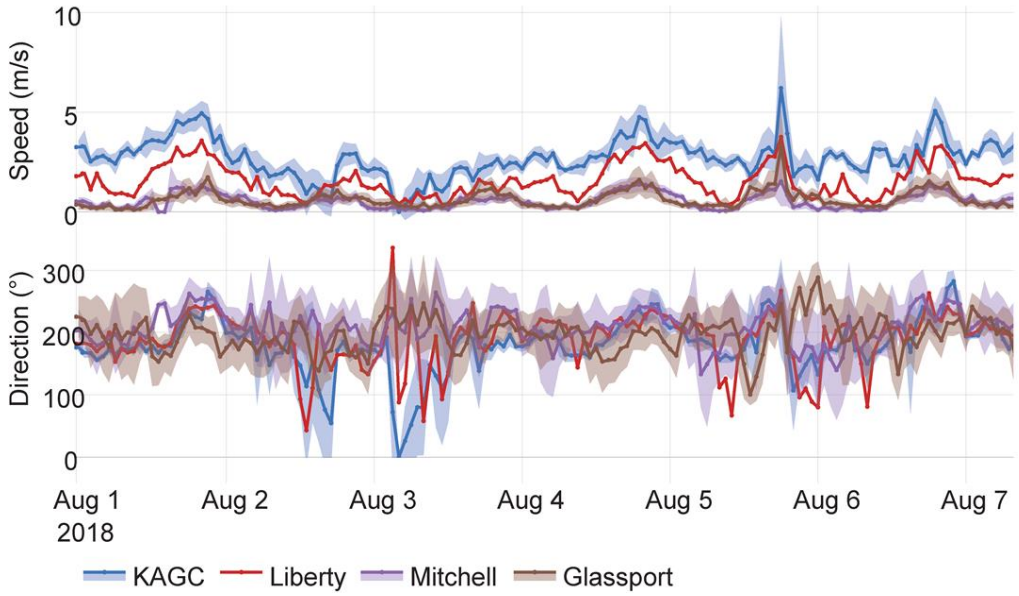

Figure 3.10: Time series of hourly averaged wind speed and wind direction from different locations. Each line shows the mean value as solid line ± the standard deviation (STD) as shade.

The wind rose plots of all the locations are generated as shown in Figure 3.11. In the wind rose plot, wind speed frequency at different wind directions is plotted in a polar coordinate with 36 bins. Each bin covers an angle of 10°, and the length of each color on the bin indicates the frequency of the corresponding wind speed. The overall wind speeds at KAGC and Liberty are much faster due to their relatively high elevation and distance from the ground. Although the Glassport sensor is located at 7.7 m AGL, it is mounted on top of a two-story building, which is similar to the Liberty site. Both the Glassport site and the VFW site have low elevations. As a result, the mean wind speeds at both Glassport and VFW are low. The Lincoln site shows low wind speed even though it is located at 5.3 m AGL and it has the highest elevation among all wind sensors in the domain. However, the mean wind speed is only 1.0 m/s, which again demonstrates the local effect at the Lincoln site. Besides the Lincoln site, wind data from all other sites will be used to validate the CFD model.

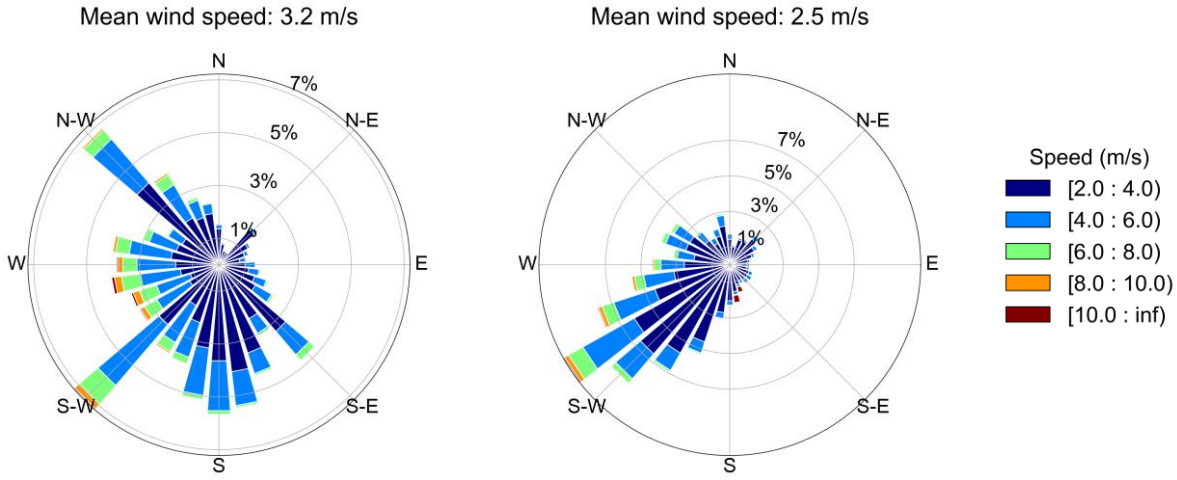

(a) KAGC: 01/2018-12/2019 (b) Liberty: 01/2018-12/2019

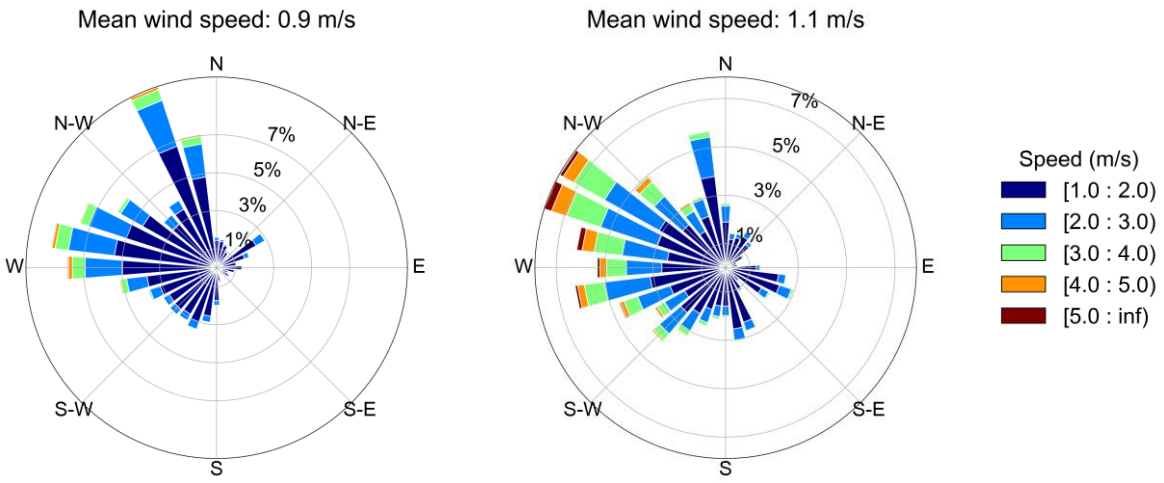

(c) Mitchell: 01/2018-12/2018 (d) Glassport: 03/2018-01/2019

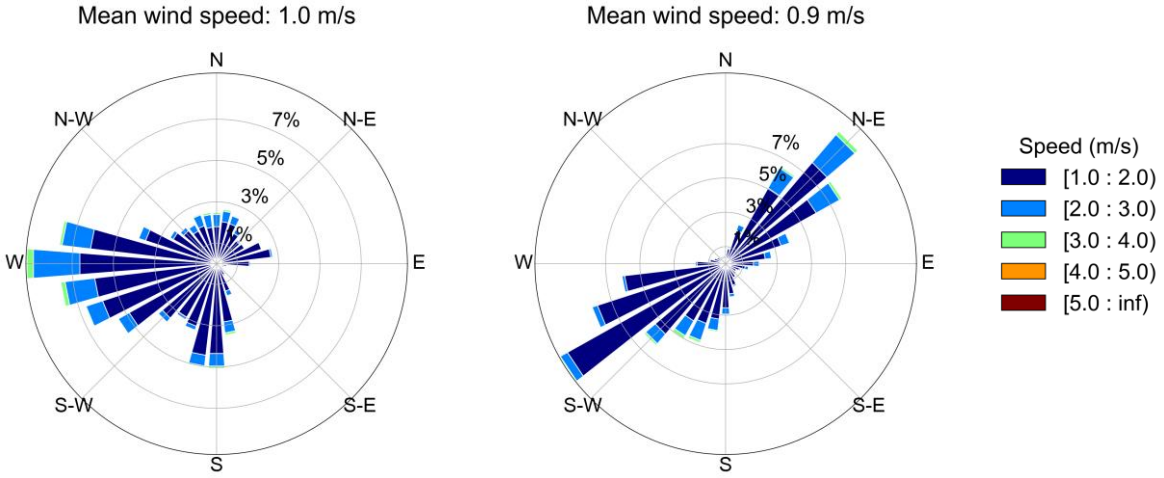

(e) Lincoln: 01/2018-04/2019 (f) VFW: 05/2018-02/2019

Figure 3.11: Wind roses and mean wind speed at different sites.

Based on six months of measurements from SODAR, the hourly mean vertical profiles (from 8 height levels: 40 m, 60 m, to 180 m) are generated for each hour of the day as shown in Figure 3.12. To have a statistical view of the shape of the vertical profiles, the wind speed profiles are normalized first. Then they are categorized using the k-mean method with 2, 3, and more clusters. Figure 3.13 shows the mean profiles from 2 clusters. About 60% of the hourly mean vertical profiles are log (or near linear) wind profiles, and about 40% of the profiles are C-shaped wind profiles. The 8-dimensional vectors (due to 8 height levels) are projected into a 2D space and

shown as scatter points for visualization. Towards the upper side, the data points have a more obvious log shape. The stronger wind starts to develop in the afternoon when the sun heats the ground, and the wind profile tends to be C-shaped. At night, the wind profile tends to be slightly log or linear. The study of the heat island effects of the plant is likely to cause the C-shaped wind profile near the SODAR site. More details of such topics can be found in the Appendix.

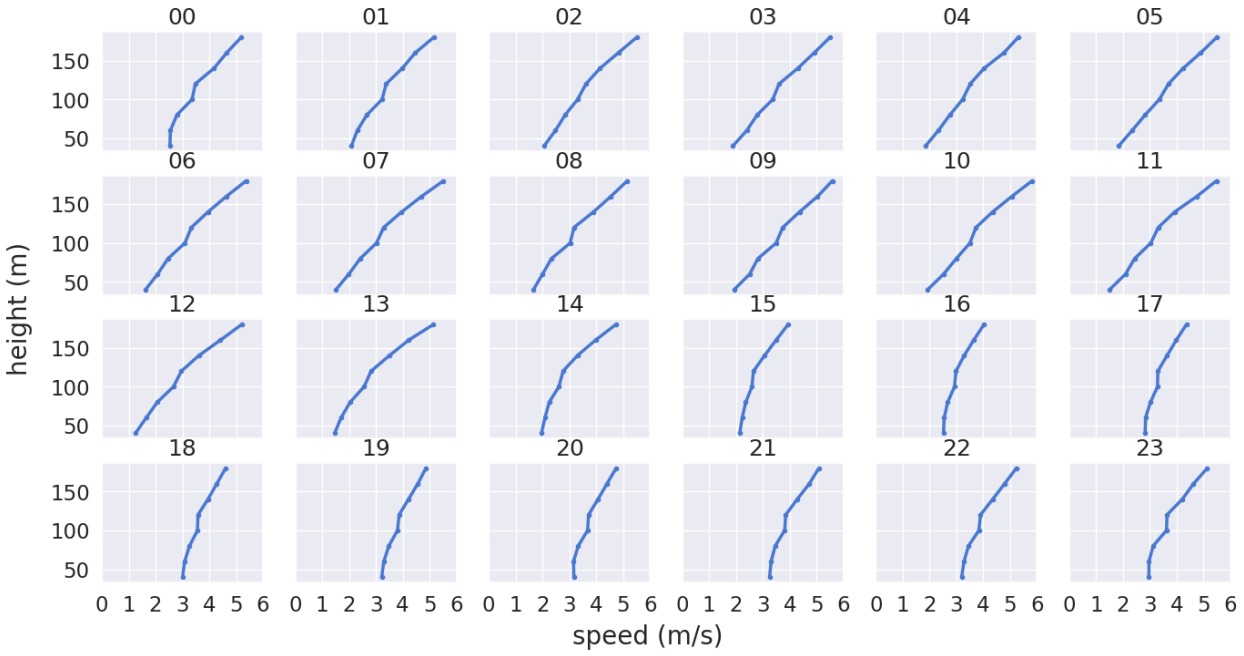

Figure 3.12: Mean vertical profiles of wind speed at each hour over a six-month period. Time is shown in Zulu. The local Eastern Standard Time zone is 4 hours behind Zulu time.

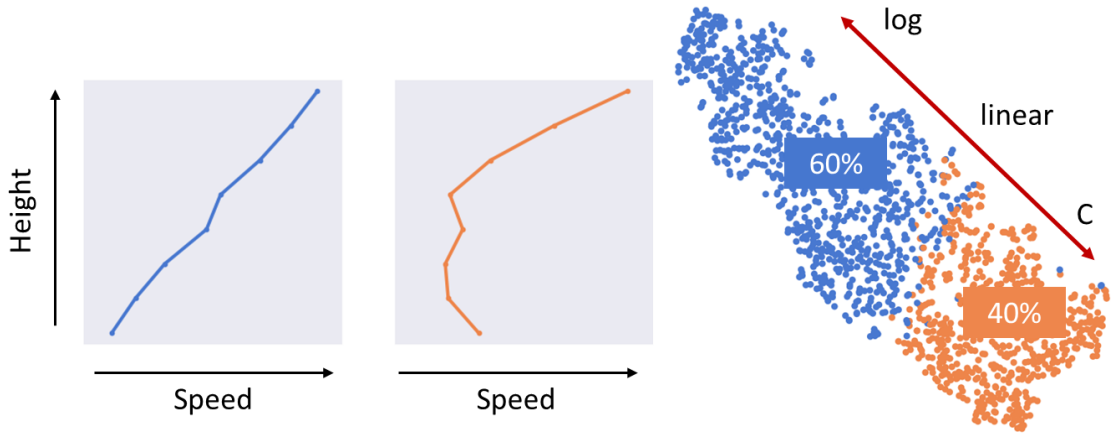

Figure 3.13: Normalized mean vertical profiles of wind speed from SODAR using 2 clusters.

SODAR data can also show the wind direction along with the height. Using all the available data from 2018 and 2019, the STD of the wind direction using the 15-minute mean data at nine height levels of the SODAR site within one hour is calculated and shown together with data from the Liberty site in Figure 3.14. Each box contains all the values of STD, and all the mean values of the boxes are connected with the solid line. Within one hour, the STD of wind direction using the 1-minute wind direction is much higher than that of the 15-minute wind direction. There is a decreasing trend of STD of wind direction with increasing height from the SODAR data. Statistically speaking, the wind speed is faster at a higher height, and the wind direction varies less. The STD values could go up to 100° across all height levels. The mean value of the STD of wind direction within 1 hour using the 15-minute data is 17.4° at 40 m AGL, and this value decreases to 8.3° at 200 m AGL.

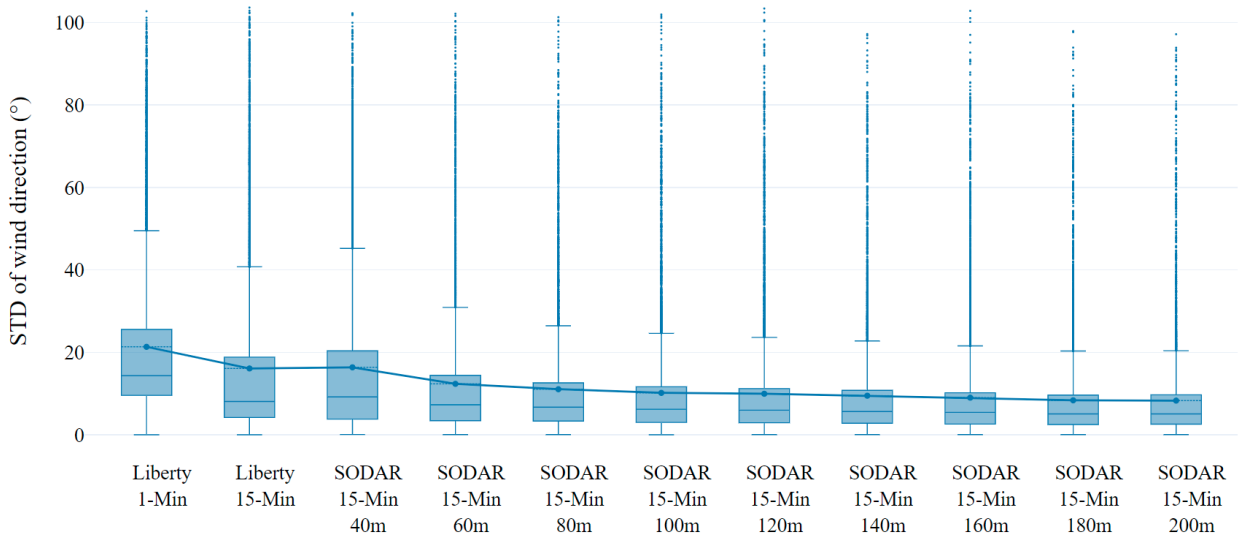

Figure 3.14: Standard deviation of the hourly wind direction using data at Liberty and the SODAR site for all wind directions.

At 40 m AGL, different wind speed ranges have different STDs of wind direction, as shown in Figure 3.15. When the wind data are filtered to only include the southwest wind, Figure

3.16 shows the mean value of the STD of wind direction within 1 hour using the 15-minute data is 8.5° at 40 m AGL, and this value decreases to 5.5° at 200 m AGL.

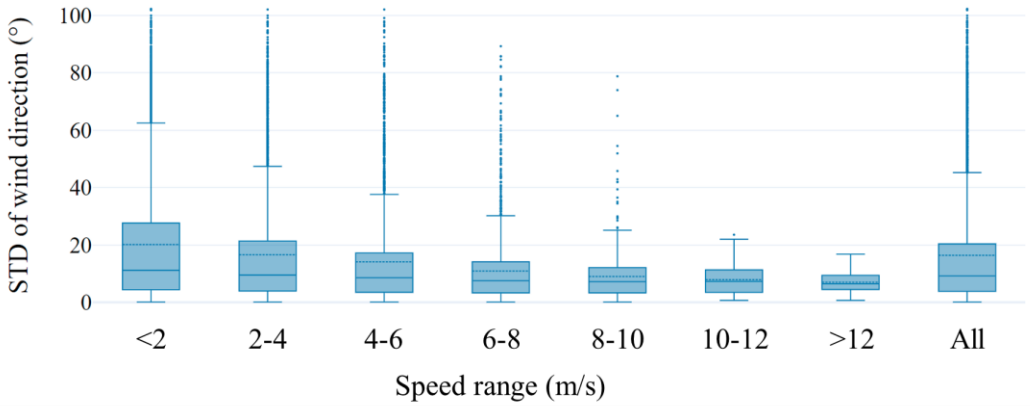

Figure 3.15: Standard deviation of the hourly wind direction at 40 m AGL for different wind speed ranges.

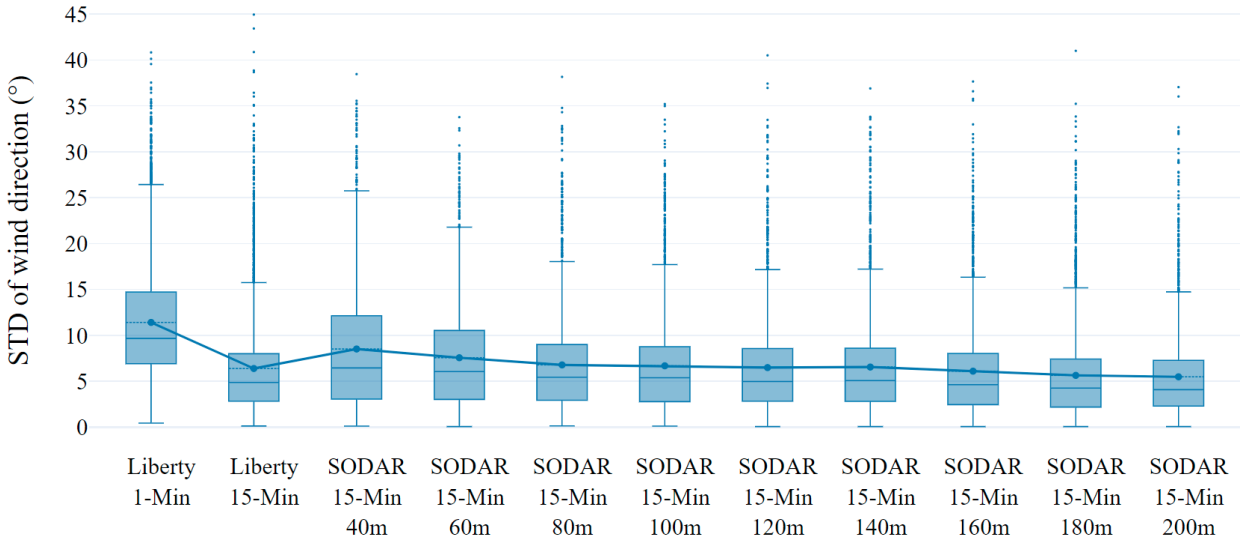

Figure 3.16: Standard deviation of the hourly wind direction using data at Liberty and the SODAR site filtered for southwest wind directions.

3.3.2 Atmospheric inversion

Surface-based temperature inversion conditions typically start after sunset and disappear within a few hours after sunrise. Table 3.3 gives the strength, height, and frequency of substantial temperature inversions estimated from the sounding data [70]. Over the 12-year period, about 43%

of the days have morning inversions of at least 1 ℃ strength near the Pittsburgh region. The average inversion strength is 3.8 ℃ with an average height of 243 m above the ground.

Table 3.3: Statistics of inversion strength, height, and frequency over recent years.

Year	2015	2016	2017	2018	2019	2008-2019
Average strength ± its STD (℃)	3.9±2.1	4.1±2.5	3.8±2.1	3.3±2	3.8±2.1	3.8±2.2
Average height ± its STD (m)	250±139	262±146	214±134	260±170	253±128	243±134
Days of inversion and frequency (%)	166 (45)	167 (46)	203 (56)	146 (40)	157 (44)	157 (43)

3.3.3 Statistics of SO_2 concentration

The RAMP (Real-time Affordable Multi-Pollutant sensor package) sensor network [71] developed and deployed in a partnership between Carnegie Mellon University and SenSevere Limited Liability Company has two sites west of the coke plant and two sites east of the plant that are all within 2 km of the coke plant. Together with the Liberty monitor, the total 5 SO_2 data sources are shown in Figure 3.17. Similar to a wind rose, in which the frequency of winds over a time period is plotted by wind direction in a polar coordinate system, the rose plot for SO_2 concentration in the study domain is plotted as shown in Figure 3.18. As some sensors could be offline for maintenance, a common time period from 01/2019 to 07/2019 is used to create the plots when all the sensors are reporting data continuously. Since all other sites do not have a wind sensor, the wind direction reported from the Liberty site is used. High SO_2 concentration is observed at the Liberty site when the wind direction is from south to southwest. The west wind can also bring high SO_2 concentration to Liberty. Over the seven months, the mean SO_2 concentration is 4.8 ppb at Liberty for all wind directions. If the wind direction is limited to be within $180° - 270°$, the

mean SO_2 concentration is increased to 8.0 ppb. With an even smaller wind direction range between $190° - 220°$, the mean concentration goes up to 15.3 ppb.

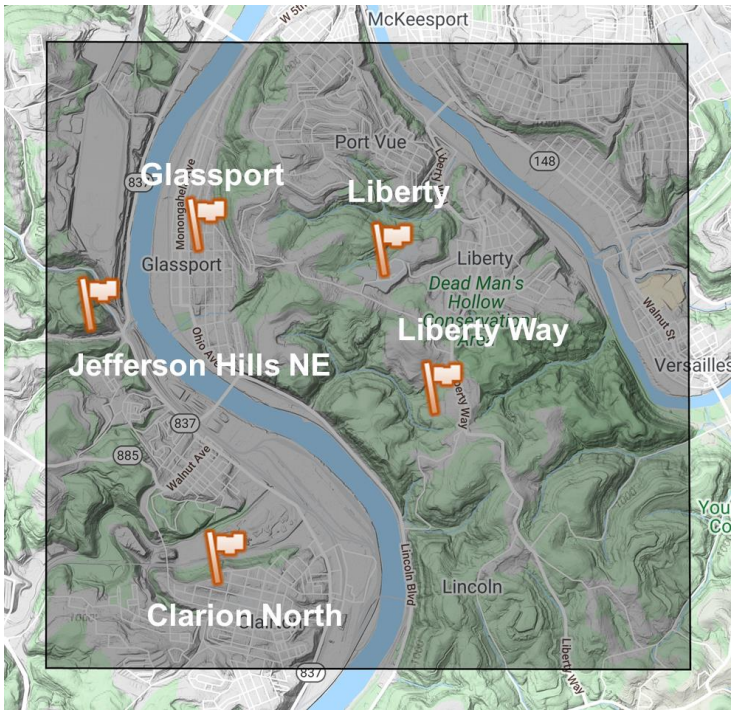

(a) All measurement sites for SO_2 in the study domain

(b) Photo of the RAMP sensor

Figure 3.17: SO_2 measurement in the study domain for CFD model validation.

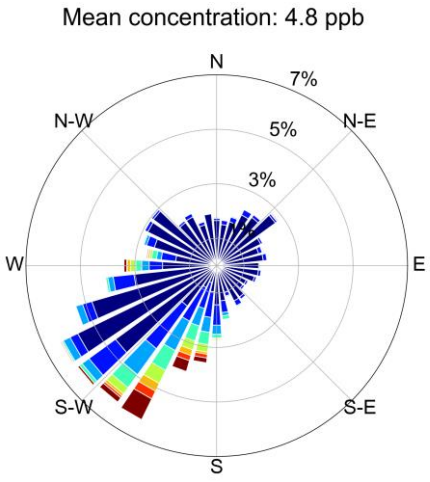

(a) Liberty, 2.2 km

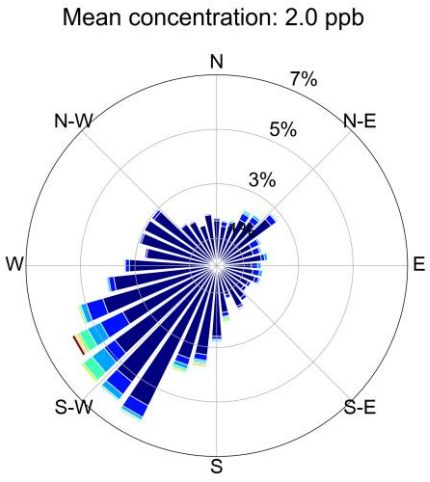

(b) Liberty Way, 1.4 km

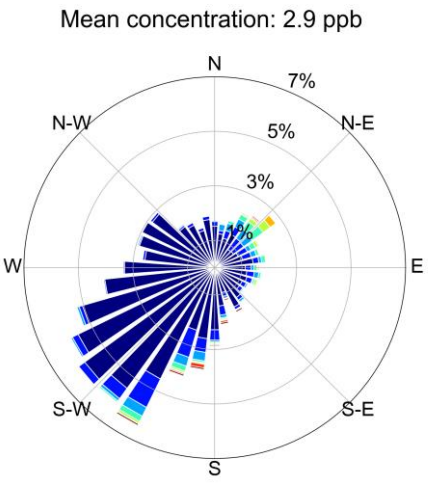

(c) Clairton North, 1.0 *km*

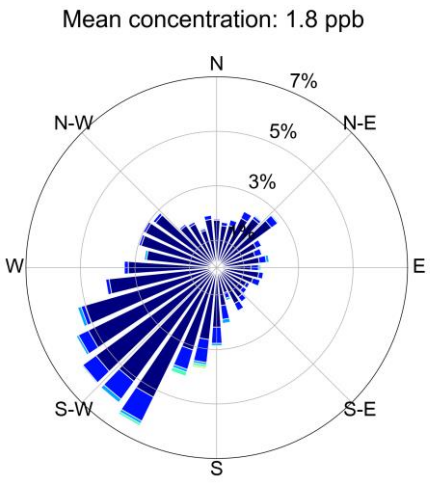

(d) Jefferson Hills NE, 2.5 *km*

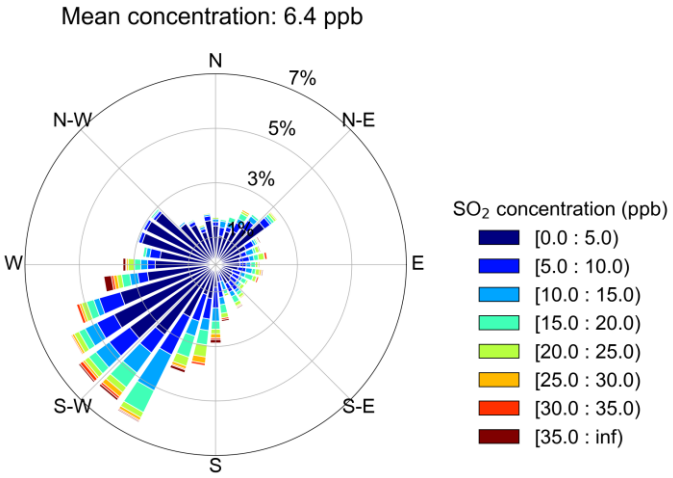

(e) Glassport, 2.8 *km*

Figure 3.18: SO_2 roses and mean SO_2 concentration at different sites and their straight-line distances to the center of the coke plant.

The Liberty Way site is closer to the coke plant, but it reports only half of the mean concentration from the Liberty site. The wind direction needs to be at around 240° to bring SO_2 directly from the plant to the Liberty Way, which is quite frequent. The SO_2 concentration is likely to miss this site after emitting from the hot stacks and being raised by the high hill right across the river. The Clairton North site observes more SO_2 when the wind direction is from the northeast, which agrees with its relative location to the plant. The Jefferson Hills NE site is located within a small valley, and it is hard for the SO_2 plume to find its way there, so the mean SO_2 concentration

is the lowest. The Glassport site shows highest SO_2 concentration is picked up when the wind direction is from the west. It is possible that the US Steel's Irvin Works, which is located within $700\ m$ west of the Glassport site, is emitting a small amount of SO_2 that is picked up by the Glassport RAMP sensor.

From Figure 3.19, the time series of wind direction and SO_2 measurements show two time periods when high SO_2 concentrations are recorded by the Liberty monitor: one is at around 00:00-03:00, 01/03/2019 and the second one is at 00:00-06:00, 01/04/2019. The emission rates are almost constant during these two time periods, at around $270\ g/s$ and $280\ g/s$.

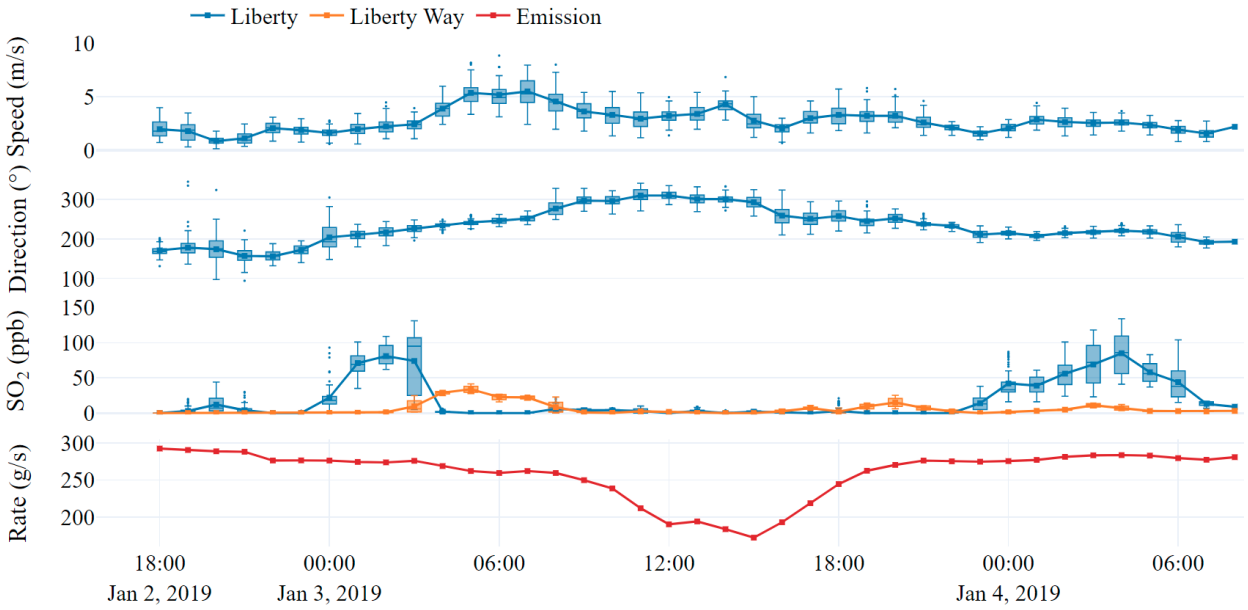

Figure 3.19: Time series of wind speed, wind direction, SO_2 measurements, and emission rate from 01/02/2019 to 01/04/2019. Two time periods with high SO_2 concentrations can be identified. One is around 03:00, 01/03/2019 and another is at 04:00, 01/04/2019.

During the first time period, at 03:00, the SO_2 concentrations vary a lot (ranging from 5 to 131 ppb), as shown in the box plot generated with the 1-minute data. Such a large range of SO_2 concentrations is linked to the dramatic wind direction change ($196° - 248°$) recorded at the Liberty site. Prior to 03:00, the SO_2 concentrations at the Liberty Way monitor are close to 0. From

00:00 to 03:00, the mean wind direction changes from $204°$ to $226°$, which is not the preferred wind direction ($240°$) to see high SO_2 concentrations from the Liberty Way monitor. However, due to the dramatic wind direction change at 03:00, the Liberty Way monitor starts to pick up SO_2. After 03:00, the wind direction gets closer to the preferred wind direction ($240°$) of Liberty Way at 05:00, when we see the peak concentration at Liberty Way. Meanwhile, the concentration from the Liberty monitor already drops to 0. After that, the concentration at Liberty Way goes down as the wind direction keeps moving to $270°$ and larger. From the peak concentrations at Liberty and Liberty Way, we can tell that the SO_2 plume should not be much wider than the distance between these two locations, which is around $1.4\ km$.

During the second time period, the wind direction is much steadier than that of the first one. When the mean wind direction changes from $233°$ at 22:00, 01/03/2019 to $210°$ (the preferred wind direction at Liberty to see high concentration) at 23:00, the monitor starts to pick up SO_2. The wind direction varies from $202°$ to $240°$ at 03:00 and 04:00, 01/04/2019, and only during these two hours, the Liberty Way monitor shows some SO_2 concentration values at $11\ ppb$ and $7\ ppb$.

3.4 Tracer release measurements

Tracer gases such as sulfur hexafluoride (SF_6) and nitrous oxide (N_2O) have been used to evaluate numerical models related to atmospheric dispersion [72,73]. In order to provide validation cases for the CFD model, a total of 5 tracer release experiments using N_2O were conducted under this study. Three different locations were identified for tracer release shown in Figure 3.20. Location 1 is at the Clairton Resident Park. The Park is surrounded by residential streets such that the released plume could be traced by driving up and down the grid of streets. This location is selected as a test experiment to get a basic idea of what the plume will look like and how far the

plume can reach during the release period. Location 2 is on the west bank of the Monongahela River so that the experiments at this site resemble how the pollutants emitted from the plant will travel across the river and reach the residential areas downwind. Location 3 is the dead-end at the top of Coursin Rd. This release is designed to simulate how pollutants would flow along hollows.

(a) Release location 1

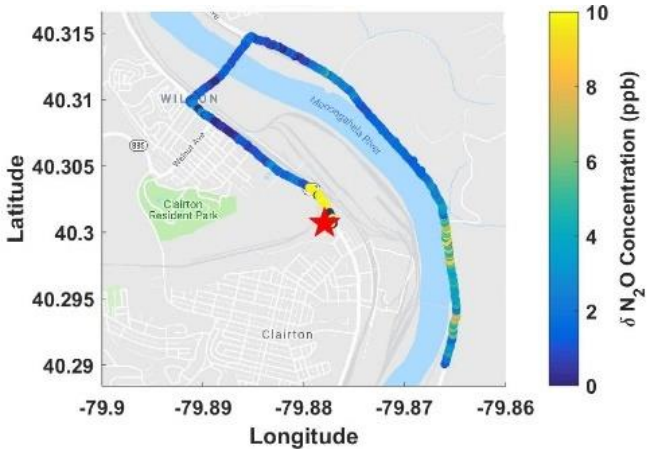

(b) Release location 2

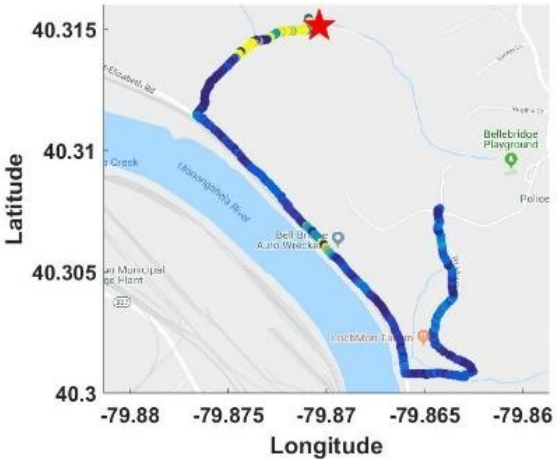

(c) Release location 3

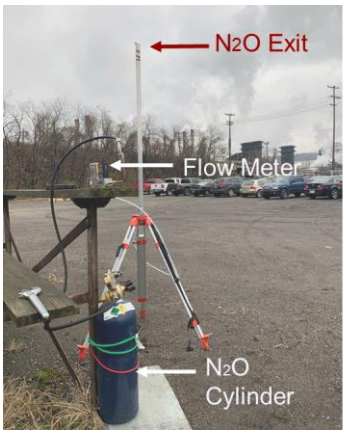

(d) Release setup

Figure 3.20: The driving paths and mean concentrations of N_2O above the ambient level of three unique tracer release experiments. The release setup consists of a cylinder that stores N_2O in the liquid phase, a flow meter that controls the emission rate, and rubber hoses that connect the cylinder outlet, the flow meter, and the gas exit on top of a 2-meter pole. The red star on the map shows the release location.

During the experiments, N_2O was released from a compressed gas cylinder at a fixed

location (marked by the red star in Figure 3.20) and at a fixed flow rate of 50 standard liters per minute. A precision gas mass flow controller from Alicat Scientific was used during the releasing process. Based on the standard temperature and pressure configurations in the controller: temperature of 298.15 K and pressure of 101.325 kPa, the flow rate is converted into 1.5 g/s. The wind speed and direction were monitored from the nearby Mitchell sensor and VFW sensor during all tracer release experiments. After the tracer gas reached a steady state (estimated about 5-10 minutes), the mobile laboratory was driven around to measure the N_2O concentration. A TILDAS (Tunable Infrared Laser Differential Absorption Spectroscopy) was used to measure the N_2O concentrations. Prior to the release tests, the background concentrations of N_2O were measured. The mean concentration stayed at 320 ppb with a standard deviation of 2 ppb. The mean concentration was subsequently subtracted from the measured N_2O concentration during the release. Only the concentrations due to the tracer release experiments were necessary for the CFD model validation. For measuring the plume formed by the emission of N_2O, the roads where the plume was expected to be found were driven by at least three times each. Figure 3.21 shows the time series of wind and N_2O measurements during a release. The arrows on the legends indicate the moving direction of the van.

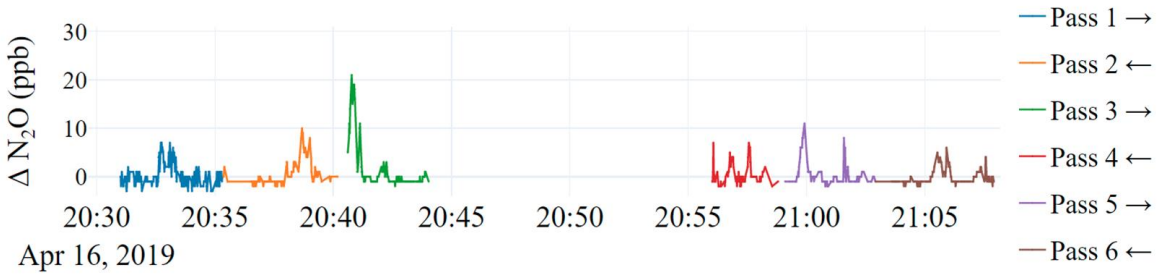

Figure 3.21: Time series of N_2O measurements in different passes during a release. The rightward arrow (→) indicates the sampling van moves to the east, and the leftward arrow (←) indicates the van modes to the west on the route.

A total of 6 passes were measured. GPS data was recorded within the lab van during the release. The GPS data was then used to match the times on the TILDAS data with the N_2O measurements. Each release lasted approximately 45 minutes. Measurements at the same location were averaged together to obtain the steady-state plume over the time of the entire release shown as the "Pass Mean" in Figure 3.22. A Gaussian is also fitted, as shown in Figure 3.22. The mean plume from measurements will be compared with the CFD-predicted plume.

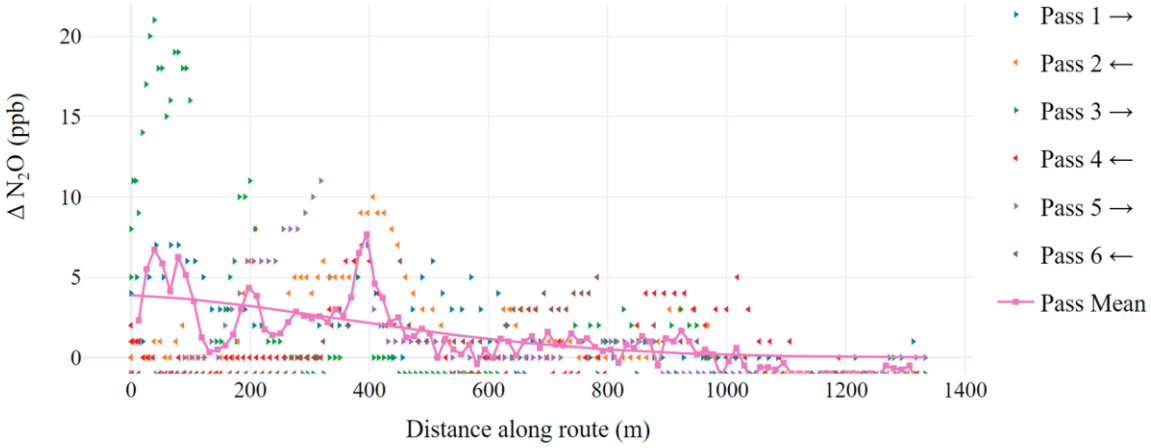

Figure 3.22: N_2O measurements during each pass and the mean of these passes. A Gaussian plume is created by fitting the mean pass data shown as the solid curve.

Although a total of 5 experiments were conducted, only three tracer experiments at location 2 were selected to be compared with simulation results. They are named tracer releases 1, 2, and 3. The detailed meteorological conditions corresponding to the three releases are shown in Figure 3.23, Figure 3.24, and Figure 3.25. In tracer releases 1 and 3, the wind directions at KAGC and Liberty were very steady, while the wind speeds were relatively high (greater than $2\,m/s$). However, the wind directions changed a lot during tracer release 2, and the wind speed is considered very calm (less than $1\,m/s$). The VFW sensor reported dramatically varying wind directions during releases 1 and 2, which could be due to some local effects. The changes in temperature are small during the 2 hour period.

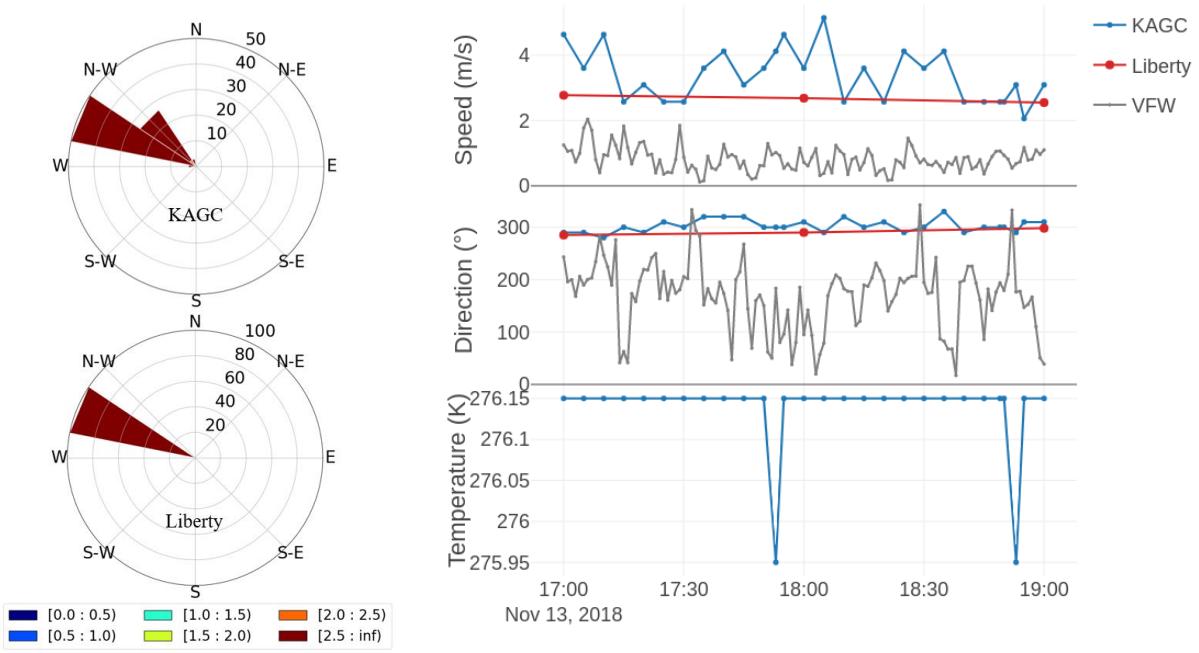

(a) Wind roses (Speed in m/s) (b) Time series of meteorological data

Figure 3.23: Weather condition reported by different sensors during trace release 1.

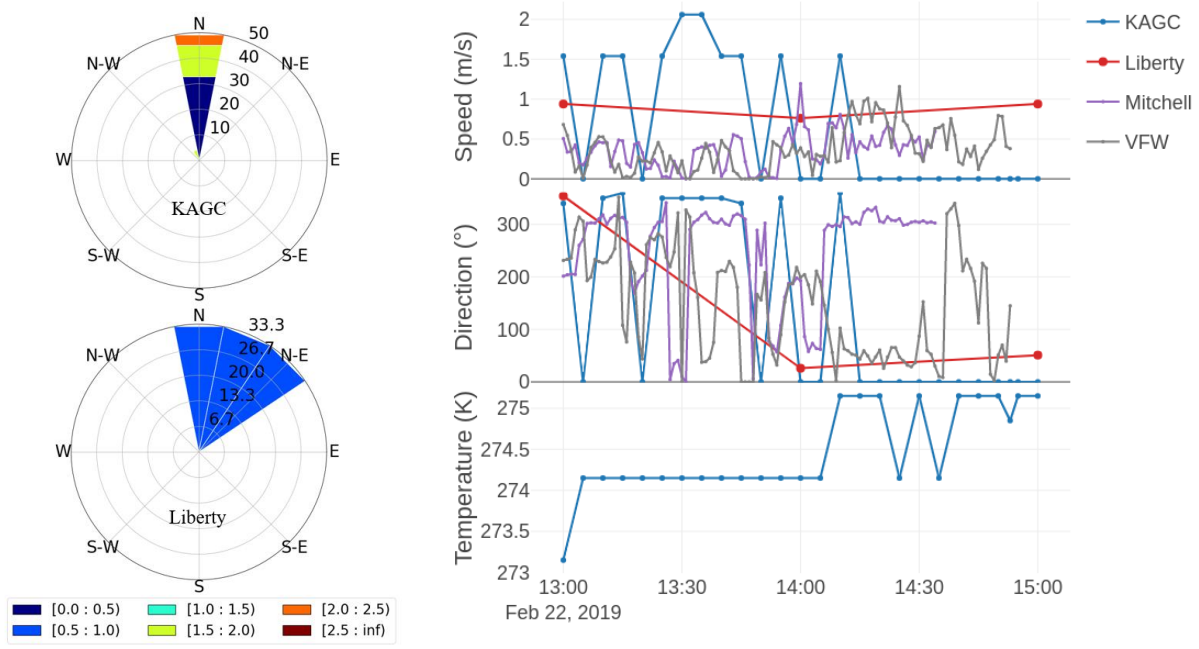

(a) Wind roses (Speed in m/s) (b) Time series of meteorological data

Figure 3.24: Weather condition reported by different sensors during trace release 2.

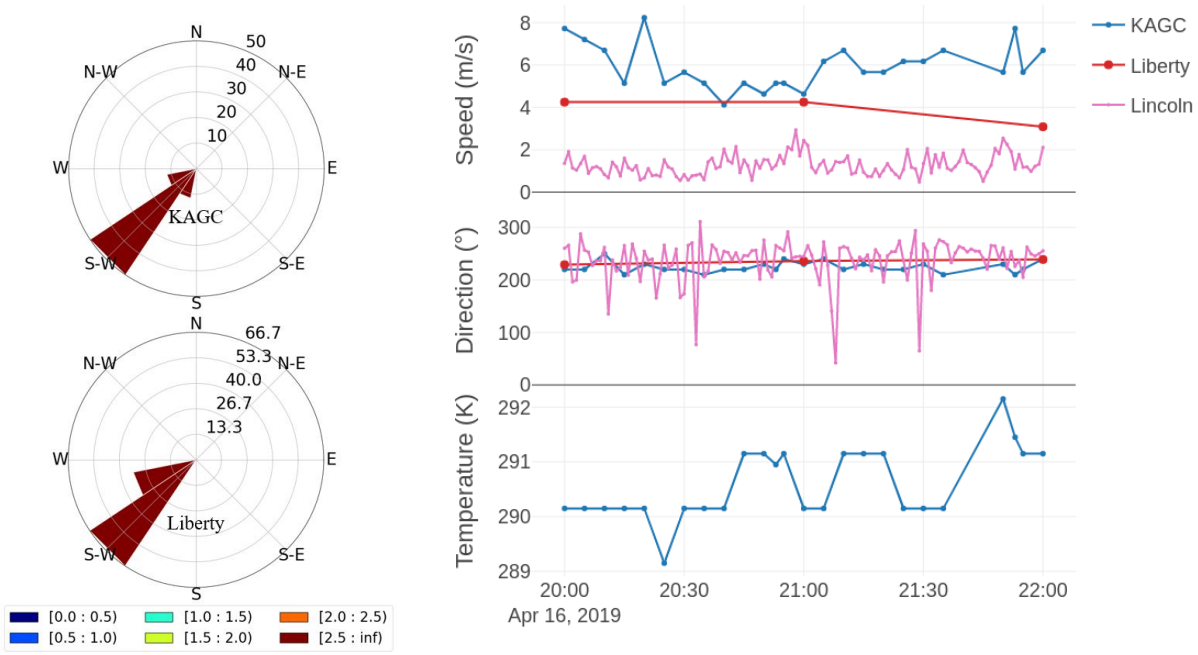

(a) Wind roses (Speed in m/s) (b) Time series of meteorological data

Figure 3.25: Weather condition reported by different sensors during trace release 3.

Chapter 4

Model setup

The process of setting up a CFD model includes pre-processing of geometry, generating the mesh, setting up solver parameters, discretization schemes, and boundary conditions. This chapter explains the process of obtaining good-quality full-hex mesh for the complex terrain and how to set the boundary conditions of different variables properly.

4.1 Geometry and mesh

A 3D computational domain covering the complex terrain near the Clairton coke plant needs to be developed for use in the CFD model. We have relied on the Pennsylvania Spatial Data Access (PASDA) [74] database to extract elevation contour maps of the Clairton coke plant region. The PASDA contour data claim to have a horizontal positional accuracy of $\pm 5\ ft$ ($1.5\ m$) and only contain the smooth ground surface. Buildings and other land covers are not included. After downloading the contour maps of Allegheny County from the PASDA website, the rest of the steps include extraction of a sub-domain ($6.4\ km \times 6.4\ km$) of interest to this project, conversion of contour maps to a CAD model with a complex surface, and creation of the 3D computational domain. The sub-domain is positioned to put the Liberty monitoring site in the center and the coke plant in the lower left (southwest) corner. In this way, when the dominant southwest wind carries the SO_2 plume to the Liberty monitoring site, the CFD model can be used to model such conditions, and the predicted SO_2 concentrations can be compared with the Liberty data. The background in Figure 4.1 (a) shows the contour map downloaded from the PASDA website in black contours lines. The center of Figure 4.1 (a) shows that the bottom surface of the study domain in grey is generated from the contour lines. The lowest point within the domain is located on the surface of the Monongahela River, and its height is set to $0\ m$. The highest point ($174\ m$) is located on the

mountain top near the southeast corner. Side boundaries are added to the ground surface to extend the model $1000\ m$ vertically as shown in Figure 4.1 (b). The contour level ranging from 0 to $200\ m$ is used to better show the terrain surface. The top boundary that covers the whole computational domain at $1000\ m$ elevation is not shown in Figure 4.1 (b).

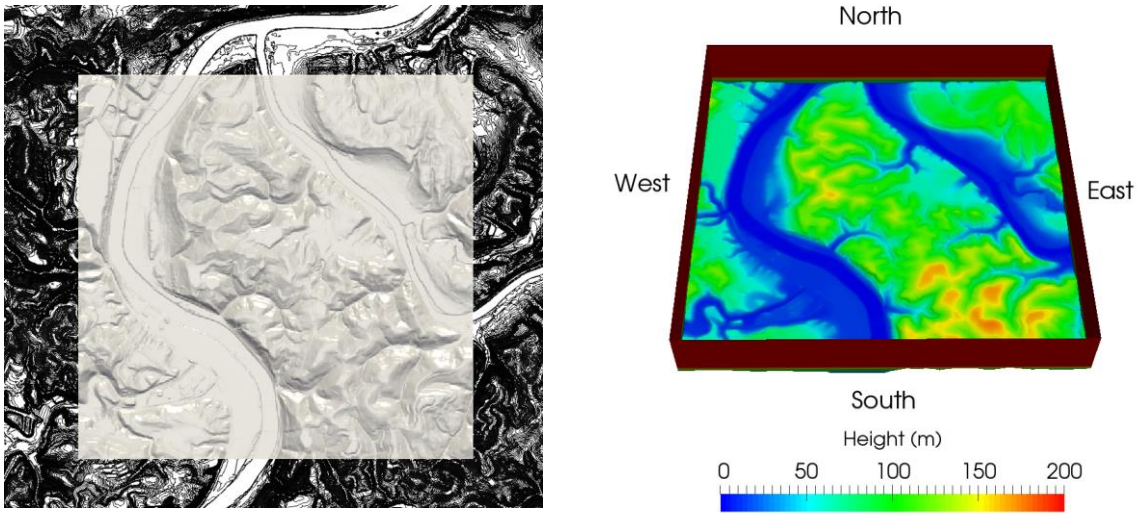

(a) Contour map (black lines) obtained from PASDA and the sub-domain in grey

(b) The bottom surface and the four side boundaries with a height of 1000 m

Figure 4.1: Top views of the complex terrain in different stages of the process to obtain computational mesh of the complex terrain.

A good-quality computational mesh with orthogonal, non-skewed, hexahedral cells (also called elements) is always desirable for CFD simulations to obtain accurate predictions with lower computational costs. Figure 4.2 shows a fully hexahedral mesh created for the study domain. The total number of cells is about 8 million. There are 409 cells in the x-direction (West to East), 409 cells in the y-direction (South to North), and 48 cells in the z-direction (Ground to Top). Each cell has a length and width of about 16 m. The height of the first cell above ground is 4 m. An expansion ratio of 1.057 is used to increase cell height in the vertical direction, starting with 4 m cell height at the ground.

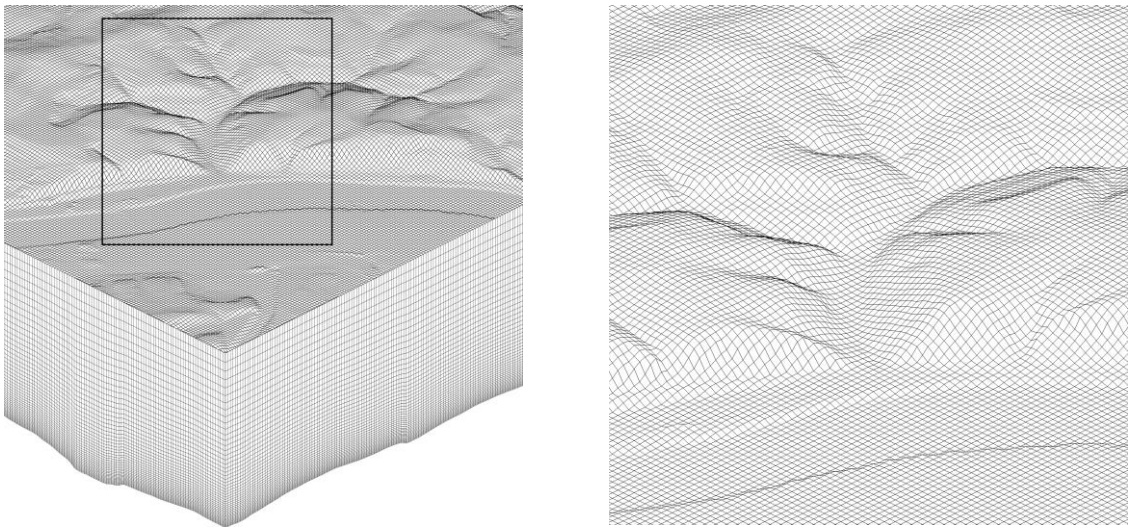

(a) Southwest corner (b) Detail of the hollow near the river

Figure 4.2: Different views of the computational mesh.

As the four sides of the domain on the ground are complex curves rather than straight lines, extra steps are needed to generate a good-quality mesh. First, the geometry and mesh generation software, ICEM CFD [75], is used to smoothly extend the terrain surface in four directions to a flat surface. Then, a single block is used to create a fully hexahedral mesh in ICEM CFD. The top view of the mesh is shown in Figure 4.3. Finally, snappyHexMesh offered by OpenFOAM is used to cut off the extensions to restore the original $6.4\ km \times 6.4\ km$ domain. As shown in Figure 4.3, without the extension to a flat surface at the edges of the domain, the single block mesh created in ICEM CFD will result in crinkles in certain locations, compromising the overall mesh quality.

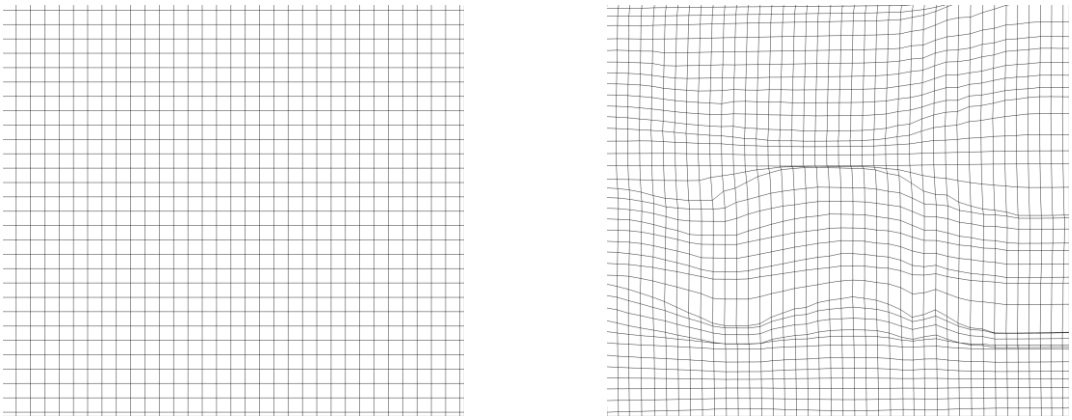

(a) With extension (b) Without extension

Figure 4.3: Top views of the mesh show the difference in mesh quality.

4.2 Variable aerodynamic roughness length

National Land Cover Database (NLCD) is considered when developing the variable aerodynamic roughness length map over the interested terrain. It is found that "Grassy" areas around "Developed" areas are also classified as "Developed" in the 2001 or later database, which can lead to inaccurate predictions [76], so we chose the 1992 database. The 1992 NLCD has a grid resolution of 30 m. Using the AERSURFACE [76] algorithm, the land cover class can be converted into the aerodynamic roughness length, as shown in Figure 4.4. Figure 4.5 shows the steps to obtain the roughness map.

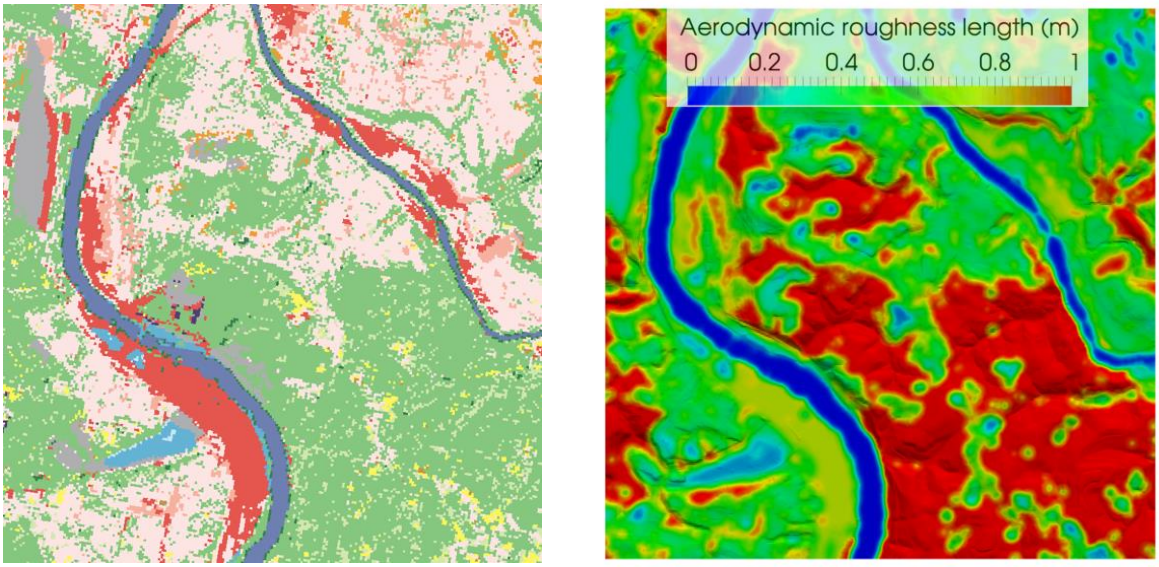

(a) The 1992 land cover data from NLCD (b) The aerodynamic roughness length map

Figure 4.4: The conversion from land cover data to aerodynamic roughness length that will be used in the CFD model to include the effects of different surface structures.

The algorithm needs latitude and longitude of a point and a radius to calculate average roughness length based on the inverse-distance weighted geometric mean, so that it can output average roughness by sectors and seasons. To get the roughness for the whole domain, the NLCD map, which is slightly larger than the study domain, is downloaded from the Multi-Resolution Land Characteristics (MRLC) Consortium website [77] shown in Figure 4.4 (a). Then, the ground

mesh (shown as grids) is overlaid on top of the satellite image for extracting the centroids of each bottom cell, as shown by circles in Figure 4.5. The computational mesh uses a different local coordinate system which is different than the UTM coordinates and there is no direct conversion from the local coordinates used in CFD to the UTM coordinates that are accepted by AERSURFACE. A linear interpolation scheme is used to get the UTM coordinates of each centroid. The interpolation needs the local coordinates of the four corners of the mesh, and corresponding UTM coordinates. As each cell has the same width and length, the centroids of all the cells on the ground can be linearly interpolated to obtain their UTM coordinates. The AERSURFACE algorithm processes each centroid to convert different land cover classes into the roughness length map shown in Table 4.1. The current roughness length map is based on a radius of 100 m to calculate for the geometric mean value and then averaged over 5 seasons described in the AERSURFACE guide [76].

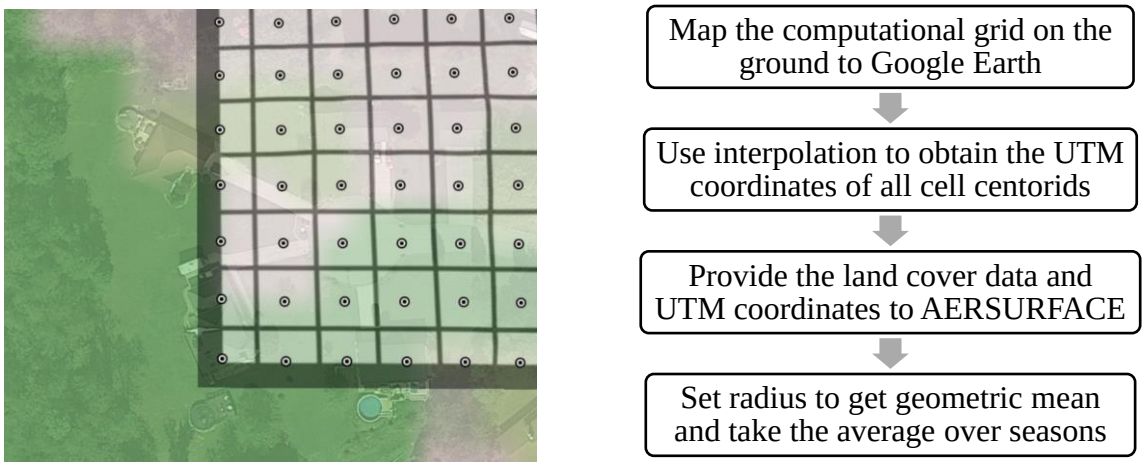

Figure 4.5: Illustration of steps to obtain the variable roughness map. The figure on the left shows the southwest corner of the study domain which uses the land cover map and satellite image from Google Earth as background. The computational grid from CFD is overlaid on top. The grid centroids are shown as ⊙.

Table 4.1: The color and number legend for different land cover classes and the corresponding mean aerodynamic roughness length.

NLCD 1992 Land Cover Classification Legend	Mean z_0 (m)
11 Open Water	0.001
21 Low Intensity Residential	0.360
23 Commercial/Industrial/Transportation	0.070
31 Bare Rock/Sand/Clay	0.050
32 Quarries/Strip Mines/Gravel Pits	0.300
33 Transitional Barren	0.200
41 Deciduous Forest	0.940
42 Evergreen Forest	1.300
43 Mixed Forest	1.080
51 Shrubland	0.150
61 Orchards/Vineyards/Other	0.190
71 Grassland/Herbaceous	0.053
81 Pasture/Hay	0.072
82 Row Crops	0.092
83 Small Grains	0.072
84 Fallow	0.030
85 Urban/Recreational Grasses	0.013
91 Woody Wetlands	0.440
92 Emergent Herbaceous Wetlands	0.180

4.3 Inlet boundary conditions

4.3.1 Curve fitting to obtain vertical profiles

From the Monin-Obukhov similarity theory, under the neutral condition, the equations for wind speed (2.28) and potential temperature (2.29) can be simplified to

$$u(z) = \frac{u_*}{\kappa}\left[ln\left(\frac{z}{z_0}\right)\right] \tag{4.1}$$

$$\theta(z) = \theta_0 \tag{4.2}$$

where the potential temperature is constant across the surface layer, and the wind profile can be determined from a reference wind speed at a reference height.

One issue with this approach is that when we use measured data from one location to generate a theoretical velocity profile, this profile does not agree with measurements made at another location at a different height. Figure 4.6 provides a qualitative view of the inconsistency. If we use the wind measurements at 2 m height at the Mitchell sensor, the wind profiles generated using this measurement do not agree with KAGC measurements made at 10 m height as shown in Figure 4.6 (a).

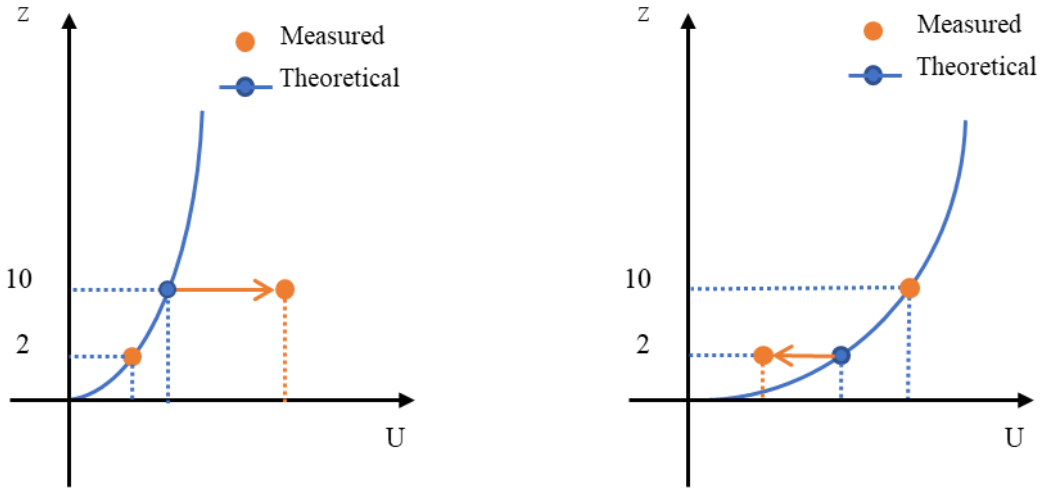

(a) Under-predicted wind speed at KAGC (b) Over-predicted wind speed at Mitchell

Figure 4.6: Inconsistency between the measurements and the theoretical wind profile when calculating the profile with one reference location.

The wind speed at 10 m height is under-predicted when compared to the measurement at KAGC. If the profile is generated using KAGC measurement made at 10 m height, wind speed is over-predicted at 2 m height compared with the Mitchell sensor as shown in Figure 4.6 (b). This inconsistency could be due to multiple reasons, such as: 1) Wind profiles are different at the two

locations due to different aerodynamic roughness lengths. 2) The wind sensor at the 2 m height only corresponds to a very local flow structure, and it does not represent the regional wind pattern surrounding that location. Wind data from sensors that are mounted higher above ground should be preferred to generate vertical profiles.

For the stable condition, although there are more parameters in the theoretical equations for wind and temperature, given the aerodynamic roughness length, the reference wind speed at a reference height, the ground heat flux, and temperature, one can easily solve for the unknown parameter u_*. It is often the case that the derived theoretical profiles of wind and temperature agree poorly with the real-world measurements. From equations (2.28) and (2.29), the more general forms of the wind speed profile and potential temperature profile are given as:

$$u(z) = \frac{u_*}{\kappa}\left[ln\left(\frac{z}{z_0}\right) + a\frac{z}{L}\right] \tag{4.3}$$

$$\theta(z) = \frac{\theta_*}{\kappa}\left[ln\left(\frac{z}{z_0}\right) + b\frac{z}{L}\right] + \theta_0 \tag{4.4}$$

where the commonly used values of $a = b = 5$ are based on experimental results.

In order to provide a consistent estimate of the atmosphere by taking into account data measured from multiple height levels, a curve-fitting method is developed. The curve-fitting method aims to minimize the non-linear least-square errors in the theoretical equations from the Monin–Obukhov similarity theory. To this end, the optimal parameters in the equations are determined. The procedure is summarized in the flowchart shown in Figure 4.7.

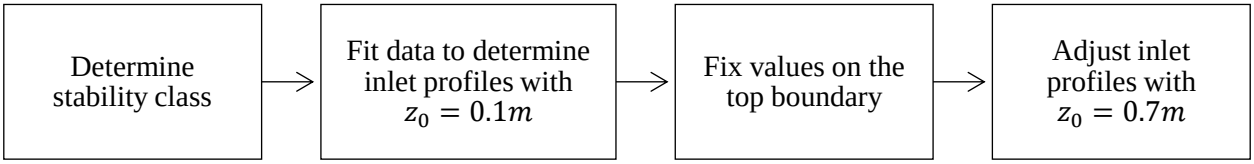

Figure 4.7: Flowchart of the curve-fitting procedure used in the present work to obtain boundary conditions at the inlet of the study domain.

First, the stability class of the ABL is determined from the vertical temperature profile of the sounding if it is available. Otherwise, the temperature profile from reanalysis is used. As for the vertical wind speed profile, if the sounding data is available, it will be preferred over the reanalysis data for selecting the model validation cases. The "curve_fit" function from the "scipy" package [78] is employed to fit the theoretical equations. The sigma values for the KAGC data and sounding data are set to 0.1 and 0.5, respectively. The KAGC data are reported by sensors on a fixed height and have less uncertainty to represent the steady wind compared to the instantaneous data from sounding. In addition, the similarity theory is applicable in the surface layer where the KAGC monitor locates. Thus, a smaller sigma value is chosen for the KAGC data. As for the sounding data, they represent the instantaneous condition of the atmosphere. To minimize the local effects from the sounding location, only data points with height above 500 m with respect to the height of the Monongahela River surface inside the study domain are used. Besides, the used data points from sounding are generally not within the surface layer, so more uncertainty (i.e., higher values of sigma) is set for them. Both the KAGC data and reanalysis are treated as measured data.

For the neutral condition, the only known is the friction velocity, and the method only needs to fit the velocity equation. Since the KAGC airport and the sounding location have similar aerodynamic roughness length estimated as $0.1\ m$, the velocity equation is fitted by setting z_0 to $0.1\ m$. In this way, the initial vertical distribution of horizontal wind speed is obtained. The velocity at the top of the study domain ($1\ km$) is determined by plugging the fitted parameters into the theoretical equation for wind speed (4.1). The aerodynamic roughness length is then changed to $0.7\ m$, which is the average value at the inlet of the study domain. With the aerodynamic roughness length at the inlet and the top velocity, a new set of parameters in the equations is obtained. The reason for changing the roughness length is to adjust the wind speeds near the ground

at the domain inlet.

For the stable conditions, there are two profiles to fit, wind speed and air temperature. In addition to the friction velocity, there are more unknown parameters to fit, including a, b and the temperature scale. The measured temperatures are in the form of absolute temperature. Within the ABL, the potential temperature profile, ($\theta(z)$, can be changed to the absolute temperature profile $T(z)$ as follows:

$$T(z) = \theta(z) + \frac{g}{c_p} z \tag{4.5}$$

where $\frac{g}{c_p}$ is a constant for the dry atmosphere, and it is called the dry adiabatic lapse rate.

Only using one set of data, for example, wind speed, to find the optimal values of these parameters could result in a large error in the calculated temperature profile compared to the measured data, as illustrated in Figure 4.8. The same is true when fitting the air temperature profile first to determine the parameters then calculating the wind speed profile.

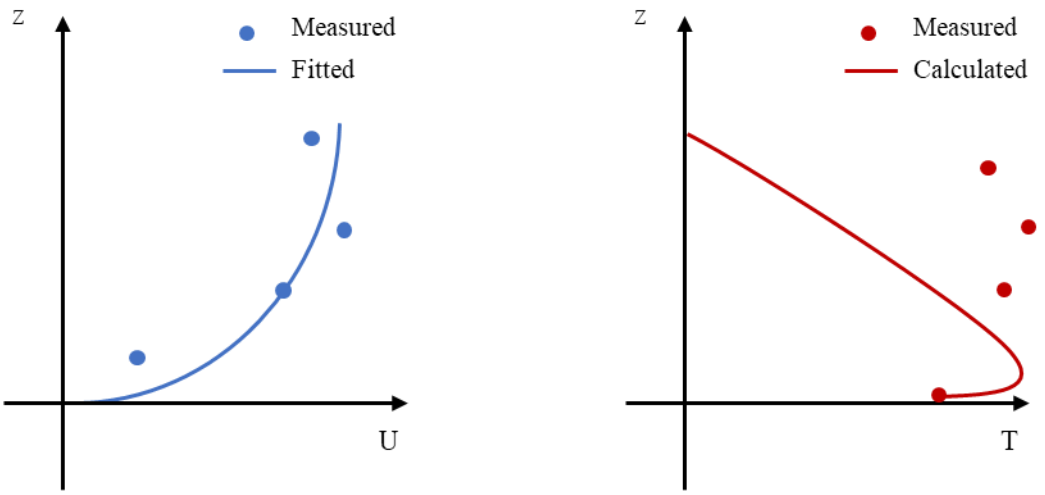

(a) Good-quality fitted profile for wind speed (b) Poorly calculated profile for temperature

Figure 4.8: Fitting wind data to obtain the wind profiles can lead to a bad agreement between the temperature data from measurements and the calculated temperature profile.

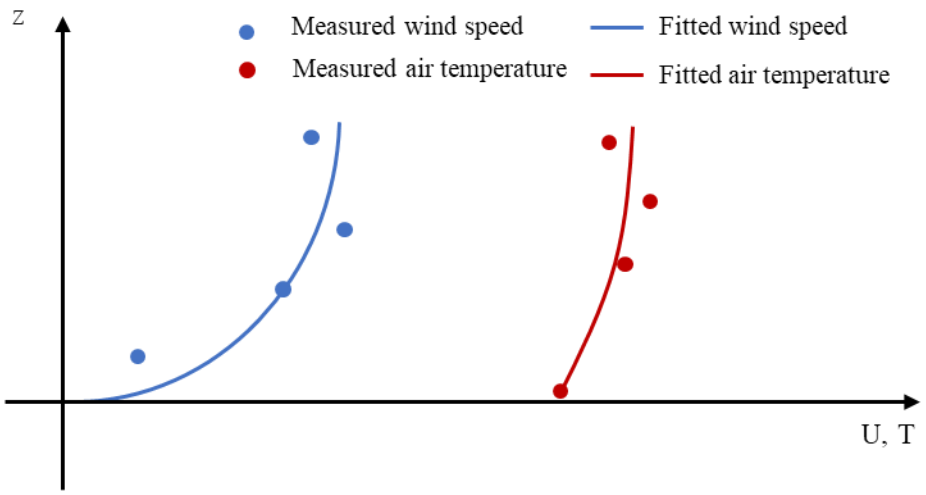

Figure 4.9: Fitting two profiles simultaneously can minimize the errors for both the vertical profiles wind speed and temperature.

As shown in Figure 4.9, a fix to the problem is to fit the wind speed profile and air temperature profiles simultaneously by creating a combined function of them and feeding the combined measurements to the curve fit algorithm. In this way, errors between theoretical profiles and the measurements for both the vertical profiles wind speed and temperature can be minimized.

With the fitted profiles, the corresponding values at each inlet cell face are calculated based on local height and specified in the model. To test the performance of the curve-fitting method, the wind speed data in March 2019 are fitted into a theoretical wind profile under neutral conditions. The R^2 value is about 0.7 when compared to the sounding data. Since the instantaneous wind profiles from sounding do not always have a logarithmic shape, if these non-logarithmic groups are ignored, the R^2 value will be higher, especially when fitting data under the neutral condition. As shown in Figure 4.10, the curve-fitting method yields a much better R^2 value of 0.9 for wind speed in case of stable conditions. As for the temperature, the R^2 value is 0.98.

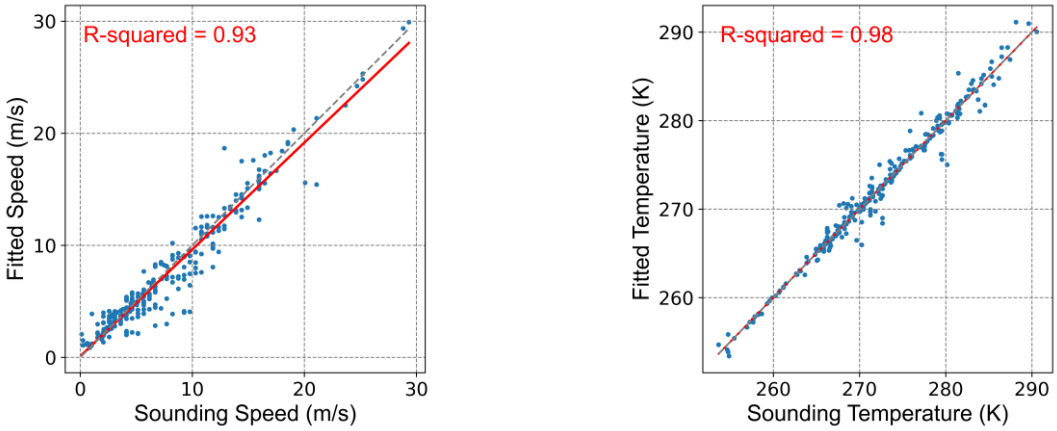

(a) Wind speed (b) Air temperature

Figure 4.10: Evaluation of the profiles from curve fitting and comparison with measurements from soundings.

Figure 4.11 shows an example of the result from the curve-fitting method. The "Fitted" curve for wind speed is shown with a $\pm 10\%$ range of the mean value. The "Fitted" curve for temperature is shown with a $\pm 1\ K$ range of the mean value. The fitted profiles are very close to those of sounding and the NARR data (shown as "Reanalysis").

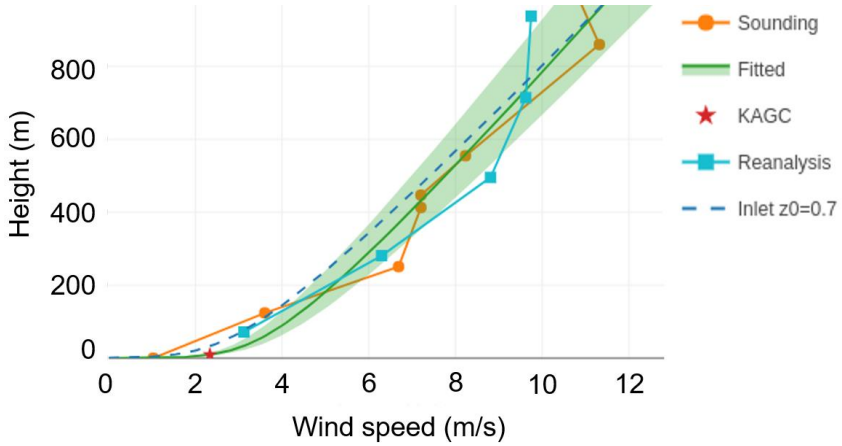

(a) Wind speed profiles

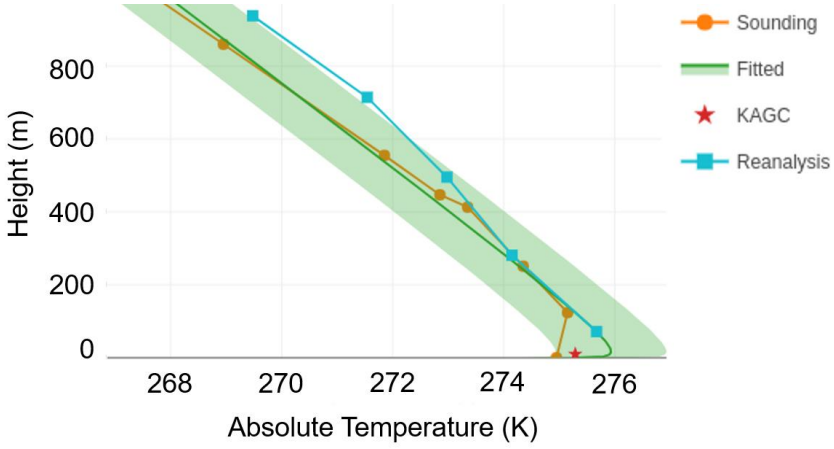

(b) Stable temperature profiles

Figure 4.11: Fitted profiles in comparison with available data.

4.3.2 Specific setup for steady-state and transient simulations

Steady-state simulations assume weather conditions to be unchanged. In order to study the effects of transient wind direction changes on SO_2 dispersion, the transient CFD model is developed. The SO_2 concentration at any specific location can be sensitive to wind conditions, especially the wind direction. The steady-state model uses the uniform 1-hour mean wind direction from the Liberty site across the height at the inlet. Unlike the steady-state CFD model, the initial conditions of the flow and concentration fields are crucial for the transient simulations since the evolution of the flow is dependent on the initial conditions. In addition, the updates on boundary conditions after the transient simulation starts also will have a significant influence on the predicted results. From the SODAR data shown in Figure 3.16, vertical wind direction changes within an hour at different height levels are different. The overall trend of STD along height is fitted using a function based on hyperbolic tangent function:

$$STD = a \times [1 - tanh(z \times b)] + c \tag{4.6}$$

The mean of the STD from the SODAR data filtered with the southwest wind direction is used to find the optimal values of the parameters. After fitting, $a = 5.556, b = 0.010$, and $c = 5.385$. The

fitted curve is shown in Figure 4.12. The wind direction distribution along with the height with respect to time, $Dir(z,t)$, is determined as:

$$Dir(z,t) = Dir_h - [Dir_h - Dir_m(t)] \times \frac{STD}{a+c} \tag{4.7}$$

where Dir_h is the hourly 1-hour mean wind direction and $Dir_m(t)$ is the 1-minute mean wind direction at time t.With equation (4.7), we modulate the wind direction changes along height using the 1-minute mean wind direction reported by the Liberty monitor.

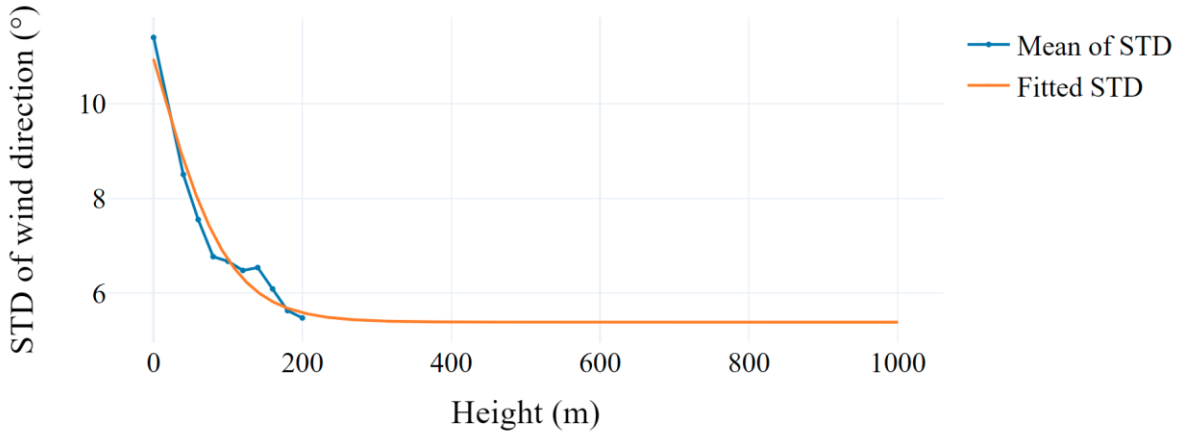

Figure 4.12: The mean STD data from Liberty and SODAR can be fitted to a smooth curve to estimate wind direction variations at different height levels.

Two examples are shown in Figure 4.13. In case 1, the 1-minute mean wind direction in degree is larger than the 1-hour mean wind direction. As the STDs in wind direction of higher levels are small than those of lower levels, wind directions at higher levels are less prone to change, so they stay closer to the 1-hour mean wind direction. Case 2 is the opposite trend in wind direction values, but the idea is the same.

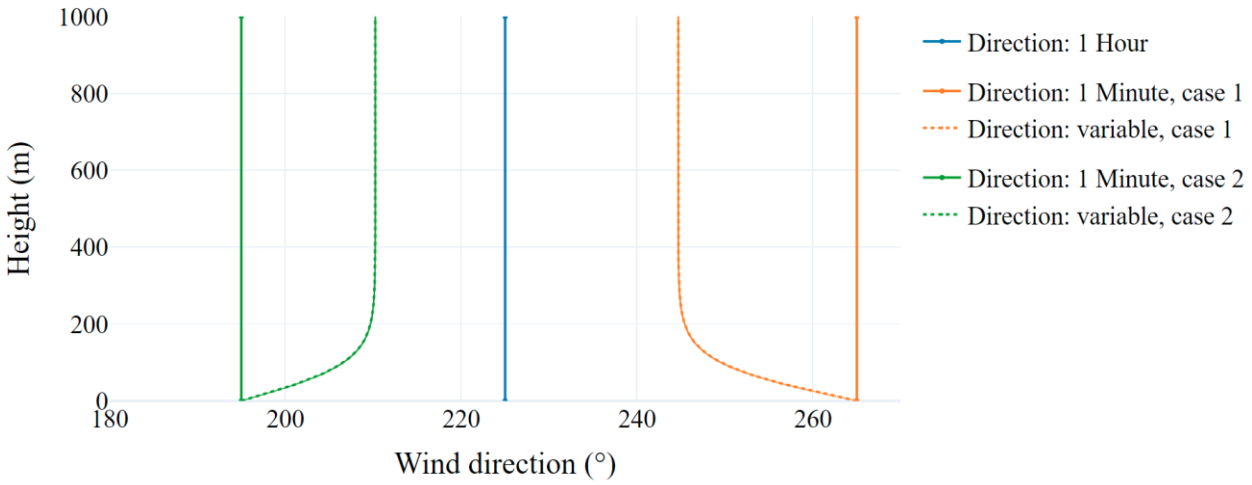

Figure 4.13: Tow cases of variable wind direction along with height. Case 1 shows a larger wind direction value from the 1-minute Liberty data than the 1-hour data (shown as "Direction: 1 Hour"). The distribution of wind direction in the vertical direction used in the transient simulation will make the wind directions at higher levels closer to the 1-hour wind direction.

The reanalysis dataset only has a 1-hour resolution at the finest level, and the difference in the vertical profiles between two consecutive hours is generally small, as shown in Figure 4.14, so the changes of weather conditions at the sub-hourly level are ignored for the 1-hour transient simulations. In summary, boundary conditions in terms of wind speed, temperature, and turbulence at the inlet and top are set the same in both steady-state and transient simulations. The transient simulations only receive updates on wind direction based on equation (4.7) and the 1-minute mean wind direction data at the Liberty site.

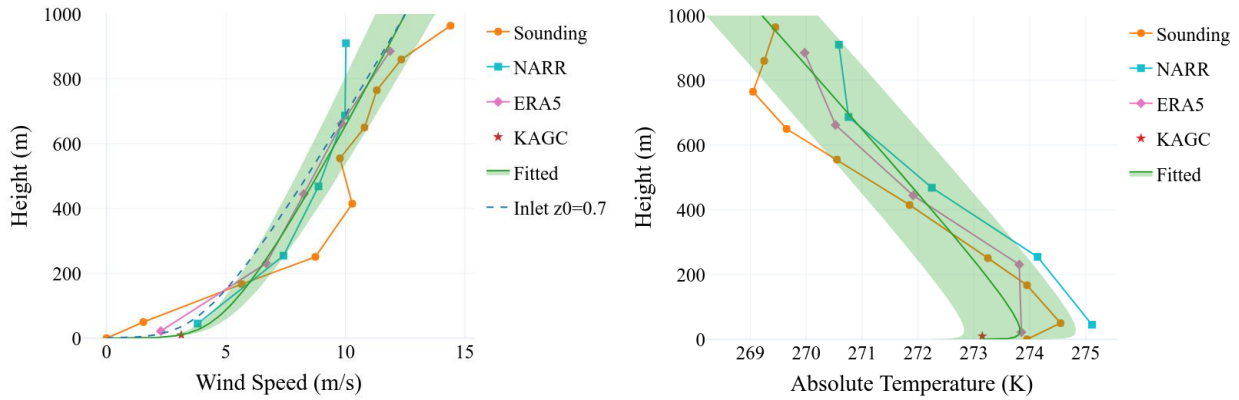

(a) Wind speed profiles at 04/01/2019 00Z (b) Temperature profiles at 04/01/2019 00Z

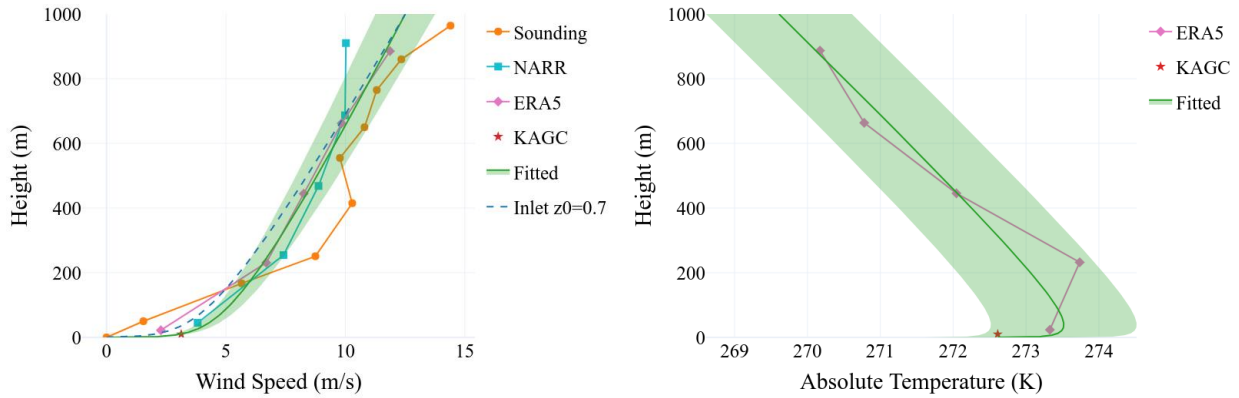

(c) Wind speed profiles at 04/01/2019 01Z (d) Temperature profiles at 04/01/2019 01Z

Figure 4.14: Changes in weather conditions within two consecutive hours are generally small as the vertical profiles of wind speed and air temperature for the two cases are close to each other.

4.4 Surface boundary conditions

The earth's surface can be treated as a rough wall when simulating the flow in the ABL. For velocity, a no-slip condition is commonly used to model viscous flows no matter what the stability class is. Even though two rivers are flowing through the study region, the speeds of the currents are considered to be negligible. The no-slip condition is applied on both the ground surface and the river surface. The potential temperature of the ground surface is treated as a fixed value under neutral conditions. In theory, the potential temperature within the whole 3D domain should be uniform, so the heat flux on the ground and throughout the vertical direction is 0. However, this

may not be true in the real world, especially when the land cover is not uniform. Still, the uniform fixed temperature can be a good approximation under neutral conditions. For stable conditions, there should be heat fluxes out of the domain at the bottom surface. On the contrary, there should be heat fluxes into the domain under unstable conditions. Due to the lack of measurement data, it is not possible to specify variable heat fluxes on the ground, so a uniform flux obtained from the reanalysis product is applied on the top boundary. An alternative way of setting the boundary condition of potential temperature on the ground is to set it as a uniform fixed value. For p_{rgh}, zero gradient is applied on the bottom surface.

For k, ε, and ν_t, which are related by the $k-\varepsilon$ turbulence model, wall functions are applied on them to bridge the inner region between the wall and the fully developed turbulent region. Traditionally, the standard rough wall function based on the sand-grain roughness has been widely used in modeling ABL flows. The law of wall is described as below:

$$u^+ = \frac{1}{\kappa} ln(Ez^+) - \Delta B(K_s^+) \tag{4.8}$$

where $u^+ = \frac{u}{u_*}$, $z^+ = \frac{zu_*}{\nu}$, and z is the distance above the wall (i.e., the height above the ground surface). The value of $\Delta B(K_s^+)$ varies with different values of the dimensionless length K_s^+ as described below:

$$\Delta B(K_s^+) = \begin{cases} 0 & K_s^+ < 2.2 \\ \frac{1}{\kappa} ln\left(\frac{K_s^+ 2.25}{87.75} + C_s K_s^+\right)^{sin\left(0.4258\left[ln K_s^+ - 0.811\right]\right)} & 2.25 \le K_s^+ \le 90 \\ \frac{1}{\kappa} ln(1 + C_s K_s^+) & K_s^+ > 90 \end{cases} \tag{4.9}$$

The wall shear stress can now be expressed as:

$$\tau_w = \rho u_* \frac{u}{u^+} = \rho \left\{ \frac{u_* y}{\frac{1}{\kappa} ln[E(K_s^+) z^+]} \right\} \frac{u_p}{z} = \rho \{\nu_{eff}\} \frac{u_p}{z} \tag{4.10}$$

The subscript p means the value on the first cell above the wall. The turbulent kinematic viscosity on the wall $\nu_{tp} = \nu_{eff} - \nu$. To enforce the law of the wall into the flow, ν_{tp} is updated as:

$$\nu_{tp} = \nu \left\{ \frac{y^+}{\frac{1}{\kappa} ln[E(K_s^+) y^+]} - 1 \right\} \tag{4.11}$$

where $E(K_s^+)$ is the function of E with respect to $K_s^+ = \frac{K_s u_*}{\nu}$. K_s is the sand grain roughness height, whose meaning resembles the aerodynamic roughness length z_0. Blocken et al. summarized the requirements of using the standard rough wall function. However, all the requirements cannot be met at the same time [50]. The main limitation is that the height of the centroid of the first computational cell above ground must be larger than the physical roughness height, which is usually 20-30 times the aerodynamic roughness length. Following this rule will make the grid very coarse near the wall when the terrain has high aerodynamic roughness length, resulting in a bad prediction of near-wall turbulence.

Based on the aerodynamic roughness and with a similar form to the sand-grain roughness model, a new type of wall function can be derived as [35] :

$$u^+ = \frac{1}{\kappa} ln\left(\frac{z_p}{z_0}\right) \tag{4.12}$$

Similar to the standard rough wall function, the new turbulent kinematic viscosity on the wall is updated as:

$$\nu_{tp} = \nu \left\{ \frac{y^+}{\frac{1}{\kappa} ln[E(z, z_0)]} - 1 \right\} \tag{4.13}$$

where $E(z, z_0) = z_p / z_0$. The turbulent kinetic energy production term G_k in equation (2.7) needs

to be balanced by the dissipation term ρε. By equating them:

$$G_k = \tau_w \frac{\partial u}{\partial z} = \rho \frac{u_*^3}{\kappa z_p} = \rho\varepsilon \tag{4.14}$$

So, ε_p is obtained, and its value is updated on the wall by the following equation:

$$\varepsilon_p = \frac{u_*^3}{\kappa z_p} = \frac{C_\mu^{3/4} k_p^{3/2}}{\kappa z_p} \tag{4.15}$$

As for k_p, it is believed that when the first cell centroid lies within the logarithmic region, a zero gradient boundary condition should be good enough.

4.5 Stack exit boundary conditions

The ten stacks from the coke plant are responsible for the majority of the SO_2 emissions from emission inventory data provided by ACHD. Table 4.2 shows the key parameters of the stacks that are related to SO_2 modeling using CFD.

Table 4.2: Stack parameters for SO_2 modeling.

Name	UTM Easting (m)	UTM Northing (m)	Elevation (m)	Height (m)	Temp. (K)	Velocity (m/s)	Diameter (m)
Stack 1	595871	4461845	231	68.58	526.49	7.59	2.44
Stack 2	595866	4461852	231	68.58	534.27	7.71	2.44
Stack 3	595742	4461989	231	68.58	539.27	7.38	2.44
Stack 13	595389	4462164	231	68.58	535.38	4.48	3.05
Stack 14	595380	4462174	231	68.58	536.49	4.30	3.05
Stack 15	595253	4462318	231	68.58	541.49	4.48	3.05
Stack 19	595273	4462117	231	76.20	519.27	3.72	4.72
Stack 20	595258	4462134	231	76.20	542.05	4.27	4.72
Stack B	595477	4462406	231	96.01	515.38	5.06	4.95
Stack C	595768	4462126	231	98.14	503.20	5.81	3.66

Figure 4.15 (a) shows the locations of the stacks with Google Earth. The element size of

the computational mesh without the stacks is about $16\,m \times 16\,m \times 4\,m$ near the ground. Such element size is sufficient for simulations of wind development, but they are not fine enough for the correct representation of these stacks. This is because the diameters of stacks range from 2.44 m to 4.95 m at the exit of the stacks. In order to add the stacks to the computation mesh, local mesh refinement around the stacks is required.

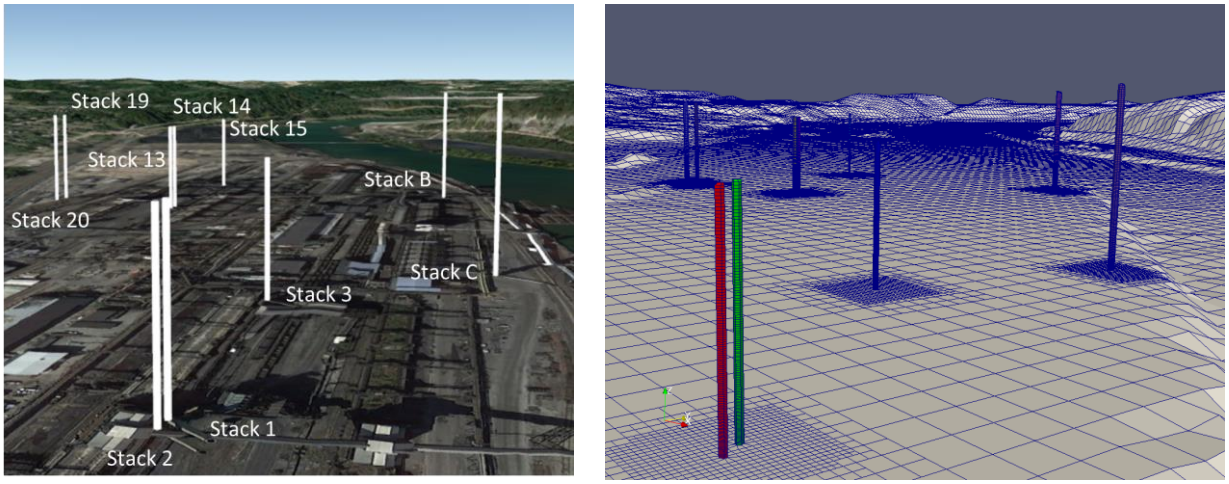

(a) Stack locations and names in Google Earth

(b) CFD mesh with stacks and local mesh refinement

Figure 4.15: Stacks are shown with Google Earth and the representation in the computational mesh in CFD.

We have used the meshing tool snappyHexMesh available in OpenFOAM for this purpose. The snappyHexMesh meshing tool takes an already existing mesh and snaps it into a new mesh using user-defined mesh parameters. In this case, the parameters include the geometry of the stacks. Then local mesh refinement is performed to make a smooth transition between the original coarse mesh and the refined mesh near the stacks. Figure 4.15 (b) shows the stacks that were added to the study domain using snappyHexMesh. Two levels of refinement near the stack exits are performed to reduce mesh size. The first refinement brings the cell size from $16\,m$ to $8\,m$ and the second refinement reduces it to $4\,m$. Further refinement of the mesh will increase the total

mesh count and thus increase the computational time. Since the stacks have very small dimensions compared to the overall computational domain, their influence on the flow field is negligible. The complete presence of the stacks from the ground to the exit is considered to be not necessary. Instead, only the stack exits are carefully modeled by maintaining the energy balance. However, the computational grid has an approximately square cross-section while the actual stack exits are circular cross-sections shown in Figure 4.16. Creating a circular cross-section stack in the grid results in a poor quality grid leading to code convergence issues. We think that it is not necessary to create a circular cross-section. Instead, we have adjusted the fluxes of energy and mass at the stack exits to account for the difference in the cross-sectional area between the square cross-section in the CFD model and the circular cross-section in the actual stacks.

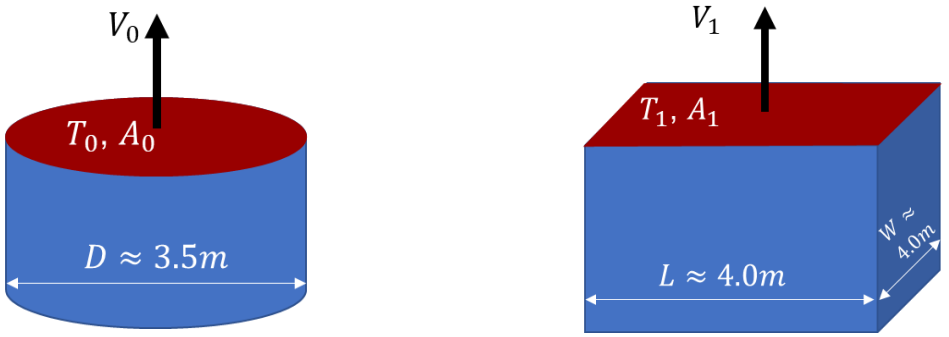

(a) Original stack with the circular exit (b) Refined mesh for with the square exit

Figure 4.16: Schematic of the difference in stack exit face between the real stack and the counterpart used in the CFD model.

For each stack exit in the real world, we have: Temperature T_0, Velocity V_0, and surface area A_0. For each cell at the stack exit, we have: Temperature T_1, Velocity V_1, and surface area A_1. Since A_1 ($\approx 15m^2$) is only a close approximation to A_0 ($\approx 13m^2$), to make sure the stack in the model is emitting the same amount of energy, we can get

$$c_p \rho T_0 V_0 A_0 = c_p \rho T_1 V_1 A_1 \tag{4.16}$$

We can set the exit face temperature $T_1 = T_0$. So, we only need to adjust the exit face velocity $V_1 = \frac{V_0 A_0}{A_1}$. To maintain the exit velocity, the "directionMixed" boundary condition provided by OpenFOAM is used, where the vertical velocity is set to the corresponding value of each stack, and the horizontal velocity is configured as zero gradient.

The final mesh around the stack exits is shown in Figure 4.17. Ideally, only the cell that has the stack exit face will be removed. However, the local refinement near the stack exits will snap the original hexahedral cell into smaller polyhedral cells, which are grouped together. After removing the stack exit cell, the attached polyhedral cells are also removed. The exposed faces surrounding a stack exit are treated as a slip wall.

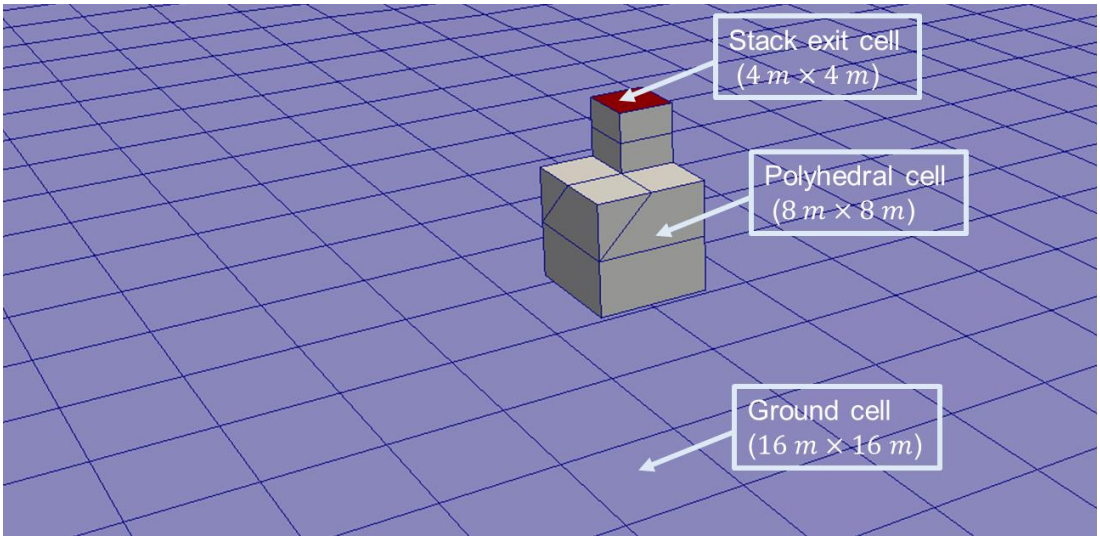

Figure 4.17: Dimensions of different cells near a stack exit that range from 16 m to 4 m.

Figure 4.18 shows temperature contours on a vertical slice through one of the stacks and the velocity vectors colored by the vertical component of velocity. High temperature and velocity are observed near the exits of the stacks. The emissions are added to the model through the source terms. The cell right above each stack exit is selected as the volume for emitting passive tracers. In addition to the emissions from the stacks, there is a small amount of SO_2 (about 10%) emitting

from other facilities of the Coke Plan, which are treated as fugitive emissions. In the CFD model, the fugitive emissions are specified over the whole plant region and emitted at the ground level.

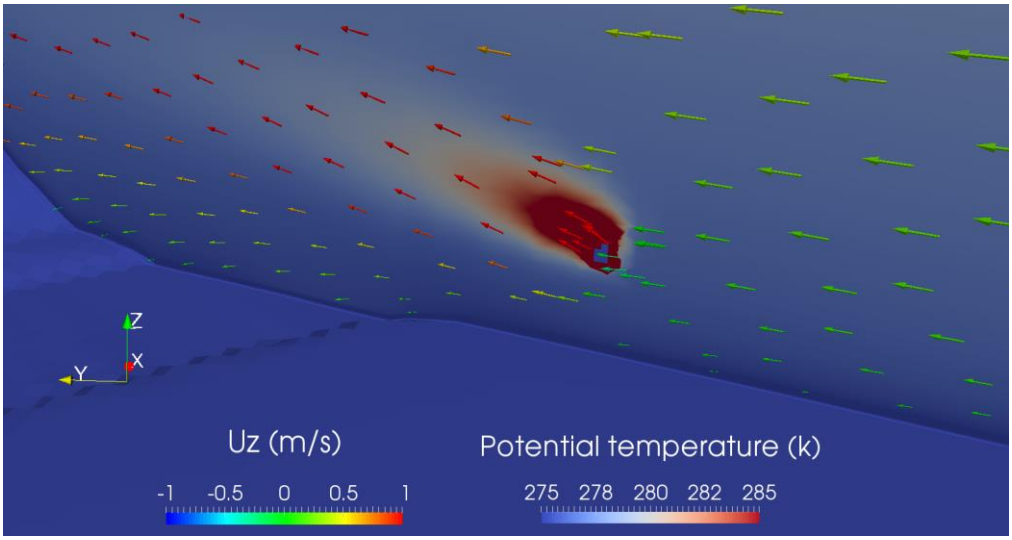

Figure 4.18: Temperature contour and velocity vectors colored by the vertical component (Uz) near one stack exit to show the effects of buoyant plume.

The SO_2 emission from the coke plant is not directly monitored. In practice, the emission rate of SO_2 is determined by converting the H_2S grain loading of the fuel burned and the fuel flow rate. From the annual, monthly, daily, and hourly hydrogen sulfide (H_2S) grain loading provided by U.S. Steel, the corresponding SO_2 emission retes are derived. Most of the time, only the monthly or daily loading is available. During such time, the hourly emission (converted to g/s) is based on the average daily emission. For example, the daily fuel flow rate at stack 1 is 51.9 million cubic feet per day ($MMCFD$), and the daily average H_2S grain loading is 5.23 grains of particulate matter per 100 dry standard cubic foot of exhaust air ($gr/\,100\,dscf$). SO_2 emission rete at stack 1in pound per day (lb/day) is calculated as

$$\begin{aligned} SO_2\ lb/day &= MMCFD \times \frac{Daily\ H_2S\ grains}{100} \times \frac{64.066}{34.1} \times \frac{1}{7{,}000} \times 1{,}000{,}000 \\ &= 728.52\ lb/day \end{aligned} \tag{4.17}$$

where 66.066 and 34.1 are the molecular weight of SO_2 and H_2S in g/mol respectively. Grain

(gr) is a mass unit, and 1 gr is equivalent to $\frac{1}{7{,}000}$ lb. Assuming constant emission rate throughout the day, the daily SO_2 emission rate of 728.52 lb/day is then converted to 3.82 g/s. Figure 4.19 shows the time series of 1-hour mean SO_2 concentration reported by the Liberty monitor and total emission rate from the coke plant scaled to 1-hour level from Jan 2018 to Jul 2019.

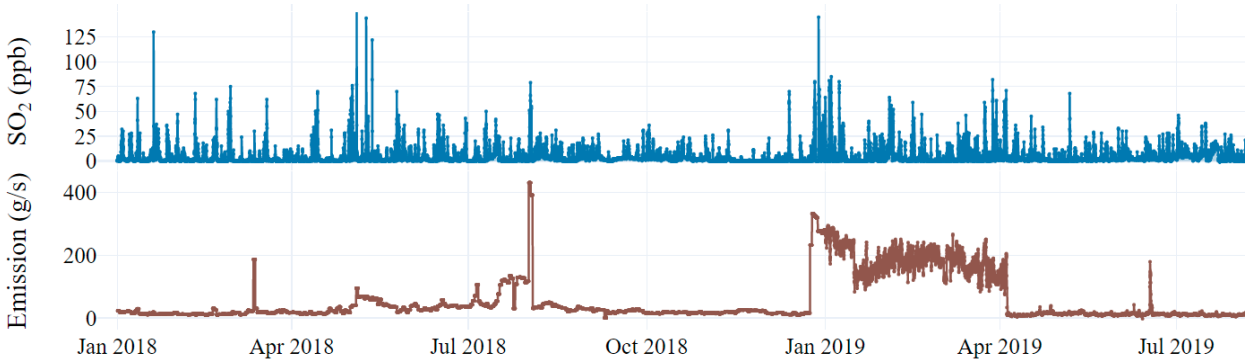

Figure 4.19: Time series of the 1-hour mean SO_2 concentration from the Liberty monitor and the total emission rate from the coke plant scaled at 1-hour level.

The year 2018 is less refined for emissions overall, but it is considered the best available short-term rate estimate. U.S. Steel started providing ACHD with hourly sulfur content and flow rates for the stacks for 2019 over a time period from 01/2019 to 04/2019. So, 2019 is the more refined year for the tall stacks, but there is still some estimation of emissions for the other processes. The time period from 01/2019 to 04/2019 will be the focus of the current study. The emissions from the ten stacks during this time period make up 90% of the total emission, and the mean hourly total emission rate for this time period is 184 g/s. As a comparison, in 2018, the mean hourly emission is 37 g/s. The overall SO_2 concentration trends in 2018 and 2019 are similar, and the corresponding annual mean of hourly concentrations are 3.92 ppb and 4.17 ppb.

4.6 Other boundary conditions

At the outlet, a zero gradient boundary condition is specified for all variables but p_{rgh}, for which a fixed value boundary condition is used. Under neutral conditions, when the potential

temperature is uniform in the vertical direction, p_{rgh} is also uniform. As a common practice, the pressure is set to be a constant value at the outlet [27,35,51]. Under stable and unstable conditions, the vertical profile of p_{rgh} is unknown without any measurements, but it would still be a good estimate to set p_{rgh} the same as in the neutral condition assuming weak compressibility. Therefore, the model predictions very close to the outlet boundary should not be used to compare with measurements. For the top boundary, based on the vertical profiles of u, θ, k, and ε, their values are set as fixed using the Dirichlet boundary condition. As for ν_t and p_{rgh}, zero gradient is applied on the top boundary. Table 4.3 summarize all the boundary conditions specified in the CFD model for different variables. The sensitivity test of the CFD model under different boundary conditions and grid configurations is presented in the Appendix.

Table 4.3: Boundary conditions specified in the CFD model.

	Inlet	Outlet	Ground	Top	Stack exit	Stack wall
u	Fixed value	Zero gradient	Fixed value	Fixed value	Direction mixed	Slip
θ	Fixed value	Zero gradient	Fixed value	Fixed gradient	Fixed value	Fixed value
k	Fixed value	Zero gradient	Zero gradient	Fixed value	Zero gradient	Zero gradient
ε	Fixed value	Zero gradient	Wall function	Fixed value	Zero gradient	Zero gradient
ν_t	Zero gradient	Zero gradient	Wall function	Zero gradient	Zero gradient	Wall function
p_{rgh}	Zero gradient	Fixed value	Zero gradient	Zero gradient	Zero gradient	Zero gradient
p	Calculated	Calculated	Calculated	Calculated	Calculated	Calculated
α_t	Calculated	Calculated	Calculated	Calculated	Calculated	Calculated

Chapter 5

Model validation

5.1 Verification of CFD model for 2D flow

An important requirement for a good CFD model is that the imposed inlet boundary conditions should yield vertical profiles that maintain horizontal homogeneity over a flat terrain [39]. After the CFD solver reaches the steady-state solution, it is expected that the ABL profiles initialized at the inlet boundary will propagate undisturbed through the computational domain to the outlet boundary. To verify the horizontal homogeneity of the model, simulations of buoyant flow under different stability conditions over a 2D flat terrain are performed using parameters in Table 5.1. The problem setup is shown in Figure 5.1, and the results are shown in Figure 5.2.

Table 5.1: Parameters that describe different stability classes.

	Reference velocity (m/s)	Reference height (m)	Aerodynamic roughness length (m)	Ground heat flux (W/m^2)	Surface temp. (k)	Friction velocity (m/s)	Monin-Obukhov length (m)
Neutral	5.12	10	0.01	0	300	0.3	NA
Stable	7.09	10	0.01	-40	273	0.4	139

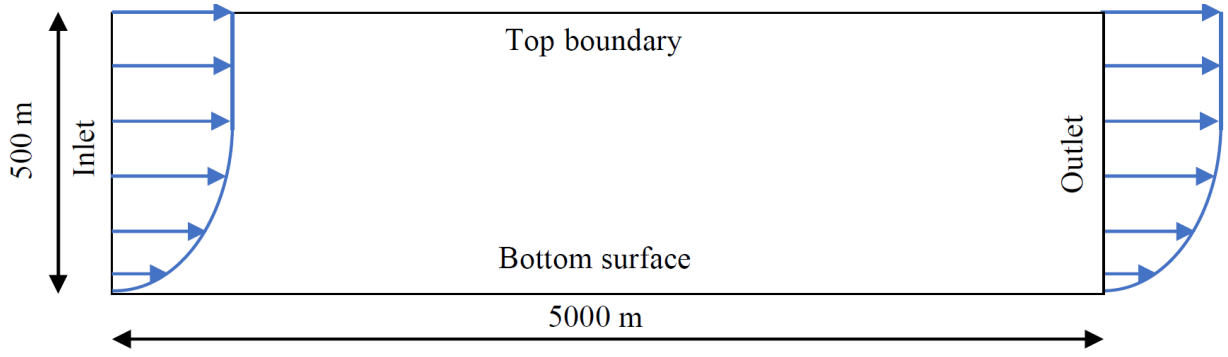

Figure 5.1: The $5000\ m\ \times 500\ m$ 2D domain used to verify the horizontal homogeneity of the CFD model.

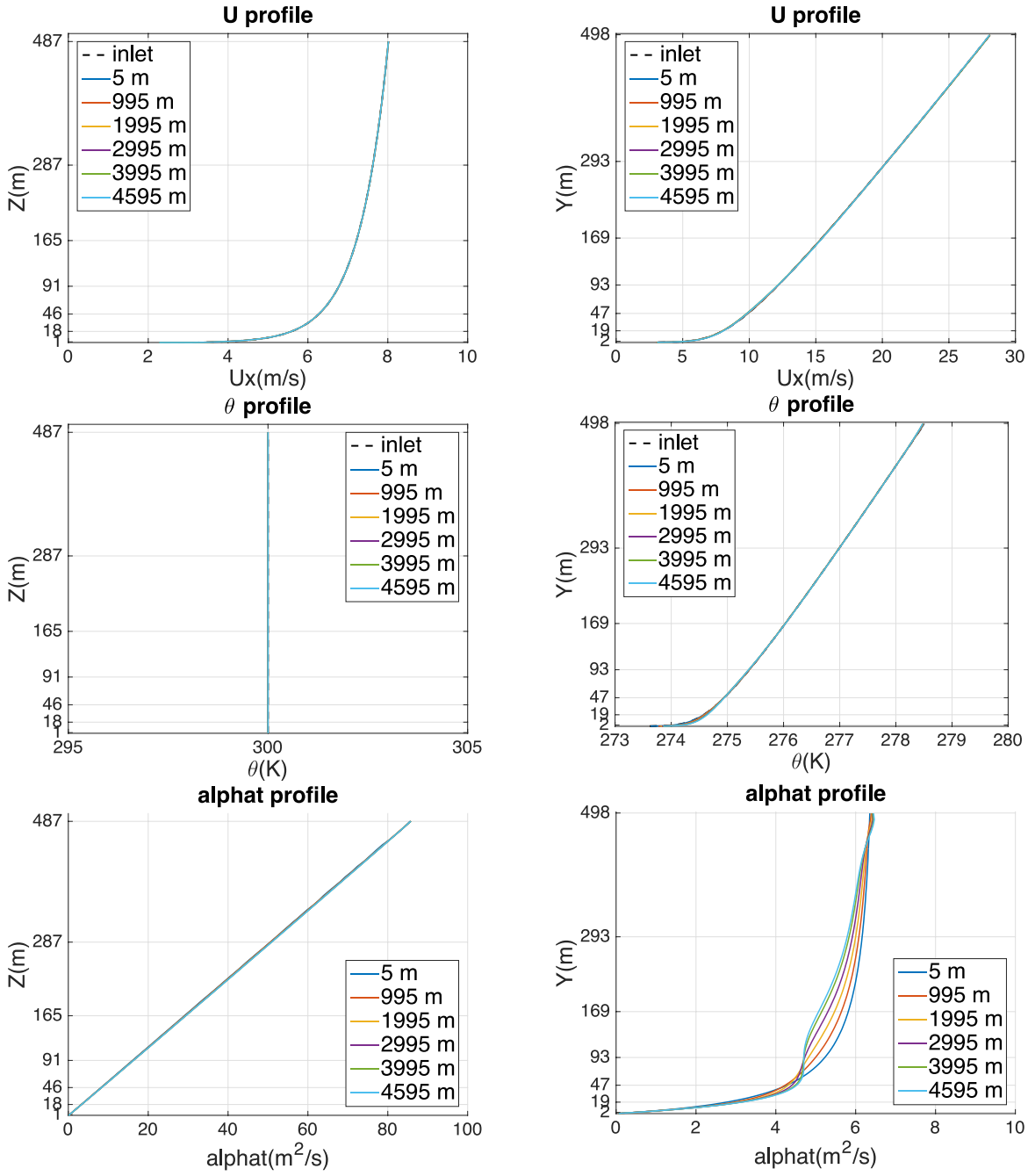

(a) Profiles for the neutral condition

(b) Profiles for the stable condition

Figure 5.2: Vertical profiles extracted at different locations away from the inlet show horizontal homogeneity under different conditions.

It can be seen from Figure 5.2 that the vertical profiles are horizontally homogeneous for the neutral conditions. For the stable conditions, the wind velocity and potential temperature profiles are homogeneous, while the turbulent diffusivity profile is modified with distance from the inlet,

with a peak error of about 10%. Our model's predictions are either similar to or superior to other similar results reported in the literature [27,35,38,44,79,80].

5.2 Validation of 3D CFD model

A steady-state CFD simulation requires that the inlet profiles be kept unchanged, and the results will show the fully developed wind and pollution patterns during the simulated period. If the weather conditions change dramatically during one or two hours, the measured data will show very different wind speeds, wind directions, and air temperatures. Under such conditions, the steady-state model will not be able to predict the variations. Therefore, for model validation, three criteria are established to select cases for simulations. First, the vertical temperature profile needs to show a clear stability class. Second, the weather condition in terms of wind speed, wind direction, and air temperature should remain quasi-steady for at least two hours. With an average wind speed of 2.5 m/s, the time it takes for the wind to travel from the inlet to the outlet of the study domain is about two hours. Third, the curve fitting algorithms should provide satisfactory vertical profiles when compared with measurements.

5.2.1 Comparison with wind measurements

Multiple validation cases are selected with varying wind speeds and seasons under neutral and stable conditions. The results of the curve fitting method for obtaining boundary conditions at the inlet and the simulation results under neutral conditions are shown in Figure 5.3 - Figure 5.5. The “Fitted” curves are shown with $\pm 10\%$ error indicated by the green-colored band. The predicted wind speeds are compared with those of measurement at multiple sensor locations. Comparisons of wind direction are not shown since all cases are selected when the mean wind direction is relatively steady, and the difference is small between each sensor location. Wind direction reported by KAGC is used at the inlet of the study domain. With the new curve fitting

algorithms, the fitted wind profiles can either under-predict or over-predict the wind speed compared to the sounding data. As long as the overall shape of the fitted profiles are not very different from the instantaneous sounding profiles, and curve fitting errors are small, the fitted profiles are considered adequate. The reanalysis data for the validation cases are not used for cure fitting, but they are plotted as a reference. For all simulation results shown in this section, the fitted curves with inlet $z_0 = 0.7\ m$ are used to represent the roughness at the inlet of the study domain.

In general, the case-to-case trend is clear and consistent. The model predicts the correct trend of decreasing wind speed from Liberty to Mitchell to the VFW sensor. The predicted wind speeds at Liberty tend to be higher than the measurements under neutral conditions. In the computational domain, the extraction height at Liberty monitor is $16\ m$ above the terrain surface. However, in the real world, this site is located on the roof of a building. Since the building is not physically present in the computational domain, the $16\ m$ extraction height may not always be appropriate. If the extraction height is lowered to $10\ m$, the predicted values under neutral conditions will be much closer to the measurements. Other findings from the comparison include:

1) The predicted wind speeds at Liberty are the best and also highest, but they always lie within the full range of speed change of measurements.
2) The predicted wind speed at VFW is the second best. Both the predicted and predicted wind speeds are the lowest compared to other locations.
3) The predicted wind speed at Glassport is always higher than the mean of the measurement.

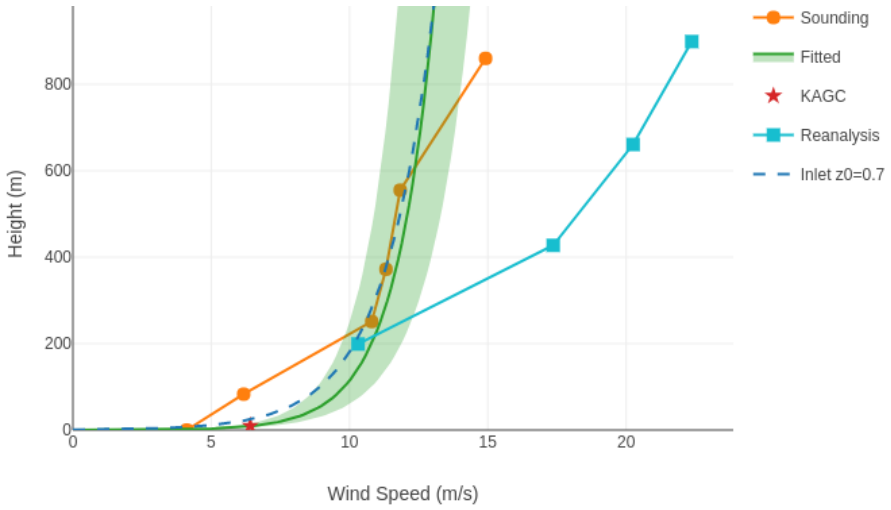

(a) Curve fitting result compared with data from different sources.

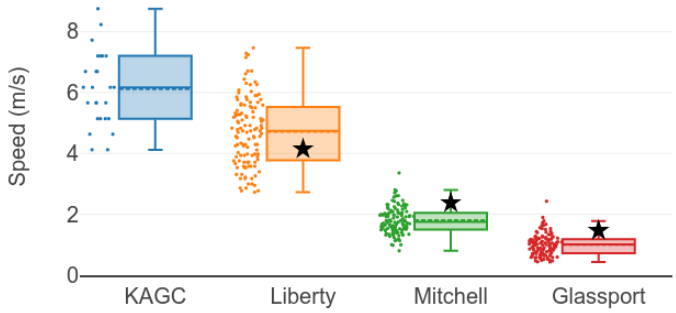

(b) Comparison between CFD predictions and measurements. ★: CFD prediction at the monitor. Each box contains measurements during the simulated 3-hour period. The dash line in each box indicates the mean value.

Figure 5.3: Neutral case 1, 04/13/2018 0 Zulu, wind direction 240°.

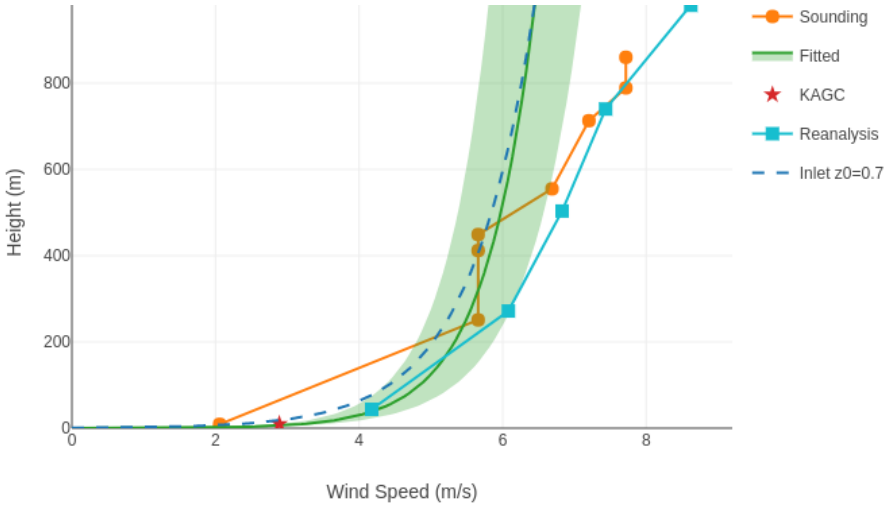

(a) Curve fitting result compared with data from different sources.

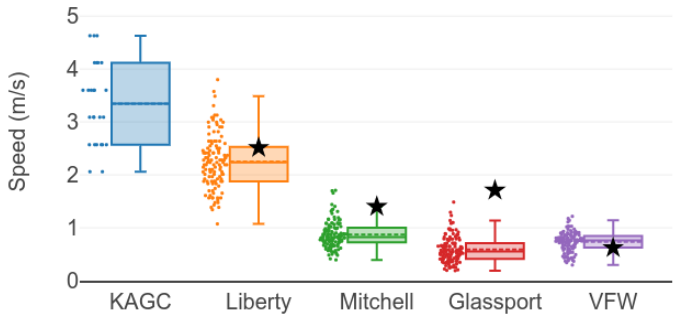

(b) Comparison between CFD predictions and measurements. ★: CFD prediction at the monitor. Each box contains measurements during the simulated 3-hour period. The dash line in each box indicates the mean value.

Figure 5.4: Neutral case 2, 08/02/2018 0 Zulu, wind direction 201°.

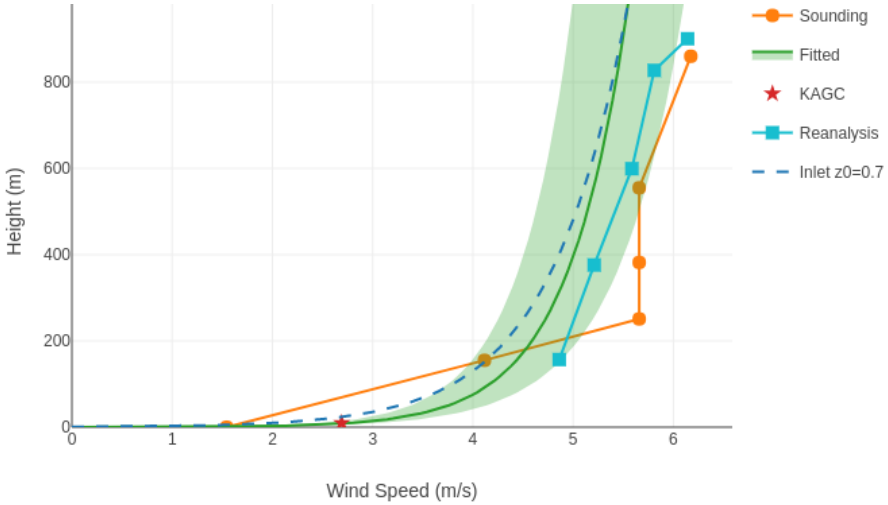

(a) Curve fitting result compared with data from different sources.

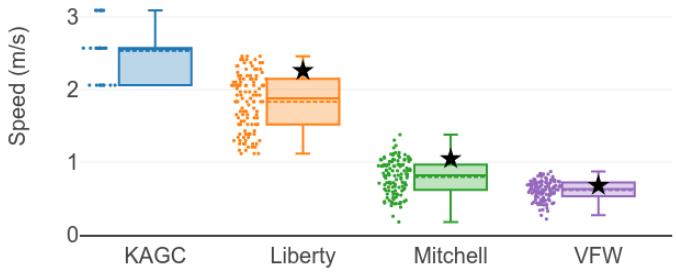

(b) Comparison between CFD predictions and measurements. ★: CFD prediction at the monitor. Each box contains measurements during the simulated 3-hour period. The dash line in each box indicates the mean value.

Figure 5.5: Neutral case 3, 10/03/2018 0 Zulu, wind direction 252°.

Figure 5.6 - Figure 5.8 shows the comparison of measurements and predictions for the stable conditions. According to the sounding data, neutral conditions usually happen at 0 Zulu, and stable conditions usually happen at 12 Zulu. Under stable conditions, the fitting algorithm achieves a better match between the “Fitted” profiles and the sounding profiles compared to the neutral conditions. Similar to the neutral condition, the model predicts a trend of decreasing wind speed from Liberty to Mitchell to the VFW sensor, as also seen in the measurements.

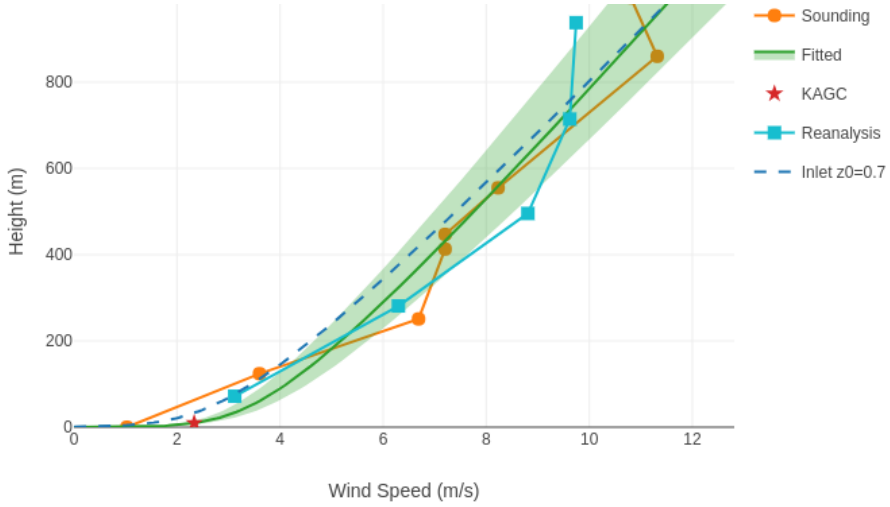

(a) Curve fitting results for wind speed compared with data from different sources.

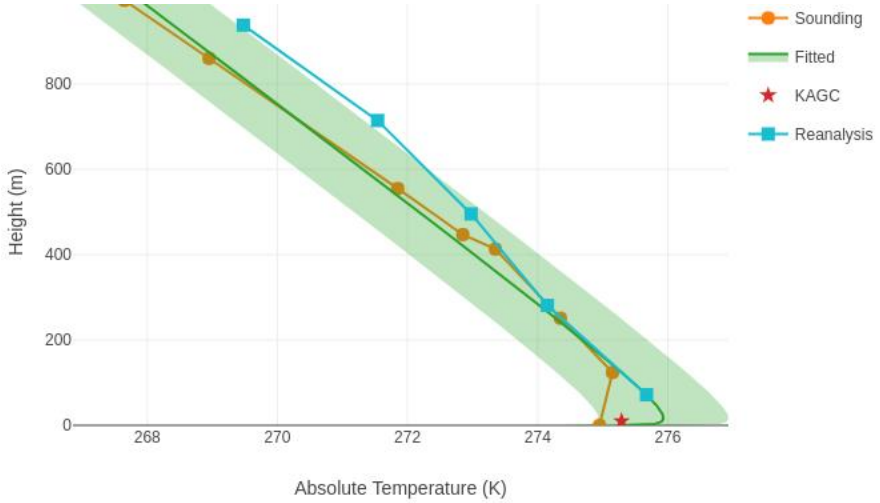

(b) Curve fitting results for temperature compared with data from different sources.

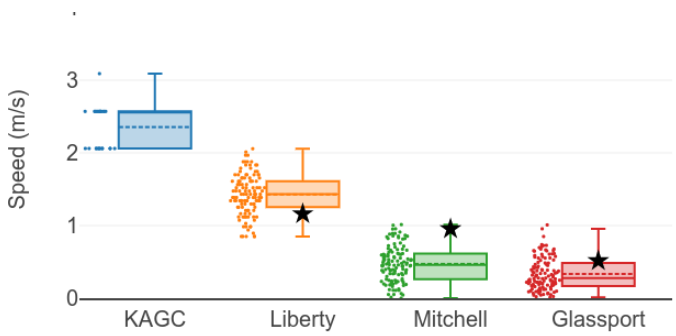

(c) Comparison between CFD predictions and measurements. ★: CFD prediction at the monitor. Each box contains measurements during the simulated 3-hour period. The dash line in each box indicates the mean value.

Figure 5.6: Stable case 1, 04/11/2018 12 Zulu, wind direction 204°.

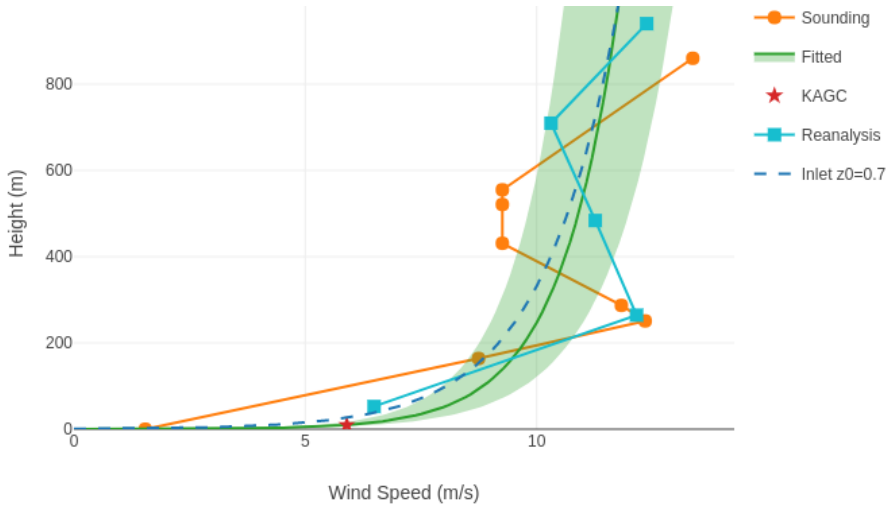

(a) Curve fitting results for wind speed compared with data from different sources.

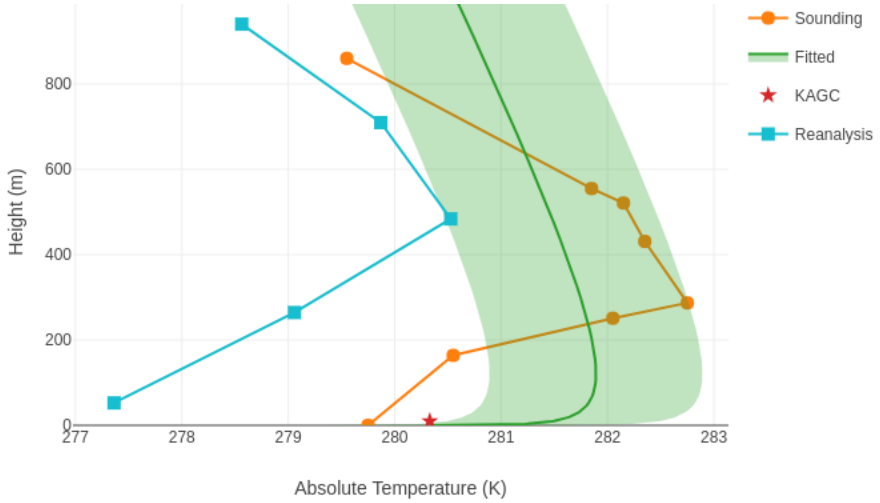

(b) Curve fitting results for temperature compared with data from different sources.

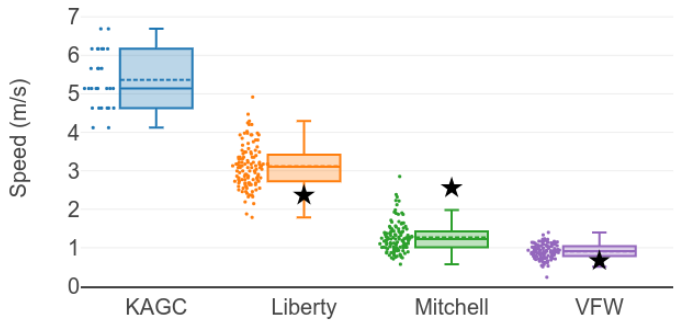

(c) Comparison between CFD predictions and measurements. ★: CFD prediction at the monitor. Each box contains measurements during the simulated 3-hour period. The dash line in each box indicates the mean value.

Figure 5.7: Stable case 2, 10/23/2018 12 Zulu, wind direction 205°.

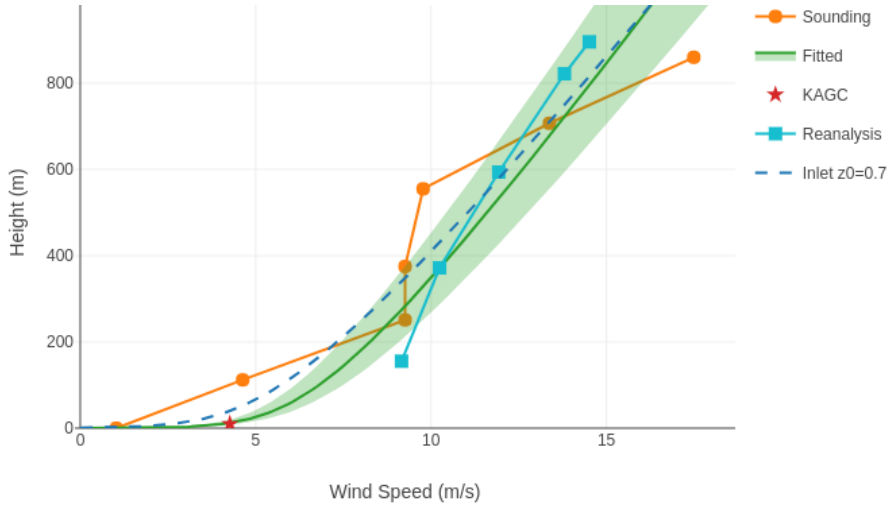

(a) Curve fitting results for wind speed compared with data from different sources.

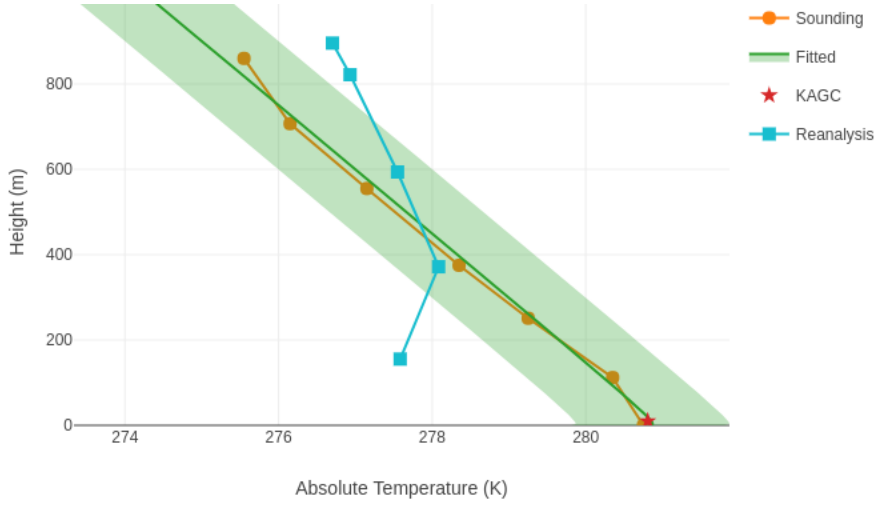

(b) Curve fitting results for temperature compared with data from different sources.

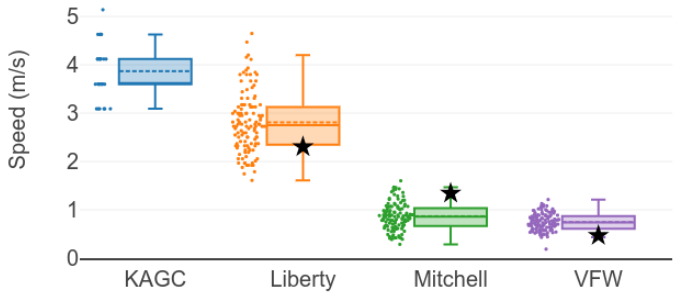

(c) Comparison between CFD predictions and measurements. ★: CFD prediction at the monitor. Each box contains measurements during the simulated 3-hour period. The dash line in each box indicates the mean value.

Figure 5.8: Stable case 3, 11/25/2018 12 Zulu, wind direction 239°.

Table 5.2 summarizes the comparisons between CFD and measurements for the six validation cases. The mean wind speeds over the simulated at each location are used to calculate the percentage error. The error of the CFD prediction is smaller when compared to wind speed from Liberty and VFW.

Table 5.2: Summary of validation cases for wind development over the complex terrain.

Location	Speed (m/s)	Neutral case number			Stable case number		
		1	2	3	1	2	3
Liberty	Measured	4.7	2.3	1.8	1.4	3.1	2.8
	Predicted	4.1	2.5	2.3	1.2	2.4	2.3
	Error (%)	-12.8	8.7	27.8	-14.3	-22.6	-17.9
Mitchell	Measured	1.8	0.9	0.8	0.5	1.3	0.9
	Predicted	2.4	1.4	1.0	1.0	2.6	1.3
	Error	33.3	55.6	25.0	100.0	100.0	44.4
Glassport	Measured	1.0	0.6	-	0.3	-	-
	Predicted	1.5	1.7	-	0.5	-	-
	Error	50.0	183.3	-	66.7	-	-
VFW	Measured	-	0.7	0.6	-	0.9	0.7
	Predicted	-	0.6	0.7	-	0.7	0.5
	Error	-	-14.3	16.7	-	-22.2	-28.6

5.2.2 Comparison with tracer release measurements

From the ERA5 temperature profiles, the stability classes are determined to be neutral

during the time periods of three tracer releases, and the wind speed and direction from KAGC are used to obtain the boundary conditions for the model. Figure 5.9, Figure 5.10, and Figure 5.11 show the concentration of measured N_2O along the driving route and the CFD-predicted concentration on the ground level with a scale ranging from 0 ppb – 10 ppb. The background concentration has been subtracted. Model-predicted N_2O concentration with the same scale is also shown. In release 1, the CFD model predicts a plume of N_2O traveling downwind from the release point, intersecting the driving route in approximately the same location where measurements detected N_2O. More importantly, the predicted N_2O concentration is close to the measured one, as indicated by intersecting green to blue color contours. In release 2, N_2O is only picked up outside the study domain. The extension of the predicted plume is close to the measured N_2O concentration. In release 3, the peak N_2O concentration above the ambient level from the measurements is around $10\ ppb$. The CFD model predicts the same concentration on the sampling route and only misses the exact location by about $100\ m$.

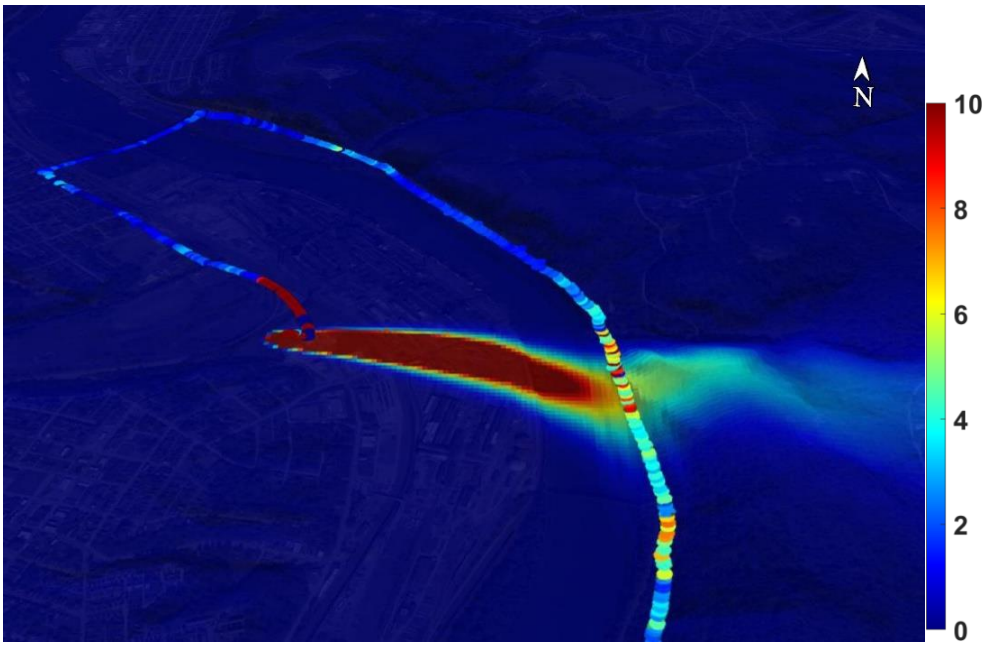

Figure 5.9: Contours of model predicted N_2O concentration compared with measurements for release 1 under northwest wind direction.

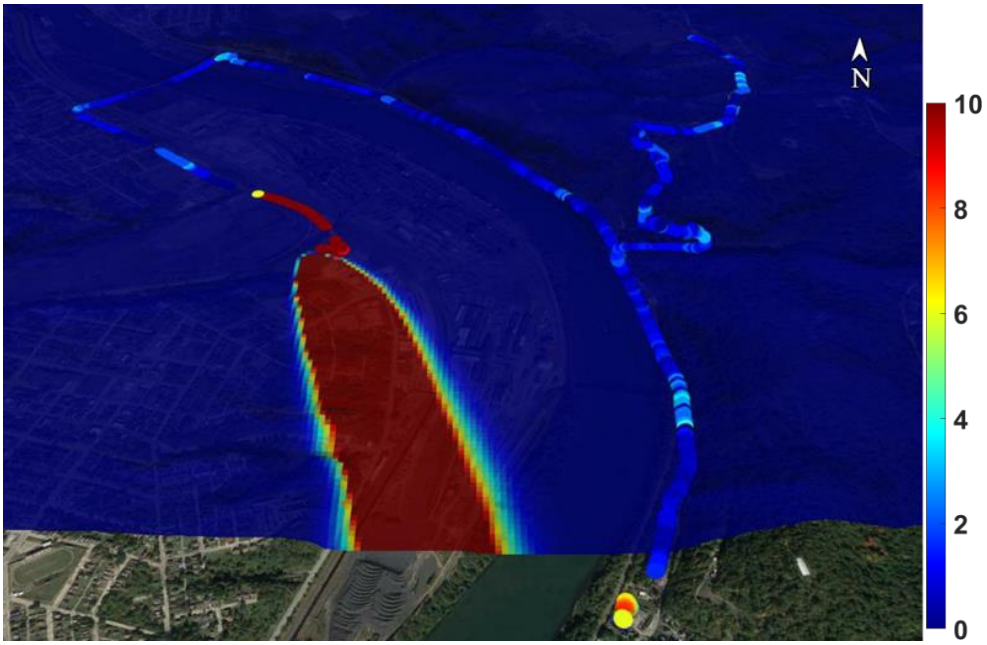

Figure 5.10: Contours of model predicted N_2O concentration compared with measurements for release 2 under southwest wind direction.

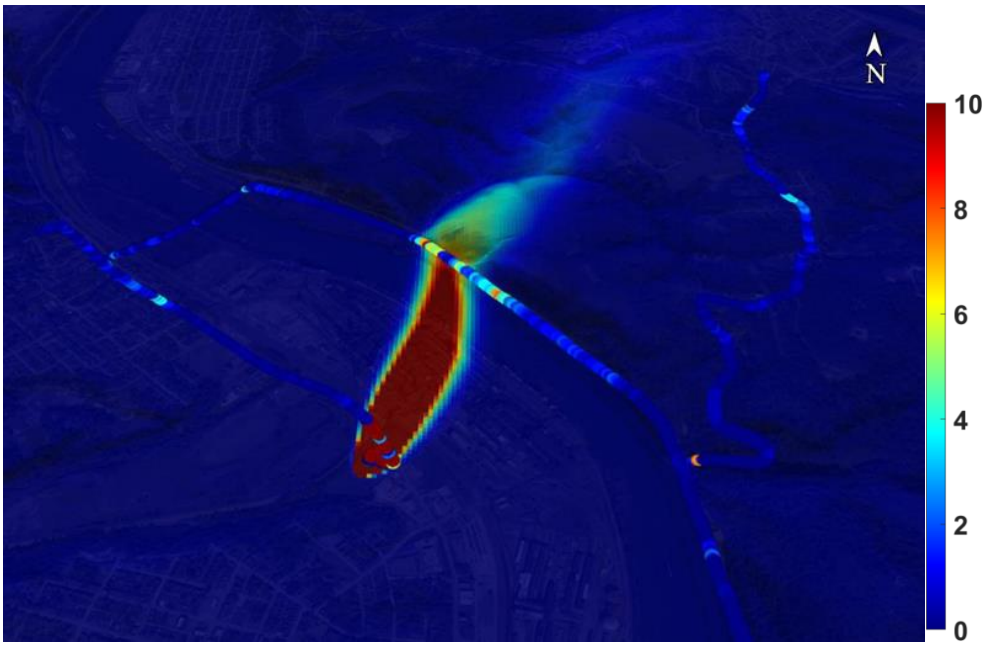

Figure 5.11: Contours of model predicted N_2O concentration compared with measurements for release 3 under northwest wind direction.

5.3 Simulations of SO_2 dispersion

5.3.1 Sampling techniques

In this work, we have compared the model predictions with single measurements at the Liberty site. This is a very challenging comparison since a slight uncertainty in the wind direction could lead to a significant mismatch of predictions and measurements of SO_2 at the Liberty sensor location. To account for the uncertainty in the wind direction, SO_2 concentration in the CFD model is sampled over a larger region that includes the Liberty sensor. Specifically, we use a cylinder and an arc, as shown in Figure 5.12. The radius of the cylinder is $500\ m$ to allow for an uncertainty of $10°$ wind direction from the plant center to the Liberty site. The height of the cylinder was initially set to $500\ m$ AGL, however, it is found to be unnecessary, so the height is reduced to $100\ m$ AGL.

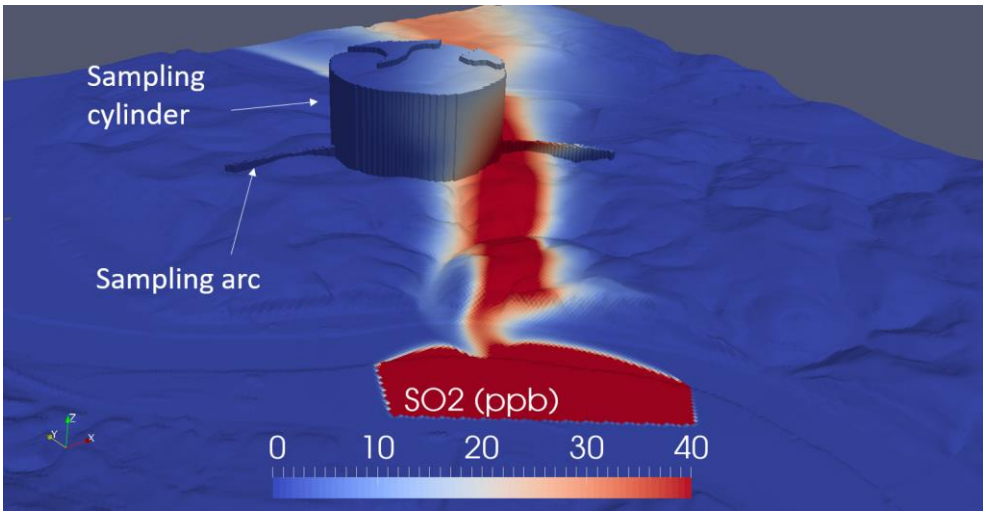

Figure 5.12: The sampling cylinder and arc used in CFD to account for the uncertainty in wind direction specified at the inlet.

Other researchers have used the sampling arc to compare model predictions with measurements to evaluate dispersion models [20,81]. The disadvantage of using the sampling cylinder is that it usually overpredicts concentrations as the sampling region gets closer to the coke

plant. The corresponding sampling cylinder and arc are also created in AERMOD at receptor locations. The maximum SO_2 concentration within the cylinder or on the arc is compared with the measurements of the Liberty site. To create the sampling arc that can capture the SO_2 plume at the vicinity of the Liberty monitor with equal distance to the center of the pant, several auxiliary lines are introduced, as shown in Figure 5.13. From the centers of the upper and lower sides of the plant, two straight lines that connect the centers to the Liberty monitor are drawn, shown in solid yellow and solid blue. Then two parallel lines are drawn, shown as the corresponding dash lines. Assuming that once emitted from the plant, the SO_2 plume only travels downstream along the dominant wind direction. The plume within the two yellow lines and the plume within the two blue lines are the two extreme cases when the Liberty monitor is able to pick up SO_2 from the plant. An arc with a radius of 2 km is drawn with two ends stopped at the two dash lines, and the resulting length of the arc is 3 km.

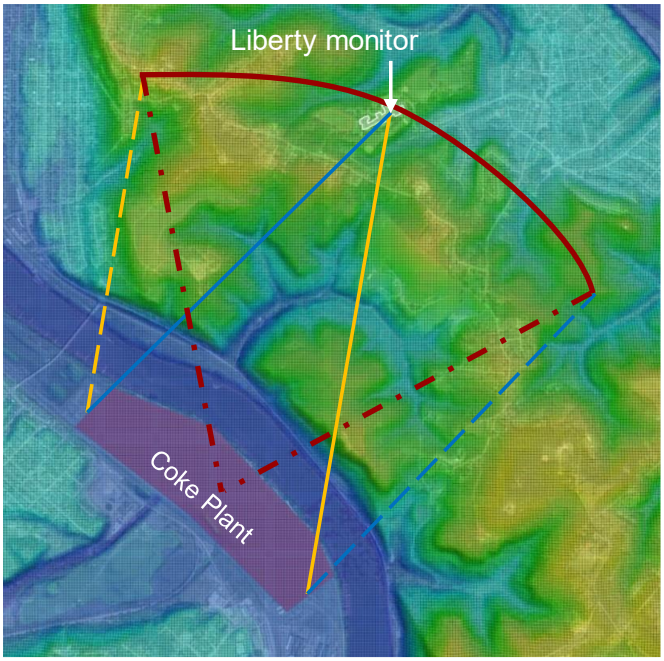

Figure 5.13: The schematic to show the creation of the sampling arc. The yellow lines and blue lines are auxiliary lines to identify the two ends of the arc (in red). The Liberty monitor lies in the middle of the sampling arc.

5.3.2 Simulations using the steady-state model

We have used the steady-state CFD model and AERMOD to simulate a number of cases. Figure 5.14 and Figure 5.15 show the comparison of SO_2 concentrations among CFD, AERMOD, and measurements during 5 hours for Jan. 4, 2019, and 6 hours for Apr. 3, 2019. The predicted wind speeds from CFD are close to those of measurements from Liberty. However, the predicted wind directions can be off by 10°. The predicted SO_2 concentrations from CFD and AERMOD are sampled using the arc method. Overall, CFD can predict the varying trend of SO_2 concentration near the Liberty monitor. The predicted steady-state plume width in the horizontal direction is found to be in good agreement with the discussion of Figure 3.19 about the estimated plume width.

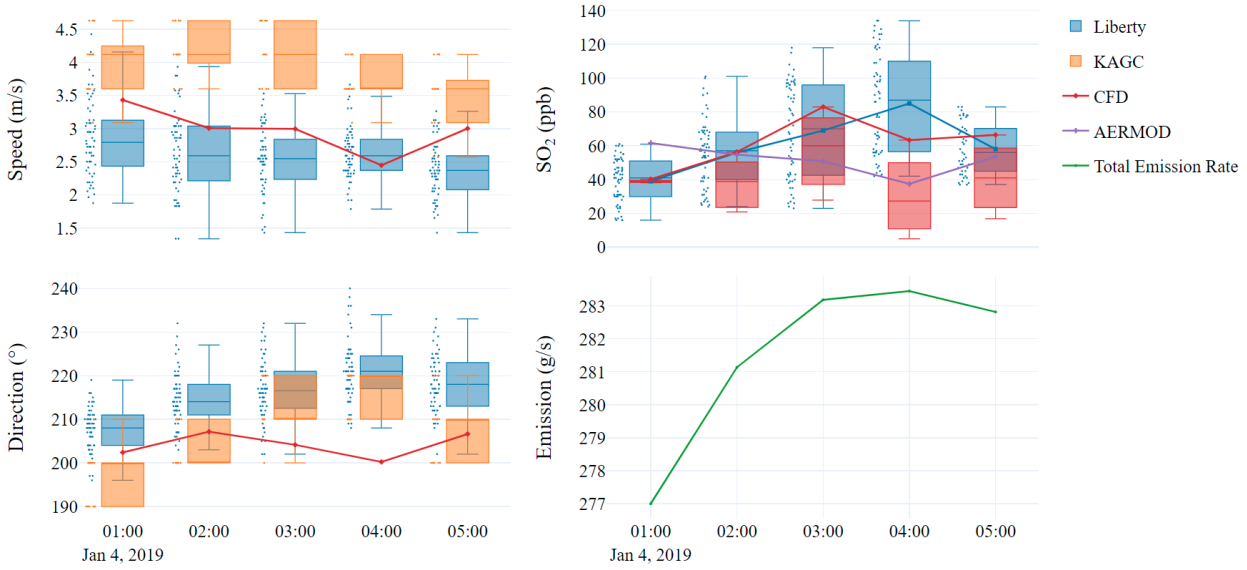

Figure 5.14: Summary of the 5-hour simulation period for Jan. 4, 2019. Wind speeds and directions from KAGC, Liberty, and the CFD model are shown. SO_2 concentrations from CFD, AERMOD using the sampling arc are compared with those of measurements. CFD results for SO_2 concentrations are presented with the box, whose values range from $1/10$ of the value extracted at the Liberty monitor to the maximum value on the arc. The maximum values from CFD are connected as a solid line in red, and the maximum values from AERMOD are connected as a solid line in purple. The total emission rate from the plant is also presented.

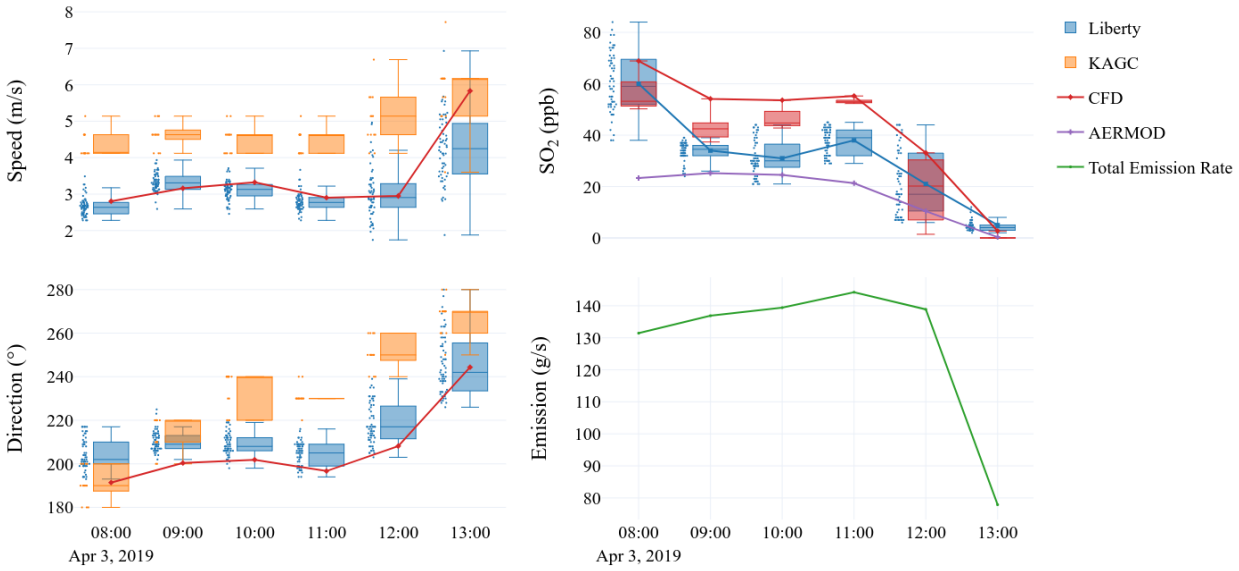

Figure 5.15: summary of the 5-hour simulation period for Apr. 3, 2019. Wind speeds and directions from KAGC, Liberty, and the CFD model are shown. SO_2 concentrations from CFD, AERMOD using the sampling arc are compared with those of measurements. CFD results for SO_2 concentrations are presented with the box, whose values range from $1/10$ of the value extracted at the Liberty monitor to the maximum value on the arc. The maximum values from CFD are connected as a solid line in red, and the maximum values from AERMOD are connected as a solid line in purple. The total emission rate from the plant is also presented.

Table 5.3: Summary of the 28 cases of SO_2 dispersion simulations.

Case number	Date	Start Hour (Zulu)	End Hour (Zulu)
1-5	01/04/2019	01	05
6-10	01/08/2019	05	09
11-16	02/03/2019	02	07
17-22	04/03/2019	08	13
23-28	03/07/2019	03	08

To provide an overall view of the model performance, a total of 28 cases are simulated over multiple days from 01/2019 to 04/2019, as given in Table 5.3. During the consecutive hours of each time period, a peak of SO_2 concentrations is identified and the wind directions are southwest as reported by the Liberty monitor. However, the SO_2 concentrations are changing with

varying wind direction and also varying inversion strength. These 28 cases represent different meteorological conditions and emission scenarios. Measurements from liberty site in pard with predictions of CFD and AERMOD for these 28 cases are shown in Figure 5.16. Comparison of model predictions with measurements in Figure 5.16 shows that the predicted maximum SO_2 concentrations within the sampling arc from CFD closely follow that of the Liberty monitor. The sampling cylinder generates similar results to those of the sampling arc in CFD, but it has a tendency of overprediction. As for AERMOD, the sampling cylinder shows much better results than the sampling arc. All the input files for AERMOD are prepared by Jason Maranche of ACHD, and the AERMOD simulation cases mirror all the CFD simulation cases.

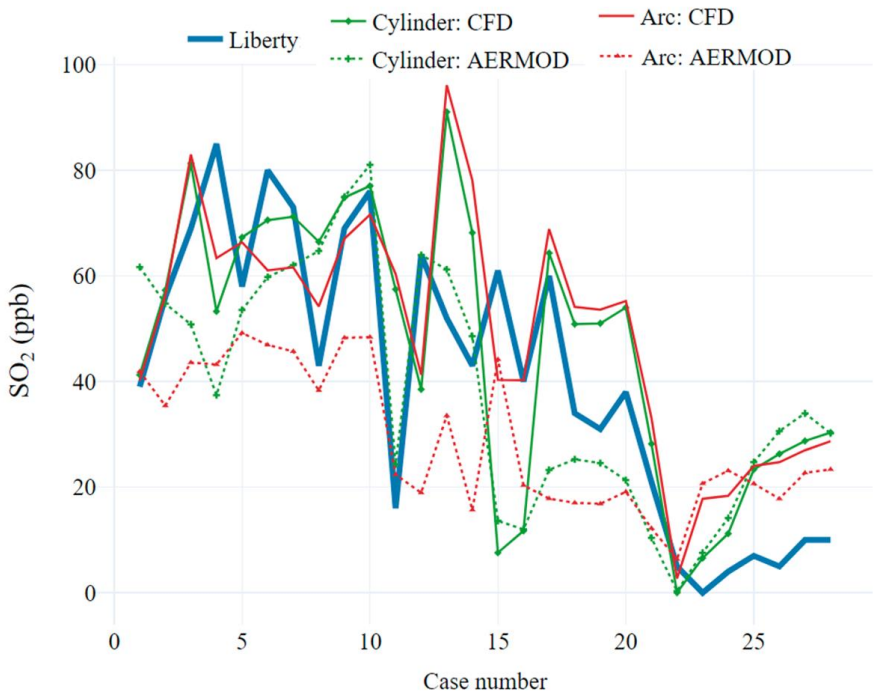

Figure 5.16: Comparison between predictions using different sampling methods and measurements at Liberty for SO_2 concentrations of the 28 cases.

Some statistical performance measures are commonly used for air quality model evaluation [82–87]. These performance measures include: the fractional bias (FB), the normalized mean

square error ($NMSE$), the geometric mean bias (MG), and the fraction of predictions within a factor of two of observations ($FAC2$). They are defined as:

$$FB = \frac{(\overline{C_o} - \overline{C_p})}{\frac{1}{2}(\overline{C_o} + \overline{C_p})} \tag{5.1}$$

$$NMSE = \frac{\overline{(C_o - C_p)^2}}{\overline{C_o}\,\overline{C_p}} \tag{5.2}$$

$$MG = e^{(\overline{\ln C_o} - \overline{\ln C_p})} \tag{5.3}$$

$$FAC2\text{: fraction of data that satisfy } \frac{1}{2} \leq \frac{C_p}{C_o} \leq 2 \tag{5.4}$$

C_p denotes model predictions, C_o denotes observations, and $\bar{C}$ denotes the average over the dataset. For a perfect model, the values of FB and $NMSE$ tend to be close to 0, while the values of MG and $FAC2$ tend to be close to 1. In reality, computational models are rarely perfect, especially considering the uncertainty in wind direction. Chang and Hanna [88] established criteria for a good dispersion model: $|FB| < 0.3$, $NMSE < 0.5$, $0.7 < MG < 1.3$ and $FAC2 > 0.5$.

Figure 5.17 shows the scatter plot of all 28 cases from two different meteorological inputs in AERMOD using the sampling cylinder. The horizontal axis shows the SO_2 concentrations from the Liberty monitor, and the vertical axis shows model predictions. From the scatter plots of these paired data, we can quickly tell when the models are overpredicting, underpredicting, or doing well. The results from the "AERMOD-LIB" model use the wind speeds at the Liberty monitor as model input, while the results from the "AERMOD-AGC" model use the wind speeds from KAGC as model input. Unlike using the fitted inlet profiles to predict the whole flow field of the computational domain in CFD, vertical profiles in AERMOD, such as wind speed, wind direction, turbulence, temperature, and temperature gradient, are estimated using all available meteorological observations. As a result, the performance of AERMOD is strongly dependent on the inputs from

observations. Figure 5.17 shows that the "AERMOD-LIB" option is much better in all performance measures compared to the "AERMOD-AGC" option. We have explored several other meteorological inputs for AERMOD, such as the SODAR data. Since The "AERMOD-LIB" option has much better performance in every aspect than those of other meteorological options, only the "AERMOD-LIB" option will be used for comparisons with CFD.

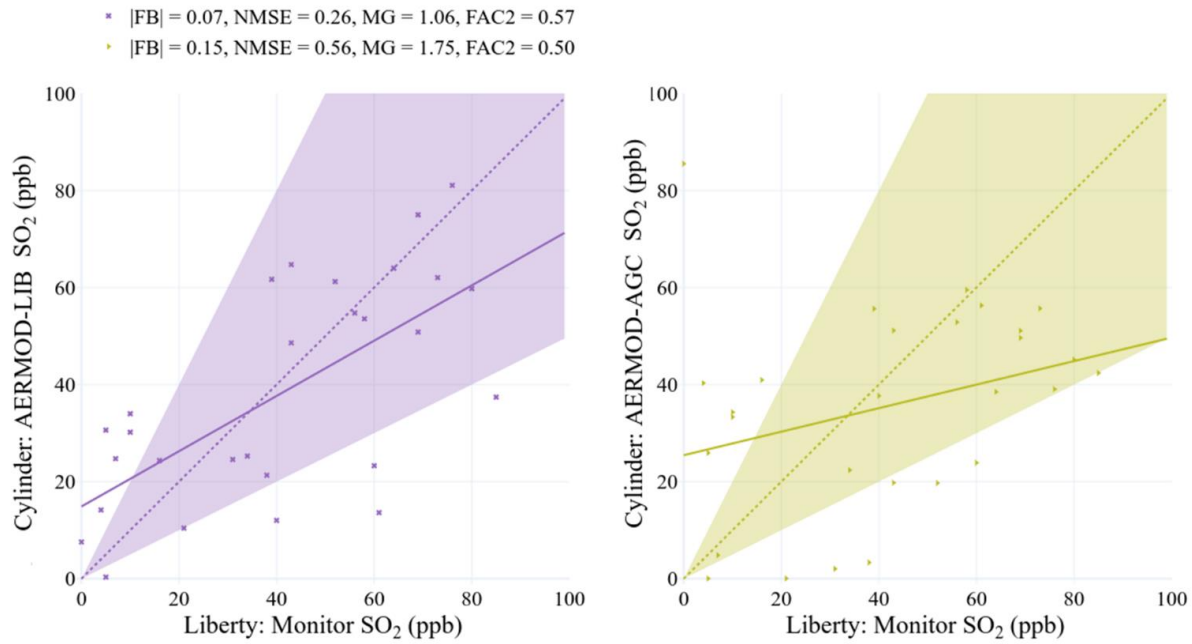

Figure 5.17: The scatter plot of all 28 cases using the sampling cylinder from two wind data input settings in AERMOD. The calculated statistical measures are also shown.

Figure 5.18 shows the scatter plot of all 28 cases using maximum values on the sampling cylinder from CFD and AERMOD. The statistical performance measures show that the CFD model is overall better with a smaller value of $NMSE$ and values that are closer to 1 for MG and $FAC2$. However, the $|FB|$ value is slightly larger than that of AERMOD. From the definition of $|FB|$, we can infer that the main reason CFD has a larger value is from the numerator, that is the difference between $\overline{C_o}$ and $\overline{C_p}$. By removing case 11 and case 13, in which the most significant

differences are found between CFD and the Liberty monitor, $|FB|$ for CFD is lowered to 0.07 while $|FB|$ for AERMOD increases to 0.09.

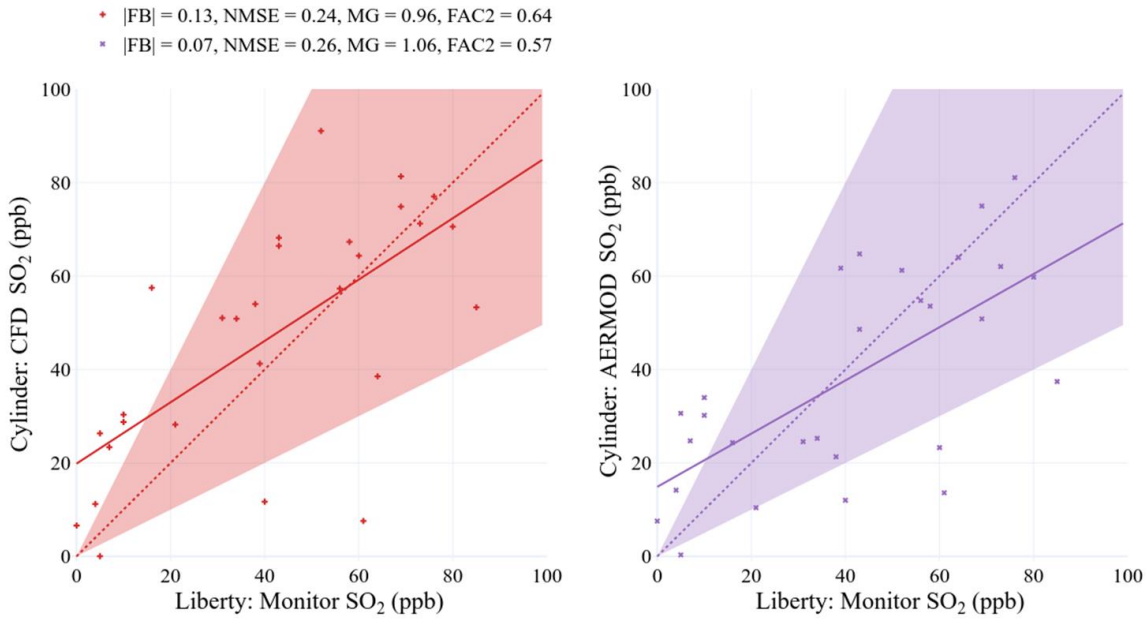

Figure 5.18: The scatter plot of all 28 cases using the sampling cylinder from CFD and AERMOD. The calculated statistical measures are also shown.

Figure 5.19 shows the scatter plot of all 28 cases using maximum values on the sampling arc from CFD and AERMOD. AERMOD tends to underpredict SO_2 concentrations as the majority of the scatter points are below the dash line. On the contrary, CFD does not have such a clear bias using the sampling arc. Again, the statistical performance measures show that the CFD model is overall better with smaller values of $NMSE$ and $|FB|$ and a value closer to 1 for $FAC2$. The $FAC2$ values using the sampling arc are generally higher than those of the sampling cylinder. The Q-Q (quantile-quantile) plot is also widely used to evaluate dispersion models [89–93].

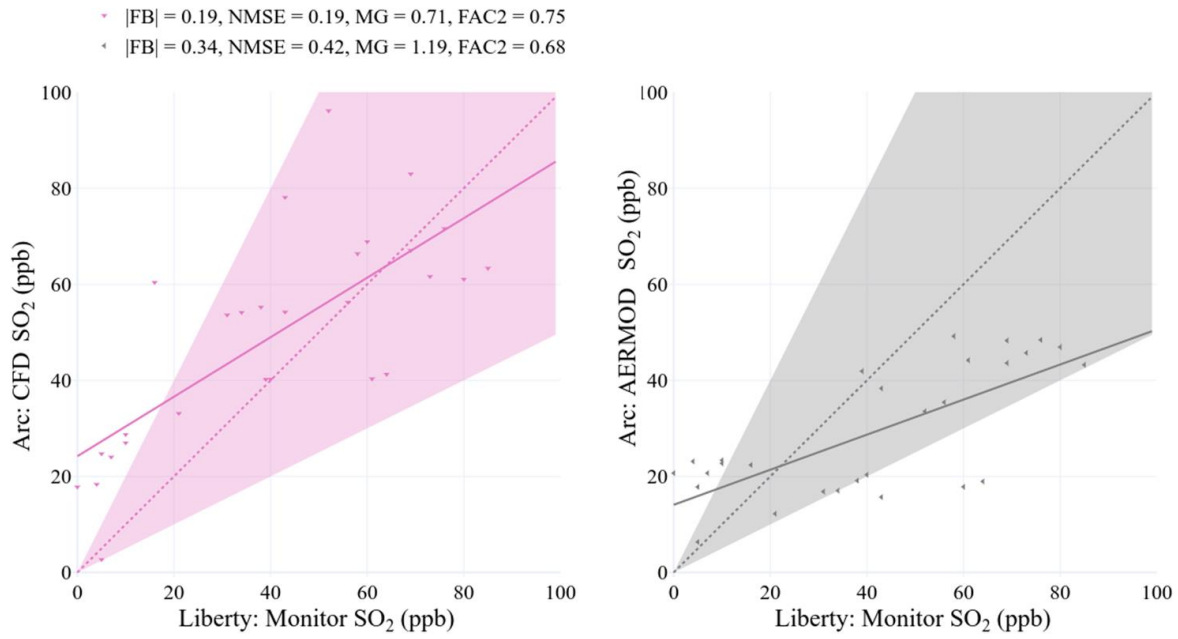

Figure 5.19: The scatter plot of all 28 cases using the sampling arc from CFD and AERMOD. The calculated statistical measures are also shown.

Using the same data from the scatter plots, the predicted and measured pollutant concentrations are sorted and then plotted as unpaired scatter points. Figure 5.20 shows the Q-Q plot of the 28 cases. For all three types of comparisons using exact Liberty location, sampling on the cylinder, and sampling on the arc, the overall distributions from CFD are closer to the measured distribution, especially towards the high SO_2 concentration range between 60 and 85 ppb. When predicting the SO_2 concentrations at the exact Liberty location, both CFD and AERMOD underpredict the overall distribution. Using the two sampling methods, the distributions from CFD and AERMOD both overpredict SO_2 concentrations at the lower concentration range.

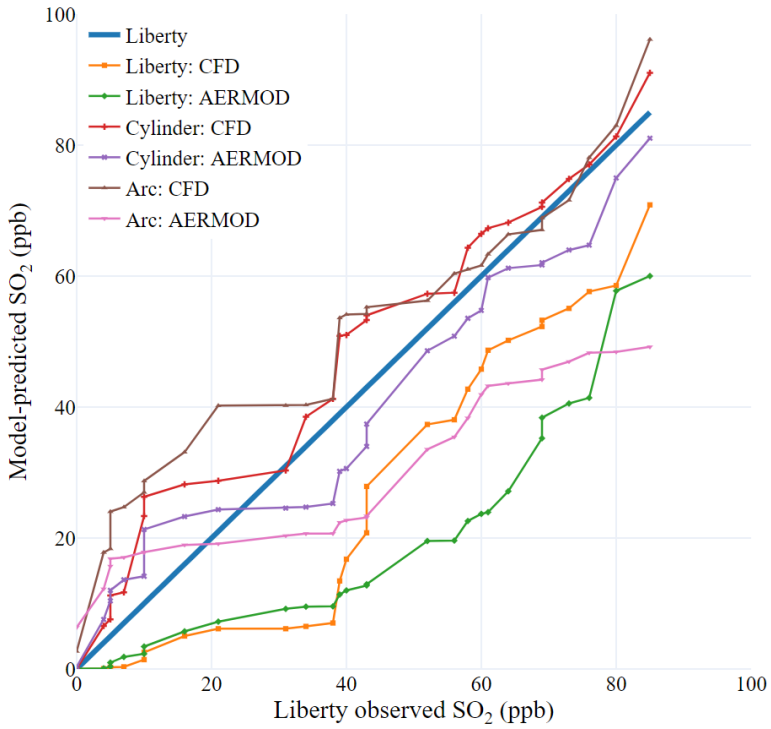

Figure 5.20: Q-Q plot for the 28 cases. “Liberty” shows the monitored data. “Liberty: CFD” shows the CFD predictions at the exact Liberty site. “Liberty: AERMOD” shows the AERMOD predictions at the exact Liberty site. “Cylinder: CFD” shows the maximum CFD predictions using the sampling cylinder.

5.3.3 Detailed comparisons of CFD and AERMOD

For case 10, CFD and AERMOD have reasonably accurate predictions of SO_2 concentrations, as shown in Figure 5.16. The difference between different sampling methods (arc or cylinder) is small. Figure 5.21 shows the wind and temperature profiles used in CFD and AERMOD for case 10. The wind speed profiles used in CFD and AERMOD are very close to each other. As for the temperature profiles, the error among ERA5, AERMOD, and the “Fitted” profile for CFD is within 1 K. The temperature profile from NARR is only shown as a reference. As discussed previously, ERA5 data have higher resolution in time and better quality than NARR data. If the profiles reported by NARR are different than EAR5, more confidence should be given to the ERA5 profiles.

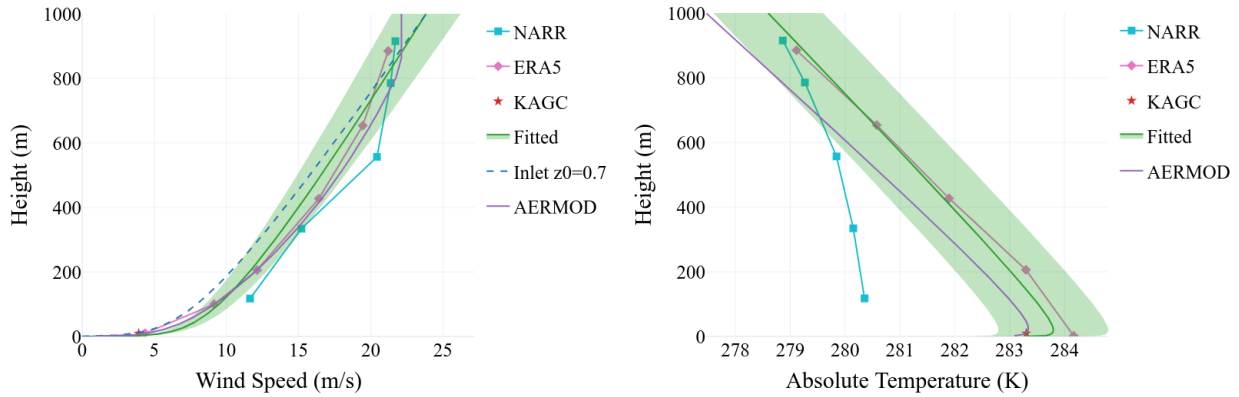

(a) Wind speed (b) Absolute temperature

Figure 5.21: Vertical profiles used in CFD and AERMOD for case 10.

For case 13, the Liberty monitor reports 52 ppb for the hourly mean SO_2 concentration. AERMOD predicts the concentration to be 61 ppb using the sampling cylinder method, but a much lower value of 34 ppb using the sampling arc method. On the contrary, CFD predicts much higher concentrations that are above 90 ppb with the cylinder and the arc sampling methods. Figure 5.22 shows the wind and temperature profiles used in CFD and AERMOD for case 13. The fitted profiles for CFD agree well with those from ERA5, and the weather condition is moderate wind speed with strong inversion. However, the profiles used in AERMOD show a much larger wind speed and near-neutral condition, in disagreement with the Sounding and ERA5 data. Larger wind speed and neutral conditions specified as boundary conditions in AERMOD are expected to provide lower SO_2 concentrations. Therefore, one could say that a better match of AERMOD predictions with the measurements, in this case, is due to unjustified boundary conditions for wind speed and temperature. The CFD model predictions are consistent in the sense that higher SO_2 concentration is obtained under lower wind speed and stronger inversion scenarios, even though the CFD model does not agree with the measurements.

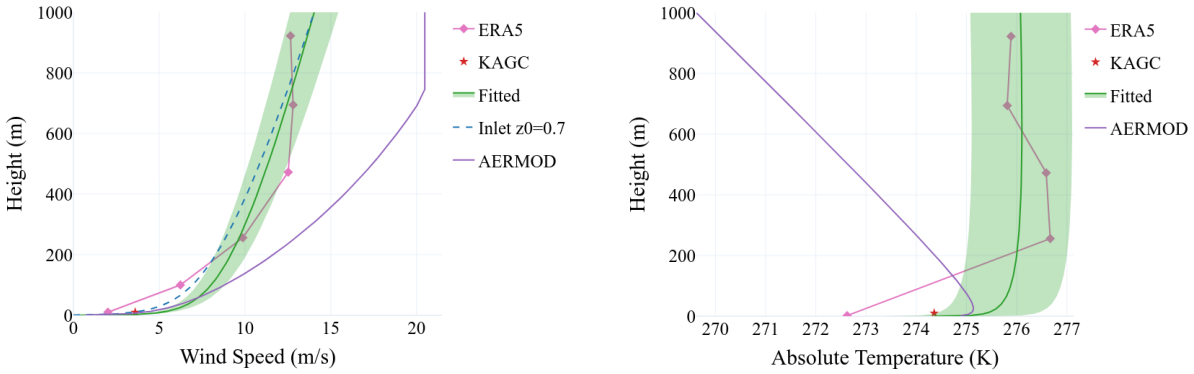

(a) Wind speed (b) Absolute temperature

Figure 5.22: Vertical profiles used in CFD and AERMOD for case 13.

For case 20, the CFD model overpredicts SO_2 concentration while AERMOD underpredicts SO_2 concentration compared to the Liberty monitor, which suggests 38 ppb. Figure 5.23 shows the vertical profiles used in CFD and AERMOD for case 20. Table 5.4 summarizes the differences between case 13 and case 20.

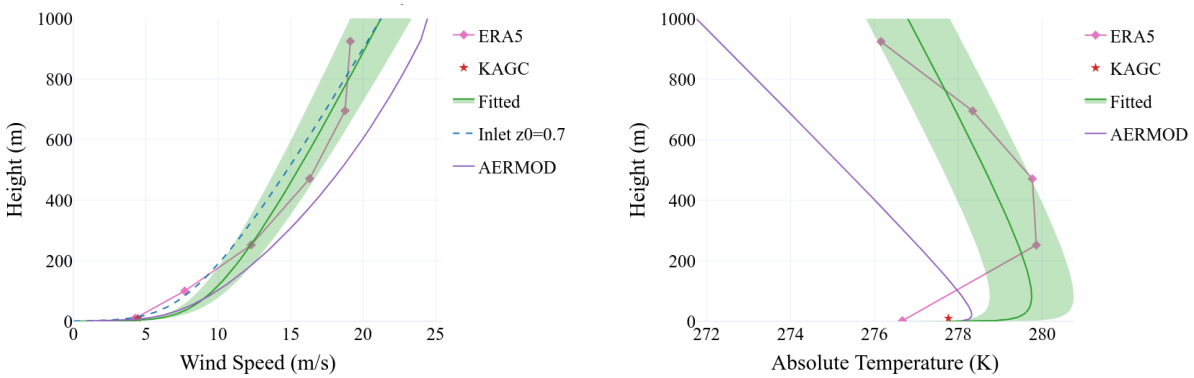

(a) Wind speed (b) Absolute temperature

Figure 5.23: Vertical profiles used in CFD and AERMOD for case 20.

Table 5.4: Summary of the differences between case 13 and case 20.

Case	Weather conditions				Total emission rate (g/s)	Measurement		Model predictions			
	Wind		Inversion			Liberty		CFD		AERMOD	
	Speed	Direction	Strength	Height		conc. (ppb)	ratio	conc. (ppb)	ratio	conc. (ppb)	ratio
13	Slow	207°	Strong	High	212	52	0.25	96	0.45	61	0.29
20	Fast	205°	Weak	Low	144	38	0.26	55	0.38	21	0.14

For case 20, the temperature profile from ERA5 and the fitted temperature profile for CFD show lower inversion height. Such weather conditions will make the predicted SO_2 concentration lower than that of case 13 if the emission scenarios are the same. An optimal dispersion condition is categorized with fast wind speed and strong turbulent mixing. The "ratio" in Table 5.4 is calculated as SO_2 concentration divided by the total emission rate. In this way, the SO_2 concentration is normalized by the total emission rate, and the ratio is only linked to the dispersion condition. Overall, if the inversion is weaker, the dispersion condition is preferable for low concentration, so the ratio is expected to be smaller. The ratios from Liberty show that case 13 and case 20 are equivalent in the overall effect of the weather condition on SO_2 concentration. However, this is not true, as suggested by the ERA5 data. For CFD and AERMOD, the ratios are smaller in case 20, which correctly reflect the change in weather condition. However, the ratio of AERMOD drops by half from case 13 to case 20, and the faster wind speed in case 20 cannot justify such a dramatic change.

5.3.4 Simulations using the transient model

Each steady-steady simulation provides the wind field and SO_2 concentration under the specified boundary conditions and emission sources for that period. Transient simulations are helpful to understand the spatial-temporal evolution of SO_2 over very short time periods. A combination of steady-state and transient simulations will help us investigate mechanisms driving non-attainment of SO_2 concentrations at existing monitors and understand acute exposure levels with temporal resolution as low as few seconds.

The Liberty site provides 1-minute mean wind direction data that are used to update the inlet wind direction for the transient simulation. Since the reanalysis data only has an hourly resolution, the vertical profile changes within 1 hour cannot be determined. At first, case 17 from

the 28 steady-state simulation cases has relatively steady wind speed during the 1-hour period, so it is chosen to determine the best strategy of updating inlet wind direction. Strategy 1 is to update the wind direction at the inlet uniformly across height. For example, the 1-hour mean Liberty wind direction at 08:00 is $204°$, which is used in the steady-state simulation to set a uniform wind direction across height. Then the steady-state result is used to initialize the transient simulation. At 08:00, when the 1-minute mean wind direction changes to $208°$, we can try to change the wind direction uniformly to $208°$. However, we know from the SODAR data that the change in wind direction along height is not uniform, as different height levels have different STDs of wind direction. Strategy 2 is to make the wind direction non-uniform based on the fitting function given in equation (4.7).

Two transient simulations are performed. Starting with a steady-state flow field, zero SO_2 in the domain, a constant emission rate of SO_2 is set once the transient simulation starts. At each minute, we only update the wind direction at the inlet and keep other boundary conditions unchanged. The results of strategies 1 and 2 are shown in Figure 5.24 and Figure 5.25. A diagonal line at 16 m AGL that starts at the southwest corner and ends at the northeast corner of the study domain is used as a sampling line. The wind direction at each minute is extracted along this line to show the variation of wind direction. Along the diagonal line, 60 minutes of predicted wind directions are shown as a box plot, in which the whisker shows the first and fourth quartiles and the solid part shows the second and third quartiles. The terrain surface below the diagonal line is shown as "Terrain". Overall, as the wind travels from the left (inlet) to the right (outlet), the upstream and downstream locations of the hills have huge variations in wind direction. In the lowest part of the domain near $3000\ m$, the wind direction change is close to $360°$.

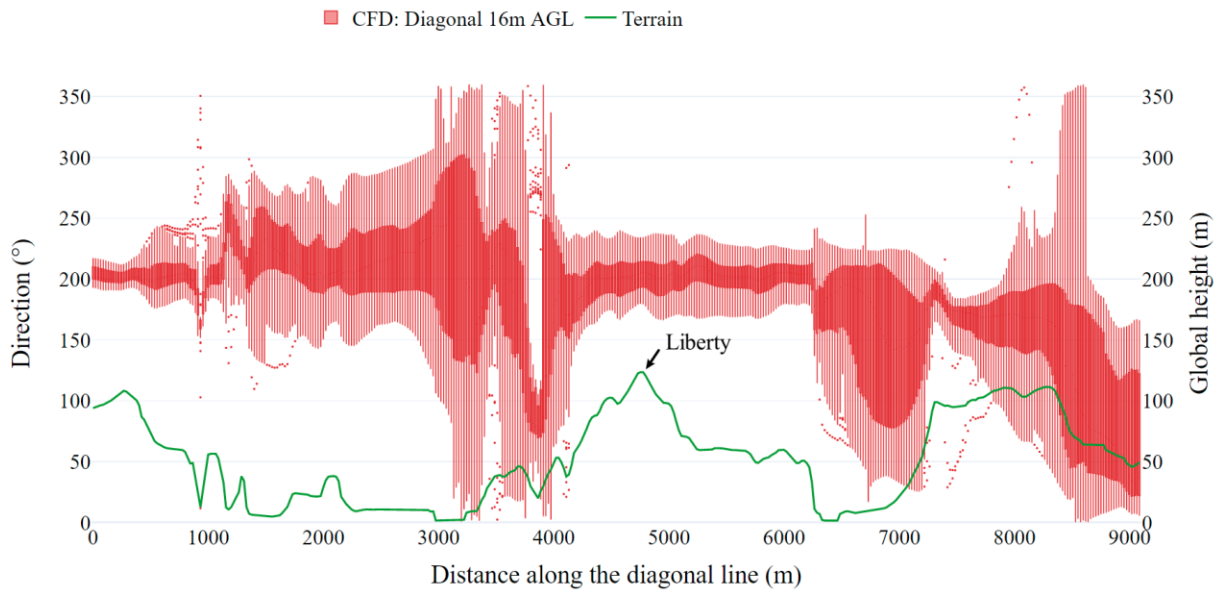

Figure 5.24: Predicted wind direction variation within 1 hour along the diagonal line when updating the inlet wind direction uniformly at every 1 minute (strategy 1).

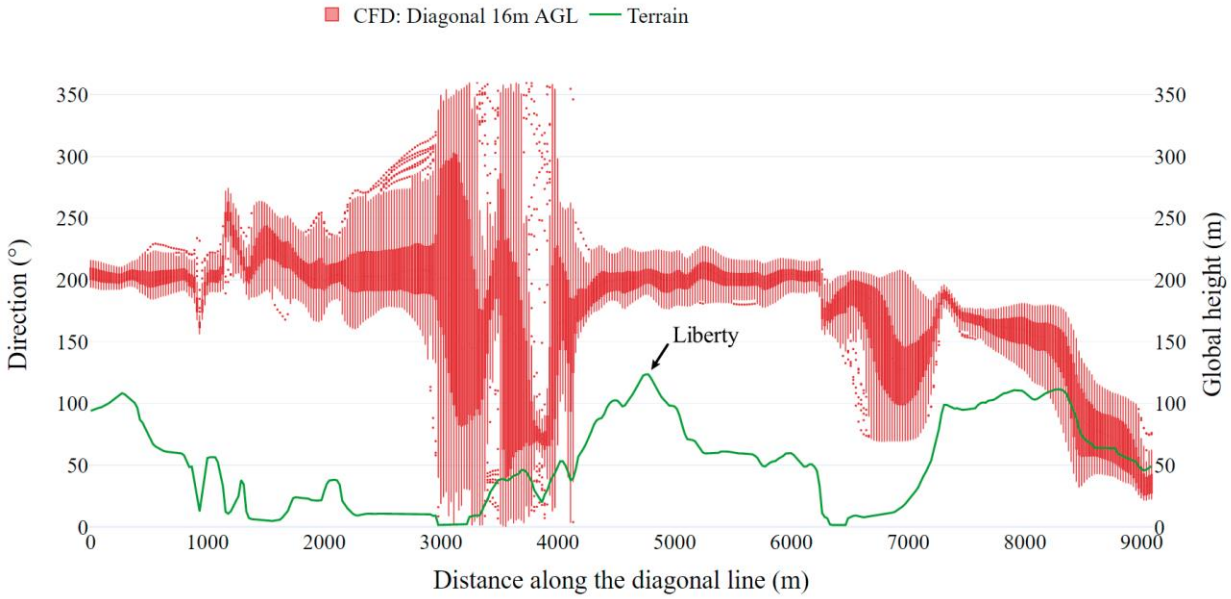

Figure 5.25: Predicted wind direction variation within 1 hour along the diagonal line for variable inlet wind direction along with height (strategy 2).

Updating inlet wind direction uniformly from strategy 1 will result in a larger variance in wind directions in the domain compared to that of strategy 2. The Liberty is located near the middle

peak of the terrain at about $4700\,m$ from the x-axis. Strategy 2 only shows a slightly larger variation in wind direction near this location compared to what is specified at the inlet.

The predicted 1-minute wind directions at the exact Liberty site are compared with those of measurements shown in Figure 5.26 and Figure 5.27. The dash line shows the mean directions of the hour. As for SO_2 concentration, only the last 40 minutes are used to calculate the mean values. This is because the SO_2 in the model is initialized to zero everywhere in the domain. As seen from Figure 5.26 and Figure 5.27, it takes about 20 minutes for the SO_2 plume to reach the Liberty site. The predicted wind direction with strategy 1 varies from 165° to 231°. Although the predicted wind direction change with time shares a similar trend to that of the measurements, the range is significantly amplified. For strategy 2, the range is 176° to 216°, which is closer to the measurements (from 193° to 217°).

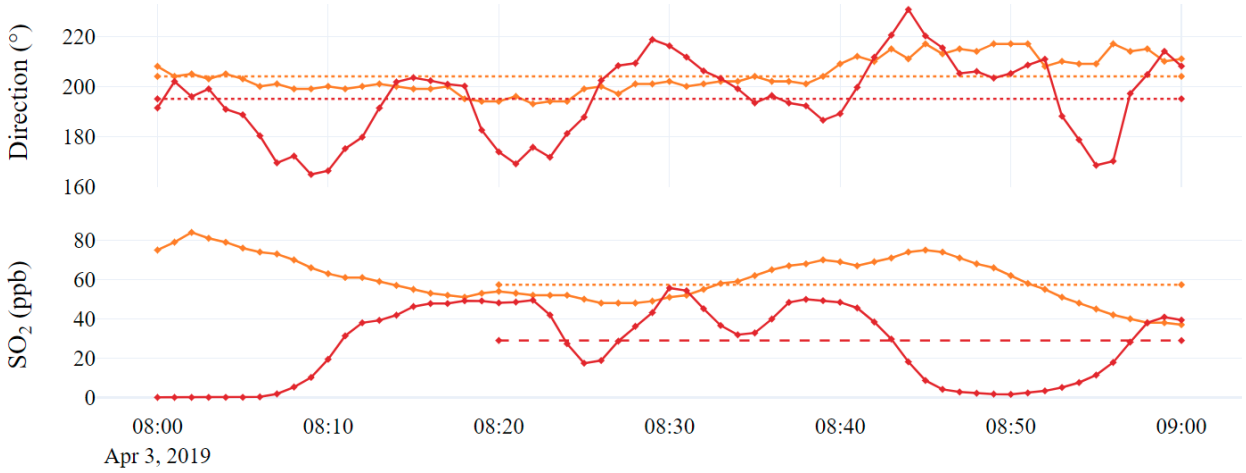

Figure 5.26: Comparison of time series in wind direction and SO_2 concentration between Liberty measurements and the results from transient simulation using strategy 1. For CFD, the extracted values at the Liberty monitor are used in the time series. The dash lines in wind direction show the 1-hour average values. The dash lines in SO_2 concentration show the 40-minute average values.

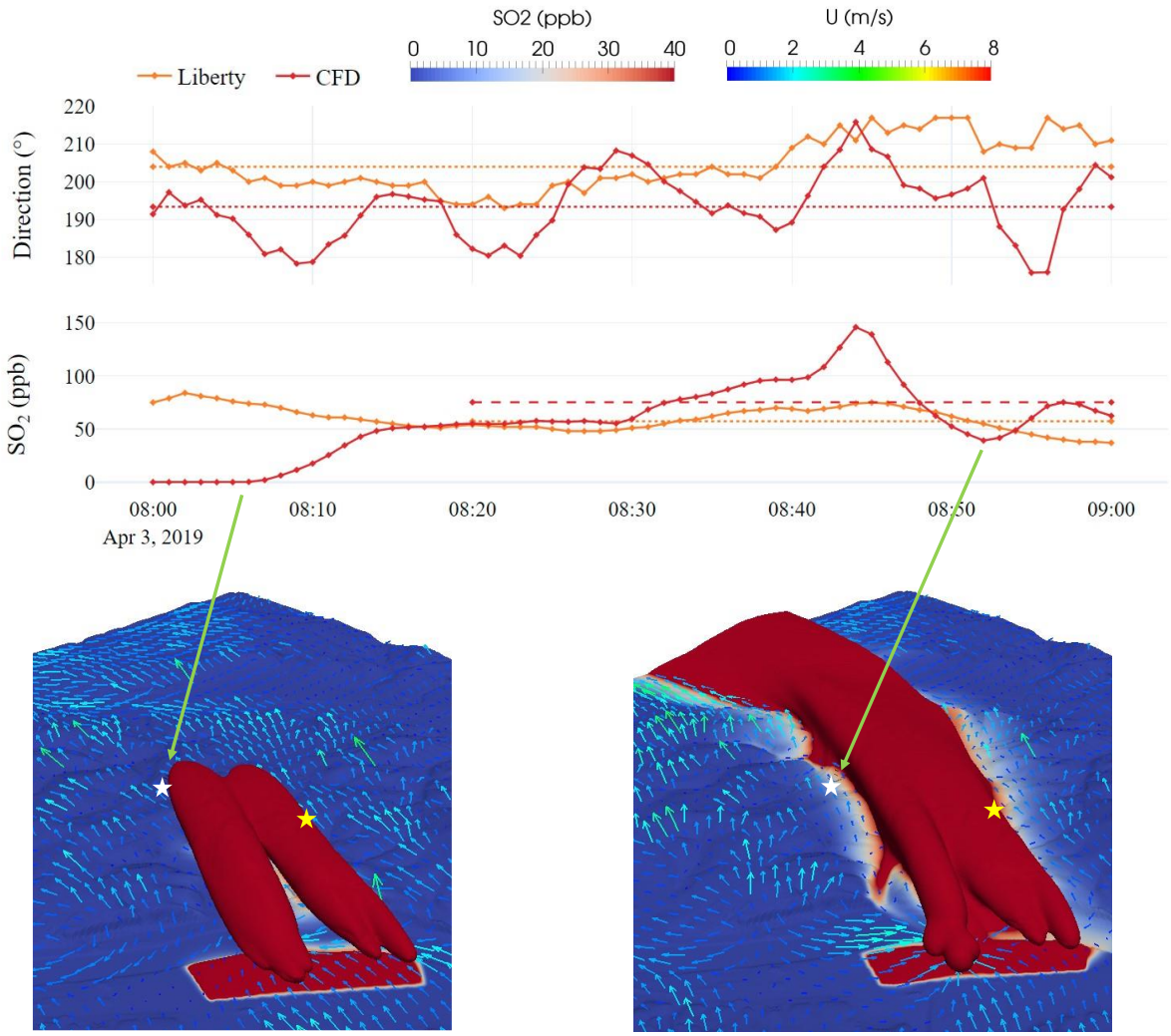

Figure 5.27: Comparison of time series in wind direction and SO_2 concentration during 08-09Z 04/03/ between Liberty measurements and the results from transient simulation. For CFD, the extracted values at the Liberty monitor are used in the time series. The dash lines in wind direction show the 1-hour average values. The dash lines in SO_2 concentration show the 40-minute average values. White star: Liberty site. Yellow star: Liberty Way site. Wind vectors on the ground levels are also shown.

Figure 5.27 shows the transient evolution of the SO_2 plume, which is created with isosurfaces at 40 ppb. At 08:05, the plume spreads to the Liberty site indicated by the white star. After that, the concentration at the Liberty continues to increase to a relatively constant value of 50 ppb and stays almost unchanged from 08:20 to 08:30. The concentration keeps accumulating

with the change in wind direction that moves the plume centerline closer to the Liberty site, so the maximum concentration is reached at 08:45. After that, the plume moves to the east of the Liberty site for a short time period at around 08:50. Then the plume moves back, and the SO_2 concentration increases again. Over time, the plume size keeps changing, and the maximum plume width is close to the distance from the Liberty site to the Liberty Way site. Such observation from CFD results aligns with the discussion of Figure 3.19 about the estimated plume width.

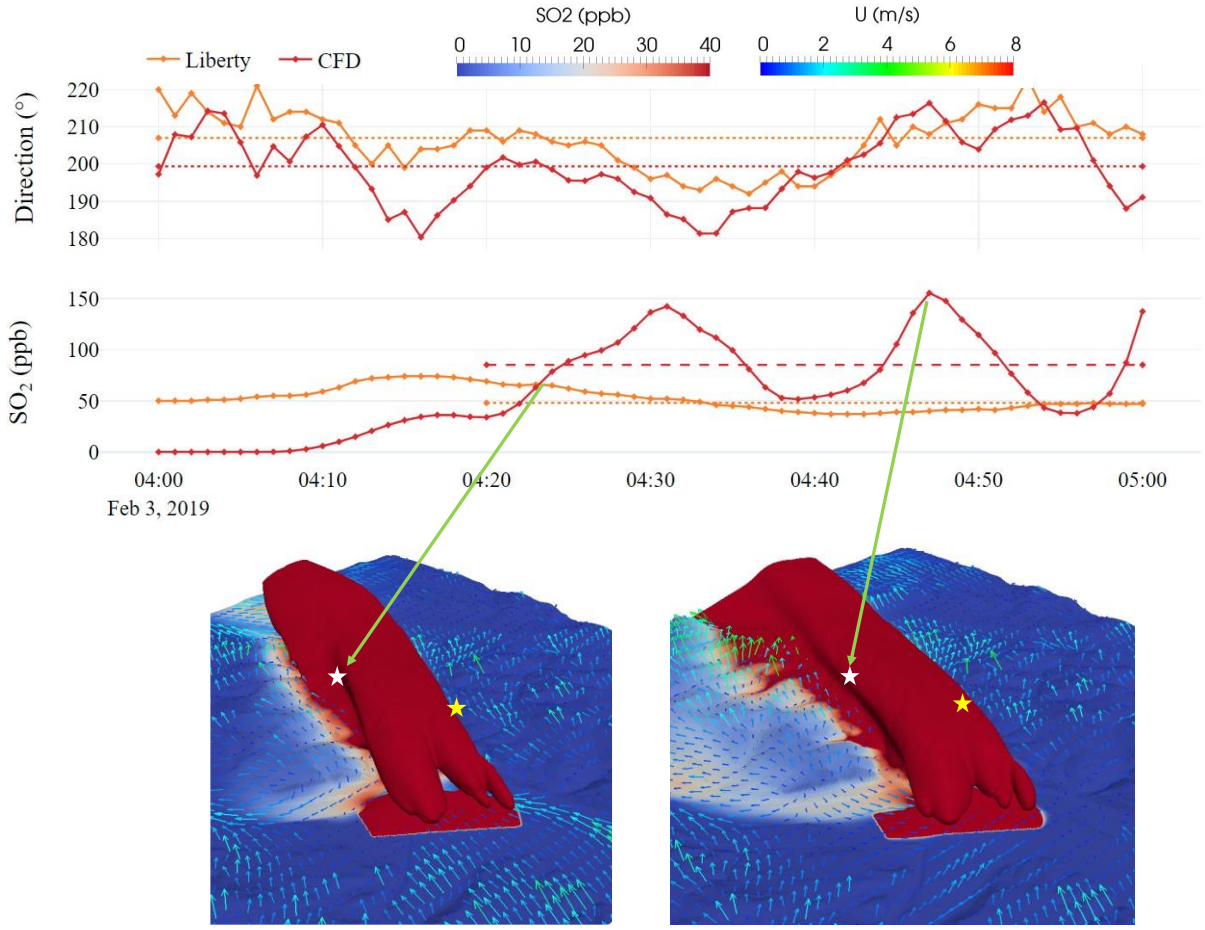

Figure 5.28: Comparison of time series in wind direction and SO_2 concentration during 04-05Z 02/03/2019 between Liberty measurements and the results from transient simulation. For CFD, the extracted values at the Liberty monitor are used in the time series. The dash lines in wind direction show the 1-hour average values. The dash lines in SO_2 concentration show the 40-minute average values. White star: Liberty site. Yellow star: Liberty Way site. Wind vectors on the ground levels are also shown.

Based on strategy 2, a second transient simulation is performed, and the time series are shown in Figure 5.28. The 40-minute average concentration at the Liberty site from CFD prediction has a much larger value than that of the measurements. Even at the highest concentration at around 04:47, the plume width is not very wide as it mostly lies between Liberty and Liberty Way. However, the variation range of predicted SO_2 concentration at the Liberty site cannot be fully understood.

There are a few reasons to explain the performance of the transient simulations:

1) The real-world emission of SO_2 is in batches with an interval of a few minutes. However, the current emission data only have a 1-hour resolution. Even the 1-hour data is derived from daily averages. Also, stacks can work on different schedules. When one stack is idle, the exit temperature should not be the same as when it is working.
2) The fit for the distribution of wind direction along height uses the SODAR data up to $200\ m$. However, it is applied across the full height ($1000\ m$) of the domain. In addition, the SODAR site is located within the plant area, the effects of the plant operation on the measured wind profile from the SODAR, in terms of heat flux and buoyant steams from the quench towers, are not clear. The fitted standard deviation in wind direction across the heigh may not be suitable at the inlet of the domain. We don't have too much confidence in this method, and there is barely any literature about varying wind direction along with the height.
3) The wind direction at the inlet is updated every 1 minute. Such updating strategy will introduce a sudden change of wind direction at the inlet. As a result, the horizontal components of the velocity vector will change, leading to accelerations in different directions. These accelerations may cause unphysical results due to the nonlinearity of the

momentum equations. Ideally, wind direction should be updated continuously.

4) The response time of the Liberty SO_2 monitor (model) is rated as “less than 120 seconds to 95% of range”. If there is a dramatic change of SO_2 concentration within the first minute then the same dramatic change within a second minute, the sensor will fail to capture these large variations. As a result, the time series of one-minute average concentration tends to be relatively smooth.

5.4 Recommendations for model deployment

The steady-state CFD model has been shown to have overall better performance than AERMOD when compared with measurements. In addition, CFD provides the whole concentration field over the entire computational domain. With the post-processing and visualization software ParaView [94], the predicted SO_2 plume can be viewed easily over the complex terrain. The SO_2 concentration contours from the 3D CFD model can be generated to quickly identify locations of high concentration, plume width, plume height. The contours can be further integrated with Google Earth to make it easier for other people besides the modeler, such as policymakers, to understand the results. Based on the comprehensive findings, the user of the CFD model can gain a better understanding of the over distribution and suggest mitigation strategies for different meteorological conditions and emission scenarios. The only obstacle to using the CFD model is that the computation time is longer than AERMOD. However, as modern computers are becoming more efficient, the issue of computation time can be addressed by properly planning simulation jobs and taking advantage of computer clusters.

Transient simulations need considerably more details as inputs compared to those of steady-state simulations. The operation activity of the plant should be considered in terms of when and where the emission takes place. The variation range of predicted SO_2 concentration at the Liberty

site gets very large toward the end of the simulated hour, which has not been fully understood. The transient simulation takes a much longer time and requires more computational resources. Table 5.5 summarizes the computational resources need for steady-state and transient simulations.

Table 5.5: Computational resources needed for steady-state and transient simulations.

Simulation type	CPU model	Cores used	Computation time	Disk storage
CFD: stead- state one hour	AMD EPYC 7742	32	3 hours	2 GB
	Intel Xeon W-2155	18	12 hours	
CFD: transient one hour	AMD EPYC 7742	32	2 days and 6 hours	75 GB
	Intel Xeon W-2155	18	9 days	
AERMOD: steady-state all hours in one year	Intel Xeon W-2155	1	< 1 hour	<1 GB

Using the Bridges2 cluster from PSC with the AMD EPYC 7742 CPU, and running the most cost-effective number of cores (32), the computation time is about 3 hours for a steady-state simulation and about 2 days and 2 hours for the 1-hour transient simulation. For comparison, on a regular server with the Intel Xeon W-2155 CPU, the computation time will be about 4 times that of the Bridges2 cluster. For a 1-hour transient simulation, it will take about 9 days to finish. Comparing to CFD, AERMOD is very efficient in computation time and only uses a small amount of disk storage. However, it should be noted that the time needed to collect inputs, especially the wind data from different sources, for AERMOD can be substantial. On the contrary, the CFD model is automated to obtain boundary conditions, which makes the setup process more straightforward.

In summary, we recommend using the steady-state CFD model in conjunction with AERMOD for investigations of SO_2 dispersion within the domain. The transient CFD model needs to be fully understood and validated before it can be used for comparison with measurements. But we think that the transient model has the potential for better performance.

Chapter 6

Exploratory studies using the CFD model

6.1 Effects of the terrain complexity

The complex terrain consists of two major parts: irregular topography and variations in land use. The results of different variables based on neutral case 1 previously presented in Figure 5.3 are used to describe the effects qualitatively. The effects of the terrain complexity on SO_2 dispersion will be discussed in the next section.

6.1.1 Irregular topography

The effects of the irregular topography on flow patterns are studied in terms of wind speed and wind direction. Figure 6.1 shows contours of the height above the ground and the wind speed vectors colored by the magnitude of the vertical wind speed.

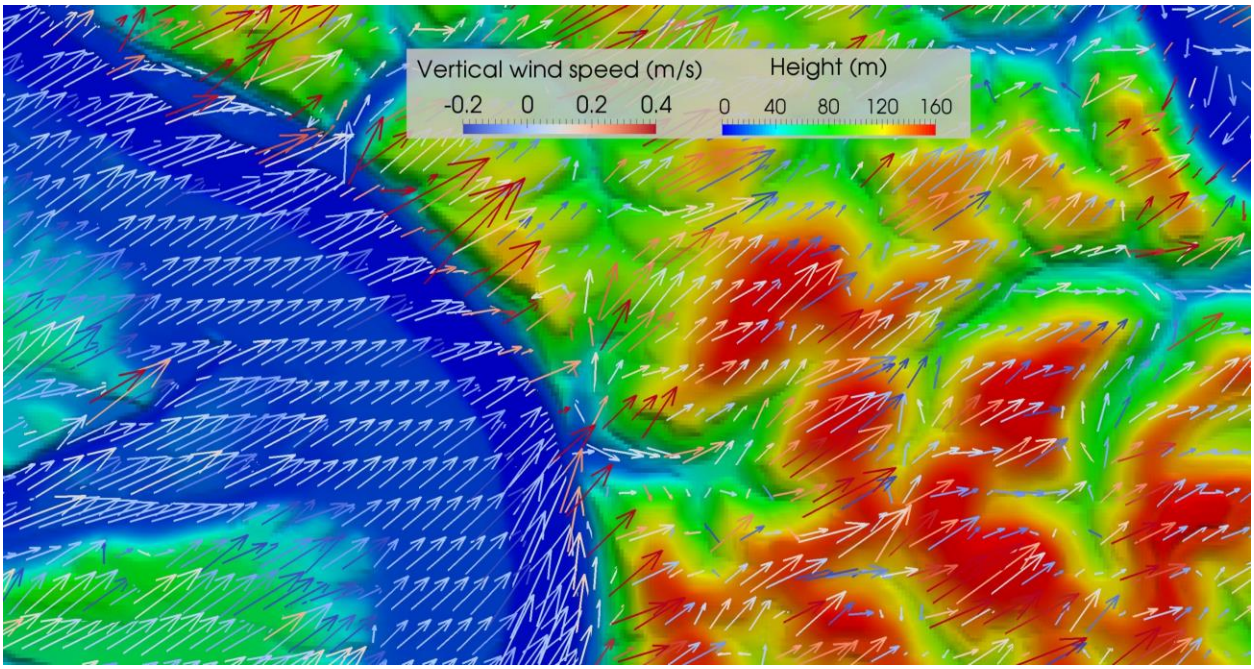

Figure 6.1: Contours of height above the ground and wind vectors colored by the magnitude of the vertical wind speed.

On the southwest side of the Monongahela River, where the terrain is relatively flat, the

vertical wind speed is near zero, and wind direction is close to uniform. The wind vectors show that wind will either climb over the hills or enter the channels of the valleys when traveling from southwest to northeast. Once entering the channels, the wind tends to move along the channels until it meets the next hill. Figure 6.2 shows contours of horizontal wind speed and wind direction extracted at $10\ m$ AGL, at which level wind speed and wind direction are strongly influenced by the terrain.

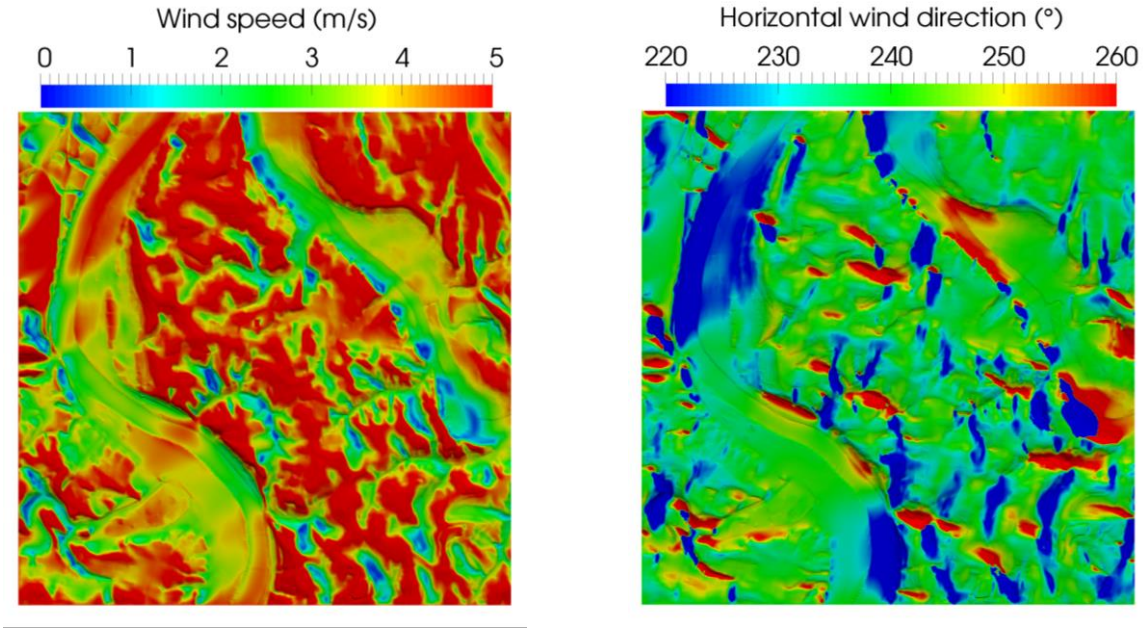

(a) Contours of wind speed (b) Contours of horizontal wind direction

Figure 6.2: Contours of horizontal wind speed and wind direction at $10\ m$ AGL.

High wind speed regions can be found on the windward-facing slopes of the hills, while low wind speed regions are found in valleys on the leeward side. The dominant wind direction is the same as the wind direction set at the inlet of the domain. The regions where the wind directions differ the most from the dominant wind direction agree with the regions where a sudden change in height is present. As shown in Figure 6.3, at $200\ m$ AGL, wind speed and wind direction become more uniform, and the effects of the topography are less significant. Without the irregular topography, the wind speed contours will be uniform at different height levels AGL, emphasizing

the importance of the inclusion of the real-world topography in the simulations of wind development.

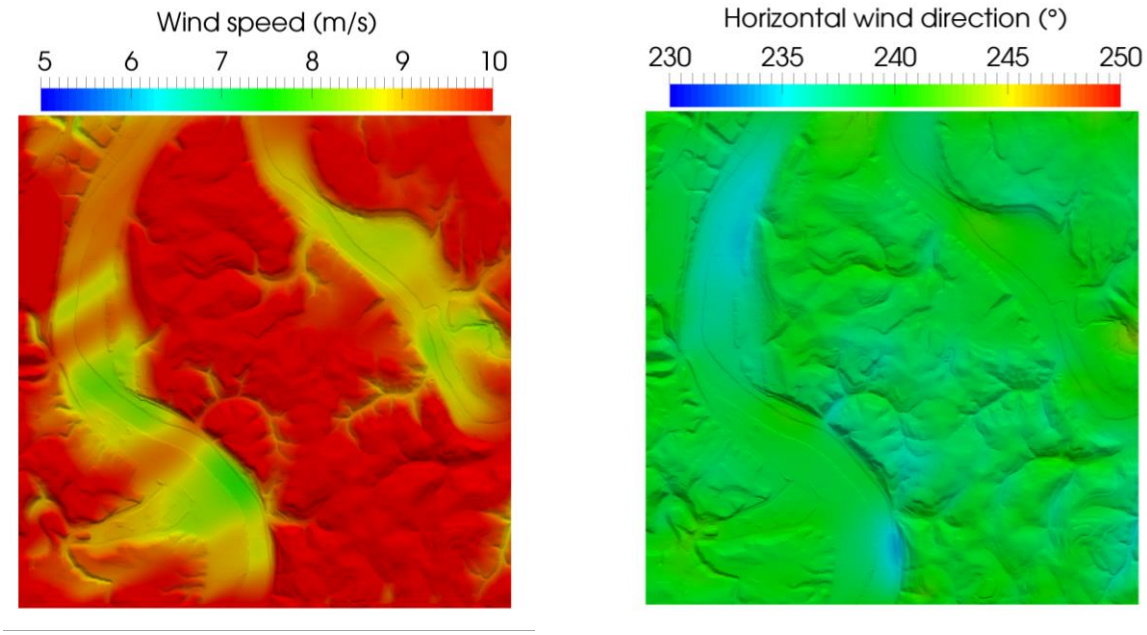

(a) Contours of wind speed (b) Contours of horizontal wind direction

Figure 6.3: Contours of horizontal wind speed and wind direction at $200\ m$ AGL.

6.1.2 Variations in land use

The current model implements variable surface roughness (z_0) in the entire computational domain to account for the effects of variations in land use. In order to compare the impact of variable z_0 on wind development and turbulence generation, we have also performed one simulation with uniform z_0. The value of a uniform z_0 is taken to be the mean value of the variable z_0, which is around $0.7\ m$. Since z_0 is a parameter specified in the wall model, the differences between the results of the variable z_0 and that of the uniform z_0 are expected to be most significant near the ground. Figure 6.4 shows contours of horizontal wind speed, and Figure 6.5 shows contours of turbulent diffusivity in the first layer of cells AGL for variable and uniform z_0.

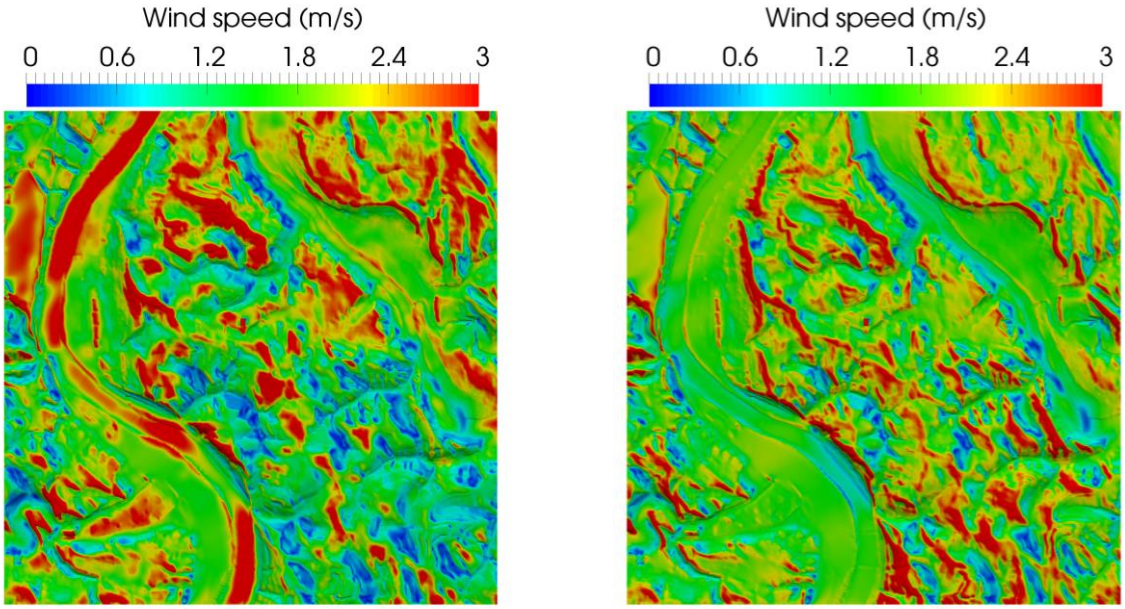

(a) Variable z_0 (b) Uniform z_0

Figure 6.4: Contours of horizontal wind speed (m/s) in the first cells AGL using variable and uniform z_0.

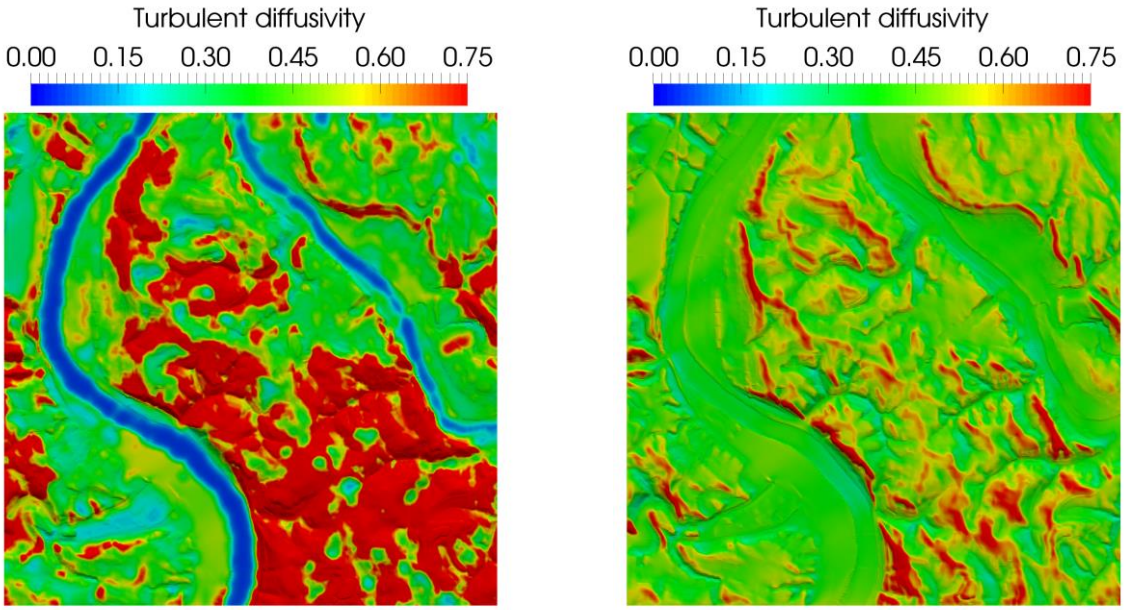

(a) Variable z_0 (b) Uniform z_0

Figure 6.5: Contours of turbulent diffusivity (m^2/s) in the first cells AGL using variable and uniform z_0.

The impact of variable surface roughness is smaller for wind speed and larger for turbulent diffusivity. However, these differences are exaggerated only near the ground, As seen from vertical profiles of horizontal wind speed, turbulent kinetic energy (TKE) and its dissipation (ε), and the turbulent diffusivity in Figure 6.6 and Figure 6.7, variable and uniform z_0 yield very similar wind and turbulence fields. Therefore, it is appropriate to specify a reasonable value of uniform z_0 representing the local land-use patterns.

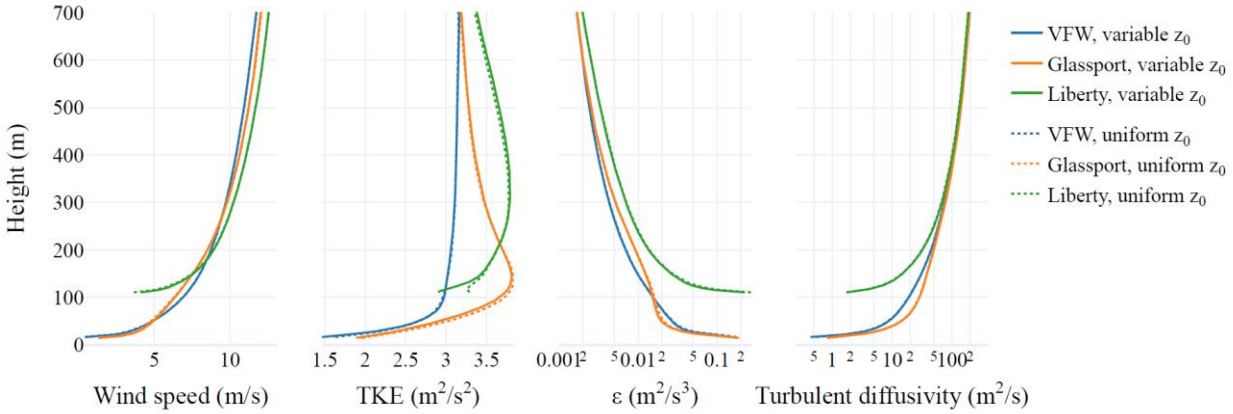

Figure 6.6: Vertical profiles up to 700 m AGL for different variables at different locations using variable and uniform z_0.

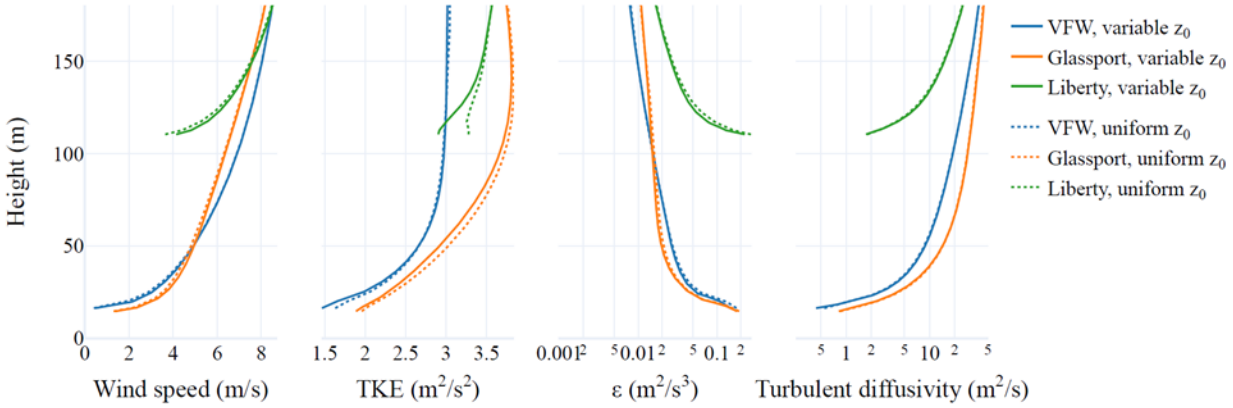

Figure 6.7: Vertical profiles to 170 m AGL for different variables at different locations using variable and uniform z_0.

6.2 Effects of atmospheric stability

The impact of stability class on SO_2 concentrations was discussed in the previous section. It is well known that a stable atmosphere leads to higher pollutant concentrations due to a lack of vertical mixing. However, the concentrations reported in the previous section are a combined result of the wind speed effects and the stability effects. Using the same wind profiles, TKE, and its dissipation rate at the inlet, two simulations are performed under the neutral condition and stable condition over the complex terrain to rule out the effects of other factors besides the atmosphere stability. In addition, the third simulation is performed under stable conditions over flat terrain by ignoring the complexity of the ground surface. Figure 6.8 shows vertical profiles of different variables at different monitoring sites under stable and neutral conditions over the complex terrain. Since the monitors are mounted at different elevations, the heights at which the variables first become available are different.

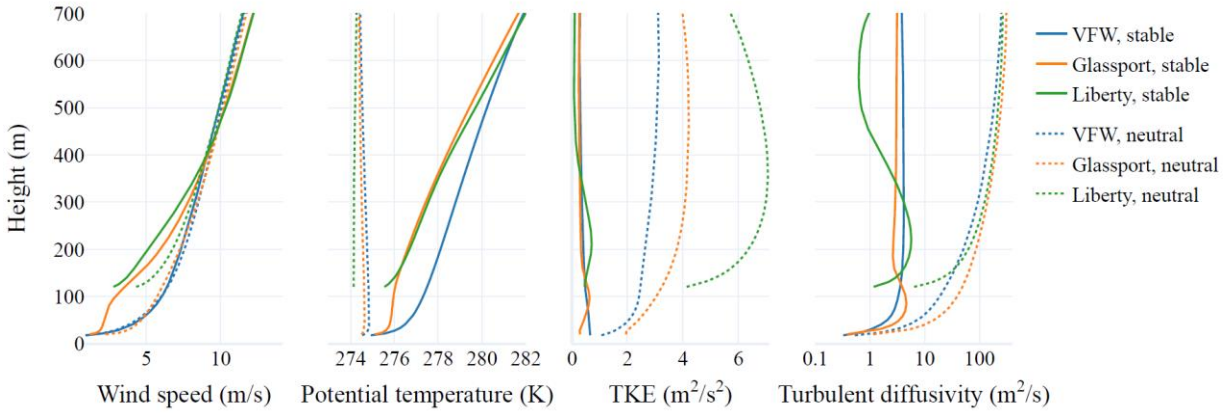

Figure 6.8: Vertical profiles to 700 m AGL for different variables at different locations under stable and neutral conditions.

As previously shown in Table 3.2, the roughness length is different at these sites. Therefore, the combined effects of elevation and roughness length lead to differences in wind speed near the ground. The Liberty site has the highest wind speed due to its high elevation and small z_0. The

VFW site and Glassport site have lower elevations and heights AGL, resulting in lower wind speeds. The vertical wind speeds follow a typical logarithmic profile, especially for the neutral condition. At about 400 m AGL, the difference between different sites becomes very small. The potential temperature profiles show the thermal stability conditions. For TKE and turbulent diffusivity, different locations show lower values consistently under the stable condition than those of the neutral condition.

Under stable conditions, the production of TKE due to buoyancy is negative, resulting in lower levels of turbulence. Figure 6.9 shows the TKE contours over the terrain surface and on a vertical plane across the domain. The TKE is reduced by half under the stable condition when compared to that of the neutral condition. By comparing Figure 6.9 (b) and Figure 6.9 (c), it can be seen that the presence of hills generates wind shear that contributes to the generation of TKE. With the increase in height above the ground, the TKE quickly drops to a low level, maintained uniformly on the vertical plane in the three cases.

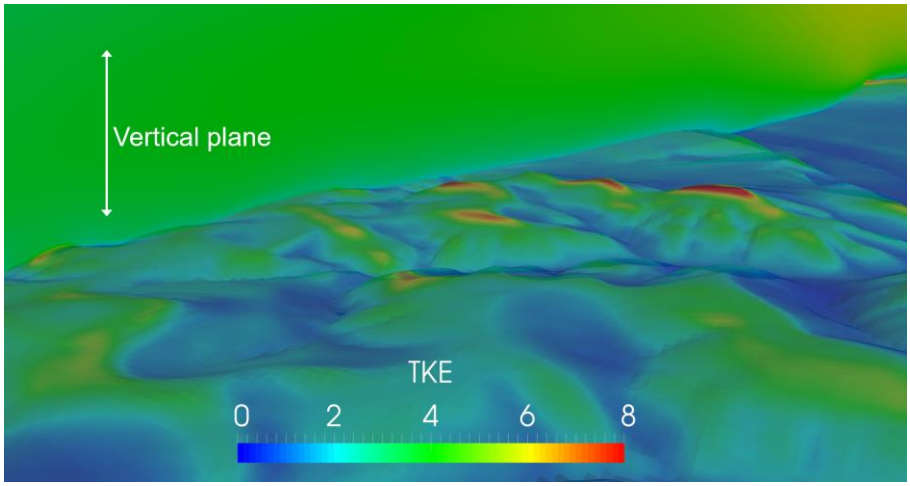

(a) Complex terrain under the neutral condition.

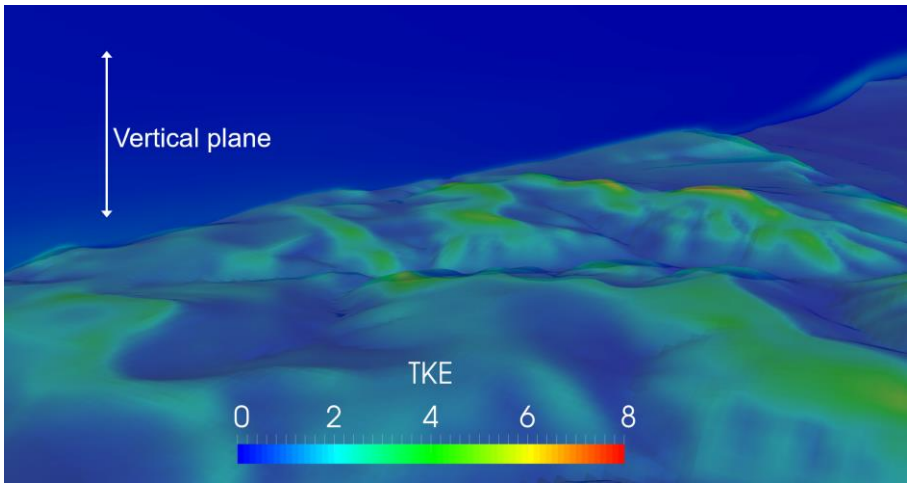

(b) Complex terrain under the stable condition.

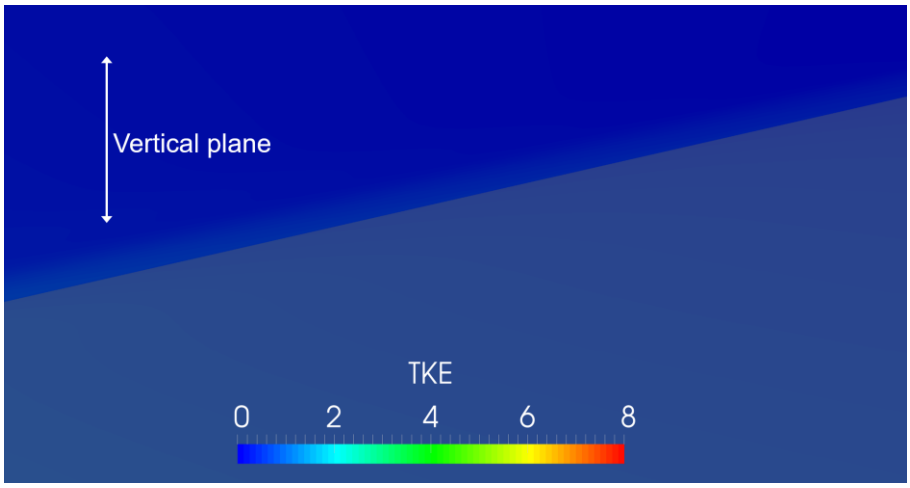

(c) Flat terrain under the stable condition.

Figure 6.9: Contours of TKE (m^2/s^2) under different thermal stability classes and terrain types.

Figure 6.10 shows the difference in SO_2 concentration under the stable and neural temperature profiles. The contours of SO_2 concentration are shown on a vertical slice passing through one of the stacks. An isosurface of SO_2 at 40 ppb is also shown for both cases. For the neutral condition, SO_2 concentration quickly drops below 40 ppb after releasing from the plant, as indicated by a smaller length of the isosurface. For the stable case, the isosurface is much longer and continues until the exit of the domain. The contour colormap on the vertical slides shows that there is a higher vertical dispersion of SO_2 for the neutral case compared to the stable case, which

is an expected outcome. The width of the two plumes over complex terrain and flat terrain under the stable condition is similar. However, the plume centerline stays at around the same height as the stack exit, and the plume covers much less area of the ground over the flat terrain.

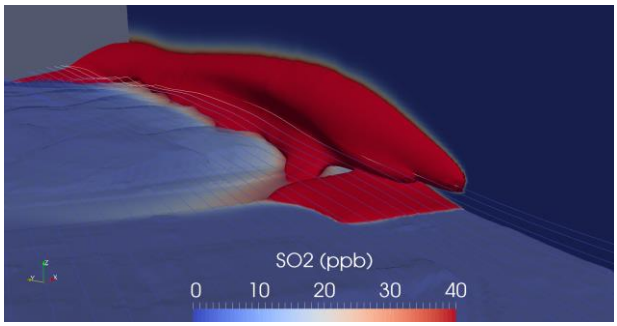

(a) Stable condition, complex terrain

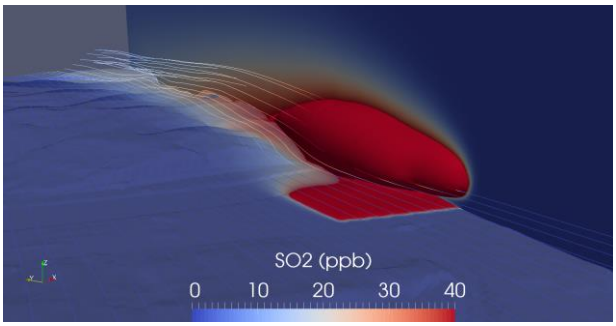

(b) Neutral condition, complex terrain

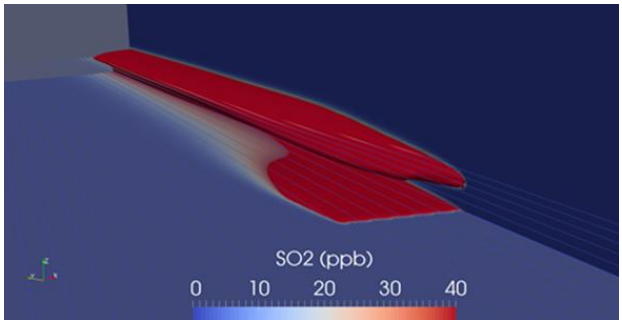

(c) Stable condition, flat terrain

Figure 6.10: SO_2 concentration contour and streamtraces under different thermal stability conditions over different terrain types.

Figure 6.11 shows the turbulent diffusivity contours under the two conditions. The hot plume emitted from the stacks generates a much higher level of turbulent diffusivity than that of the background. Due to inversion, the high level of turbulent diffusivity is quickly destroyed due to the suppression of negative buoyancy. The overall low level of turbulent diffusivity leads to higher SO_2 concentration under the stable condition. On the contrary, the buoyancy effect on generating turbulence is not suppressed under the neutral condition, so the high level of turbulent diffusivity can travel further downstream, which results in lower SO_2 concentration.

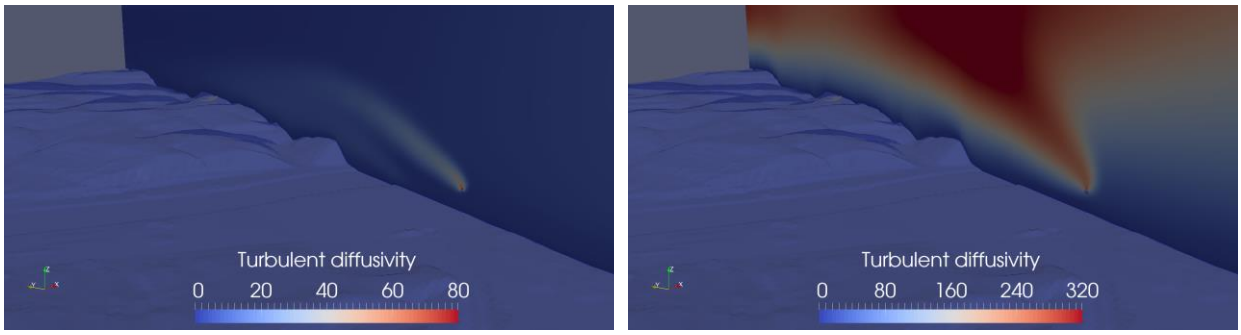

(a) Stable condition (b) Neutral condition

Figure 6.11: Turbulent diffusivity (m^2/s) contour under different thermal stability conditions.

To give a quantitative view of the effects of atmospheric stability, 4 cases under inversions of different strength are selected from the 28 cases. The fitted wind speed and potential profiles for the 4 cases are shown in Figure 6.12. To better compare the strength of the inversion, the ground temperatures for the four cases are reduced to 273.15 K. In the actual simulations, each case uses its ground temperature from KAGC. The inversion strength increases from case 1 to 4.

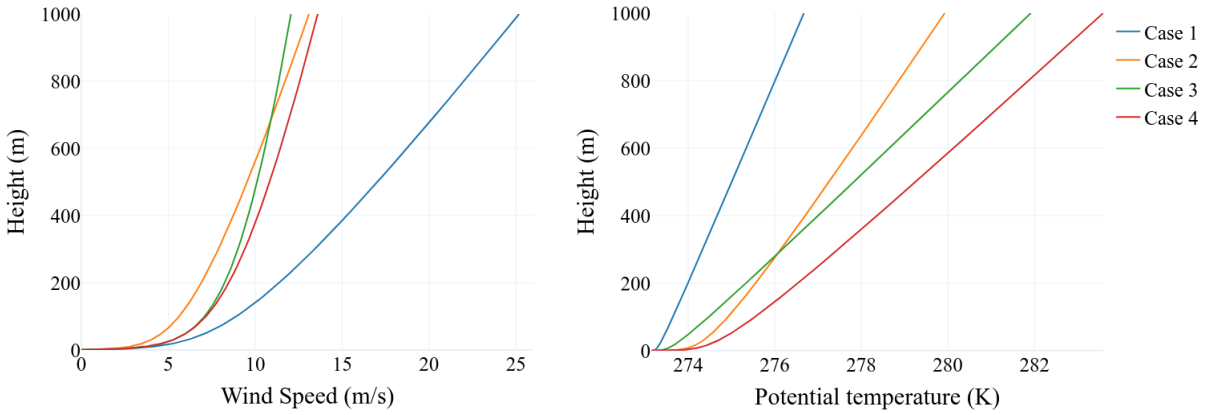

(a) Wind speed profiles (a) Potential temperature profiles

Figure 6.12: Fitted vertical profiles that are specified at the inlet for the four cases of different wind conditions and inversion strengths.

The contours of SO_2 concentration for the 4 cases are shown in Figure 6.13 and Figure 6.14. The detailed results are summarized in Figure 6.15 and Table 6.1. Since the emission rates for the 4 cases are not the same, SO_2 concentrations are normalized as shown in Figure 6.16.

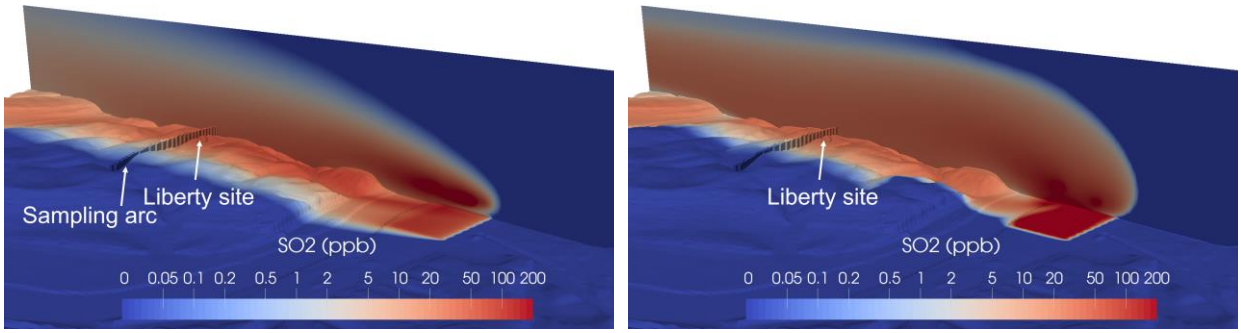

(a) Case 1

(b) Case 2

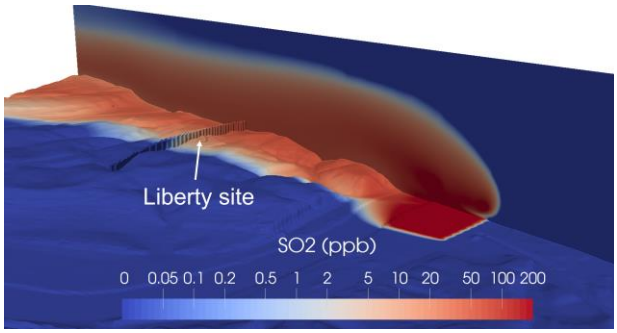

(c) Case 3

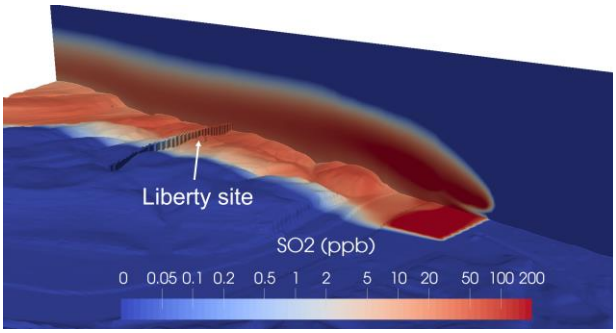

(d) Case 4

Figure 6.13: Contours of SO_2 concentration (in log scale) on the ground and on the slice that passes through the plant center and aligns with the inlet wind direction.

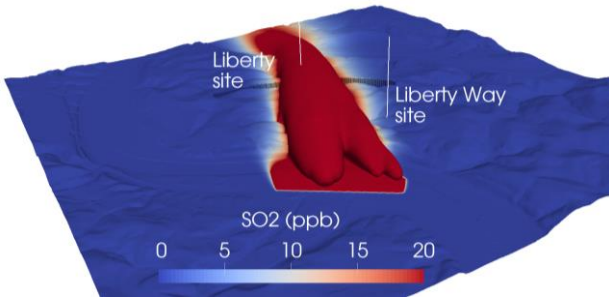

(a) Case 1

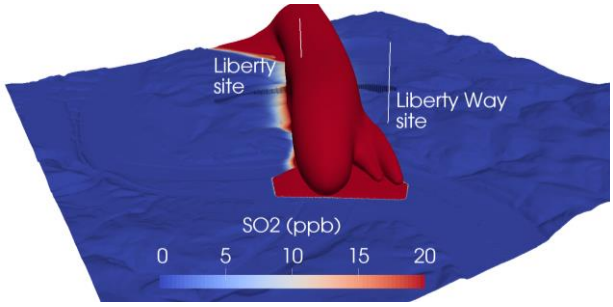

(b) Case 2

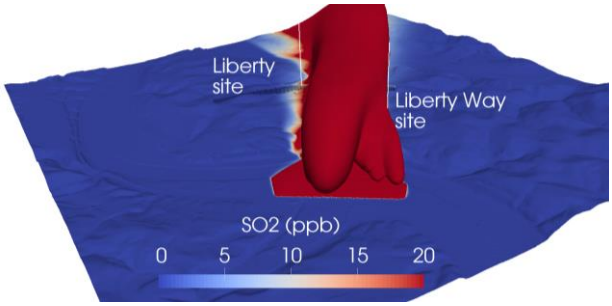

(c) Case 3

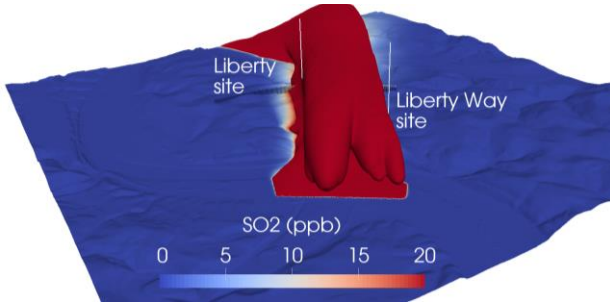

(d) Case 4

Figure 6.14: Contours of SO_2 concentration (in linear scale) on the ground the plume created with isosurfaces of 20 ppb. Two vertical lines up to 1000 m are shown at the monitoring sites.

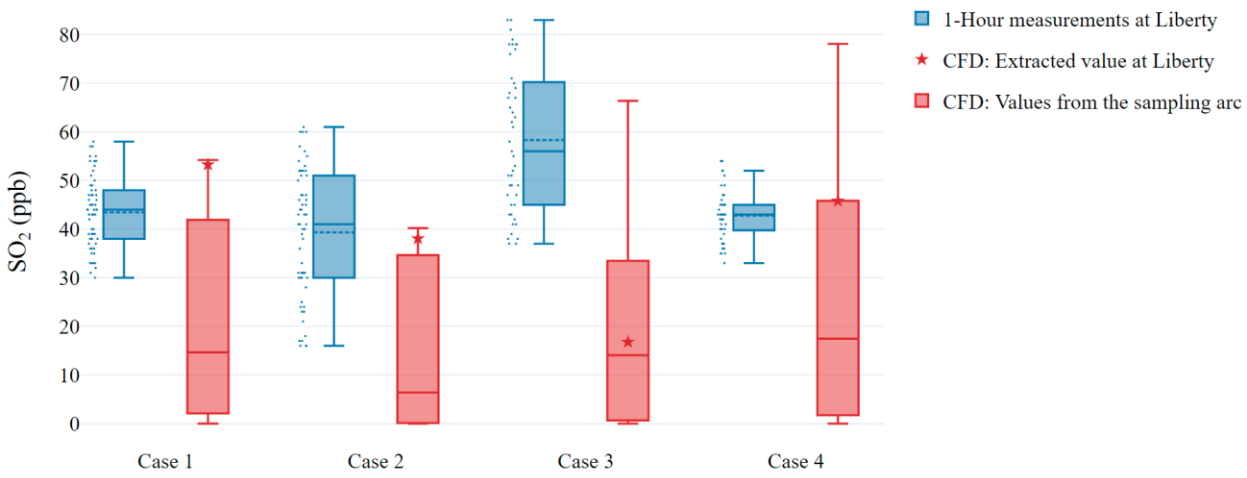

Figure 6.15: Box plots of the measurements and the CFD predictions for the 4 cases. The dash line in the box of Liberty measurements shows the mean value.

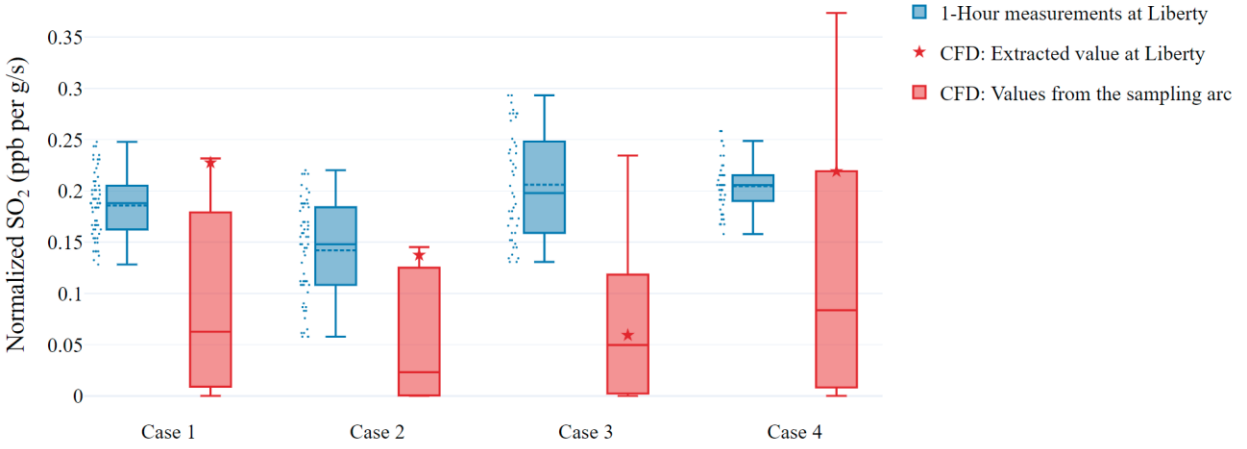

Figure 6.16: Box plots of the measurements and the CFD predictions normalized by emission rates for the 4 cases.

Table 6.1: Summary of the four cases of different wind conditions and inversion strengths.

Case	Wind direction (°)	Emission rate (g/s)	Monitor: 1-hour average data (ppb)	CFD: extracted value at monitor (ppb)	Monitor: max 1-minute average data (ppb)	CFD: max value on arc (ppb)
1	209	234	43	53	58	54
2	208	277	39	38	61	40
3	218	283	58	17		66
4	214	209	43	46		78

Case 1 has a much faster wind speed than other cases, making the plume near the plant stay low to the ground, as shown in Figure 6.14 (a). The wind carries SO_2 directly from the plant to the Liberty site, and the plume centerline passes through the Liberty site. Thus, the CFD prediction extracted at the exact Liberty site is close to the maximum value on the sampling arc, as shown in Figure 6.15.

Case 2 has stronger inversion strength but much lower wind speed, which makes the dispersion condition worse. Worse dispersion condition is usually associated with high concentration. However, the SO_2 concentrations at the Liberty reported by the sensor and from CFD show smaller values compared to those of case 1. This means the wind speed plays an essential role in SO_2 concentration at the Liberty site. Overall, high concentrations are found over a larger volume of the computational domain than in case 1, especially in the vertical direction.

Case 3 has ever strong inversion strength compared to that of case 2. However, the extracted concentration at Liberty from the CFD prediction is much lower than the measured one. This is due to a shift in wind direction. As the wind is more from the west, it makes the plume shift to the east of the Liberty site, as shown in Figure 6.14 (c). The maximum value on the sampling arc is closer to the 1-hour mean SO_2 concentration from measurements. The increase in inversion strength makes the overall SO_2 concentration higher near the plant and makes the plume height lower. Figure 6.15 shows that the measured SO_2 has a very wide range, which suggests very unsteady weather conditions or emission scenarios. As wind direction set at the inlet is of extreme importance in the prediction extracted at the Liberty site, using the sampling arc can provide a range of SO_2 to compare with measurements.

Case 4 shows the highest concentration on the sampling arc as the inversion strength is the strongest. The sampling arc shows a much wider range of SO_2 concentrations than that of the

measurements, but the extracted value at Liberty agrees very well with the hourly mean value from measurements. It is possible that the wind direction is rather steady, and the plume centerline misses the Liberty site, but high concentrations still exist in neighboring locations as picked up by the sampling arc. This case suggests that it is possible that exceedance is missed by the single Liberty monitor. The two vertical lines at the monitoring sites shown in Figure 6.14 (d) indicate that the plume width is about the distance between the Liberty site and the Liberty Way site under such strong inversion.

6.3 Importance of ground cooling

Under calm wind conditions and over mountains and valleys, nocturnal cooling of the ground causes the air close to the ground to rapidly become cooler than the air above. As the cooling effects continue over time, the air near mountain tops becomes cooler and denser than the air at the same elevation over the valley. This makes the air on the mountains sink to the bottom of the valley. As a result, the vertical wind speed becomes negative near the ground; thus, the mountain breeze (also referred to as downdraft, katabatic wind, or drainage flow) is formed, as shown in Figure 6.17 (a). When the sun comes out, the air near the mountain tops warms quicker than the air at the same elevation over the valley. The uneven heating creates upward flow as shown in Figure 6.17 (b); thus the valley breeze is formed.

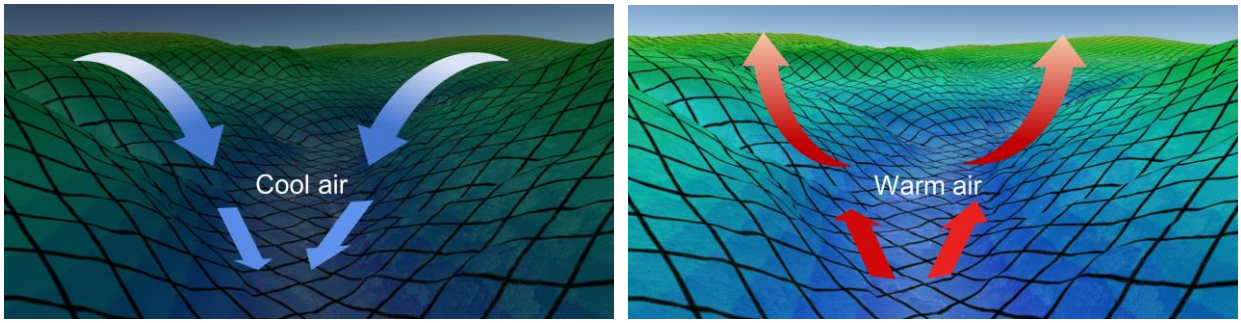

(a) Mountain breeze at night (b) Valley breeze during the day

Figure 6.17: Schematic of the mountain-valley breezes that are formed at different times of the day due to uneven heating of air.

Many studies showed that mesoscale circulations like sea-land breezes and mountain-valley breezes play important roles in pollution dispersion over complex terrain. Monteiro et al. used a mesoscale model to investigate a high ozone episode at a mountainous site near the Mediterranean region, and found that mountain breeze and sea breeze circulations are the driving forces for the ozone peaks [95]. Guo et al. used a WRF model and nested grids (whose size ranges from $36\ km$ to $0.444\ km$) to study the effects of mountain-valley breezes on the transport of photochemical pollution in Hong Kong [96]. However, mountain–valley breezes are small-scale weather phenomena, and a finer scale is needed to study their effects on near-source pollution dispersion. Yi et al. used measurements and a steady-state CFD model to study nocturnal drainage flows over a subalpine forest, and concluded that drainage flows are restricted to a relatively shallow layer of air beneath the canopy ($16\ m$), with little vertical mixing across a relatively long horizontal fetch [97]. Pypker et al. used SODAR measurements during typical summer evenings to investigate the structure of the air flow up to about $100\ m$ over a forest region. Two distinct drainage jets were found $10-20\ m$ above the canopy top (with a height of $30\ m$), and $10\ m$ below the canopy top. In this study, the spatial scale is local scale (with a grid size of $16\ m$), and the circulations of breezes and local distortion of the airflow due to uneven heating can be complicated. Combined with surface structures, such as forest canopy, the transient simulation of such phenomena will be a challenging task.

To simplify the problem for the pollution dispersion under calm wind conditions with ground cooling, we will first focus on the condition when a hypothetical 2D flat terrain is cooling at a constant rate. As the stack exits are around $80\ m$ AGL, and considering the effects drainage flow is likely to be limited to the ground level, using the hypothetical 2D flat terrain is a good start point. Two transient simulation cases are presented: the neutral case is with constant temperature

and stable case is with constant ground cooling rate. As shown in Figure 6.18, a 6.4 km $\times$ 1 km flat terrain is created, and a uniform horizontal wind speed of 0.0005 m/s is set at the inlet. The flow is initialized with uniform velocity same at the inlet. The potential temperature of the air at the inlet and for the initial condition is set to 300 K. Turbulent kinetic energy of 1 m^2/s^2 and its dissipation rate of 0.1 m^2/s^3, which are common values in the ABL, are set at the inlet and as the initial condition of the flow. A single stack with a heigh of 80 m AGL is located at 2000 m downstream. The stack emits SO_2 at a fixed rate at a temperature of 300 K. The following two cases are simulated for 8 hours:

- Neutral case: constant potential temperature (300 K) on the ground surface,
- Stable case: constant cooling rate (1 K/hour) on the ground surface.

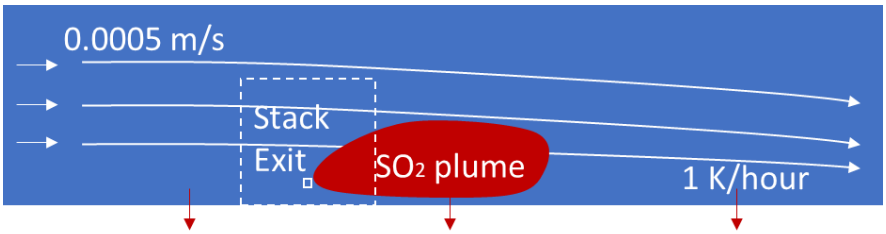

Figure 6.18: Schematic of the 2D simulation of downdraft flow under calm wind speed and a constant ground cool rate.

Zoomed-in views (the box in the dash line shown in Figure 6.18) near the stack exit of contours for SO_2 mass fraction and turbulent viscosity for the two cases are shown in Figure 6.19 and Figure 6.20. The contour scale in Figure 6.19 is set to log to better show the distribution of SO_2 within the plume. During the first two hours, SO_2 dispersion to the atmosphere is dominated by pure diffusion under the low wind speed condition, and the SO_2 plume is close to a semicircle above the stack height for both the neutral case and the stable case. Near the surface, the turbulent diffusivity is lower in the stable case, SO_2 does not diffuse to the ground. As turbulent mixing is low under the low wind speed condition, the ground cooling only makes the temperature near the

surface drops with time, so its effects are restricted to a relatively shallow layer of air near the ground, similar to the findings from Yi et al. [97]. Even after 8 hours of cooling, the temperature above 10 m is still the same as the initial temperature of 300 K. Besides, the negative velocity is also very low under the stable case. As time goes by, the asymmetric flow field keeps developing due to the presence of the stack exit. The stable plume has a much higher concentration near the stack exit and covers a larger area than that of the neutral plume, which agrees with the effects of atmosphere stability discussed in the previous section.

In summary, we find that the ground cooling under extreme low wind conditions is not an important phenomenon for the SO_2 emitted at the stack height. However, more transient simulations with different inlet speeds and ground heat fluxes are needed to better understand the effects of uneven heating on SO_2 dispersion over the 3D complex terrain.

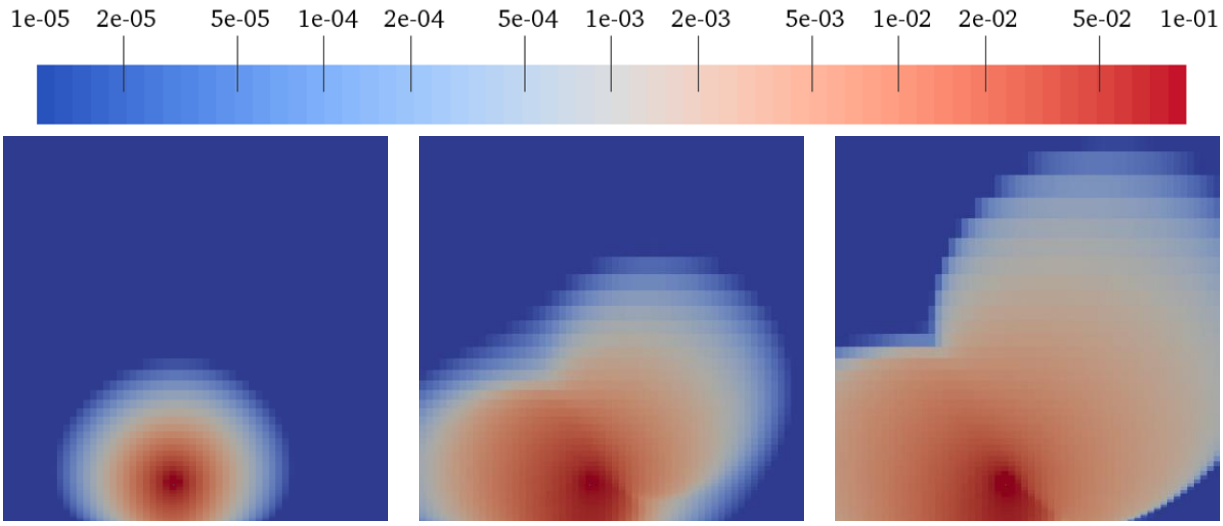

(a) Neutral case, 2 hours (b) Neutral case, 6 hours (c) Neutral case, 8 hours

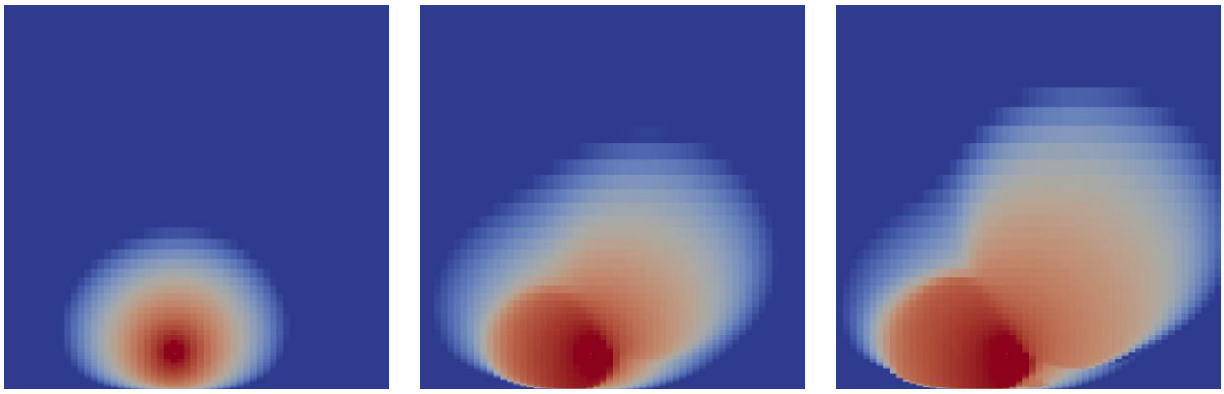

(d) Stable case, 2 hours (d) Stable case, 6 hours (d) Stable case, 8 hours

Figure 6.19: Comparison of SO_2 mass fraction at different hours for the two cases.

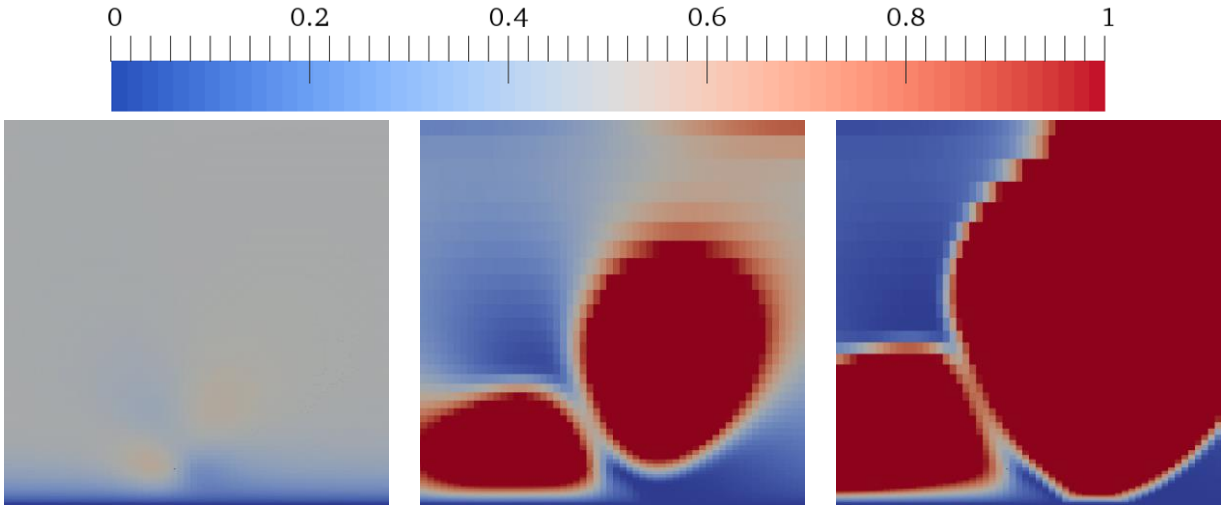

(a) Neutral case, 2 hours (b) Neutral case, 6 hours (c) Neutral case, 8 hours

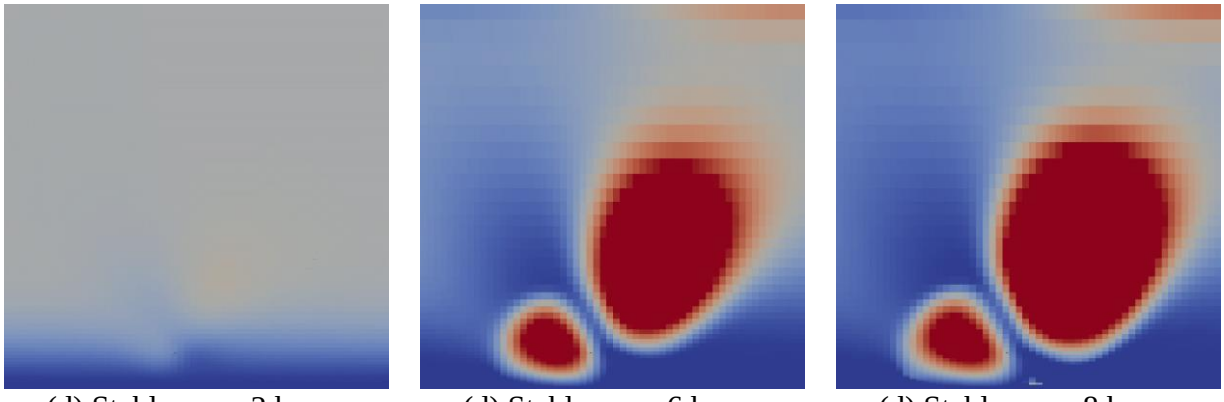

(d) Stable case, 2 hours (d) Stable case, 6 hours (d) Stable case, 8 hours

Figure 6.20: Comparison of turbulent viscosity (m^2/s) at different hours for the two cases.

Chapter 7

Conclusion and future work

In this study, wind development and pollution dispersion within the ABL over a complex terrain are investigated through comparisons between CFD model predictions and field measurements. A CFD modeling methodology that includes the generation of a good quality fully-hex computational mesh, construction of boundary conditions using existing meteorological data, turbulence model parameterizations, and treatment of aerodynamic roughness length is discussed. The following conclusions can be drawn:

1) The proposed curve-fitting method provides a consistent estimate of the atmosphere guided by the ground sensors and vertical profiles from sounding and reanalysis data. It can generate good-quality inlet boundary conditions in terms of vertical profiles of horizontal wind speed and temperature for use in the CFD model.
2) Validation of the CFD model against measurements suggests that the assumption of quasi-steady-state periods seems reasonable. The CFD model agrees reasonably well with measurements for a number of cases.
3) The overall performance of the developed CFD model is better than that of AERMOD in different statistical measures. More importantly, the CFD model predictions are more consistent than AERMOD under different dispersion conditions, as the vertical profiles of wind speed and temperature used in CFD agree better with those of sounding. It should, however, be mentioned that these cases were selected during periods of relatively small variations in wind speed and direction.
4) SO_2 plume width on the ground level is estimated to be similar to the distance between the Liberty site and the Liberty Way site from the time series of the concentration data. The

CFD-predicted plume width agrees with such estimation. However, due to wind direction, high concentrations caused by inversion are sometimes not picked up by Liberty monitor, but they still exist in the vicinity as predicted by CFD. More SO_2 monitors can be deployed in the study domain to help determine the width, the duration of the SO_2 plume, and compare them with CFD under different wind directions.

5) If changes in wind speed and direction are larger, the steady-state assumption may not be valid, and a transient model may be needed. In the transient simulations of SO_2 dispersion within 1 hour, the predicted wind directions agree well with measurements. However, the predicted SO_2 concentrations at the Liberty site show an amplified range towards the end of the simulated hour. Improvements on the initial condition and the boundary condition are needed to restrain the prediction from the transient CFD model.
6) The influence of the complex terrain in terms of topography on wind development and pollution dispersion is significant. The predicted SO_2 plume will be different in shape if the complex terrain is simplified to flat terrain. Also, the predicted SO_2 concentrations at Liberty are much higher using the flat terrain. As for aerodynamic roughness length, its main influence is limited to the horizontal wind speed and turbulence near ground level. Above $10\ m$ AGL, using the variable or uniform aerodynamic roughness length makes no difference in the results.
7) It is widely established that stronger inversion strength leads to higher pollutant concentrations in the atmosphere. However, when it comes to measurements from a single monitor, multiple factors, including wind speed, can lead to high concentrations. For a given emission rate and wind direction, the steady-state CFD model shows that faster wind speed keeps the high concentration plume low to the ground. The predicted concentration

can be higher than a low wind speed condition with stronger inversion strength.

In the future, potential improvements and extensions of the present study include:

1) The current wind measurements within the study domain are generally low to the ground, and there are only a small number of them. The wind data collected at lower elevations are prone to high variances. More anemometers can be deployed in the study domain at different height levels. The future study should also make good use of the SODAR measurements to guide on fitting vertical profiles, especially when there is disagreement among the sounding data, reanalysis data, and theoretical profiles.
2) The performance of the transient simulation needs to be improved. Currently, the transient simulation predicts much higher concentrations towards the end of the simulated hour. This is likely due to the wind direction changes at the inlet. A precursor simulation upstream of the current study domain can be performed to provide a smooth change in wind direction at the inlet. With more details added to the boundary conditions, such as the minute-level emission scenario of the coke plant or even the heat release data, the transient CFD model is expected to provide more reasonable results. Once the transient CFD model is validated with measurements, the difference between steady-state simulation results and the mean of the transient simulations results can be explored. In addition, the importance of drainage flow on SO_2 concentrations can be further studied with different initial wind conditions and ground cooling rates using transient simulations.
3) With the Python scripts that automatically generate simulation cases and schedule jobs over computer clusters, more simulation cases can easily be performed to further explore the strength and weaknesses of the CFD model. ACHD can take advantage of the developed CFD model to understand SO_2 dispersion under different conditions and provide guidance

on reducing SO_2 emissions in Allegheny County.

References

[1] Mackiewicz-Walec E, Krzebietke S, Lenart L, Rogalski L, Smoczyński L. Changes in sulphur dioxide concentrations in the atmospheric air assessed during short-term measurements in the vicinity of Olsztyn, Poland. Journal of Elemntology 2012. https://doi.org/10.5601/jelem.2014.19.2.634.

[2] Turalioğlu FS, Nuhoğlu A, Bayraktar H. Impacts of some meteorological parameters on SO2 and TSP concentrations in Erzurum, Turkey. Chemosphere 2005;59:1633–42. https://doi.org/10.1016/j.chemosphere.2005.02.003.

[3] Zalakeviciute R, López-Villada J, Rybarczyk Y. Contrasted Effects of Relative Humidity and Precipitation on Urban PM2.5 Pollution in High Elevation Urban Areas. Sustainability 2018;10:2064. https://doi.org/10.3390/su10062064.

[4] Liu Y, Zhou Y, Lu J. Exploring the relationship between air pollution and meteorological conditions in China under environmental governance. Scientific Reports 2020;10:1–11. https://doi.org/10.1038/s41598-020-71338-7.

[5] Tirabassi T, Fortezza F, Vandini W. Wind circulation and air pollutant concentration in the coastal city of ravenna. Energy and Buildings 1991;16:699–704. https://doi.org/10.1016/0378-7788(91)90040-A.

[6] Cichowicz R, Wielgosiński G, Fetter W. Effect of wind speed on the level of particulate matter PM10 concentration in atmospheric air during winter season in vicinity of large combustion plant. Journal of Atmospheric Chemistry 2020;77:35–48. https://doi.org/10.1007/s10874-020-09401-w.

[7] Liu Z, Shen L, Yan C, Du J, Li Y, Zhao H. Analysis of the Influence of Precipitation and Wind on PM2.5 and PM10 in the Atmosphere. Advances in Meteorology 2020;2020. https://doi.org/10.1155/2020/5039613.

[8] Stull RB. An Introduction to Boundary Layer Meteorology. Dordrecht: Springer Netherlands; 1988. https://doi.org/10.1007/978-94-009-3027-8.

[9] Sadar AJ. Allegheny County Surface Temperature Inversion Analysis - 2018. Pittsburgh: 2019.

[10] Wallace JM, Hobbs P v. Atmospheric Science. Second. Academic Press; 2006. https://doi.org/10.1016/C2009-0-00034-8.

[11] Tampieri F. Turbulence and Dispersion in the Planetary Boundary Layer. 2017. https://doi.org/10.1007/978-3-319-43604-3.

[12] Temel O, Bricteux L, van Beeck J. Coupled WRF-OpenFOAM study of wind flow over complex terrain. Journal of Wind Engineering and Industrial Aerodynamics 2018;174:152–69. https://doi.org/10.1016/j.jweia.2018.01.002.

[13] Monin AS, Obukhov AM. Basic laws of turbulent mixing in the surface layer of the atmosphere. Contrib Geophys Inst Acad Sci USSR 1954;151:163–87.

[14] Foken T. 50 years of the Monin-Obukhov similarity theory. Boundary-Layer Meteorology 2006;119:431–47. https://doi.org/10.1007/s10546-006-9048-6.

[15] Businger JA, Wyngaard JC, Izumi Y, Bradley EF. Flux-Profile Relationships in the Atmospheric Surface Layer. Journal of the Atmospheric Sciences 1971;28:181–9. https://doi.org/10.1175/1520-0469(1971)028<0181:fprita>2.0.co;2.

[16] Panofsky HA, Dutton JA. Atmospheric Turbulence. New York: John Wiley & Sons; 1984.

[17] Oke TR, Mills G, Christen A, Voogt JA. Urban Climates. Cambridge: Cambridge University Press; 2017. https://doi.org/10.1017/9781139016476.

[18] Cimorelli AJ, Perry SG, Venkatram A, Weil JC, Paine RJ, Wilson RB, et al. AERMOD: A

Dispersion Model for Industrial Source Applications. Part I: General Model Formulation and Boundary Layer Characterization. Journal of Applied Meteorology 2005;44:682–93. https://doi.org/10.1175/JAM2227.1.
[19] Perry SG. CTDMPLUS: A Dispersion Model for Sources near Complex Topography. Part I: Technical Formulations. Journal of Applied Meteorology 1992;31:633–45. https://doi.org/10.1175/1520-0450(1992)031<0633:CADMFS>2.0.CO;2.
[20] Demeal E, Carissimo B. Comparative evaluation of an Eulerian CFD and Gaussian plume models based on Prairie Grass dispersion experiment. Journal of Applied Meteorology and Climatology 2008;47:888–900. https://doi.org/10.1175/2007JAMC1375.1.
[21] U.S. Environmental Protection Agency. AERMOD Model Formulation and Evaluation 2016.
[22] McMurry PH, Shepherd MF, Vickery JS. Particulate matter science for policy makers: A NARSTO assessment. Cambridge University Press; 2004.
[23] Muller CL, Chapman L, Grimmond CSB, Young DT, Cai X. Sensors and the city: A review of urban meteorological networks. International Journal of Climatology 2013;33:1585–600. https://doi.org/10.1002/joc.3678.
[24] Karamchandani P, Vijayaraghavan K, Yarwood G. Sub-grid scale plume modeling. Atmosphere 2011;2:389–406. https://doi.org/10.3390/atmos2030389.
[25] Huser A, Nilsen PJ, Skåtun H. Application of k−ε model to the stable ABL: Pollution in complex terrain. Journal of Wind Engineering and Industrial Aerodynamics 1997;67–68:425–36. https://doi.org/10.1016/S0167-6105(97)00091-3.
[26] Sládek I, Bodnár T, Kozel K. On a numerical study of atmospheric 2D and 3D—flows over a complex topography with forest including pollution dispersion. Journal of Wind Engineering and Industrial Aerodynamics 2007;95:1424–44. https://doi.org/10.1016/j.jweia.2007.02.024.
[27] Pontiggia M, Derudi M, Busini V, Rota R. Hazardous gas dispersion: A CFD model accounting for atmospheric stability classes. Journal of Hazardous Materials 2009;171:739–47. https://doi.org/10.1016/j.jhazmat.2009.06.064.
[28] Amorim JH, Rodrigues V, Tavares R, Valente J, Borrego C. CFD modelling of the aerodynamic effect of trees on urban air pollution dispersion. Science of the Total Environment 2013;461–462:541–51. https://doi.org/10.1016/j.scitotenv.2013.05.031.
[29] Bonifacio HF, Maghirang RG, Glasgow LA. Numerical Simulation of Transport of Particles Emitted From Ground-Level Area Source Using Aermod and CFD. Engineering Applications of Computational Fluid Mechanics 2014;8:488–502. https://doi.org/10.1080/19942060.2014.11083302.
[30] Tominaga Y, Industrial TS-J of WE and, 2011 U. Tominaga Y, Stathopoulos T. CFD modeling of pollution dispersion in a street canyon: comparison between LES and RANS. J Wind Eng Ind Aerodyn 2011; 99:340e8. Elsevier 2011;0:340–8.
[31] Dörenkämper M, Witha B, Steinfeld G, Heinemann D, Kühn M. The impact of stable atmospheric boundary layers on wind-turbine wakes within offshore wind farms. Journal of Wind Engineering and Industrial Aerodynamics 2015;144:146–53. https://doi.org/10.1016/j.jweia.2014.12.011.
[32] Dhunny AZZ, Lollchund MRR, Rughooputh SDDVDDV. Wind energy evaluation for a highly complex terrain using Computational Fluid Dynamics (CFD). Renewable Energy 2017;101:1–9. https://doi.org/10.1016/j.renene.2016.08.032.
[33] Forthofer JM, Butler BW, Wagenbrenner NS. A comparison of three approaches for

simulating fine-scale surface winds in support of wildland fire management. Part I. Model formulation and comparison against measurements. International Journal of Wildland Fire 2014;23:969–81. https://doi.org/10.1071/WF12089.
[34] Blocken B, Stathopoulos T, van Beeck JPAJ. Pedestrian-level wind conditions around buildings: Review of wind-tunnel and CFD techniques and their accuracy for wind comfort assessment. Building and Environment 2016;100:50–81. https://doi.org/10.1016/j.buildenv.2016.02.004.
[35] Balogh M, Parente A, Benocci C. RANS simulation of ABL flow over complex terrains applying an Enhanced k-ε model and wall function formulation: Implementation and comparison for fluent and OpenFOAM. Journal of Wind Engineering and Industrial Aerodynamics 2012;104–106:360–8. https://doi.org/10.1016/j.jweia.2012.02.023.
[36] Bechmann A, Sørensen NN. Hybrid RANS/LES method for wind flow over complex terrain. Wind Energy 2010;13:36–50. https://doi.org/10.1002/we.346.
[37] Breedt HJ, Craig KJ, Jothiprakasam VD. Monin-Obukhov similarity theory and its application to wind flow modelling over complex terrain. Journal of Wind Engineering and Industrial Aerodynamics 2018;182:308–21. https://doi.org/b.
[38] Pieterse JEJEE, Harms TMM. CFD investigation of the atmospheric boundary layer under different thermal stability conditions. Journal of Wind Engineering and Industrial Aerodynamics 2013;121:82–97. https://doi.org/10.1016/j.jweia.2013.07.014.
[39] Toparlar Y, Blocken B, Maiheu B, van Heijst GJ. CFD simulation of the near-neutral atmospheric boundary layer: New temperature inlet profile consistent with wall functions. Journal of Wind Engineering and Industrial Aerodynamics 2019;191:91–102. https://doi.org/10.1016/j.jweia.2019.05.016.
[40] Richards PJ, Hoxey RP. Appropriate boundary conditions for computational wind engineering models using the k-ϵ turbulence model. Journal of Wind Engineering and Industrial Aerodynamics 1993;46–47:145–53. https://doi.org/10.1016/0167-6105(93)90124-7.
[41] Li C, Zhou S, Xiao Y, Huang Q, Li L, Chan PW. Effects of inflow conditions on mountainous/urban wind environment simulation. Building Simulation 2017;10:573–88. https://doi.org/10.1007/s12273-017-0348-1.
[42] Miao Y, Liu S, Chen B, Zhang B, Wang S, Li S. Simulating urban flow and dispersion in Beijing by coupling a CFD model with the WRF model. Advances in Atmospheric Sciences 2013;30:1663–78. https://doi.org/10.1007/s00376-013-2234-9.
[43] van der Laan, Paul; Kelly, Mark C.; Sørensen NN, van der Laan MP, Kelly MC, Sørensen NN. A new k-epsilon model consistent with Monin-Obukhov similarity theory. Wind Energy 2017;20:479–89. https://doi.org/10.1002/we.2017.
[44] Alinot C, Masson C. k-ε Model for the Atmospheric Boundary Layer Under Various Thermal Stratifications. Journal of Solar Energy Engineering 2005;127:438. https://doi.org/10.1115/1.2035704.
[45] Launder BE, Spalding DB. The numerical computation of turbulent flows. Computer Methods in Applied Mechanics and Engineering 1974;3:269–89. https://doi.org/10.1016/0045-7825(74)90029-2.
[46] Crespo A, Manuel F, Moreno D, Fraga E, Hernandez J. Numerical Analysis of Wind Turbine Wakes. Proceedings of an International Workshop Held at the European Culture Center of Delphi, Greece 1985:15–25.
[47] Rodi W. Turbulent Buoyant Jets and Plumes. 1982.

[48] Kitada T. Turbulence structure of sea breeze front and its implication in air pollution transport-Application of k-ε turbulence model. Boundary-Layer Meteorology 1987;41:217–39. https://doi.org/10.1007/BF00120440.
[49] Schlichting H, Gersten K. Boundary-Layer Theory. Berlin, Heidelberg: Springer Berlin Heidelberg; 2017. https://doi.org/10.1007/978-3-662-52919-5.
[50] Blocken B, Stathopoulos T, Carmeliet J. CFD simulation of the atmospheric boundary layer: wall function problems. Atmospheric Environment 2007;41:238–52. https://doi.org/10.1016/j.atmosenv.2006.08.019.
[51] Parente A, Gorlé C, van Beeck J, Benocci C. Improved k-ε model and wall function formulation for the RANS simulation of ABL flows. Journal of Wind Engineering and Industrial Aerodynamics 2011;99:267–78. https://doi.org/10.1016/j.jweia.2010.12.017.
[52] Cavar D, Réthoré P-E, Bechmann A, Sørensen NN, Martinez B, Zahle F, et al. Comparison of OpenFOAM and EllipSys3D for neutral atmospheric flow over complex terrain. Wind Energy Science 2016;1:55–70. https://doi.org/10.5194/wes-1-55-2016.
[53] Taylor PA, Teunissen HW. The Askervein Hill project: Overview and background data. Boundary-Layer Meteorology 1987;39:15–39. https://doi.org/10.1007/BF00121863.
[54] Berg J, Mann J, Bechmann A, Courtney MS, Jørgensen HE. The Bolund Experiment, Part I: Flow Over a Steep, Three-Dimensional Hill. Boundary-Layer Meteorology 2011;141:219–43. https://doi.org/10.1007/s10546-011-9636-y.
[55] Toja-Silva F, Pregel-Hoderlein C, Chen J. On the urban geometry generalization for CFD simulation of gas dispersion from chimneys: Comparison with Gaussian plume model. Journal of Wind Engineering and Industrial Aerodynamics 2018;177:1–18. https://doi.org/10.1016/j.jweia.2018.04.003.
[56] Kampa M, Castanas E. Human health effects of air pollution. Environmental Pollution 2008;151:362–7. https://doi.org/10.1016/j.envpol.2007.06.012.
[57] Solomon D. Air Quality Design Values. United States Environmental Protection Agency 2021. https://www.epa.gov/air-trends/air-quality-design-values.
[58] Vozar S. 2019 Air quality annual report. Pittsburgh: 2019.
[59] Dutzik T, Barber Z. Cutting through the Smoke: Why the Allegheny County Health Department Must Turn the Corner on Decades of Weak Clean Air Enforcement. n.d.
[60] Weller HG, Tabor G, Jasak H, Fureby C. A tensorial approach to computational continuum mechanics using object-oriented techniques. Computers in Physics 1998;12:620. https://doi.org/10.1063/1.168744.
[61] Pope SB. Turbulent Flows. Weinheim, Germany: Cambridge University Press; 2000. https://doi.org/10.1017/CBO9780511840531.
[62] Ferziger JH, Perić M, Street RL. Computational Methods for Fluid Dynamics. 4th ed. Springer International Publishing; 2020. https://doi.org/10.1007/978-3-319-99693-6.
[63] Patankar S v. Numerical Heat Transfer and Fluid Flow. vol. 53. CRC Press; 2018. https://doi.org/10.1201/9781482234213.
[64] Jasak H. Error Analysis and Estimation for the Finite Volume Method with Applications to Fluid Flows. Direct 1996;M:394. https://doi.org/10.1016/S0020-7683(02)00168-3.
[65] Issa RI. Solution of the implicitly discretised fluid flow equations by operator-splitting. Journal of Computational Physics 1986;62:40–65. https://doi.org/10.1016/0021-9991(86)90099-9.
[66] Jones WP, Launder BE. The prediction of laminarization with a two-equation model of turbulence. International Journal of Heat and Mass Transfer 1972;15:301–14.

[67] Henkes RAWM, van der Vlugt FF, Hoogendoorn CJ. Natural-convection flow in a square cavity calculated with low-Reynolds-number turbulence models. International Journal of Heat and Mass Transfer 1991;34:377–88. https://doi.org/10.1016/0017-9310(91)90258-G.
[68] Greenshields C. Energy Equation in OpenFOAM. CFD Direct 2016. https://cfd.direct/openfoam/energy-equation.
[69] APSLEY DD, CASTRO IP. A LIMITED-LENGTH-SCALE k-ε MODEL FOR THE NEUTRAL AND STABLY-STRATIFIED ATMOSPHERIC BOUNDARY LAYER. Boundary-Layer Meteorology 1997;83:75–98. https://doi.org/10.1023/A:1000252210512.
[70] Sadar AJ. Allegheny County Surface Temperature Inversion Analysis - 2019. Pittsburgh: 2020.
[71] Tanzer R, Malings C, Hauryliuk A, Subramanian R, Presto AA. Demonstration of a Low-Cost Multi-Pollutant Network to Quantify Intra-Urban Spatial Variations in Air Pollutant Source Impacts and to Evaluate Environmental Justice. International Journal of Environmental Research and Public Health 2019;16:2523. https://doi.org/10.3390/ijerph16142523.
[72] Laporthe S, Virgone J, Castanet S. A comparative study of two tracer gases: SF6 and N2O. Building and Environment 2001;36:313–20. https://doi.org/10.1016/S0360-1323(00)00005-6.
[73] Miao Y, Liu S, Zheng Y, Wang S, Li Y. Numerical study of traffic pollutant dispersion within different street canyon configurations. Advances in Meteorology 2014;2014. https://doi.org/10.1155/2014/458671.
[74] Pennsylvania Spatial Data Access (PASDA) Allegheny County - 2006 Contours. Allegheny County Division of Computer Services Geographic Information Systems Group n.d. https://www.pasda.psu.edu/.
[75] ANSYS. ICEM CFD user's manual. 2017.
[76] U.S. Environmental Protection Agency. AERSURFACE V13016 User's Guide. 2013.
[77] Multi-Resolution Land Characteristics (MRLC) consortium. MRLC Viewer 2017. https://www.mrlc.gov/viewer.
[78] Virtanen P, Gommers R, Oliphant TE, Haberland M, Reddy T, Cournapeau D, et al. SciPy 1.0: fundamental algorithms for scientific computing in Python. Nature Methods 2020;17:261–72. https://doi.org/10.1038/s41592-019-0686-2.
[79] Richards PJ, Norris SE. Appropriate boundary conditions for computational wind engineering: Still an issue after 25 years. Journal of Wind Engineering and Industrial Aerodynamics 2019;190:245–55. https://doi.org/10.1016/j.jweia.2019.05.012.
[80] Sumner J, Masson C. k-epsilon Simulations of the Neutral ABL: Achieving Horizontal Homogeneity on Practical Grids. Aiaa2010 2010:1–13.
[81] Rood AS. Performance evaluation of AERMOD, CALPUFF, and legacy air dispersion models using the Winter Validation Tracer Study dataset. Atmospheric Environment 2014;89:707–20. https://doi.org/10.1016/j.atmosenv.2014.02.054.
[82] Balczo M, Balogh M, Goricsan I, Nagel T, Suda JM, Lajos T. Air quality around motorway tunnels in complex terrain - computational fluid dynamics modeling and comparison to wind tunnel data. Quarterly Journal of the Hungarian Meteorological Service 2011;115:179–204.
[83] Connan O, Leroy C, Derkx F, Maro D, Hébert D, Roupsard P, et al. Atmospheric dispersion of an elevated release in a rural environment: Comparison between field SF6 tracer measurements and computations of Briggs and ADMS models. Atmospheric

Environment 2011;45:7174–83. https://doi.org/10.1016/j.atmosenv.2011.09.023.
[84] Teggi S, Costanzini S, Ghermandi G, Malagoli C, Vinceti M. A GIS-based atmospheric dispersion model for pollutants emitted by complex source areas. Science of the Total Environment 2018;610–611:175–90. https://doi.org/10.1016/j.scitotenv.2017.07.196.
[85] Hashemi S, Mowla D, Esmaeilzadeh F. Assessment and Simulation of Gaseous Dispersion by Computational Fluid Dynamics (CFD): A Case Study of Shiraz Oil Refining Company. American Journal of Environmental Science and Engineering 2020;4:17. https://doi.org/10.11648/j.ajese.20200402.12.
[86] Gousseau P, Blocken B, van Heijst GJF. Quality assessment of Large-Eddy Simulation of wind flow around a high-rise building: Validation and solution verification. Computers and Fluids 2013;79:120–33. https://doi.org/10.1016/j.compfluid.2013.03.006.
[87] Hanna SR, Hansen OR, Dharmavaram S. FLACS CFD air quality model performance evaluation with Kit Fox, MUST, Prairie Grass, and EMU observations. Atmospheric Environment 2004;38:4675–87. https://doi.org/10.1016/j.atmosenv.2004.05.041.
[88] Chang JC, Hanna SR. Air quality model performance evaluation. Meteorology and Atmospheric Physics 2004;87:167–96. https://doi.org/10.1007/s00703-003-0070-7.
[89] Rzeszutek M, Szulecka A, Oleniacz R, Bogacki M. Assessment of the AERMOD dispersion model over complex terrain with different types of meteorological data: Tracy Power Plant experiment. E3S Web of Conferences 2017;22:00149. https://doi.org/10.1051/e3sconf/20172200149.
[90] Venkatram A, Brode R, Cimorelli A, Lee R, Paine R, Perry S, et al. A complex terrain dispersion model for regulatory applications. Atmospheric Environment 2001;35:4211–21. https://doi.org/10.1016/S1352-2310(01)00186-8.
[91] Hernández JF, Cremades L, Baldasano JM. Simulation of tracer dispersion from elevated and surface releases in complex terrain. Atmospheric Environment 1997;31:2337–48. https://doi.org/10.1016/S1352-2310(97)00027-7.
[92] Kumar P, Singh SK, Ngae P, Feiz AA, Turbelin G. Assessment of a CFD model for short-range plume dispersion: Applications to the Fusion Field Trial 2007 (FFT-07) diffusion experiment. Atmospheric Research 2017;197:84–93. https://doi.org/10.1016/j.atmosres.2017.06.025.
[93] Leone V, Cervone G, Iovino P. Impact assessment of PM10 cement plants emissions on urban air quality using the SCIPUFF dispersion model. Environmental Monitoring and Assessment 2016;188. https://doi.org/10.1007/s10661-016-5519-5.
[94] Ahrens J, Geveci B, Law C. ParaView: An End-User Tool for Large Data Visualization, Visualization Handbook. Elsevier; 2005.
[95] Monteiro A, Strunk A, Carvalho A, Tchepel O, Miranda AI, Borrego C, et al. Investigating a high ozone episode in a rural mountain site. Environmental Pollution 2012;162:176–89. https://doi.org/10.1016/j.envpol.2011.11.008.
[96] Guo H, Ling ZH, Cheung K, Jiang F, Wang DW, Simpson IJ, et al. Characterization of photochemical pollution at different elevations in mountainous areas in Hong Kong. Atmospheric Chemistry and Physics 2013;13:3881–98. https://doi.org/10.5194/acp-13-3881-2013.
[97] Yi C, Monson RK, Zhai Z, Anderson DE, Lamb B, Allwine G, et al. Modeling and measuring the nocturnal drainage flow in a high-elevation, subalpine forest with complex terrain. Journal of Geophysical Research Atmospheres 2005;110:1–13. https://doi.org/10.1029/2005JD006282.

[98] Boukhriss M, Zhani K, Ghribi R. Study of thermophysical properties of a solar desalination system using solar energy. Desalination and Water Treatment 2013;51:1290–5. https://doi.org/10.1080/19443994.2012.714925.
[99] The Processing of CALMET Files for Allegheny County's PM2.5 SIP Analysis. 2007.
[100] Warren L, Paine R, Moore G. Modeling Characterization for Highly Industrialized Areas and Fugitive Heat Releases. A&WMA Specialty Conference Guideline on Air Quality Models: The New Path, 2016.

Chapter 8

Appendix

8.1 Sensitivity test of the CFD model

To evaluate the sensitivity of the CFD model, multiple extraction lines are created, as shown in Figure 8.1, and different variables on the extraction lines can be compared.

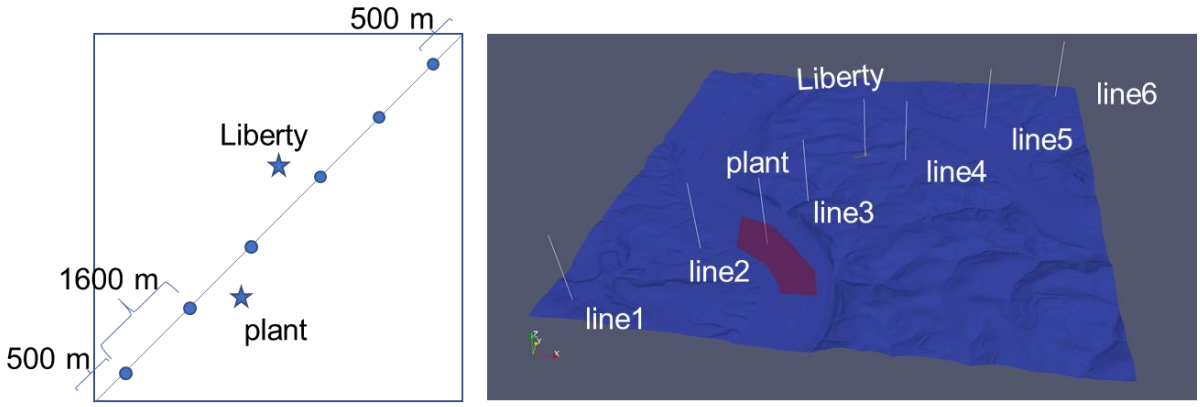

Figure 8.1: Extraction lines across the computational domain to be used in the sensitivity test of the CFD model.

8.1.1 Effects of stack exit conditions

Two important boundary conditions on each stack exit are the exit velocity and temperature, which are currently set using annualized data. Two simulations cases are performed, and their results are shown in Figure 8.2. The "Exit condition" case uses the annualized data of all the ten stacks, and the "Ambient condition" case ignores the exit velocity and temperature. It can be seen that the stack exit condition doesn't have much influence on the horizontal wind speed near the inlet and the outlet of the domain. But it creates highly buoyant flow near the plant, so the wind speed is faster compared to the ambient condition case. In addition, the stack exit condition plays a key role in SO_2 dispersion and vertical distribution. The buoyant flow created with the stack exit condition generates more turbulence and vertical velocity that can elevate and quickly disperse the SO_2 plume. As a result, the concentrations at multiple locations and heights are much

lower compared to the results of the ambient condition.

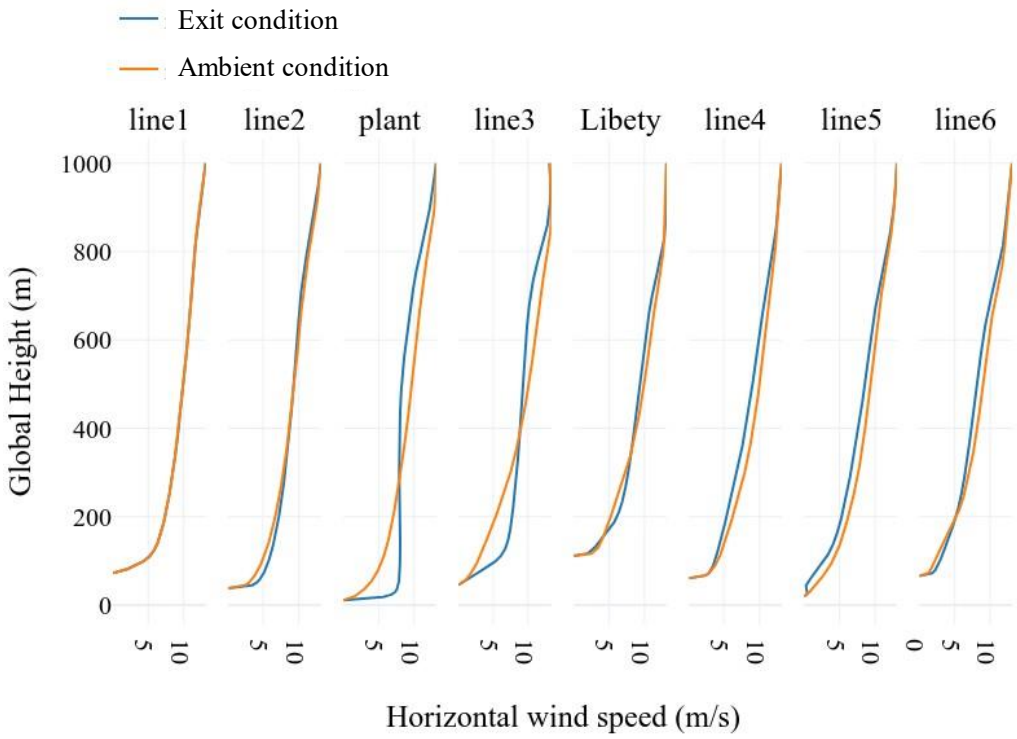

(a) Horizontal wind speed distribution along with the height

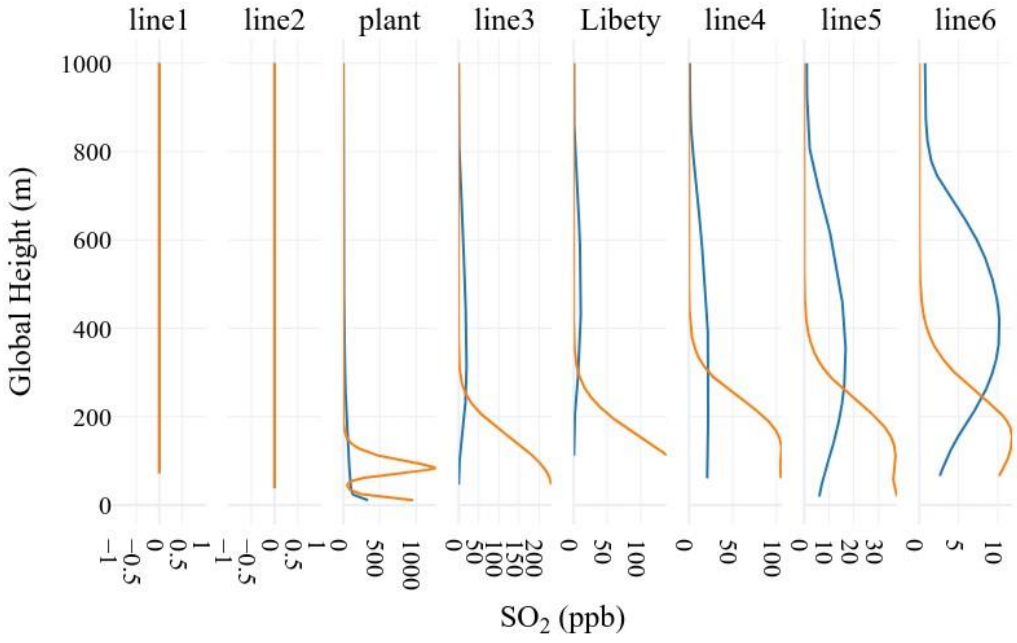

(b) SO_2 concentration distribution along with the height

Figure 8.2: Comparison of results from the annualized exit condition and ambient condition.

8.1.2 Effects of variable physical properties of air

The moisture in the air can change different physical properties of air, such as density, viscosity, specific heat, and thermal diffusivity. As a result of different relative humidity levels, the temperature profiles and buoyancy effects in the environment could differ from those with dry air. Boukhriss et al. showed different physical properties of moist air at different temperatures and relative humidity levels[98]. For air temperature at around 25°C, the difference in the specific heat of air is within 2% for different levels of relative humidity. Currently, the CFD model assumes a constant specific heat of air at $1{,}000\ J/kg \cdot K$ that covers the temperate range from about $260K$ to about $550K$. The high temperature near stack exits drops very quickly to ambient temperature, so the overall specific heat in the whole domain can be treated as constant with errors below 2%. As the air temperature gets lower with increasing height, the overall influence of humidity is negligible. Even at 90% of relative humidity, the amount of water vapor per unit mass of air is in the order of 0.01, so the effect of moisture on the scalar transport can be considered negligible. Variable specific heat, density, thermal conductivity, dynamic viscosity as functions of temperature are fitted as functions of air temperature shown in Figure 8.3.

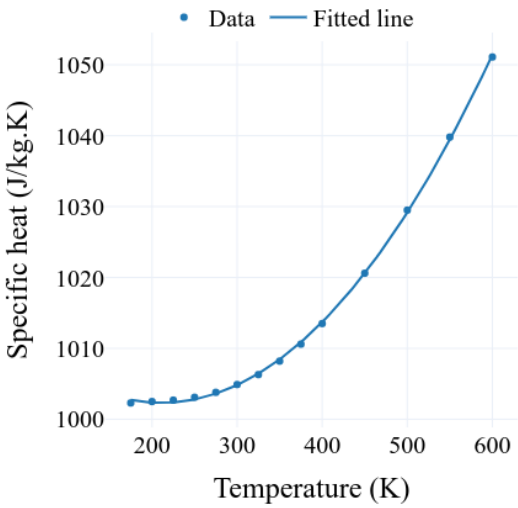

(a) Specific heat

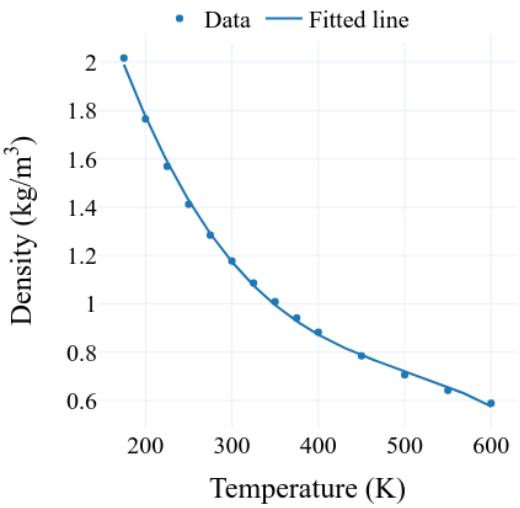

(b) Density

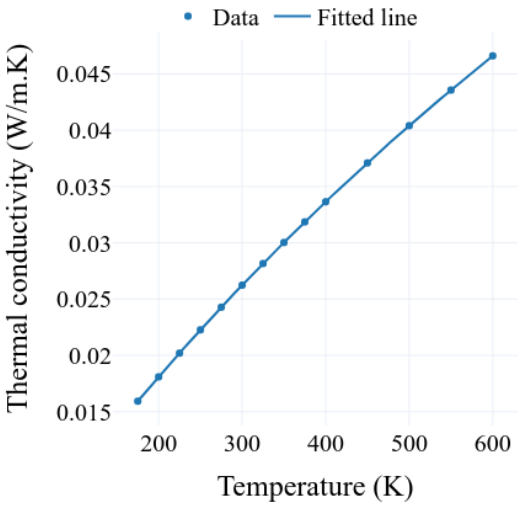

(c) Thermal conductivity

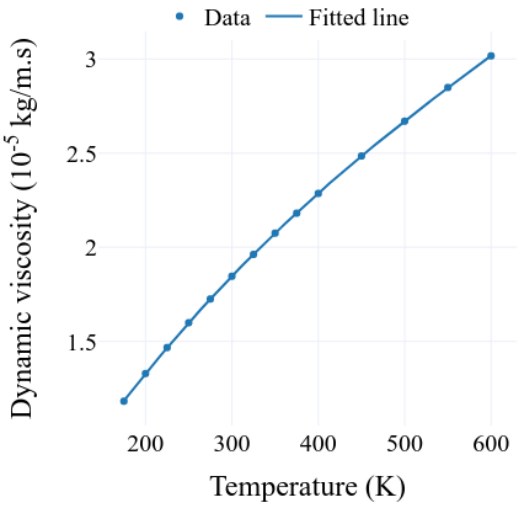

(d) Dynamic viscosity

Figure 8.3: Curve fitting results of different physical properties of air as a function of temperature.

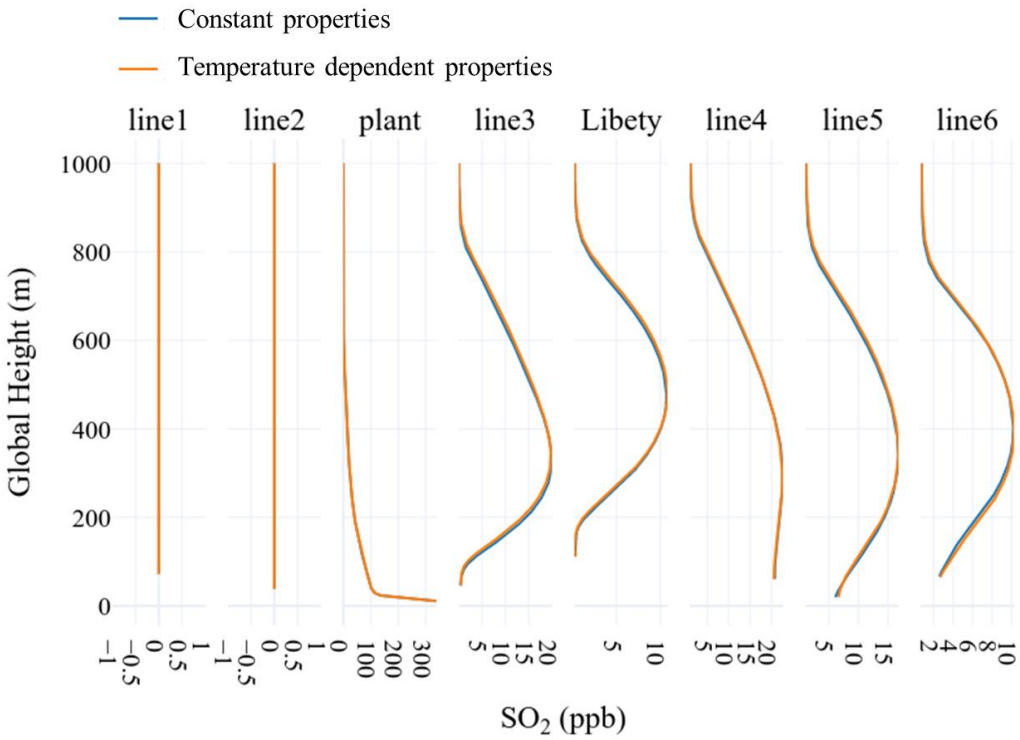

Figure 8.4: Comparison of SO_2 concentration distribution using constant properties and temperature-dependent properties.

8.1.3 Mesh independence study

To determine the best mesh configuration and to perform the independence study, five different meshes are created. Their configurations are listed in Table 8.1.

Table 8.1: Summary of different mesh configurations in the mesh independence study.

Name	x-, y-direction		z-direction			Total cell count (million)
	Cell size (m)	Cell count	First cell height (m)	Growth rate	Cell count	
Mesh-1	31	205	8	2.00	18	0.8
Mesh-2	31	205	4	1.06	48	2.0
Mesh-3	31	205	3	1.06	68	2.9
Mesh-4	16	409	4	1.06	48	8.0
Mesh-5	11	575	4	1.06	48	16.0

Comparisons of results from all mesh configurations are shown in Figure 8.5 and Figure 8.6. From Figure 8.5, we can conclude that the cell size in z-direction does not have any noticeable

influence on wind speed. Further refining the first cell height below will violate the aerodynamic-based wall functions used in the CFD model, where the aerodynamic roughness z_0 is large. The maximum value of z_0 is around 1.3 m. The wall function will modulate the wind speed at such height to be 0 at the first cell centroid. A cell should be at least 2.6 m in height. The results from Mesh-3 are very close to that of Mesh-2, so we think the first cell height of 4 m will be enough. From Figure 8.6, we can conclude that increasing the cell count from 205 to 409 will make some difference in the results. Mesh-2 has 31 m long cell, which is too coarse compared to the dimension of the stack exits (~3 m). It will require much more local refinement to the mesh to properly configure the stack exits. There is no need to increase the cell count to 575 as the results from Mesh-4 are already very close to those of Mesh-5. Mesh-5 has double the cell count than that of Mesh-4, which will require much longer computational time. In summary, we believe Mesh-4 is the best configuration.

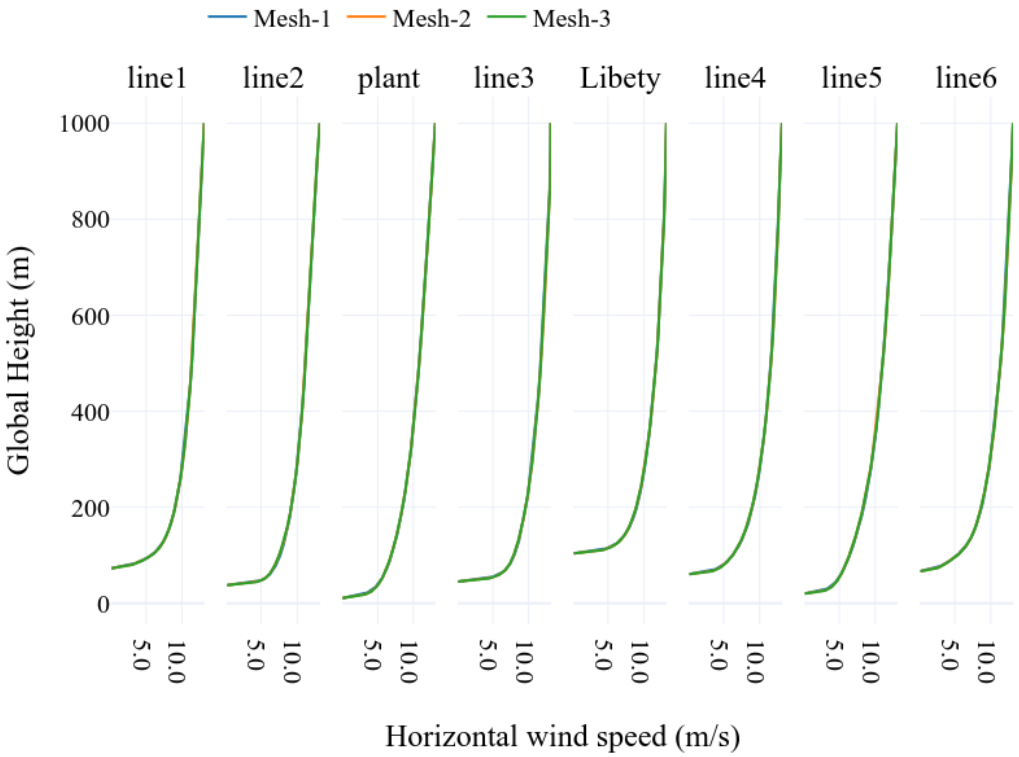

(a) Horizontal wind speed distribution along with the height

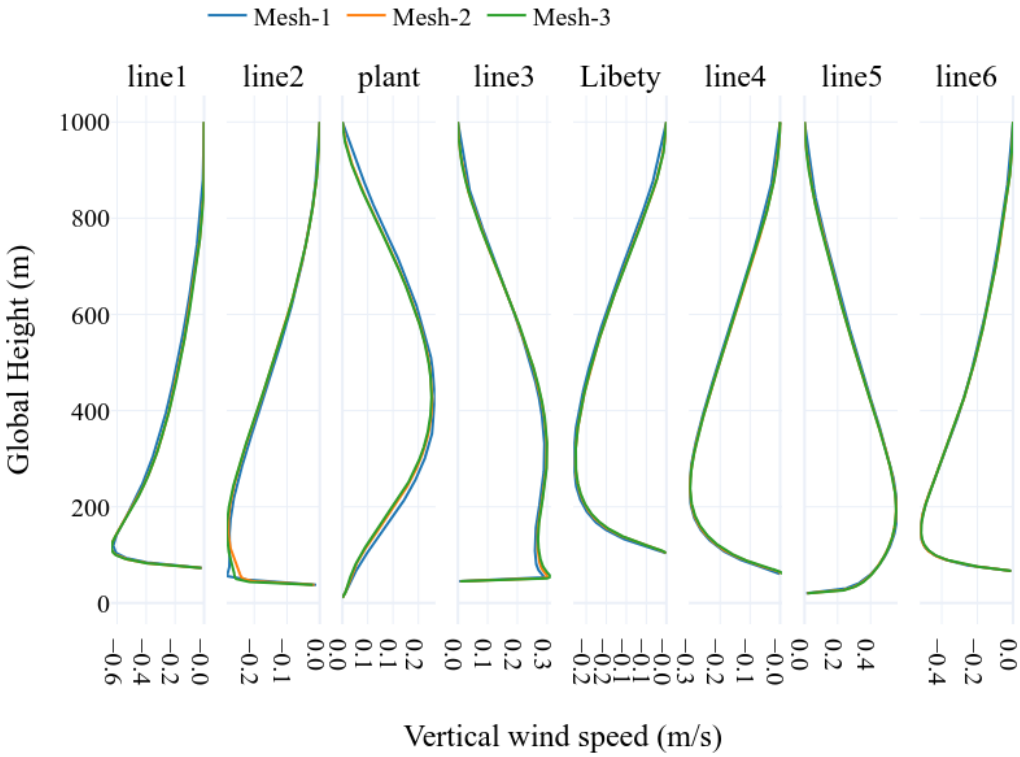

(b) Vertical wind speed distribution along with the height

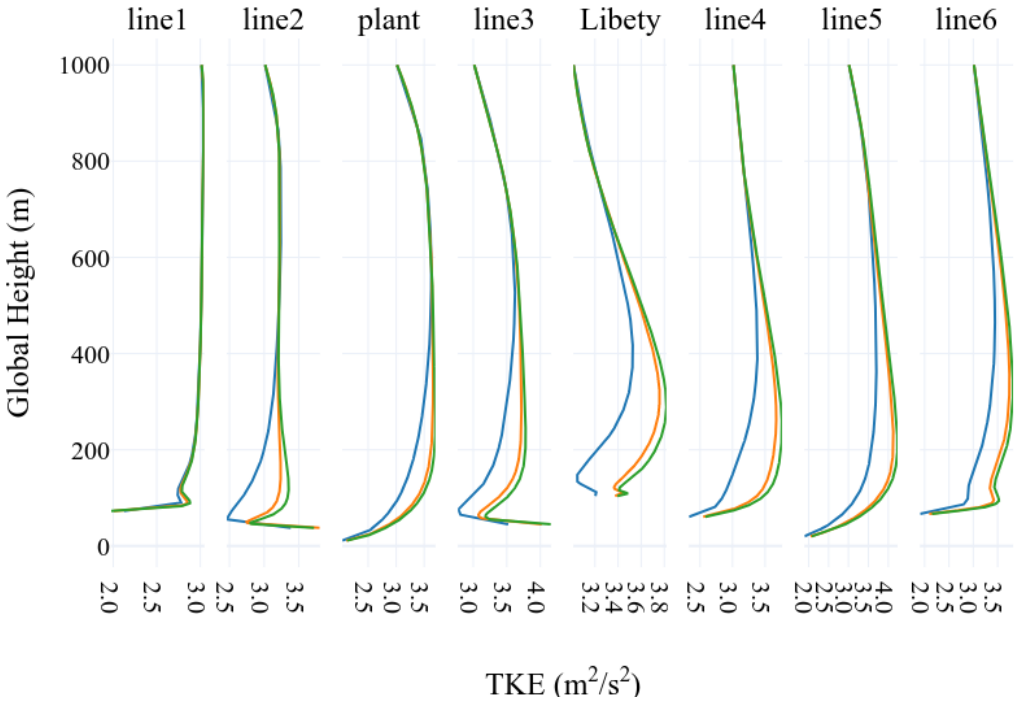

(c) Turbulent kinetic energy distribution along with the height

Figure 8.5: Comparison of results from Mesh-1, Mesh-2, and Mesh-3.

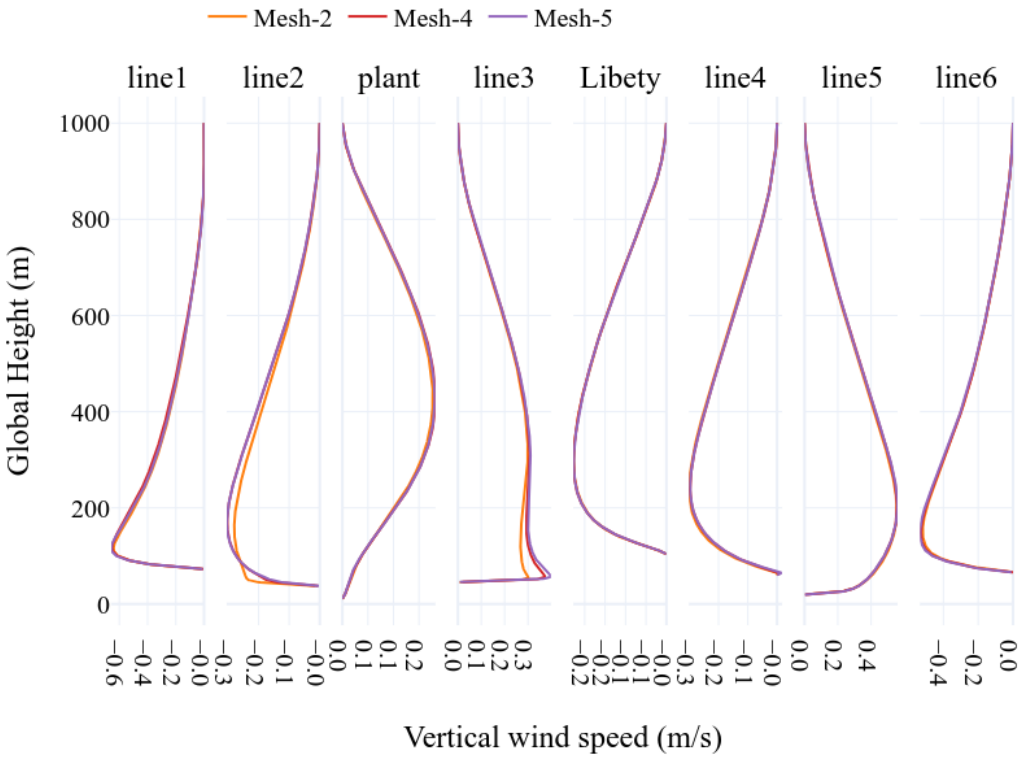

(a) Vertical wind speed distribution along with the height

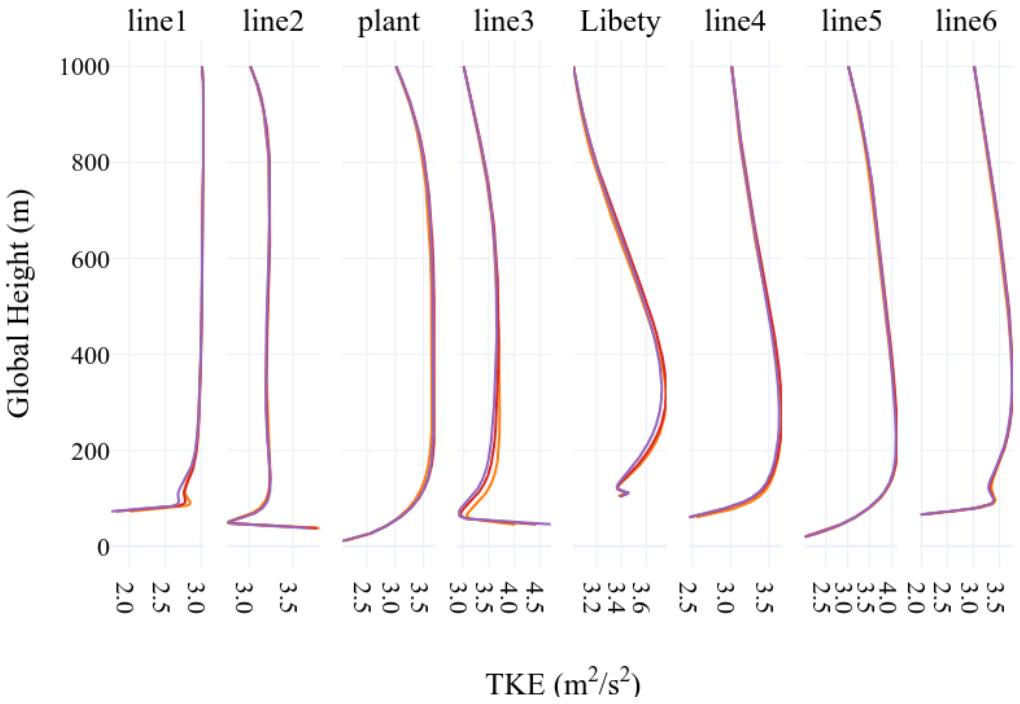

(b) Turbulent kinetic energy distribution along with the height

Figure 8.6: Comparison of results from Mesh-2, Mesh-4, and Mesh-5.

8.2 Cavity effect at the Lincoln site

Since the PASDA contour data only provides the height of the bare ground, it is difficult to locally elevate the 3D terrain surface according to the canopy height around the Lincoln site. In order to investigate the tree-created cavity effect, a 2D terrain with the bare ground is created focusing on the wind field at Lincoln, as shown in Figure 30 (a). Figure 30 (c) shows a closer look near the Lincoln site. Since this case is created to represent the bare ground, there is no cavity at the Lincoln site in the model. Then, another 2D terrain with displacement height included representing trees is created, as shown in Figure 30 (b). Figure 30 (d) shows a closer look at the Lincoln site, and it has a cavity in the model to represent the tree line. The two 2D domains have a length of $5000\ m$ along the wind direction (x-direction) and a height of 1000m in the vertical direction similar to the 3D domain. The hill in the middle of the domain has a length of $200\ m$ and a height of $120\ m$, which are estimated from the Google Earth distance measurement tool to resemble the real-world situation in the study domain. The displacement height is set to $4\ m$.

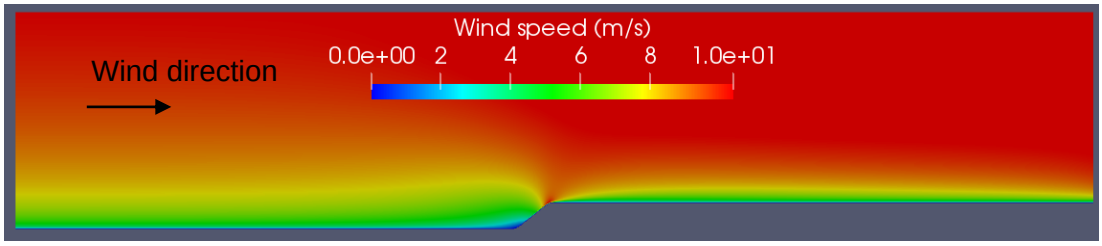

(a) Wind speed contours with bare ground

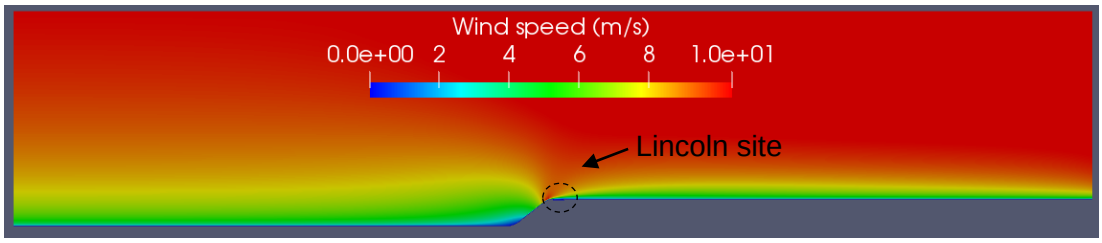

(b) Wind speed contours with the displaced ground

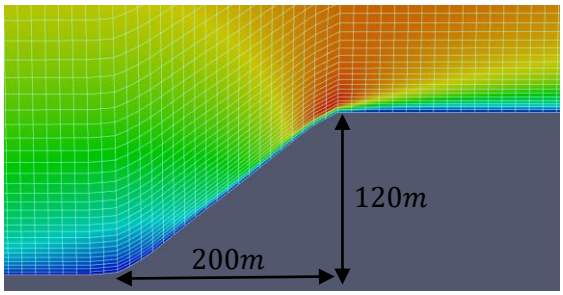

(c) A closer look near the Lincoln site with the bare ground

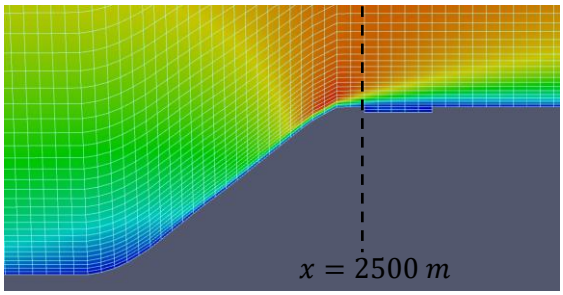

(d) A closer look near the Lincoln site with the displaced ground

Figure 8.7: Wind speed contours with the bare ground and the displaced ground.

Overall, the wind speed contours from the two cases look almost identical, as shown in Figure 8.7 (a) and (b). So, the trees do not have much influence on the general wind in the domain. In Figure 8.7 (d), the wind speed contour inside the cavity shows dark blue color, which means that the wind speed is about $1m/s$. Besides the contours, the vertical wind profiles near the cavity ($x = 2500\ m$) are extracted and shown in Figure 8.8.

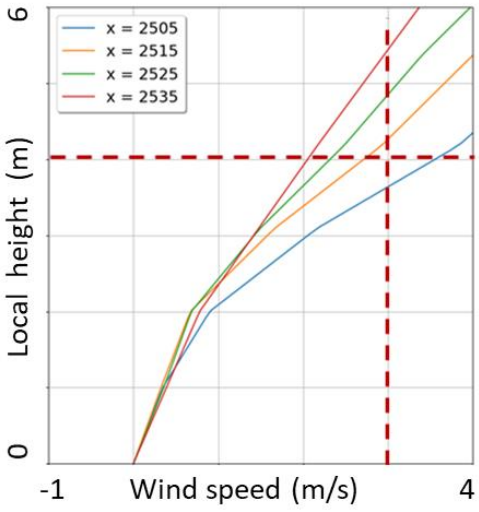

(a) Bare ground

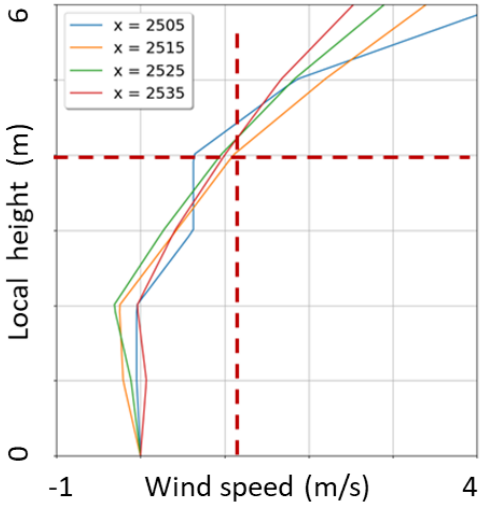

(b) Displaced ground

Figure 8.8: Predicted profiles at the Lincoln site using the simplified 2D terrain.

The horizontal red dash lines represent the height of the anemometer at 4 m AGL. If the

trees are represented by the corresponding displacement height, the wind speed inside the cavity is around 1 m/s as shown in Figure 8.8 (b). But if the bare ground is used, the wind speed goes up to about 3 m/s. The difference in the two 2D simulations confirms that the wind speed is higher over bare ground compared to when the tree cavity is created in the model. Both drone-based measurements and the model predictions in the 2D terrain suggest that the wind measurements at the Lincoln site are strongly influenced by the local cavity effect created by the dense canopy.

8.3 Heat island effect at the plant site

Based on the estimated amount of heat produced by the plant during the operation and the total area of the plant shown as the red boxes in Figure 8.9 (a), the averaged heat flux is estimated to be 5572.73 W/m^2 [99]. Using satellite imagery, the land surface temperature can be derived [100] as shown in Figure 8.9 (b). It is found that the temperature of the plant is usually 10 K higher than the ambient temperature. To investigate the influence of heat flux and high temperature on the flow field, they need to be specified in the model. Similar to the red boxes shown in Figure 8.9 (a), the coke plant is divided into three regions in the computational domain shown in Figure 8.10 (a). Within the three regions, the average heat flux is specified on the ground surface. It can be seen from the velocity contour in Figure 8.11 (a) that the flow speeds up immediately downstream of the regions of the heat, compared to the velocity contour without the heat island in Figure 8.11 (b). However, the effect mostly remains local to the plant area. Right across the river, the velocity contours and vertical profiles are very close in the two cases. In addition, the heat island effect does not have an impact on wind speed predictions at the downwind sensor locations. For example, the predicted wind speed at the Lincoln site (500 m downstream of the plant) is 1.7 m/s and 1.6 m/s with and without the heat island effect, respectively. We can conclude that the heat flux from the plant does not have much influence on the flow across the river and high above the

ground. In Figure 8.10 (b), the extracted wind profile shows the flow near the ground speeds up due to the heat island effect, cause the wind profile to deviate from the theoretical log shape and end up with a C-shaped profile from 40 m to 200 m AGL.

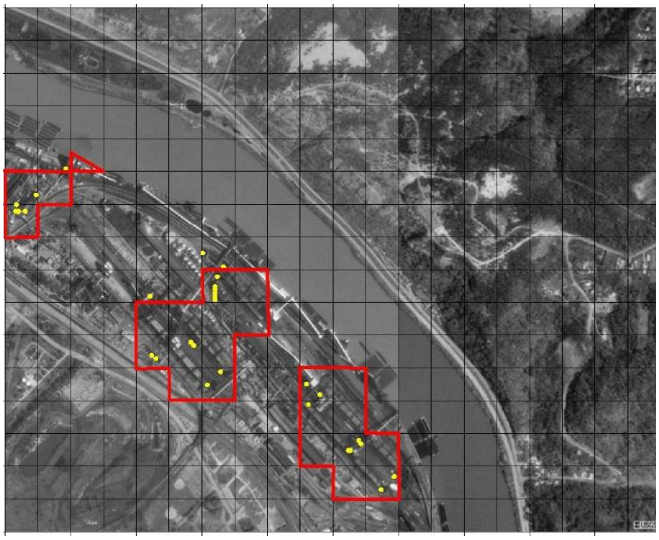

(a) Combustion sources in yellow dots and heat flux areas in red boxes

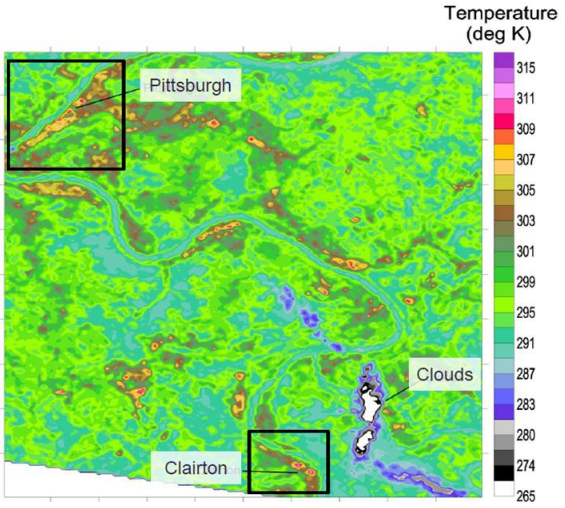

(b) The land surface temperature derived from satellite imagery

Figure 8.9: Heat flux studies on the coke plant that can be related to the heat island effect.

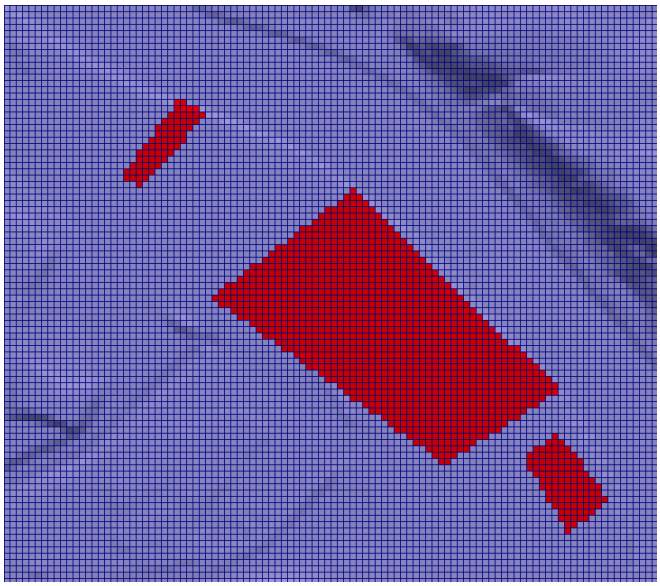

(a) Selection of 3 regions of the heat island in the computational domain

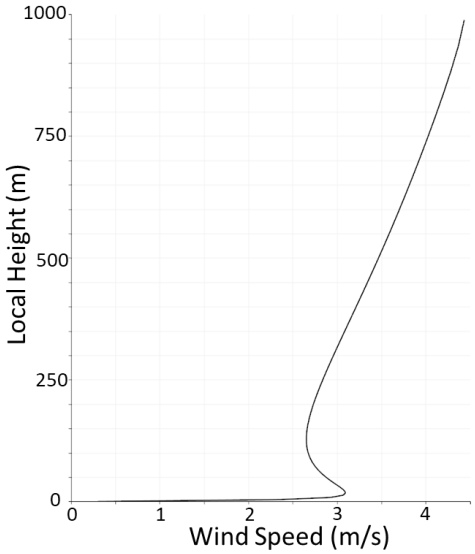

(b) Predicted wind profile extracted at the SODAR site

Figure 8.10: Representation of the heat island effect in CFD and the wind profile.

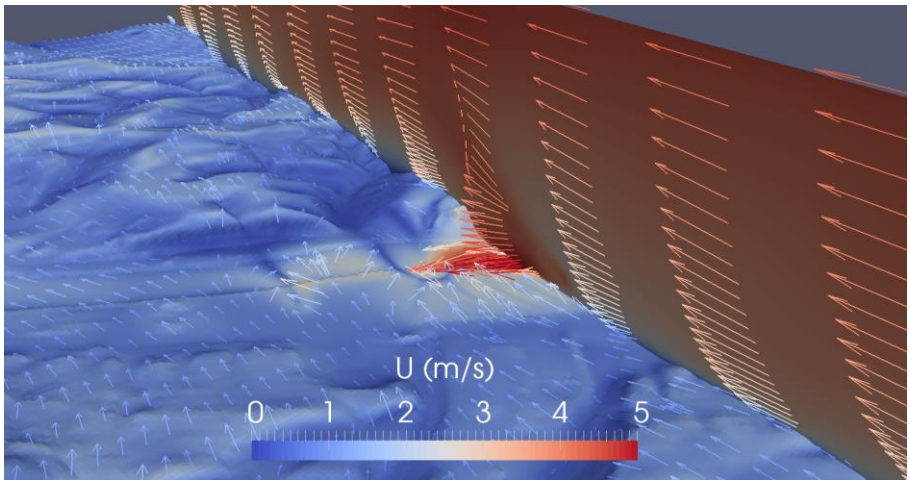

(a) Heat island is on

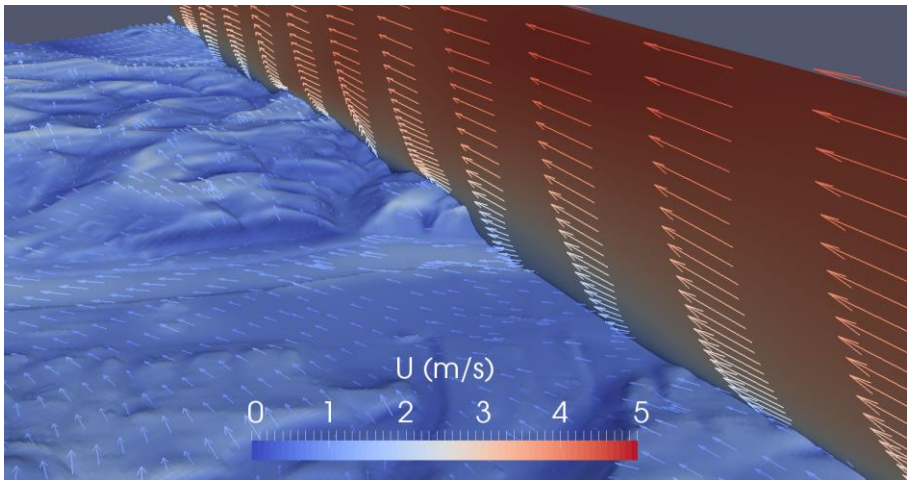

(b) Heat island is off

Figure 8.11: Velocity vectors and magnitude contours on the ground and slice cut along dominant wind direction with the heat island on and off.